ANALYSIS OF SALT-BEARING AQUEOUS SOLUTIONS IN SYNTHETIC FLUID INCLUSIONS BY MICROTHERMOMETRY AND CRYOGENIC RAMAN SPECTROSCOPY

DOCTORAL THESIS

University of Leoben
Department of Applied Geosciences and Geophysics
Mineralogy and Petrology

Mag. Miriam Baumgartner

Supervisor:
Ao.Univ.-Prof. Dr. Ronald J. Bakker

-2009-

Referees:	Ao.Univ.-Prof. Dr. Ronald J. Bakker
	Ao.Univ.-Prof. Dr. Walter Prochaska

I declare in lieu of oath, that I wrote this thesis and performed the associated research myself, using only literature cited in this volume.

Leoben, May 2009

ACKNOWLEGMENT

First of all, I would like to thank my supervisor **Prof. Ronald J. Bakker** for the initiation of the project and for offering me the PhD position. I have appreciated working with him in the *mysterious* world of fluid inclusions, thermodynamics and metastabilities. This thesis could not have been executed without his continuing interest, constructive criticism and helpful discussions. Thank you for the good collaboration and the great help in the last years!

I would like to thank also **Prof. Walter Prochaska** for crush-leach analyses and for his work as a referee of this thesis. **Prof. Larryn Diamond** (University of Bern) and **Dr. Christoph Bauer** (University of Graz) are kindly acknowledged for the use of their Raman equipment in times where our instrument was *on strike*.
Many thanks also go to **Prof. Oskar Thalhammer**, **Prof. Johann Raith** and **Dr. Federica Zaccarini** for the nice welcome at the Department and the good collaboration in the last years. Many thanks also to **Judtith Bergthaler** for her administrative work.

Special thanks must go to **Helmut Mühlhans** for sample preparations and for helping me with the technical equipment. I greatly appreciated the relaxing coffee breaks and conversations with you!

A great deal of thanks must also go to **Janine Pink** for a great friendship, for the many laughs and of course for improving my English. I also appreciated the animated discussions with **Lorenz Scheucher** at lunch and after work. Thank you for being such good colleagues!

I want to express special thanks to **Markus Kahn**, who calmed me down when I was like a "*bubble in trouble*". Thank your for your love, patience and support whenever I have needed it!

Many thanks also go to all my **friends**, especially those who diverted me from work and offered me a place to stay when I needed to escape.

Finally, I would like to thank my **family** for their encouragement and their love.

This project was financially supported by the Austrian Research Fund (FWF). Project Number: P18209-B06.

ABSTRACT

Fluid inclusions, containing salt-H_2O mixtures of NaCl-H_2O, $CaCl_2$-H_2O, $MgCl_2$-H_2O, $FeCl_2$-H_2O, $FeCl_3$-H_2O, LiCl-H_2O, $ZnCl_2$-H_2O, NaCl-$CaCl_2$-H_2O, NaCl-$MgCl_2$-H_2O and $CaCl_2$-$MgCl_2$-H_2O, were synthesised in natural quartz to study phase equilibria and salt hydrate nucleation at low temperatures. Variable freezing and melting behaviours occur depending on the composition and the salinity of the inclusions. Most systems show unpredictable phase equilibria and highly metastable phase assemblages during cooling experiments. In general, the results reveal that saline fluid enclosed in inclusions reacts more often into metastable states than into stable ones. Therefore, eutectic and peritectic temperatures, which are normally used to define the salt system in natural fluid inclusions, cannot be used. Additionally, phase transitions (e.g. at the eutectic or peritectic) are observed in temperature intervals in inclusions and may occur slightly prematurely or delayed, than anticipated from theoretical considerations. By means of optical investigations it may be difficult to observe accurate temperatures of phase transitions due to recrystallisation processes in the inclusions or simply due to microscopic resolution. Furthermore, optical identification cannot be applied to microcrystalline aggregates of hydrates and ice, which occur regularly in frozen inclusions. These results complicate the investigation of fluid composition in natural inclusions.

In the present study, Raman spectroscopy is used to detect eutectic points and phase transitions, which are optically not able to identify. $CaCl_2$-H_2O bearing inclusions demonstrate the complexity of phase equilibria in salt-H_2O systems, which occur during cooling experiments. In general, metastable phase equilibria are observed at low temperatures. The phase assemblages range from supercooled metastable liquid to ice nucleation in the presence of supersaturated brine at temperatures down to -190 °C. In addition, the formation of metastable $CaCl_2$-hydrates in highly saline inclusions was confirmed by Raman spectroscopy. Raman spectra of antarcticite ($CaCl_2 \cdot 6H_2O$), $CaCl_2 \cdot 4H_2O$ (α- and γ-modification) and sinjarite ($CaCl_2 \cdot 2H_2O$) were gained, which can be used as references for natural fluid inclusion studies. In addition, Raman spectra of different salt hydrates, such as $NaCl \cdot 2H_2O$, $MgCl_2 \cdot 12H_2O$ and $FeCl_2 \cdot 6H_2O$, are presented in the study. The spectra illustrate, that the different salt hydrates can be distinguished due to the occurrence of characteristic vibrational modes in the stretching region of water (2900 to 3900 cm^{-1}).

This study reveals that microthermometry is still the main tool for analysing the salinity and composition of fluid inclusions. Additionally, Raman spectroscopy must be used to verify microthermometric results or to specify in more detail the analysed phase changes. The results obtained from synthetic fluid inclusions present fundamental knowledge of phase equilibria (stable or metastable) at low temperatures, which can be used for the interpretation of natural fluid inclusions. In addition, Raman spectra of salt-hydrates were gained, which can be used as reference spectra to compare them with spectra obtained from natural inclusions. The application of cryogenic Raman spectroscopy to identify the salt composition of natural fluid inclusion is shown by the analysis of inclusions in dolomites (Cantabrian mountains, NW Spain).

A new Raman spectroscopic method to estimate the salinity of fluid inclusions is introduced in the present study. The morphology of Raman spectra of aqueous solutions (H_2O-NaCl mixtures) in the stretching region of water can be analysed by deconvolution using Gaussian-Lorentzian functions. The presence of salt in aqueous solutions induces a peak shift, which can be correlated to the amount of dissolved ions in a solution. For an aqueous solution in a fluid inclusion, the morphology of a Raman spectrum produced by a polarised laser beam is also influenced by the optical properties of the host crystal (birefringence), by the orientation of the mineral-fluid interface and by the depth of the inclusion within the sample. Those parameters cause polarisation effects, which are reflected in the morphology of the Raman spectrum. The impact of the individual effects on the spectra have been evaluated in detail in the present study. For natural inclusions, the morphology of the Raman spectra of aqueous solutions is simultaneously modified by all of these effects and cannot be ignored in the interpretation of salinities. From the results it is concluded that interference-free spectra can be obtained by orientating the optical axis of the host quartz crystal parallel to the plane of the polarisation of the Raman laser beam. If orientation of the sample is not feasible, the salinity of aqueous solutions can be analysed by acquiring multiple spectra throughout at least 90° rotation of the sample and determining the lowest peak positions of the deconvolved Gaussian-Lorentzian contributions. Those peak positions are in good agreement with results obtained from reference solutions and reveal the real salinity of the inclusions as proven in the study.

ZUSAMMENFASSUNG

Flüssigkeitseinschlüsse in den binären Salzsystemen von $NaCl$-H_2O, $CaCl_2$-H_2O, $MgCl_2$-H_2O, $FeCl_2$-H_2O, $FeCl_3$-H_2O, LiCl, $ZnCl_2$ und in den ternären Systemen von $NaCl$-$CaCl_2$-H_2O, $NaCl$-$MgCl_2$-H_2O und $CaCl_2$-$MgCl_2$-H_2O wurden in natürlichen Quarz synthetisiert, um Phasengleichgewichte bei Tieftemperaturbedingen zu untersuchen. In Abhängigkeit der Zusammensetzung und Salinität der Einschlüsse können unterschiedliche Frier- und Schmelzverhalten beobachtet werden. Die meisten Einschlüsse zeichnen sich durch das Auftreten von unvorhersehbaren, hoch metastabilen Phasenvergesellschaftungen aus. Eutektische und peritektische Reaktionen, die grundsätzlich zur Identifizierung des Zusammensetzung der fluiden Phase in Flüssigkeitseinschlüssen herangezogen werden, sind häufig durch das Fehlen stabiler Phasengleichgewichte nicht zu beobachten. Zusätzlich zeichnet sich das Verhalten von Flüssigkeitseinschlüssen dadurch aus, dass Phasenübergänge nicht bei theoretisch ermittelten Temperaturen, sondern in zeitlich verzögerten Temperaturintervallen auftreten. Zudem frieren Fluide häufig zu mikrokristallinen Aggregaten, wobei die Phasen optisch voneinander nicht zu unterscheiden sind. Optische Untersuchungen reichen oft nicht aus, um genaue Phasenübergänge in Flüssigkeitseinschlüssen zu bestimmen.

Die Anwendung von Raman-spektroskopischen Untersuchungen ermöglicht eine genaue Charakterisierung von Phasengleichgewichten, sowie der Phasenübergänge die in Flüssigkeitseinschlüssen auftreten. Die Ergebnisse von $CaCl_2$-H_2O-hältigen Einschlüssen demonstrieren die Komplexität der Phasengleichgewichte bei tiefen Temperaturen. Generell sind die Einschlüsse durch das Auftreten von metastabilen Phasenvergesellschaftungen charakterisiert. Stark unterkühlte Lösungen, sowie Eis in der Anwesenheit übersättigter Lösungen, können bei Temperaturen bis zu -190 °C beobachtet werden, wobei die theoretisch stabilen Salzhydrat Modifikationen abwesend sind. Im Gegensatz dazu, kann die Nukleation metastabiler Salzhydrate in hoch salinaren Einschlüssen beobachtet werden. Die verschiedenen Hydratspektren können auf Grund ihrer spezifischen Raman Banden, die in dem Wellenzahl-Bereich von 2900 bis 3900 cm^{-1} auftreten, den spezifischen Hydratphasen zugeordnet werden. Die Studie präsentiert Raman Spektren von Antarcticite ($CaCl_2.6H_2O$), $CaCl_2{\cdot}4H_2O$ (α- und γ-Modifikation) sowie Sinjarite ($CaCl_2{\cdot}2H_2O$). Weiters konnten Raman Spektren von Hydrohalite ($NaCl{\cdot}2H_2O$), $MgCl_2{\cdot}12H_2O$ und $FeCl_2{\cdot}6H_2O$ in den Einschlüssen aufgenommen werden.

Die Ergebnisse der Studie zeigen, dass mikrothermometrische Untersuchungen an Flüssigkeitseinschlüssen allein nicht ausreichend sind, um die Zusammensetzung und die Salinität von Einschlüssen zu bestimmen. Raman-spektroskopische Untersuchungen sind notwendig, um Phasengleichgewichte und Phasenreaktionen genau zu verstehen. Weiters liefern die Ergebnisse grundlegendes Basiswissen von Phasengleichgewichten bei tiefen Temperaturen, die für die Untersuchung natürlicher Einschlüsse in Mineralien ausschlaggebend sind. Die Raman Spektren der einzelnen Salzhydrate dienen als Referenzspektren für die Interpretation von Spektren natürlicher Einschlüsse unbekannter Zusammensetzung. Die Zusammensetzung natürlicher Flüssigkeitseinschlüsse in Dolomit (Kantabrisches Gebirge, NW Spanien) konnte mittels Raman Spektroskopie in Kombination mit Mikrothermometrie ermittelt werden.

Die Arbeit beinhaltet weiters eine neue spektroskopische Methode zur Bestimmung der Salinität von Flüssigkeitseinschlüssen. Raman Spektren wässriger Lösungen ($NaCl$-H_2O Mischungen) im Streckschwingungsbereich von Wasser (2900 bis 3900 cm^{-1}), ändern systematisch ihre Morphologie in Abhängigkeit der Salzkonzentration der Lösungen. Die einzelnen Spektren können mit Gauss-Lorentz

Funktionen analysiert werden, wobei eine Verschiebung der Peakpositionen zu höheren Wellenzahlen mit zunehmender Salinität beobachtet werden kann. Die Morphologien der Raman Spektren, die durch einen polarisierenden Laser generiert werden, sind von zusätzliche Effekten, wie den optischen Eigenschaften des Wirtsminerals, die Orientierung der Mineral-Fluid-Grenzfläche sowie durch die Tiefe des Einschlusses im Mineral, beeinflusst. Diese Parameter verursachen Polarisierungseffekte, die sich in den Spektren widerspiegeln. Die Auswirkung der einzelnen Effekte auf die Spektren wurde mit „simulierten“ Flüssigkeitseinschlüssen und synthetischen Einschlüssen evaluiert. Raman Spektren von natürlichen Flüssigkeitseinschlüssen werden simultan von diesen Effekten modifiziert. Die Resultate zeigen, dass ungestörte Spektren durch eine definierte Orientierung des Wirtsminerals erhalten werden können. Wenn eine exakte kristallographische Orientierung des Minerals nicht möglich ist, kann die Salintät durch systematische Rotation der Probe bestimmt werden. Dabei werden Spektren über einen Rotationswinkel von mindestens 90° aufgenommen, wobei die niedrigsten ermittelten Peakpositionen (Gauss-Lorentz Analyse) die Bestimmung der Salintät ermöglichen.

TABLE OF CONTENTS

1. AIM OF THE THESIS

The main objective of this study was the characterisation of major cations and anions in aqueous solutions in fluid inclusions, i.e. dissolved salts, by using non-destructive methods, such as microthermometry and Raman spectroscopy. The investigations were made on experimentally trapped fluids of known compositions and densities in natural quartz. Fluid inclusions were synthesised in thermal shock-fractured quartz cores by using cold-seal autoclaves. Phase equilibria in the H_2O system, binary salt-H_2O systems ($NaCl$-H_2O, $CaCl_2$-H_2O, $MgCl_2$-H_2O, $FeCl_2$-H_2O, $FeCl_3$-H_2O, $LiCl$-H_2O, $ZnCl_2$-H_2O) and ternary salt-H_2O systems ($NaCl$-$CaCl_2$-H_2O, $NaCl$-$MgCl_2$-H_2O, $CaCl_2$-$MgCl_2$-H_2O) were studied at low temperatures. In addition, the synthesised inclusions were monitored with Raman spectroscopy during temperatures cycles to characterise phase equilibria and phase transitions. Raman spectra of relevant salt hydrates were gained to use them as reference spectra for the investigation of natural fluid inclusions.

2. BACKGROUND INFORMATION

2.1. Fluid inclusions – Methods and applications

The properties and compositions of fluids are of major importance for the understanding of rock forming processes such as diagenesis, metamorphism and hydrothermal processes. Minerals have the capacity to trap small amounts of fluid in inclusions (imperfections in the crystal lattice) during their genesis, which can give direct evidence of the palaeo-geological environment. Usually, fluid inclusions are filled with aqueous solutions and gases (Fig. 2.1a). Furthermore, they also may contain solid phases (daughter crystals), which precipitate in course of over-saturation in the inclusions (Fig. 2.1b).

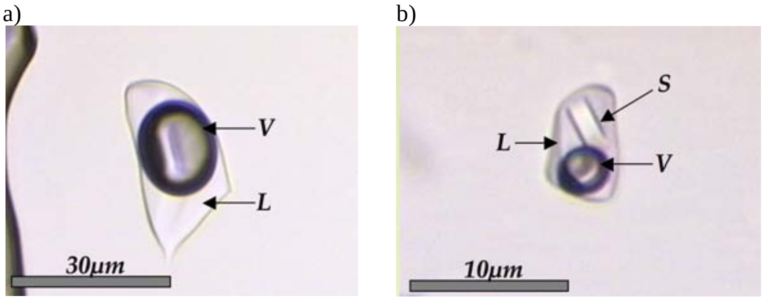

Figure 2.1. Fluid inclusions at room temperature containing a) liquid (L) and vapour (V) and b) liquid (L), vapour (V) and a solid phase (S).

The determination of fluid composition and density is the major task in fluid inclusion research and allows the interpretation of the formation conditions (temperature and pressure) and processes, which took place in the rock. Optical investigations on inclusions can only be used to define phase configuration of the enclosed components at room temperature, i.e. liquid, vapour and solid, but the composition cannot be determined. Microthermometry (heating and cooling of inclusions) is the most important analytical method and is nowadays a standard technique for fluid inclusion studies. It is the only non-destructive method, which can be applied to obtain directly qualitative and quantitative information on the composition and on trapping conditions of fluid inclusions.

2.2.1. Pressure and temperature studies (Heating of inclusions)

In general, fluid is trapped in a crystal at elevated temperatures and pressures (1 in Fig. 2.2a). The fluid is isolated in the crystal and has a constant density (isochoric system), formed at a certain point of the isochore. During uplift, subsequent cooling and pressure release proceed along the specific isochore of trapping (2 in Fig. 2.2a). The fluid contract and thereby a bubble (vapour) is formed at a specific temperature (3 in Fig. 2.2a), which is defined as the homogenisation temperature (T_h). At this temperature the isochore intersect the bubble curve and the single phase (liquid or vapour) separate into two phases (liquid and vapour). For homogeneous trapped inclusions, it is considered that this temperature is the minimum temperature of trapping. The volume fraction liquid/vapour changes along the bubble point curve in dependence on the initial fluid density (density at the trapping). Experimental heating of inclusions allows the observation of homogenisation temperatures and reveals thereby the minimum temperature of formation. The trapping conditions can be interpreted from the observed temperature, if the geothermal gradient of the geological setting or the burial depth is known (1 in Fig. 2.2a).

Three different types of homogenisation may occur during heating of inclusions: (1) homogenisation into the liquid phase, (2) homogenisation into the vapour phase and (3) critical homogenisation. Figure 2.2b illustrates a schematic diagram of the phase relationships in the binary NaCl-H_2O system. This system is defined by a relatively large immiscibility field, in which two phases coexist (liquid and vapour). Fluid inclusions may follow three different isochoric paths dependent on their density during heating. Inclusions with a density less than the critical specific volume (1 in Fig. 2.2b), will homogenise into the liquid (T_h(1) in Fig. 2.2b), whereas inclusions with a specific volume larger than the critical value (2 in Fig. 2.2b), homogenise into the vapour (T_h(2) in Fig. 2.2b). Critical homogenisation (T_h(3) in Fig. 2.2b) of an inclusion is only reached, when the fluid is trapped along the critical isochore (3 in Fig. 2.2b). Thereby, the meniscus between liquid and vapour disappear upon the critical point.

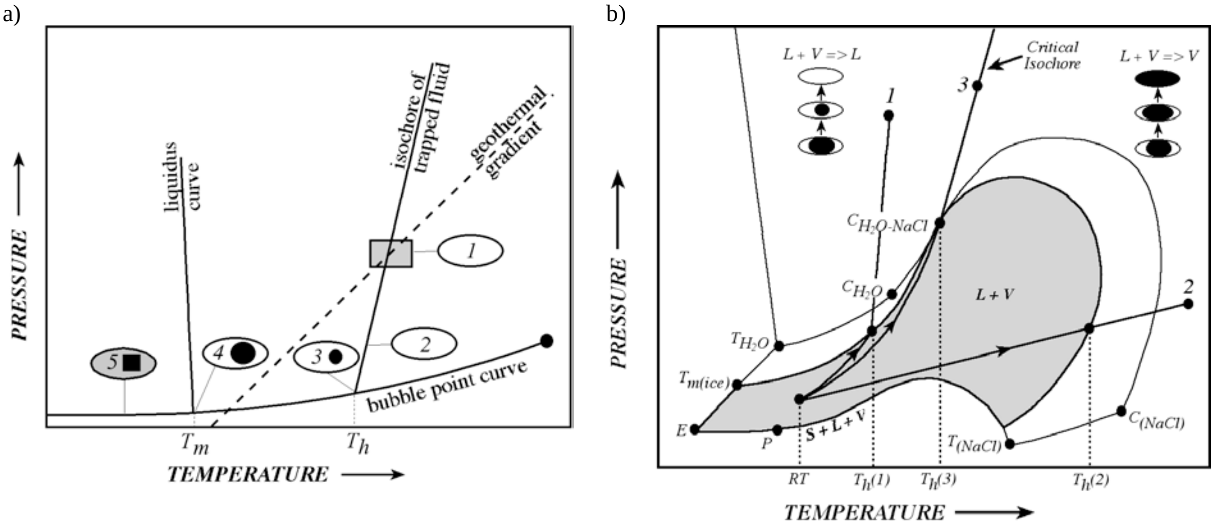

Fig. 2.2. a) Schematic P-T illustration (modified after Zwart, 1995) of a fluid inclusion trapped at elevated temperature and pressure during cooling. See text for further details. b) Schematic phase diagram (modified after Knight and Bodnar, 1989) in the NaCl-H_2O system, illustrating the homogenisation of fluid inclusions depending on of their densities. See text for further details. T_m=melting temperature; T_h=homogenisation temperature; T=triple point; E=eutectic; P=peritectic; C=critical point; L= liquid; V=vapour; S=solid; RT=room temperature;

2.2.2. Determination of fluid composition (Freezing of inclusions)

The salinity of inclusions reflects in principle the mole ratio of water and salts. Microthermometry is the only method, which can be used to obtain directly quantitative information on the salinity of fluid inclusions. In theory, aqueous solutions freeze when passing the liquidus curve (Fig 2.2a) during cooling. Fluid enclosed in inclusion behaves metastable during cooling and show typically a delay in freezing (liquid is present at much lower temperatures than might be expected). Therefore, inclusions have to be supercooled to induce solidification, whereas the amount of supercooling varies and is dependent on the inclusion shape, volume and composition (e.g. Shepherd et al., 1985). In the contrary, melting of phases (4 in Fig. 2.2a) in principle occurs in stable conditions and the observed temperatures are reliable parameters of true phase changes.

In practice, natural fluid inclusions do not consist of a single component fluid. Most fluid inclusions from diagenetic environments contain aqueous solutions with various different solutes. Dissolved salts, especially chlorides like NaCl, which reluctantly integrate into crystal lattices, are major components in natural fluid systems (e.g. Roedder, 1984; Yardley and Graham, 2002). Those solutes have a huge influence on the fluid properties and therefore, the identification of the dissolved salts is a major objective in fluid inclusion research. The presence of salts in a fluid can be inferred from relatively low melting temperatures of ice (freezing point depression). The melting temperature is a direct function of composition and therefore the ice melting temperature can be used to calculate the salinity with proper equations of state. The melting of ice in an aqueous solution below 0 °C is indicative for the presence of salt, but the type of salt cannot be determined. At present, salinity calculations from ice melting temperatures are normally based on the $NaCl-H_2O$ system and the salinity is given in equivalent mass% NaCl.

Multi component salt systems show various complex phase assemblages at low temperatures (ice and salt hydrates). The final melting temperatures of salt hydrates can also be used to determine the salinity, if the phase can be clearly identified (see Bakker, 2003 and references therein). Identification of hydrate crystals in inclusions by purely optical means, i.e. colour, habitus, birefringence and refraction index (e.g. Davis et al., 1990) can be performed with large single hydrate crystals. Nevertheless, various salt hydrates show similar optical properties and this method cannot be applied to microcrystalline aggregates of hydrates and ice, which may regularly occur in frozen inclusions. Eutectic or rather peritectic reactions can be used to define the salt system (e.g. Borisenko, 1977), because they occur at specific temperatures dependent on the salt system (e.g. Linke, 1958; Linke, 1965). Those temperatures are difficult to monitor accurately in inclusions and in addition the theoretic temperatures of phase transitions may occur in relatively small temperature ranges (e.g. $CaCl_2-H_2O$ eutectic at -49.8 °C and $CaCl_2-KCl-H_2O$ eutectic at 50.5 °C; Borisenko, 1977). Furthermore, eutectic temperatures of multi-component salt-H_2O systems are still unknown. In addition, the approach presupposes the presence of stable phase assemblages and the availability of reliable data of phase relationships. Due to metastabilities, precipitation of stable phase assemblages in salt-H_2O fluid systems is often inhibited in fluid inclusions and thereby phase transitions are often absent. Microthermometry cannot be adequately interpreted with optical methods only.

Raman spectroscopy has been improved in fluid inclusions studies in the last decades to determine the composition of inclusions (e.g. Burke and Lustenhouwer, 1987; Pasteris et al., 1988; Wopenka et al., 1990; Burke, 2001; Nasdala et al., 2004). This method was mainly focused on gas components and solid phases enclosed in the inclusions. Water as the solvent for salts has its most prominent Raman bands in the so-called stretching region (between 2900 and 3900 cm^{-1}), which presents a broad and complex profile. Dissolved electrolytes, which are present as mono-atomic ions are not Raman active, but they can influence the characteristic Raman bands of the solvent. The structure of liquid water is significantly altered if charged ions are present, which interact with the permanent dipole moments of the water molecule. With increasing number of cations and anions in the solution, the liquid structure becomes more and more coordinated (e.g. Rull and deSaja, 1986). The shape of the Raman contour shows systematically changes, which are dependent on the amount of dissolved anions and cations in the solution. Therefore, the liquid water spectra can be used to determine the salinity of fluid inclusions (Mernagh and Wilde, 1989; Dubessy et al., 2002; Baumgartner and Bakker, 2008; see Chapter 5.6).

Additionally, water and dissolved salts form salt hydrates (e.g. $NaCl^{\cdot}2H_2O$; see Fig. 2.3) at low temperatures with a well-defined number of H_2O molecules in the crystal lattice (e.g. Franks, 1972). Those molecules have a limited amount of vibration possibilities, which are most prominent in the stretching region of water. The Raman bands are characteristic for each specific salt hydrate, which offers the possibility to identify the type of dissolved salt from specific hydrate phases (Dubessy et al., 1982; Dubessy et al., 1992; Bakker, 2004). At low temperatures the vibrations of H_2O molecules are more restricted and therefore the Raman bands are more sharply defined (narrow half width/high amplitude intensity). With increasing temperature (closer to the melting points of the salt hydrates), H_2O is getting more loosely bond and the Raman bands become less well defined. Therefore, Raman spectra are measured at the lowest possible temperature (-190 °C; lower limit of the heating/freezing stage by using liquid nitrogen), to obtain accurate spectroscopic signals. Raman spectroscopy offers the only possibility for a non-destructive identification of phases and phase assemblages in fluid inclusions during microthermometrical experiments. The phase transitions, e.g. final melting, can only be fully understood by Raman spectral identification of the phase. Because eutectic reactions may inhibited due to metastability or are optically not visible, the type of dissolved salt in water can only be identified by analyses of salt hydrate spectra in frozen inclusions.

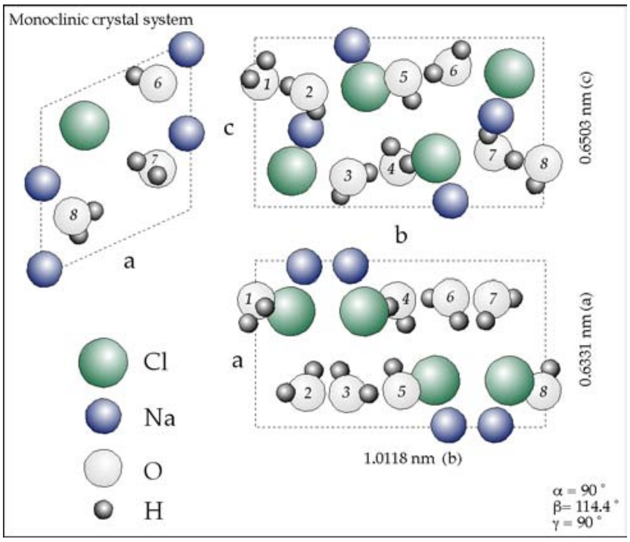

Fig. 2.3. Crystal structure of $NaCl\cdot 2H_2O$ (Bakker et al., 2007).

2.2. Phase relationships of H_2O and salt-H_2O systems at low temperatures

2.2.1. H_2O

The phase diagram of water (Fig. 2.4a) is characterised by the triple point at 0.61 kPa and 0.01 °C, where three phases are stable, i.e. ice, liquid and vapour. At standard conditions (101.33 kPa and 25 °C), water occurs in the liquid state. The critical point of water is located at 374 °C. The freezing temperature of water is defined at 0 °C, whereas hexagonal ice is formed (Ih; see Fig. 2.4b). Several modifications of ice are known, whereas their stabilities are mainly defined by pressure (e.g. Franks, 1972; Ming-Chou et al., 1988; Fortes, 2004). Microthermometry is performed at atmospheric pressure and temperature down to -196 °C (using liquid nitrogen as cooling medium). Therefore, only the hexagonal modification of ice is of relevance and occurs during cooling processes (see Fig. 2.4b).

Water enclosed in inclusions, behave different from the theoretically known phase relationship according to equilibrium thermodynamics. Freezing of pure H_2O inclusions occurs in a metastable field. The nucleation temperature of ice is observed between -35 °C and -40 °C (e.g. Bakker, 2004), well below the stable melting temperature of ice.

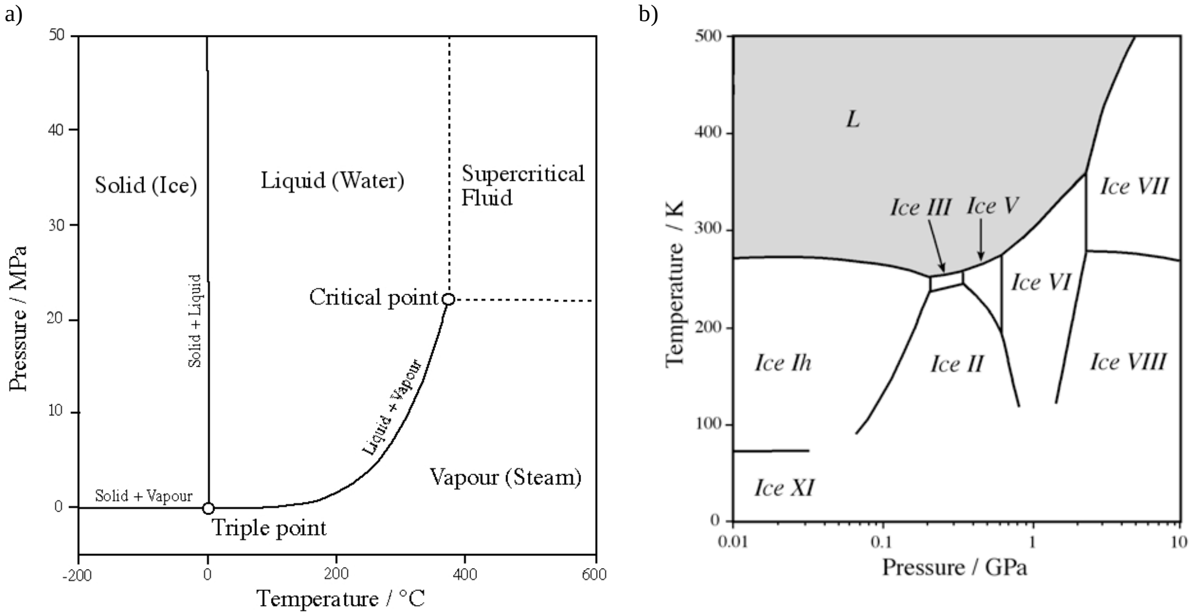

Fig. 2.4. a) Phase diagram of water (modified after Diamond, 2003). b) The equilibrium water ice phase diagram (modified after Fortes, 2004). L=liquid; V=vapour; I=ice; T=triple point; Ice Ih=hexagonal ice.

2.2.2. NaCl-H_2O

The binary NaCl-H_2O system is defined by an eutectic point at -21.2 °C (*eut* in Fig. 2.5), corresponding to a salt composition of 23.3 mass% NaCl (Linke, 1965). A peritectic point (*per* in Fig. 2.5), with an incongruently melting hydrate occurs below 100 °C. This hydrate, $NaCl\cdot 2H_2O$, is known as the mineral hydrohalite and it decomposes at the peritectic reaction at 0.1 °C (at a salt composition of 26.3 mass% NaCl) to halite (Linke, 1965). The invariant points of solutions in equilibrium with solids in the binary NaCl-H_2O system are modelled at -21.32 °C and 23.19 mass% NaCl (eutectic) and at 0.12 °C and 26.27 mass% NaCl (peritectic) by Spencer et al. (1990). A metastable eutectic exist at -28°C (e.g. Crawford, 1981; Roedder, 1984; see Fig. 2.5), where the metastable solubility curve of ice intersects the extended solubility curve of halite.

Ice and hydrohalite nucleate at low temperatures in fluid systems up to 61 mass% NaCl. Dependent on the salinity, various melting and dissolution behaviours occur above the eutectic temperature: (1) ice dissolution (0 to 23.3 mass% NaCl); (2) hydrohalite dissolution (23.3 to 26.3 mass% NaCl); and (3) halite dissolution (> 26.3 mass% NaCl).

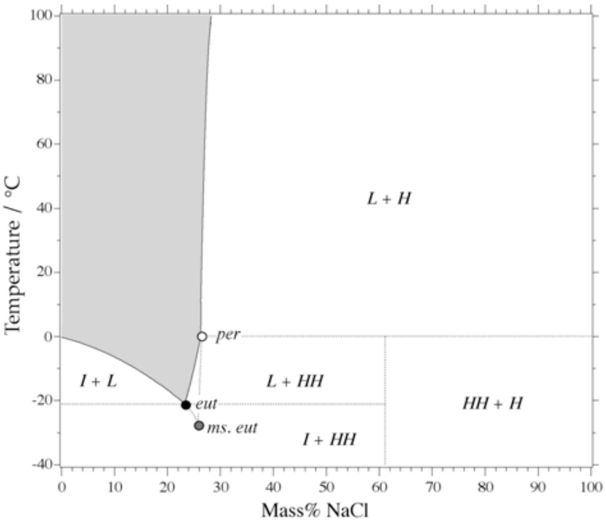

Fig. 2.5. Vapour saturated phase relationships in the NaCl-H_2O system below 100 °C constructed from solubility data presented in Linke (1965), including the metastable eutectic (ms. eut). I=ice; L=liquid; HH=hydrohalite; H=halite; eut=eutectic; per=peritectic

NaCl is one of the most prominent salts, which occurs in geological relevant fluid systems and therefore, a whole range of studies exist among the binary NaCl-H_2O system. Salinity estimations from ice melting temperatures are determined by e.g. Potter et al. (1978) and Bodnar (1993). Vapour saturated solubilities of hydrohalite and halite was studied by Sterner et al. (1988). Phase equilibria studies at high temperatures in the NaCl-H_2O were performed by e.g. Knight and Bodnar (1989), Bodnar et al. (1985) and Bodnar (1994). The phase equilibrium at low temperatures in inclusions is described by e.g. Crawford (1981), Roedder (1984) and Shepherd et al. (1985). Cryogenic studies on synthetic NaCl-H_2O fluid inclusions were performed by e.g. Davis et al. (1990), Bakker (2004) and Ni et al. (2006). The previous studies confirm that initial freezing occurs at temperatures well below the eutectic, and instead of solidification, a supercooled brine remains stable. Roedder (1984) reported the sluggishness of hydrohalite precipitation during cooling NaCl-containing fluid inclusions. Bakker (2004) confirmed the presence of hydrohalite in initial frozen inclusions in quartz by Raman spectroscopy. Eutectic melting occurs at about -21 °C, which coincides with the predicted eutectic. Nevertheless, metastable eutectic melting at about -28 °C is not uncommon in inclusions (Roedder, 1984; Davis et al., 1990). It can be inhibited by the use of slow heating rates (Crawford, 1981). Metastable behaviour is observed among the final melting of hydrohalite. Melting may occur at temperatures above 0°C (Roedder, 1984; Bakker, 2004). High saline inclusions (> 26 mass% NaCl) are characterised by the incongruent melting of hydrohalite into halite at 0.1 °C. During cooling, halite reacts to hydrohalite and should be consumed completely in inclusions containing 26.3 to 61.9 mass% NaCl. Nevertheless, hydrohalite is often formed only as a rim around the halite crystal (Crawford, 1981; Roedder, 1984; Davis et al., 1990). Such assemblages do not represent stable equilibria. Stepwise heating and cooling is useful to promote a complete reaction from halite to hydrohalite (Crawford, 1981). At room temperature high saline inclusions contain halite and liquid as a stable phase assemblage. Nevertheless, it is reported that inclusions with a salinity < 35 mass% rarely nucleate halite (Bodnar and Vityk, 1994) and instead, oversaturated brine is stable at room temperatures.

2.2.3. $CaCl_2$-H_2O

The binary $CaCl_2$-H_2O system (e.g. Linke, 1958; Crawford, 1981) has an eutectic point at -49.8 °C (*eut* in Fig. 2.6a), at which the first melt forms during a heating procedure. Two peritectic points (*per1* and *per2* in Fig. 2.6a) with incongruently melting hydrates occur at 30.1 °C, where $CaCl_2 \cdot 6H_2O$ (antarcticite) decomposes to $CaCl_2 \cdot 4H_2O$ (tetrahydrate) and at 45.1 °C, where tetrahydrate decomposes to $CaCl_2 \cdot 2H_2O$ (sinjarite).

Ice and antarcticite nucleate at low temperatures in fluid systems up to 50.7 mass% $CaCl_2$. Dependent on the salinity, various melting and dissolution behaviours occur above the eutectic temperature: (1) ice dissolution (0 to 30.2 mass% $CaCl_2$); (2) antarcticite dissolution (30.2 to 50.0 mass% $CaCl_2$); (3) peritectic melting of antarcticite (50.0 to 60.6 mass% $CaCl_2$); and (4) peritectic melting of tetrahydrate (56.6 to 75.5 mass% $CaCl_2$). A detailed description of melting sequences is given by Schiffries (1990).

Fluid inclusions may behave different to the theoretical freezing and melting behaviours due to the effect of metastability. Therefore, the ß- and γ-tetrahydrate modifications may nucleate during cooling procedures and can be metastably present with ice at low temperatures. The liquidus in systems with ß- and γ-tetrahydrate occurs at lower temperatures than with the α-modification (Fig. 2.6b). Consequently, the peritectic melting conditions with antarcticite and sinjarite are significantly lowered. Incongruently melting of tetrahydrate into sinjarite occurs at 41.0 °C and 37.5 °C with the β- and γ-modification, respectively (*perβ* and *perγ* in Fig. 2.6b). Incongruent melting of antarcticite to α-tetrahydrate (Fig. 2.6a) does not occur with the β- and γ-modifications. The presence of those hydrates results in the formation of a double eutectic, with a maximum temperature of the liquidus at the composition of antarcticite (*m* at 30.2 °C in Fig. 2.6b). These new eutectic points occur at 29.5 °C and 52.3 mass% $CaCl_2$ for the β-modification and at 29.0 °C and 53.0 mass% $CaCl_2$ for the γ-modification.

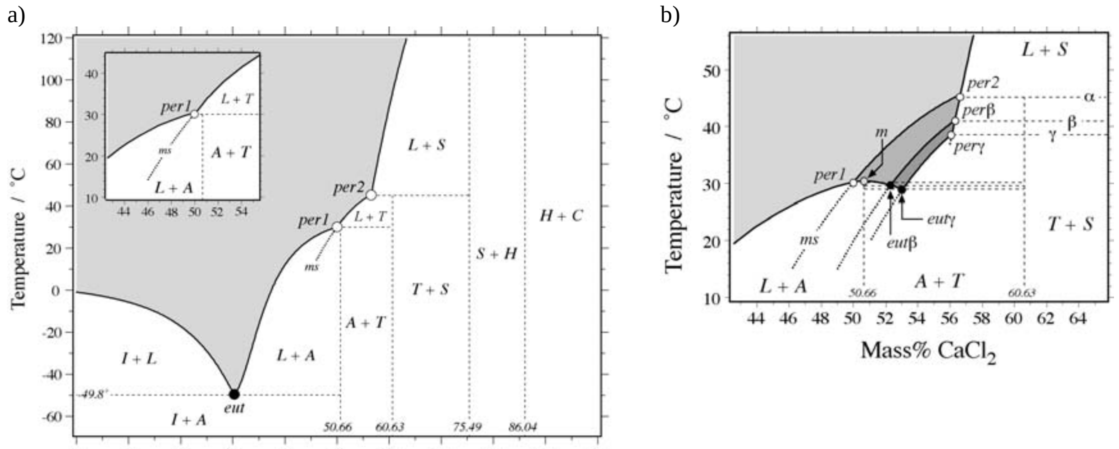

Fig. 2.6. a) Vapour saturated phase relationships in the $CaCl_2$-H_2O system below 120 °C constructed from solubility data presented by Linke (1958). b) Detailed section of the phase relations between 40 and 70 mass% $CaCl_2$, including the metastable tetrahydrate modifications (α-, β- and γ-modification). L=liquid; I=ice; A=Antarcticte; T=tetrahydrate; S=sinjarite; H=$CaCl_2 \cdot H_2O$; C=$CaCl_2$; eut=eutectic; per=peritectic; ms=metastable

An evaluation of thermodynamic consistency of solubilities in the saturated $CaCl_2$-H_2O system was done by Zeng et al. (2007). Furthermore, a comparison of different experimental data and solubility predictions are given. Thermodynamic properties and phase transitions of $CaCl_2$-hydrates at temperatures above 270 K, were described by Meisingset and Grønvold (1986). Analyses of natural $CaCl_2$-bearing fluid inclusions in quartz, halite, fluorite and calcite were interpreted in the ternary NaCl-$CaCl_2$-H_2O fluid system by Davies et al. (1990), Schiffries (1990), Zwart and Touret (1994) and Samson and Walker (2000). Those studies report unusual metastable phase equilibria at low temperatures in fluid inclusions containing high concentrations of $CaCl_2$. Most fluid inclusions studies are discussed in terms of the ternary NaCl-$CaCl_2$-H_2O sytem, because it is more relevant for natural systems (see Chapter 2.2.9).

2.2.4. $MgCl_2$-H_2O

The $MgCl_2$-H_2O system is defined by various salt hydrates, i.e. $MgCl_2{\cdot}12H_2O$, $MgCl_2{\cdot}8H_2O$ (α- and β-modification), $MgCl_2{\cdot}6H_2O$ (bischoffite), $MgCl_2{\cdot}4H_2O$ and $MgCl_2{\cdot}2H_2O$ (Linke, 1965). The ice-$MgCl_2{\cdot}12H_2O$ eutectic (*eut1* in Fig. 2.7a) occurs at -33.6 °C at a composition of 21.0 mass% $MgCl_2$. Two modifications of $MgCl_2{\cdot}8H_2O$, i.e. α- and β-modification, are known. Eutectic reactions (including $MgCl_2{\cdot}12H_2O$ and $MgCl_2{\cdot}8H_2O$) occur at -16.8 °C (31.6 mass% $MgCl_2$) and at -17.4 (32.2 mass % $MgCl_2$) for α- and β-$MgCl_2{\cdot}8H_2O$, respectively. The maximum temperature of the liquidus between the eutectics occurs at the composition of $MgCl_2{\cdot}12H_2O$ at -16.4 °C (*m* in Fig. 2.7). Incongruent melting of $MgCl_2{\cdot}8H_2O$ occurs at -3.4 °C (34.4 mass% $MgCl_2$; *per1* in Fig. 2.7b) and at -9.6 (33.9 mass% $MgCl_2$) for the α- and β-modification, respectively. The Bischoffite-$MgCl_2{\cdot}4H_2O$ peritectic is defined at 116.7 °C at composition of 46.2 mass% $MgCl_2$ (*per2* in *Fig. 2.7a*). $MgCl_2{\cdot}8H_2O$ modifications may show a delay in crystallisation along the liquidus curve (Dubessy et al., 1982). Therefore, a metastable eutectic reaction at -19.4 (33.3 mass% $MgCl_2$; *eut2* in Fig. 2.7b) may occur, including the phases $MgCl_2{\cdot}12H_2O$ and bischoffite.

Spencer and Loewenstein (1992) summarised modelled (e.g. Spencer et al., 1990) and experimental data (e.g. Linke and Seidell, 1965) of phase equilibria in the $MgCl_2$-H_2O system. The eutectic points of $MgCl_2{\cdot}12H_2O$-ice and $MgCl_2{\cdot}12H_2O$-$MgCl_2{\cdot}8H_2O$ are given at -33.02 °C at a composition of 21.26 mass% and -16.84 °C at a compositions of 31.60 mass% $MgCl_2$, respectively (Spencer et al., 1990).

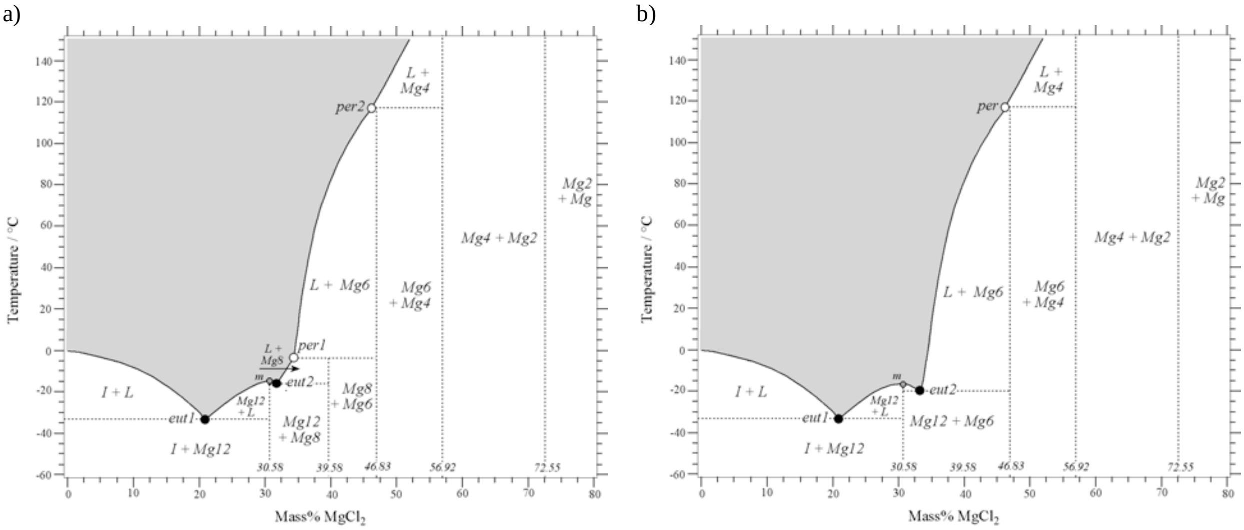

Fig. 2.7. a) Vapour saturated phase relationships in the $MgCl_2$-H_2O system below 150 °C constructed from solubility data presented in Linke (1965). b) Vapour saturated phase relationships in the $MgCl_2$-H_2O system below 150 °C in the metastable absence of $MgCl_2{\cdot}8H_2O$. L=liquid; I=ice; Mg12=$MgCl_2{\cdot}12H_20$; Mg8=$MgCl_2{\cdot}8H_2O$, Mg6=$MgCl_2{\cdot}6H_2O$; Mg4=$MgCl_2{\cdot}4H_2O$; Mg2=$MgCl_2{\cdot}2H_2O$: Mg=$MgCl_2$; eut=eutectic; per=peritectic; m=maximum.

Synthetic $MgCl_2$-H_2O fluid inclusions were studied by cryogenic Raman spectroscopy by Bakker et al. (2004). He reported the inhibition of $MgCl_2$-hydrates nucleation during cooling processes. $MgCl_2 \cdot 12H_2O$ nucleation was only observed by initial slow cooling from room temperature. Eutectic melting was observed at -33.1, which is in good agreement with the theoretical value. Davis et al. (1990) observed metastable eutectic reactions in $MgCl_2$-bearing fluid inclusions in laboratory grown halite crystals in a ternary H_2O-NaCl-$MgCl_2$ fluid system. A full interpretation of the phase relationships is not given. Nevertheless, the observed eutectic reactions indicate the precipitation of $MgCl_2 \cdot 12H_2O$, $MgCl_2 \cdot 8H_2O$ and/or bischoffite. Radvanec et al. (2004) reported the precipitation of Mg-hydrate (most probably bischoffite) in natural fluid inclusions in magnesite (talc-magnesite deposit, Slovakia). A further study (Radvanec et al., 2004) on fluid inclusions from a magnesite deposit, reveals melting points of salt hydrates, which correspond most probably to Mg-hydrates ($MgCl_2 \cdot 12H_2O$ and $MgCl_2 \cdot 8H_2O$). In general, natural fluid inclusions studies are discussed in terms of the ternary NaCl-$MgCl_2$-H_2O system (e.g. Dubois and Marignac, 1997), because it is more relevant for natural systems (see Chapter 2.2.10).

2.2.5. $FeCl_2$-H_2O

In the binary $FeCl_2$-H_2O system, three stable hydrates, i.e. $FeCl_2 \cdot 6H_2O$, $FeCl_2 \cdot 4H_2O$ and $FeCl_2 \cdot 2H_2O$, occur in frozen solutions containing up to 50 mass% $FeCl_2$ (Linke, 1958; Kirgincev et al., 1972). The eutectic is defined at -36.5 °C at a compositions of 30.4 mass% $FeCl_2$ (*eut* in Fig. 2.8.), where either ice or $FeCl_2 \cdot 6H_2O$ melts, dependent on the initial salt composition. $FeCl_2 \cdot 6H_2O$ melts incongruently at 12.3 °C (37.6 mass% $FeCl_2$; *per1* in Fig. 2.8) and form $FeCl_2 \cdot H_2O$, which on his part melts incongruently into $FeCl_2 \cdot 2H_2O$ at 76.5 °C (47.4 mass% $FeCl_2$; *per2* in Fig. 2.8).

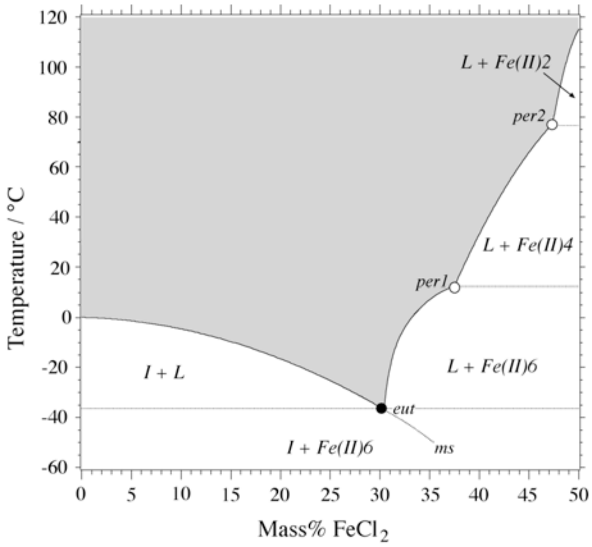

Fig. 2.8 Vapour saturated phase relationships in the $FeCl_2$-H_2O system below 120 °C constructed from solubility data presented by Linke (1958) and Kirgincev et al. (1972). L=liquid; I=ice; Fe(II)6=$FeCl_2 \cdot 6H_20$; Fe(II)4=$FeCl_2 \cdot 4H_2O$; Fe(II)3=$FeCl_2 \cdot 2H_2O$; eut=eutectic; per=peritectic; ms=metastable liquidus.

Studies of $FeCl_2$-containing fluid inclusions are rarely. Nevertheless, some investigations on natural fluid inclusions indicate the presence of $FeCl_2$ in inclusions (e.g. Koděra et al., 2004; Koděra et al., 2005). Radvanec et al. (2004) reported hydrate nucleation in inclusions from talc-magnesite deposits during cooling experiments. The hydrate could not be clearly identified, but it probably belongs to a $FeCl_2$-hydrate. The nucleation of $FeCl_2$-hydrates in natural fluid inclusions during cooling experiments is also indicated by Koděra et al. (2002) and Koděra et al. (2003), who investigated rocks from magnesite and Fe-skarn deposits. Molnár et al. (1999), denoted the precipitation of $FeCl_2$-hydrates in inclusions in granitic and metavulcanic rocks (Sudbury, Canada).

The occurrence of $FeCl_2$-hydrates in those studies was only interpreted from phase reactions during microthermometry, but not confirmed by other qualitative analysis (e.g. Raman spectroscopy). Baldassaro (1998) studied low temperature phase relations in the ternary $NaCl$-$FeCl_2$-H_2O system in synthetic inclusions. $FeCl_2$-hydrate nucleation was not observed and eutectic as well as peritectic reactions were absent. The presence of iron in natural fluid inclusions (from hypersaline granitic fluids) was identified by the use of laser ICP and synchotron-XRF microprobe analysis (Rankin et al., 1992).

2.2.6. $FeCl_3$-H_2O

The $FeCl_3$-H_2O phase equilibria at low temperatures are characterised by the occurrence of various hydrates. Solubility data are given by Linke (1958) and Kirgincev et al. (1972). The eutectic point between ice and $FeCl_3 \cdot 10H_2O$ is defined at -35.0 °C at 28.7 mass% $FeCl_3$ (*eut1* in Fig. 2.9). $FeCl_3 \cdot 10H_2O$ decomposes into $FeCl_3 \cdot 6H_2O$ at 37.0 °C and 60 mass% $FeCl_3$ (*per* in Fig. 2.9). With increasing salinity, a second eutectic point occurs at 27.4 °C (68.4 mass% $FeCl_3$; *eut2* in Fig. 2.9), a third at 30.0 °C (73.2 mass% $FeCl_3$; *eut3* in Fig. 2.9), a fourth at 55.0 (78.6 mass% $FeCl_3$; *eut4* in Fig. 2.9) and a fifth at 66.0 °C (84.0 mass% $FeCl_3$; *eut5* in Fig. 2.9). The maxima between the eutectics are given at 37 °C (60 mass% $FeCl_3$; *m1* in Fig. 2.9), at about 32 °C (71 mass% $FeCl_3$; *m2* in Fig. 2.9), at about 56 °C (78 mass% $FeCl_3$; *m3* in Fig. 2.9) and at about 74 °C (81.8 mass% $FeCl_3$; *m4* in Fig. 2.9).

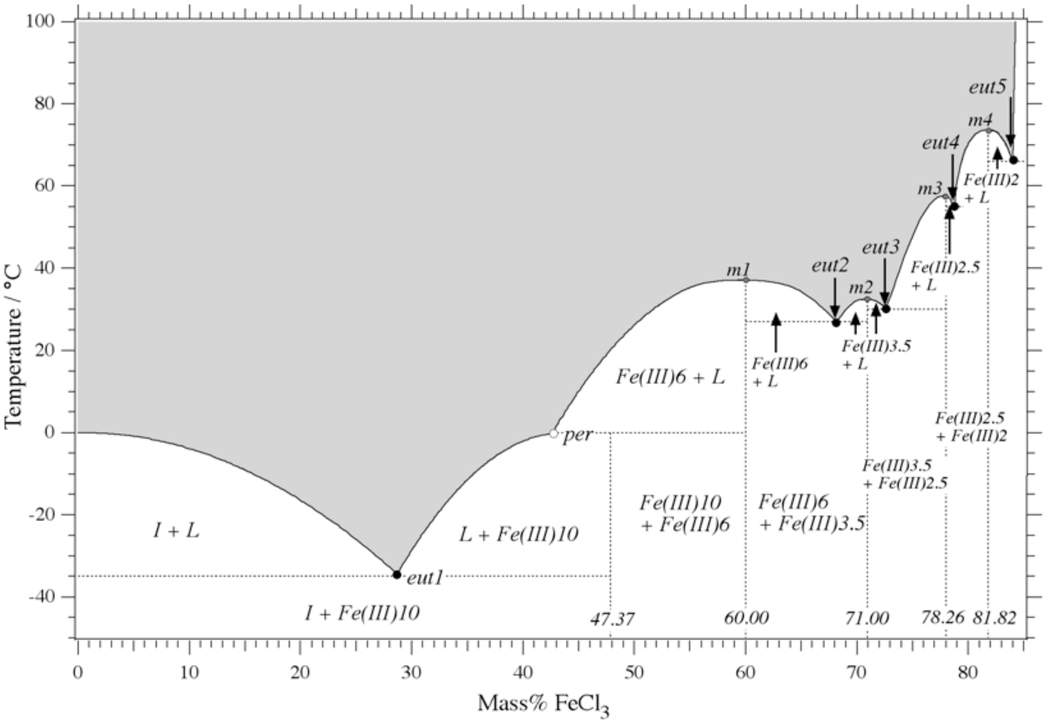

Fig. 2.9 Vapour saturated phase relationships in the $FeCl_3$-H_2O system below 100 °C constructed from solubility data presented by Linke (1958) and Kirgincev et al. (1972). L=liquid; I=ice; Fe(II))10=$FeCl_3 \cdot 10H_20$; Fe(III)6=$FeCl_3 \cdot 6H_2O$; Fe(III)3.5=$FeCl_3 \cdot 3.5H_2O$; Fe(III)2.5=$FeCl_3 \cdot 2.5H_2O$; Fe(III)2=$FeCl_3 \cdot 2H_2O$; eut=eutectic; per=peritectic; m=maximum.

2.2.7. LiCl-H_2O

The LiCl-H_2O system is characterised by the stability of four hydrates, i.e. $LiCl\cdot5H_2O$, $LiCl\cdot3H_2O$, $LiCl\cdot2H_2O$ and $LiCl\cdot H_2O$ (Fig. 2.10). The solubility data among the binary LiCl-H_2O system is quite inconsistent (see Pátek and Klomfar, 2006; and references therein). The temperature of the eutectic point is given by a great scatter of values in literature (see Figure 2.11). Pátek and Klomfar (2006) summarised the data given in literature and defined the phase transition temperature by using thermal analysis or by extrapolation of solubility curves (the reaction points are defined by intersection). The present study uses the solubility data given by Yanatieva (1946), whereas the reaction points of phase transitions (eutectic and peritectic) refer to the extrapolated values from Pátek und Klomfar (2006). The ice-$LiCl\cdot5H_2O$ eutectic is located at -78.2 °C at a compositions of 25.33 mass% LiCl (*eut* in Fig. 2.10; triangle in Fig. 2.11). Furthermore, peritectic reactions occur at -67.2 °C (29.05 mass% LiCl), at -19.5 °C (37.59 mass% LiCl), at 19.9 °C (45.32 mass% LiCl) and at 95.85 °C (56.30 mass% LiCl) corresponding to the $LiCl\cdot5H_2O \rightarrow LiCl\cdot3H_2O$, $LiCl\cdot3H_2O \rightarrow LiCl\cdot2H_2O$; $LiCl\cdot2H_2O \rightarrow LiCl\cdot H_2O$ and $LiCl\cdot H_2O \rightarrow LiCl$ transitions, respectively (*per1-4* in Fig. 2.10).

The presence of LiCl in fluid inclusions is generally derived from low eutectic points. Only in rarely cases the presence is identified by direct qualitative means, e.g. Raman spectroscopy. Cathlineau et al. (1994) identified $LiCl\cdot5H_2O$ in fluid inclusions with cryogenic Raman spectroscopy in magmatic rocks. The interpretation of the observed spectrum is based on the work of Dubessy et al. (1992). LiCl-solutions were experimentally cooled in order to nucleate $LiCl\cdot5H_2O$ and Raman reference spectra were recorded. Thermodynamic studies in the ternary LiCl-$CaCl_2$-H_2O system were performed by Zeng et al. (2008).

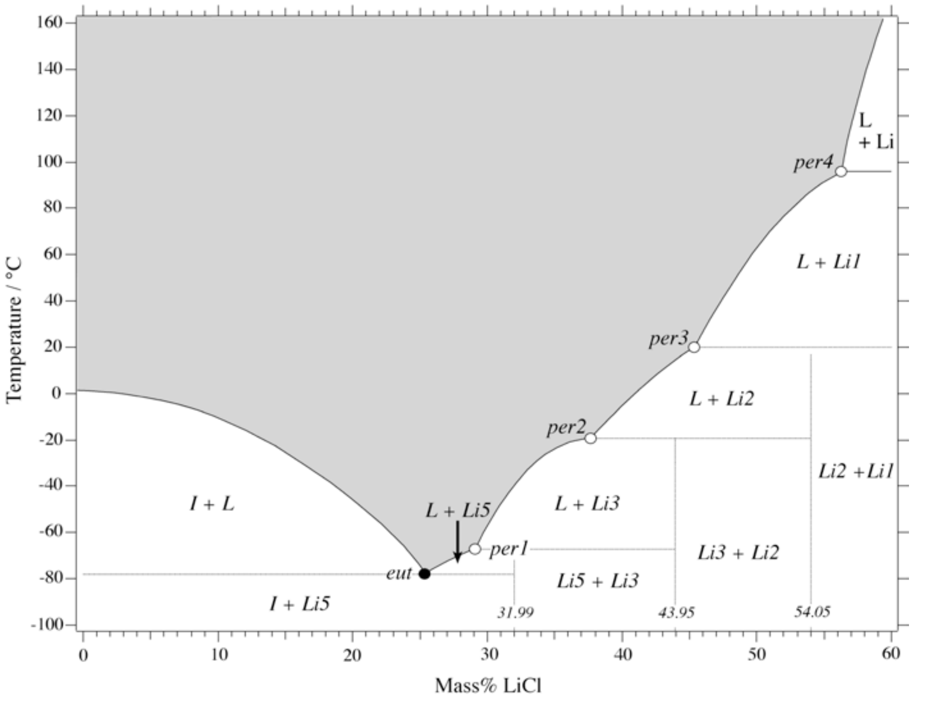

Fig. 2.10. Vapour saturated phase relationships in the LiCl-H_2O system below 160 °C constructed from solubility data given by Yanatieva (1946) and supplemented with reaction points (eutectic and peritectic) experimentally determined by Pátek und Klomfar (2006). L=liquid; I=ice; Li5=$LiCl\cdot5H_20$; Li3=$LiCl\cdot3H_2O$; Li2=$LiCl\cdot3H_2O$; Li2=$LiCl\cdot2H_2O$; Li1=$LiCl\cdot H_2O$; eut=eutectic; per=peritectic.

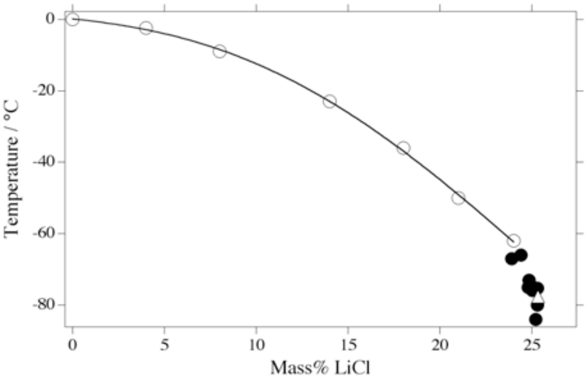

Fig. 2.11. Polynomical fit through solubility values of ice (open circles) given by Yanatieva (1946). Filled circles show the eutectic points given in literature (see Pátek und Klomfar, 2006 and references therein). The ice-$LiCl\cdot5H_2O$ eutectic (triangle) is experimentally defined at -78.2 °C at a compositions of 25.33 mass% LiCl by Pátek and Klomfar (2006).

2.2.8. $ZnCl_2$-H_2O

The $ZnCl_2$-H_2O phase equilibria at low temperatures are characterised by various different hydrates (Fig. 2.12) (Linke, 1965; Kirgincev et al., 1972). Two eutectic reactions, i.e. ice-$ZnCl_2\cdot4H_2O$ (*eut1* in Fig. 2.12) and $ZnCl_2\cdot2.5H_2O$-$ZnCl_2\cdot1.5H_2O$ (*eut2* in Fig. 2.12), are observed at -62 °C with a compositions of 51 mass% $ZnCl_2$ and at 11.5 °C with a composition of 77.0 mass% $ZnCl_2$, respectively. Additionally, four peritectic points (*per1-4* in Fig. 2.12) are observed at -30.0 °C (61.5 mass% $ZnCl_2$), at -6.5 °C (71.6 mass% $ZnCl_2$), at 26 °C (80.9 mass% $ZnCl_2$) and at 28.0 °C (81.3 mass% $ZnCl_2$). Furthermore three metastable reaction points are described by Kirgincev et al. (1972), which occur at 0.0 °C (75.5 mass% $ZnCl_2$), at 9.0 °C (78.3 mass% $ZnCl_2$) and at 26.3 °C (81.2 mass% $ZnCl_2$), including the phases $ZnCl_2\cdot3H_2O$-$ZnCl_2\cdot1.5H_2O$; $ZnCl_2\cdot2.5H_2O$-$ZnCl_2\cdot H_2O$ and $ZnCl_2\cdot1.5H_2O$-$ZnCl_2$, respectively.

Fluid inclusions studies on $ZnCl_2$-rich solutions are rare. Anderson et al. (1995) determined the local structure and speciation of zinc in hypersaline fluid inclusions by micro-XAFS. Raman spectroscopic studies on $ZnCl_2$ hydrate melts were performed by Yamaguchi et al. (1989) to study the structural features of Zn^{2+} in hydrates and in solutions.

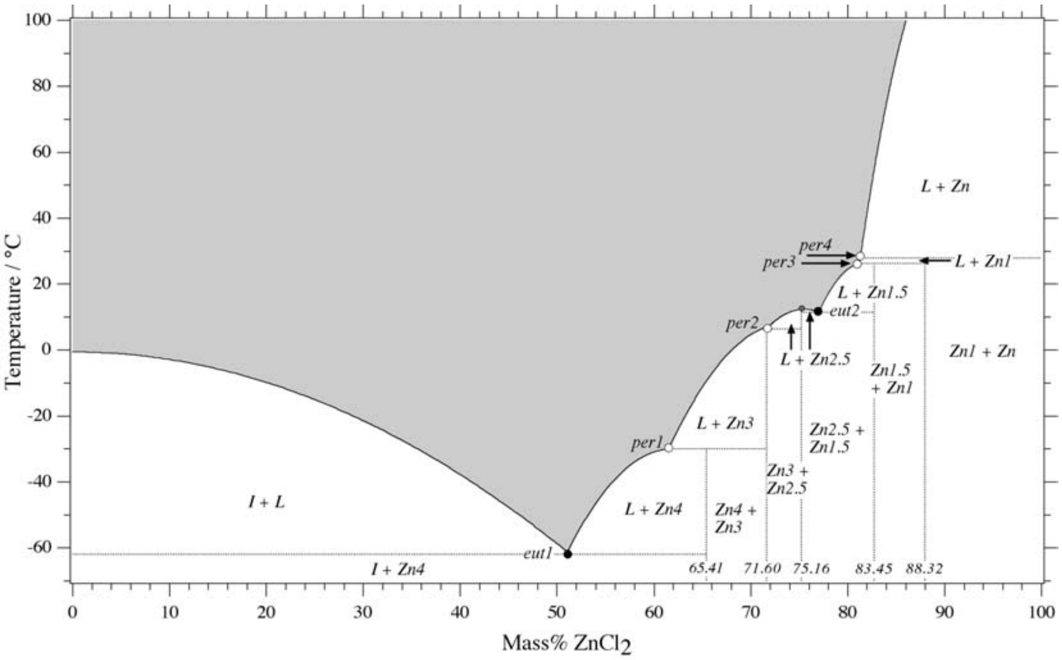

Fig. 2.12. Vapour saturated phase relationships in the $ZnCl_2$-H_2O system below 100 °C constructed from solubility data given by Linke (1965) and Kirgincev et al. (1972). L=liquid; I=ice; Zn4=$ZnCl_2\cdot4H_2O$; Zn3=$ZnCl_2\cdot3H_2O$; Li2.5=$ZnCl_2\cdot2.5H_2O$; Zn1.5=$ZnCl_2\cdot1.5H_2O$; Zn1= $ZnCl_2\cdot H_2O$; Zn=$ZnCl_2$; eut=eutectic; per=peritectic.

2.2.9. NaCl-CaCl$_2$-H$_2$O

The ternary NaCl-CaCl$_2$-H$_2$O system is defined by a relatively low eutectic at -52 °C with a salt composition of 1.8 mass% NaCl and 29.4 mass% CaCl$_2$ (Yanatieva, 1946; Fig. 2.13). Fluid compositions in the subsolidus triangle of ice and liquid (I + L field in Fig. 2.13) freeze by the nucleation of ice, hydrohalite and antarcticite. First melting occurs at the eutectic at -52 °C, where antarcticite dissolves. Ice, hydrohalite and liquid are stable above this temperature and follow the ice/hydrohalite cotectic until hydrohalite melts, and ice and liquid remain. At this temperature, the ratio of NaCl/CaCl$_2$ is fixed, because further ice melting only results in a dilution. Final melting of ice defines the salinity in terms of mass% NaCl and mass% CaCl$_2$. Fluids with an initial composition in the field hydrohalite and liquid (HH + L field in Fig.2.13) contain the same phase assemblage at low temperatures as describe before. Again, at the eutectic temperature, ice melts. At the cotectic ice dissolves completely and the last melting of hydrohalite reflects the total salinity of the inclusions. Inclusions, which are halite saturated at room temperature, show various melting sequences in dependence of the salt amount (see Schiffries, 1990). The temperature of halite dissolution is related to the total amount of NaCl and CaCl$_2$ in those inclusions. More details on phase equilibria at low temperatures in the ternary NaCl-CaCl$_2$-H$_2$O system is described by Schiffries (1990), Shepherd et al. (1985) and Crawford (1991).

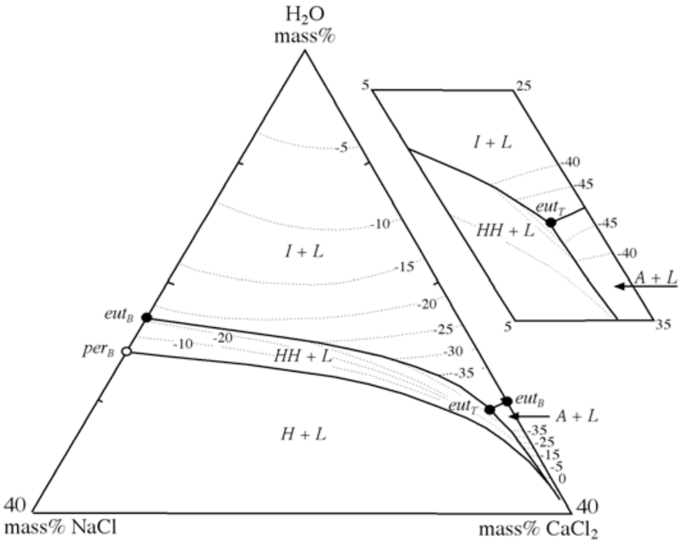

Fig. 2.13 Vapour saturated phase relationships and isotherms (dotted lines) in the NaCl-CaCl$_2$-H$_2$O modified after Shepherd et al. (1985). I=ice; L=liquid; HH=hydrohalite; A=antarcticite; eut$_T$=ternary eutectic; eut$_B$=binary eutectic; per$_B$=binary peritectic.

NaCl and CaCl$_2$ are the most prominent chlorides in natural fluid systems. Therefore, a whole range of fluid inclusion studies are discussed in this ternary water system (e.g Vanko et al., 1992; Kwak and Hing Tan, 1981; Molnár et al., 1999; Schmidt Mumm and Wolgramm, 2002; Derome et al., 2007). Further, theoretical studies and applications to fluid inclusion investigations were done by e.g. Haynes (1985), Ananthaswamy and Atkinson (1982), Oakes et al. (1990), Zwart and Touret (1994) and Spencer et al. (1990). Samson and Walker (2000) prepared standard solutions of H$_2$O-NaCl-CaCl$_2$ fluids to obtain reference Raman spectra of hydrates at low temperatures. The solubility of halite in the ternary system was estimated by Williams-Jones and Samson (1990) to evaluate the NaCl and CaCl$_2$ content of halite bearing inclusions using the final melting temperatures of ice or rather halite. Freezing and melting behaviours of inclusions in laboratory-grown halite crystals was studied by Davis et al. (1990) by optical investigations during microthermometric runs. The obtained eutectic temperature corresponds to predicted temperatures of salt hydrate melting. The presence of metastable phase assemblages is also reported in the study. Observations of low metastable eutectic temperatures (between -90 and -75 °C) were made. The metastable phases could not be clearly identified by purely optical means, but it is assumed that $CaCl_2 \cdot nH_2O$ precipitates (presumably $CaCl_2 \cdot 4H_2O$). Schiffries (1990) identified antarcticite crystals in liquid-absent natural fluid inclusions from mafic pegmatites (Bushveld) by Raman spectroscopy. Unusual phase equilibria were observed during microthermometric investigations on fluid inclusions with a high content of $CaCl_2$. Analyses of natural $CaCl_2$-bearing fluid inclusions in quartz, halite, fluorite and calcite (Davies et al., 1990; Schiffries, 1990; Zwart and Touret, 1994; Samson and Walker, 2000) were interpreted in a ternary H_2O-NaCl-$CaCl_2$ fluid system. In these studies, the presence of $CaCl_2$ was not verified by direct means, i.e. Raman spectroscopy, but was inferred from relatively low melting temperatures in the inclusions. Synthetic fluid inclusions containing H_2O-NaCl-$CaCl_2$ (Vanko et al., 1988) have revealed metastable phase behaviour at low temperature. The previous works illustrate, that $CaCl_2$ containing inclusions are strongly dedicated by metastable processes, i.e. expected phase nucleations are absent and metastable phase assemblages are present.

2.2.10. NaCl-$MgCl_2$-H_2O

The phase relationships in the NaCl-$MgCl_2$-H_2O system are shown in Figure 2.14a (modified after Borisenko, 1977). The phase relationships and phase transitions in the stability field of the Mg-hydrates are not included in most previous studies, because experimental data in the ternary NaCl-$MgCl_2$-H_2O system are quite inconsistent (see Spencer et al., 1990). Spencer et al. (1990) presented thermodynamically modelled data of phase relationships in the ternary NaCl-$MgCl_2$-H_2O. This data is used to construct a detailed phase diagram in the stability field of the Mg-hydrates shown in Figure 2.14b. The modelled values for the binary eutectics and peritectic differ slightly from data given by Linke (1958; see Chapter 2.2.2 and 2.2.4). The modelled data in the ternary system reveal the peritectic of NaCl-bischoffite-$MgCl_2 \cdot 8H_2O$ at -3.50 °C, at a composition of 0.21 mass% NaCl and 34.25 mass% $MgCl_2$. The peritectic including the phases NaCl-$MgCl_2 \cdot 8H_2O$-$MgCl_2 \cdot 12H_2O$ is defined at -17.14 °C (0.52 mass% NaCl and 31.25 mass% $MgCl_2$). The NaCl-$NaCl \cdot 2H_2O$- $MgCl_2 \cdot 12H_2O$ peritectic is defined at -22.12 °C (2.68 mass% NaCl and 24.45 mass% $MgCl_2$). The ternary eutectic, involving the phases $NaCl \cdot 2H_2O$-$MgCl_2 \cdot 12H_2O$-ice, is modelled at -35.24 °C (4.96 mass% NaCl and 18.18 mass% $MgCl_2$).

Fluid inclusion studies were performed by Dubois and Marignac (1997), who confirm the presence of NaCl and $MgCl_2$ in the inclusions by observing eutectic melting temperatures at about -35 °C. Davies et al. (1990) studied fluid inclusions in experimental grown halite crystal in the ternary NaCl-$MgCl_2$-H_2O system. Various complex phase assemblages, including $MgCl_2.nH_2O$ ($MgCl_2.8H_2O$, $MgCl_2.6H_2O$), were observed at low temperatures. Stable as well as metastable eutectic melting was observed. The identification of the phase assemblages was only studied by optical observations and interpreted from eutectic melting temperatures. The presence of halite, hydrohalite, $MgCl_2 \cdot 12H_2O$, $MgCl_2 \cdot 8H_2O$ and bischoffite, is discussed in the article, but is not confirmed by the use of qualitative analytical methods (e.g. Raman spectroscopy).

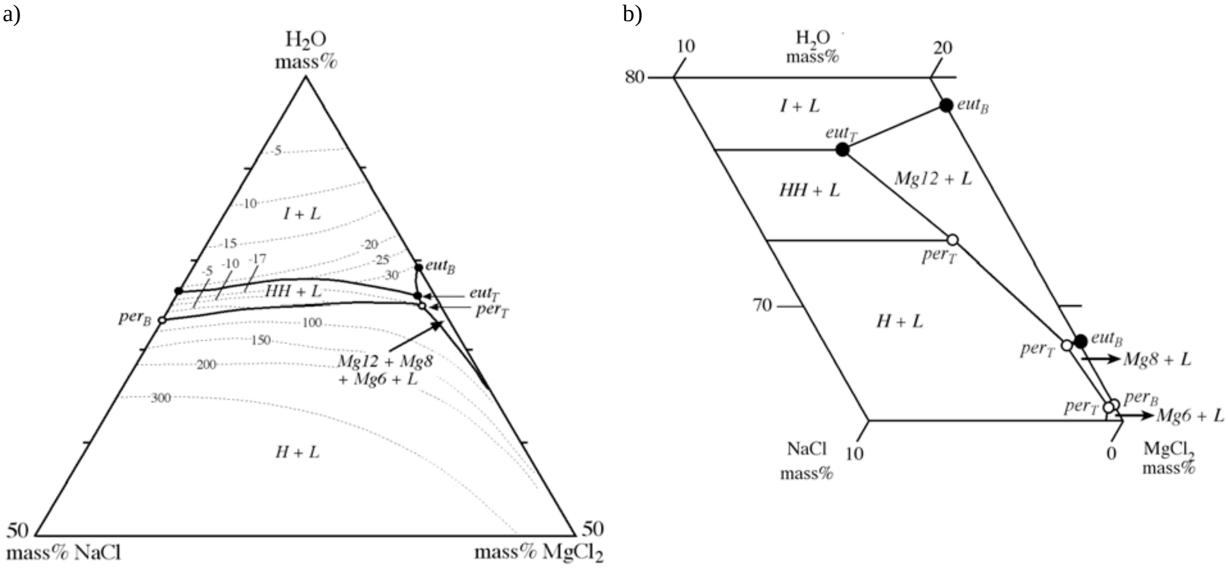

Fig. 2.14. a)Vapour saturated phase relationships and isotherms (dotted lines) in the NaCl-$MgCl_2$-H_2O modified after Borisenko (1977). b) Detail section of the vapour saturated phase relationship in the NaCl-$MgCl_2$-H_2O constructed after values given by Spencer et al. (1990). I=ice; L=liquid; HH=hydrohalite; Mg12=$MgCl_2 \cdot 12H_2O$; Mg8=$MgCl_2 \cdot 8H_2O$; Mg6=$MgCl_2 \cdot 6H_2O$; eut_T=ternary eutectic; per_T=ternary peritectic; eut_B=binary eutectic; per_B=binary peritectic.

2.2.11. $CaCl_2$-$MgCl_2$-H_2O

The phase relationships in the $CaCl_2$-$MgCl_2$-H_2O system, shown in Figure 2.15a, are constructed after the data given by Prutton and Tower (1932), Yanatieva (1946) and Linke (1965). The system is defined by the antarcticite-$MgCl_2 \cdot 12H_2O$-ice eutectic at -55.0 °C at 26.0 mass% $CaCl_2$ and 5 mass% $MgCl_2$ (Yanatieva, 1946). Prutton and Tower (1932) define this point at -52.2 °C at 27.4 mass% $CaCl_2$ and 2.93 mass% $MgCl_2$. This observation is in good agreement with modelled data from Spencer at el. (1990), with values given at -52.2 °C at 27.1 mass% $CaCl_2$ and 3.5 mass% $MgCl_2$. The Bischoffite-$MgCl_2 \cdot 8H_2O$-antarctcite and $MgCl_2 \cdot 8H_2O$-$MgCl_2 \cdot 12H_2O$-bischoffite peritectic are determined experimentally at -6.7 °C at 9.9 mass% $CaCl_2$ and 26.4 mass% $MgCl_2$ and at -20.7 °C at 10.6 mass% $CaCl_2$ and 23.2 mass% $MgCl_2$, respectively (Prutton and Tower, 1932). The peritectic points are modelled at -6.6 °C (9.4 mass% $CaCl_2$ and 27.2 mass% $MgCl_2$) and at -22.5 °C (11.7 mass% $CaCl_2$ and 22.5 mass% $MgCl_2$) by Spencer et al. (1990).

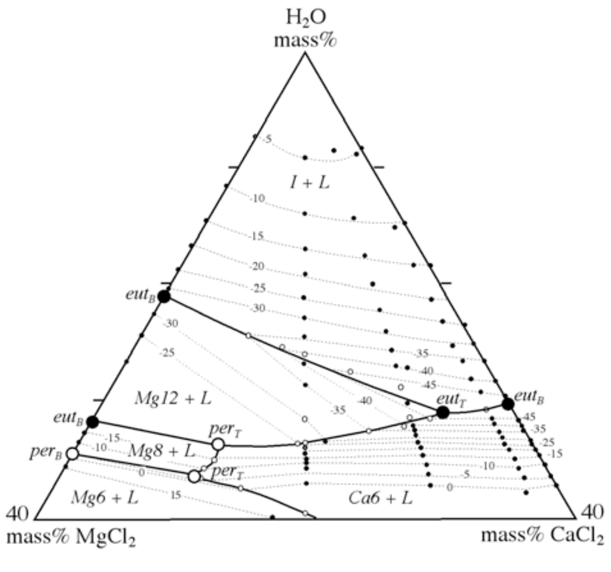

Fig. 2.15. Vapour saturated phase relations and isotherms (dotted lines) in the $MgCl_2$-$CaCl_2$-H_2O system. Solubility data (open dots) and values for isotherms (filled dots) refer to Yanatieva (1946). The ternary is supplemented from data given by Prutton and Tower (1932). Binary reactions points refer to Linke (1957, 1965). L=liquid; I=ice; Mg12=$MgCl_2 \cdot 12H_2O$; Mg8=$MgCl_2 \cdot 8H_2O$; Mg6=$MgCl_2 \cdot 6H_2O$; Ca6=$CaCl_2 \cdot 6H_2O$; eut_B=binary eutectic; eut_T=ternary eutectic; per_B=binary peritectic; per_T=ternary peritectic.

3. SYNTHESIS OF FLUID INCLUSIONS

Little information is still available on the physical and chemical properties of fluids from geological environments. The synthesis of fluid inclusions of known compositions and trapping conditions (temperature and pressure) allows experimental studies on fluid behaviour. The experimental results build the base for the interpretation of fluid-rock interaction in natural systems.

First experimental studies on fluid trapped in minerals were performed by Sorby (1857), who studied the crystal formation from aqueous chloride solutions. In the course of the crystal growth, fluid was trapped in “cavities”. Laemmlein (1929) fissured halite crystals, whereas the fractures were filled with an aqueous NaCl solution. Due to fracture healing, the formation of fluid inclusions was studied. Nowadays, the methods of synthesis have upgraded and various kinds of syntheses exist. In general, all syntheses are performed by fracture healing processes. Hydrothermal–apparatus systems are nowadays used so promote the healing process, which allow the synthesis of fluid inclusion at elevated temperatures and pressure. Thereby, fluid trapped at certain formation conditions can be studied, which mimic natural systems. Different types of synthesis are described by e.g. Shelton and Orville (1980); Bodnar and Sterner (1987), Pironon (1990), Dubessy et al. (2000), Teinturier and Pironon (2003) and Hack and Mavrogenes (2006).

3.1. Sample preparation

Fluid inclusions were synthesised according to the method described by Bodnar and Sterner (1987). The source material for the synthesis was natural, fluid-inclusion free quartz. Cores with a diameter of 3 mm were drilled from the quartz by using a diamond hollow drill. The quartz cores were cracked by heating them up to 400 °C and subsequent immersing them into cold distilled water. The cores were cleaned in an ultrasonic bath for several minutes and afterwards dried at about 100 °C to remove all the water from the cracks. Pure gold-tubes of about 4 cm length were used as synthesis chamber. After flame cleaning those tubes were welded on one side and afterwards filled with the quartz core, a few microliter of aqueous solution and a small amount of silica. The silica was added to promote the fracture healing during the experimental run. After filling, the tubes were immediately closed by welding. The prepared capsules were insert into the pressure vessels, were the synthesis was performed for about 14 days by defined pressure and temperature conditions. During the synthesis, fracture healing of the quartz took place and thereby fluid got enclosed in inclusions. After removing the capsules from the autoclaves the tubes were opened. The gained quartz cores were cut in discs of 1mm and were polished on both sides. The discs were used for microthermometric as well as for Raman spectroscopic investigations. Figure 3.1 illustrates schematically the formation of fluid inclusions during the synthesis.

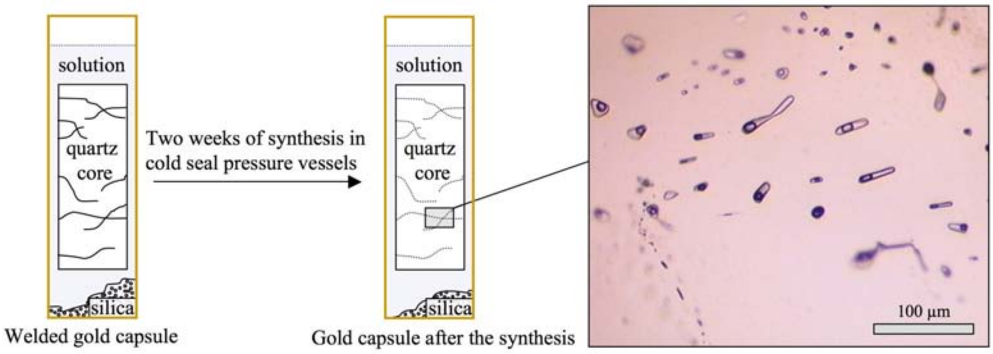

3.1. Schematic image of a gold capsule before and after synthesis modified after Keppler and Audétat (2005).

3.2. Hydrothermal laboratory

A pressure pump system (Fig. 3.2), connected to ten cold seal pressure vessels with external furnace (Fig. 3.3a), was used for the synthesis of fluid inclusions. Argon gas was used as pressure medium. Up to 100 MPa, a membrane compressor (see Fig. 3.2) was used to compress the argon in the system, whereas an air-driven liquid pump was used for achieving pressures up to 1000 MPa (see Fig. 3.2). After loading the gold capsules (see Chapter 3.1) into the pressure vessels (Fig. 3.3b), the vessels were connected to the pressure pump system and in addition to a water-cool-system (to cool the lower part of the autoclaves). The vessels were locked by a valve from the pressure pump system at the start of the synthesis. External furnaces (see Fig. 3.3a) were used to heat the vessel up to experimental conditions (temperature limit 800 °C). Internal thermocouples recorded the temperature directly adjacent to the gold capsules. Due to heating, the pressure in the vessel increased (see blue line in Fig. 3.4a). After reaching the desired experimental temperature, the vessels were connected (by opening the valve) to the pump system and the desired experimental pressure was adjusted (see blue line in Fig. 3.4a). The temperature and pressure conditions during the experimental run were controlled via a computer (Fig. 3.4 and Fig. 3.5). In general, the pressure and temperature in the system can be hold constant during the synthesis (about 14 days). The pressure is very sensitive to any changes in temperature (see Fig. 3.5). Small fluctuations in experimental conditions were caused by the water-cool-system (see Fig. 3.5). Variations in the water flow, due to e.g. the day/night circle, directly affect the experimental conditions. At the end of the synthesis, cooling of the pressure vessels was performed along the specific isochoric path of the experiments. The pressure was released in adjustment to the temperature decrease, to prevent decrepitation or stretching of the fluid inclusions (Fig. 3.4b). More details of hydrothermal techniques are described by Ulmer and Barnes (1987).

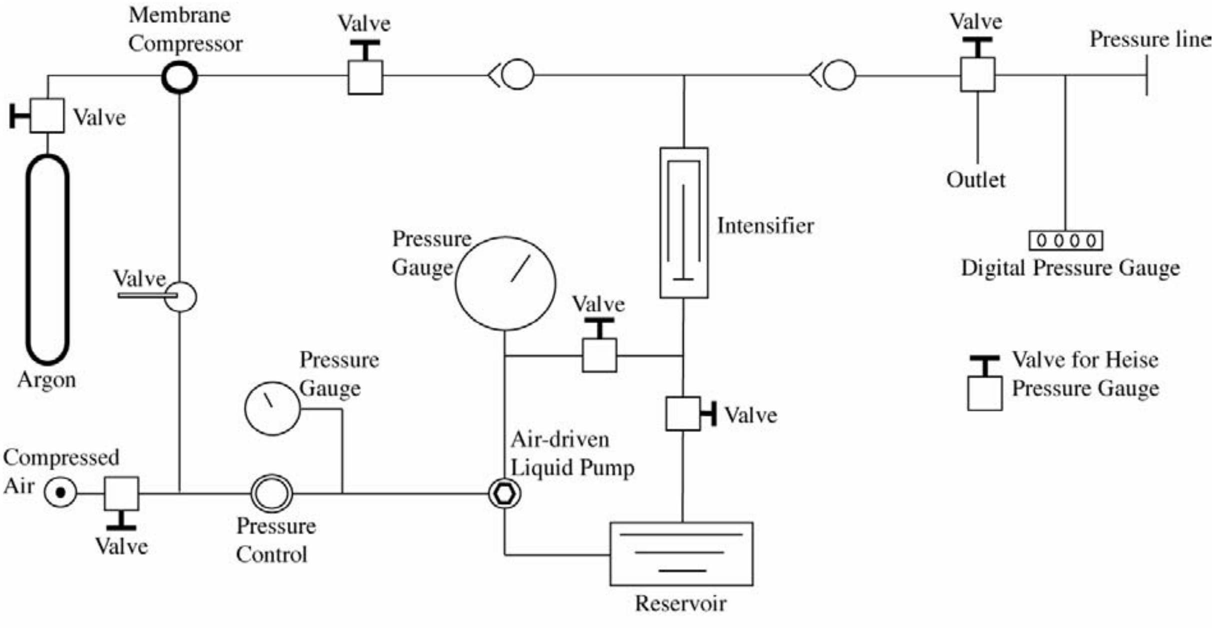

Fig. 3.2. Schematic image of the pressure-pump system

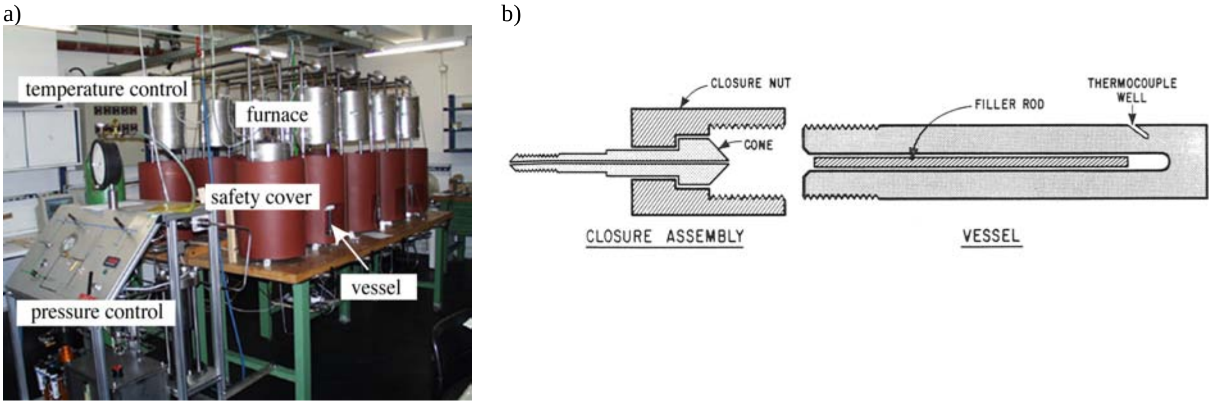
a)

b)

Fig. 3.3. (a) High-temperature-pressure-laboratory. (b) Cross section of cold-seal vessel and closure assembly (Kerrick, 1987)

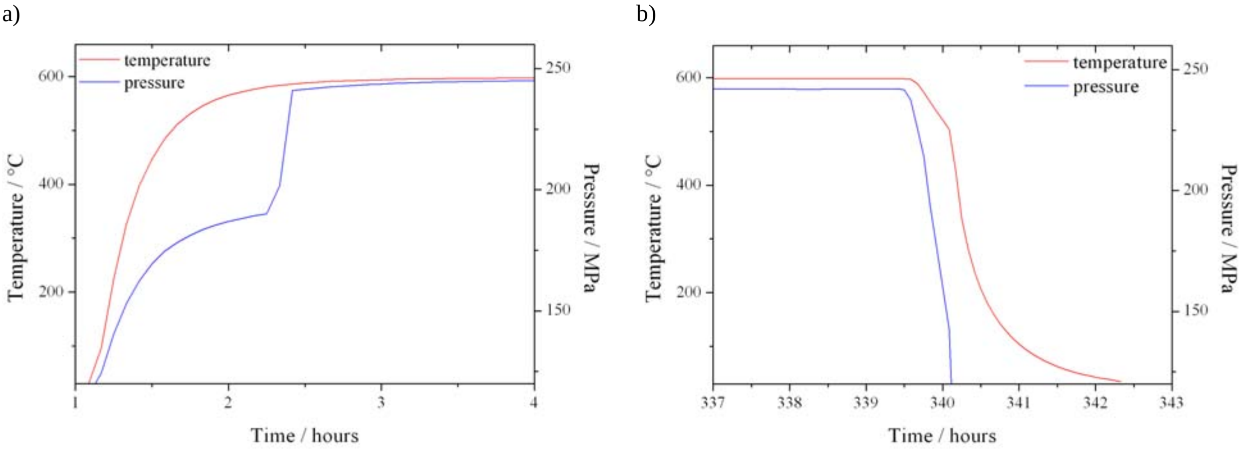
a)

b)

Fig. 3.4. a) Experimental temperature and pressure conditions during the start of the synthesis (experiment 002) b) Experimental conditions during cooling down the pressure vessel along a specific isochoric path (experiment 002).

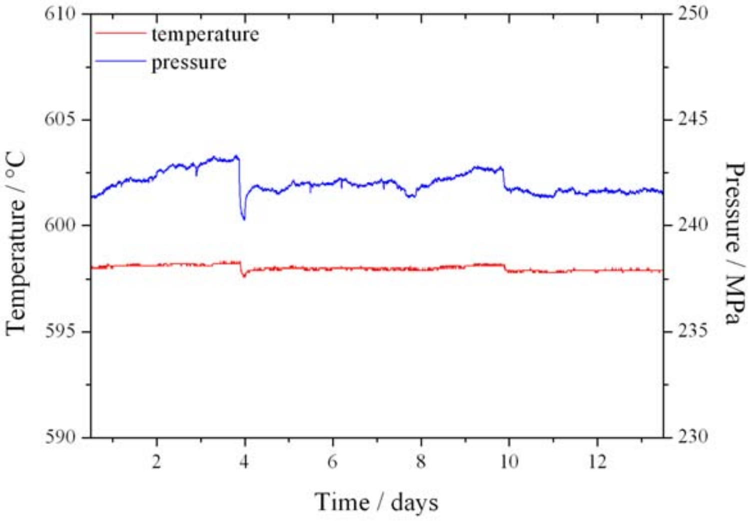

3.5. Experimental conditions (temperature and pressure) during the run of the synthesis of experiment 002.

3.3 Experimental conditions

The chosen composition for the synthesis of fluid inclusions can be divided into the pure H_2O system, binary salt-H_2O systems ($NaCl$-H_2O, $CaCl_2$-H_2O, $MgCl_2$-H_2O, $FeCl_2$-H_2O, $FeCl_3$-H_2O, $LiCl$-H_2O, $ZnCl_2$-H_2O) and ternary salt-H_2O systems ($NaCl$-$CaCl_2$-H_2O, $NaCl$-$MgCl_2$-H_2O, $CaCl_2$-$MgCl_2$-H_2O).

3.3.1 H_2O

Various samples of pure H_2O inclusions were synthesised with the experimental conditions given in Table 3.1. The crack healing process took place at about 600 °C at pressures of about 86 to 87 MPa. The desired pressure of experimentation was selected to obtain critical homogenisation temperatures of water at about 374 °C for all of the experiments. In special cases, experiments were performed with drilled quartz cores of well-known orientation, used for the investigation of polarisation effects (see Chapter 5.6).

Table 3.1. Experimental conditions of the synthesis of H_2O fluid inclusions. *P* (pressure) and *T* (temperature) represent the experimental conditions.

Experiment	Orientation*	days	*P* / MPa	*T* / °C
001	unknown	record failure	record failure	record failure
003	unknown	15	87.4 (±0.6)	589.1 (±1.3)
027	$[0001]$	15	86.4 (±0.6)	588.1 (±0.6)
028	$[10\bar{1}0]$	15	86.5 (±1.0)	600.2 (±0.1)
029	$[10\bar{1}0]$	15	86.1 (±0.5)	601.3 (±0.1)
040	unknown	15	86.0 (±1.0)	600.1 (±0.1)
041	$[2\bar{1}\bar{1}0]$	15	86.5 (±0.8)	602.2 (±0.2)
042	$[10\bar{1}1]$	15	86.4 (±0.4)	600.3 (±1.1)
054	unknown	13	85.9 (±0.2)	600.3 (±0.1)

* Line orientation parallel to the length of the cylindrical quartz core

3.3.2 Binary salt-H_2O systems

In the binary salt-H_2O system various experiments were synthesised in the laboratory with their experimental conditions given in Table 3.2. Crack healing for all experiments took place at about 600 °C at varying pressures between 99 and 311 MPa. The desired pressure of experimentations in the NaCl-H_2O, $CaCl_2$-H_2O and $MgCl_2$-H_2O systems was calculated according to equation of state of Zhang and Frantz (1987) using the program *ISOC* (Bakker, 2003) to obtain homogenisation temperatures at about 400 °C. Calculations of isochors for the synthesis in the salt systems $FeCl_2$-H_2O, $FeCl_3$-H_2O, LiCl-H_2O and $ZnCl_2$-H_2O were not practicable because of the lack of proper equation of states. The experimental conditions were chosen to be sure that the trapping of the inclusions during the synthesis was homogenous and was in the one-phase field.

Table 3.2. Experimental conditions of fluid inclusions synthesised in binary salt-H_2O systems. P is pressure and T is temperature.

Salt-System	Experiment	mass%	days	P / MPa	T / °C
NaCl-H_2O	002	23	14	226.0 (±0.5)	598.0 (±0.1)
NaCl-H_2O	004	23	14	225.6 (±0.4)	602.6 (±0.3)
NaCl-H_2O	008	4	16	129.9 (±0.5)	599.2 (±0.2)
NaCl-H_2O	009	6	14	137.2 (±1.8)	601.3 (±0.1)
NaCl-H_2O	010	8	14	145.7 (±1.8)	600.3 (±0.2)
NaCl-H_2O	011	10	15	158.5 (±0.5)	600.6 (±0.5)
NaCl-H_2O	012	12	14	164.8 (±0.2)	600.4 (±0.2)
NaCl-H_2O	013	14	14	174.9 (±0.8)	601.4 (±0.1)
NaCl-H_2O	014	16	13	193.3 (±1.6)	600.6 (±0.6)
NaCl-H_2O	015	18	14	195.7 (±0.3)	601.3 (±0.1)
NaCl-H_2O	016	20	14	206.2 (±0.4)	600.3 (±0.2)
NaCl-H_2O	017	16	15	195.2 (±0.2)	599.4 (±0.3)
NaCl-H_2O	018	22	14	229.7 (±1.1)	600.3 (±0.3)
NaCl-H_2O	019	24	14	231.3 (±0.1)	600.3 (±0.3)
NaCl-H_2O	055	23	14	148.6 (±0.4)	600.2 (±0.4)
$CaCl_2$-H_2O	005	30	15	309.9 (±0.6)	601.2 (±0.2)
$CaCl_2$-H_2O	020	30	15	196.6 (±1.1)	601.0 (±0.2)
$CaCl_2$-H_2O	021	45	15	280.2 (±0.4)	600.1 (±1.0)
$CaCl_2$-H_2O	022	15	14	148.5 (±0.8)	600.3 (±0.2)
$CaCl_2$-H_2O	037	10	17	135.8 (±0.4)	599.6 (±0.6)
$CaCl_2$-H_2O	039	10	15	197.0 (±0.7)	600.7 (±0.2)
$CaCl_2$-H_2O	044	15	16	148.1 (±0.3)	599.8 (±0.5)
$CaCl_2$-H_2O	045	30	15	195.9 (±0.1)	601.2 (±0.2)
$MgCl_2$-H_2O	025	15	15	194.5 (±0.9)	601.3 (±0.1)
$MgCl_2$-H_2O	026	30	15	309.7 (±1.8)	600.2 (±0.2)
$MgCl_2$-H_2O	030	30	15	310.1 (±2.9)	600.0 (±0.3)
$MgCl_2$-H_2O	046	15	15	193.6 (±3.4)	599.9 (±1.0)
$MgCl_2$-H_2O	047	30	15	310.6 (±0.3)	601.2 (±0.2)

Table 3.2. Continued

Salt-System	Experiment	mass%	days	*P* / MPa	*T* / °C
$FeCl_2$-H_2O	RJB 006	11	5	145.9 (±38.9)	594.0 (±0.3)
$FeCl_2$-H_2O	RJB 007	36	9	150.1 (±46.1)	566.3 (±3.0)
$FeCl_2$-H_2O	RJB 011	30	10	201.3 (±0.3)	600.7 (±0.2)
$FeCl_3$-H_2O	RJB 008	25	8	201.9 (±2.3)	600.2 (±0.1)
$FeCl_3$-H_2O	RJB 016	15	13	200.6 (±0.1)	602.8 (±0.2)
LiCl-H_2O	053	10	14	100.0 (±0.1)	599.8 (±0.5)
LiCl-H_2O	056	25	13	130.8 (±0.2)	600.0 (±0.6)
$ZnCl_2$-H_2O	048	40	17	268.1 (±0.6)	579.1 (±0.1)
$ZnCl_2$-H_2O	049	30	18	194.8 (±0.4)	600.2 (±0.2)
$ZnCl_2$-H_2O	052	10	14	98.7 (±0.2)	600.0 (±0.2)

3.3.3 Ternary salt-H_2O systems

In the ternary salt systems, experiments with varying salinity and composition were synthesised in the laboratory with their experimental conditions given in Table 3.3. The crack healing process took place at about 600 °C at varying pressures between 164 and 314 MPa. The desired pressures of experiments in the system NaCl-$CaCl_2$-H_2O and NaCl-$MgCl_2$-H_2O were calculated according to Zhang and Frantz (1987) using the program *ISOC* (Bakker, 2003). Calculations of isochors for the synthesis in the salt system $CaCl_2$-$MgCl_2$-H_2O were not practicable because of the lack of proper equation of states. The experimental conditions were chosen to be sure that the trapping of the inclusions during the synthesis was homogenous and was in the one-phase field.

Table 3.3 Experimental conditions of fluid inclusions synthesised in ternary salt-H_2O systems. *P* is pressure and *T* is temperature.

Salt-System	Experiment	mass% $NaCl_2$	mass% $CaCl_2$	mass% $MgCl_2$	days	*P* / MPa	*T* / °C
NaCl-$CaCl_2$-H_2O	006	12	12	-	15	227.4 (±0.8)	600.2 (±1.3)
NaCl-$CaCl_2$-H_2O	007	1.4	29.8	-	15	301.8 (±0.6)	600.2 (±0.2)
NaCl-$CaCl_2$-H_2O	023	1.4	29.8	-	16	314.0 (±2.0)	599.8 (±0.9)
NaCl-$CaCl_2$-H_2O	024	10	20	-	16	268.8 (±1.7)	600.5 (±0.7)
NaCl-$CaCl_2$-H_2O	031	1.4	29.8	-	13	314.0 (±0.7)	599.6 (±0.1)
NaCl-$MgCl_2$-H_2O	032	10	-	20	18	151.1 (±0.8)	601.3 (±0.2)
NaCl-$MgCl_2$-H_2O	033	10	-	13	18	156.8 (±0.5)	600.1 (±0.1)
NaCl-$MgCl_2$-H_2O	035	2	-	24	18	123.4 (±0.1)	600.1 (±0.1)
NaCl-$MgCl_2$-H_2O	038	10	-	13	15	200.3 (±0.4)	600.8 (±0.2)
$CaCl_2$-$MgCl_2$-H_2O	050	-	10	10	14	164.1 (±0.4)	600.8 (±0.9)
$CaCl_2$-$MgCl_2$-H_2O	051	-	10	20	14	164.1 (±0.2)	599.5 (±0.5)

4. METHODS

4.1. Microthermometry

The principle of microthermometry is based on heating and cooling of inclusions to induce phase changes. This allows the estimation of several parameters like homogenisation temperatures (T_h), freezing temperatures (T_{xx}), melting temperatures (T_m), eutectic temperatures (T_E), peritectic temperatures (T_P) and temperatures of phase transitions. Those obtainable parameters are used for the interpretation of the composition of the fluid system as well as of formation conditions.

Microthermometry was performed with a LINKAM MDS 600 heating-freezing stage, which was attached on a microscope stage. The sample chamber was heated by thermal conduction to 600 °C and cooled to -196 °C by liquid nitrogen. The stage was calibrated with synthetic fluid inclusions of CO_2 (melting at – 56.6 °C) and H_2O (melting at 0.0 °C and critical homogenisation at 374.0 °C). The analytical failure of the measurements is about 0.2 °C. All observations were made with an Olympus 100x long-working-distance objective (LMPlanFI, 0.80 numerical aperture). Microthermometric studies were performed to study phase relationships of salt containing aqueous solutions at low temperatures by cooling synthesised fluid inclusions in quartz. As nucleation (freezing of the aqueous solutions) is often inhibited in fluid inclusions due to metastabilities, different cycling runs were performed with using different cooling and heating parameters. The cooling and heating rates vary between 3°/min up to 30°/min. Additionally, subsequent heating and freezing was performed with using stepwise time delays up to one hour. Heating of inclusions was performed to obtain the homogenisation temperatures.

4.2. Salinity estimations from final melting points of solids

The salinity of fluid inclusions can be calculated from final ice or hydrate melting points, gained from microthermometric investigations. Salinity calculations in the pure H_2O system were performed with the software AqSo5e (Bakker, 2003; according to Potter et al. 1978). Calculations in the $NaCl-H_2O$ system were performed with the software BULK (Bakker 2003; according to Bodnar, 1993). Polynomial best fits through the solubility data of ice (Fig. 4.1a; Eq. 4.1), antarcticite (Fig. 4.1b; Eq. 4.2), α-tetrahydrate (Fig. 4.1c; Eq. 4.3), sinjarite (Fig. 4.1d; Eq. 4.4), β-tetrahydrate (Fig. 4.1e; Eq. 4.5) and γ-tetrahydrate (Fig. 4.1f; Eq. 4.6) were performed in the $CaCl_2-H_2O$ system (values given by Linke, 1958). Equation 4.1, 4.2, 4.3, 4.5 and 4.6 were used for salinity calculations.

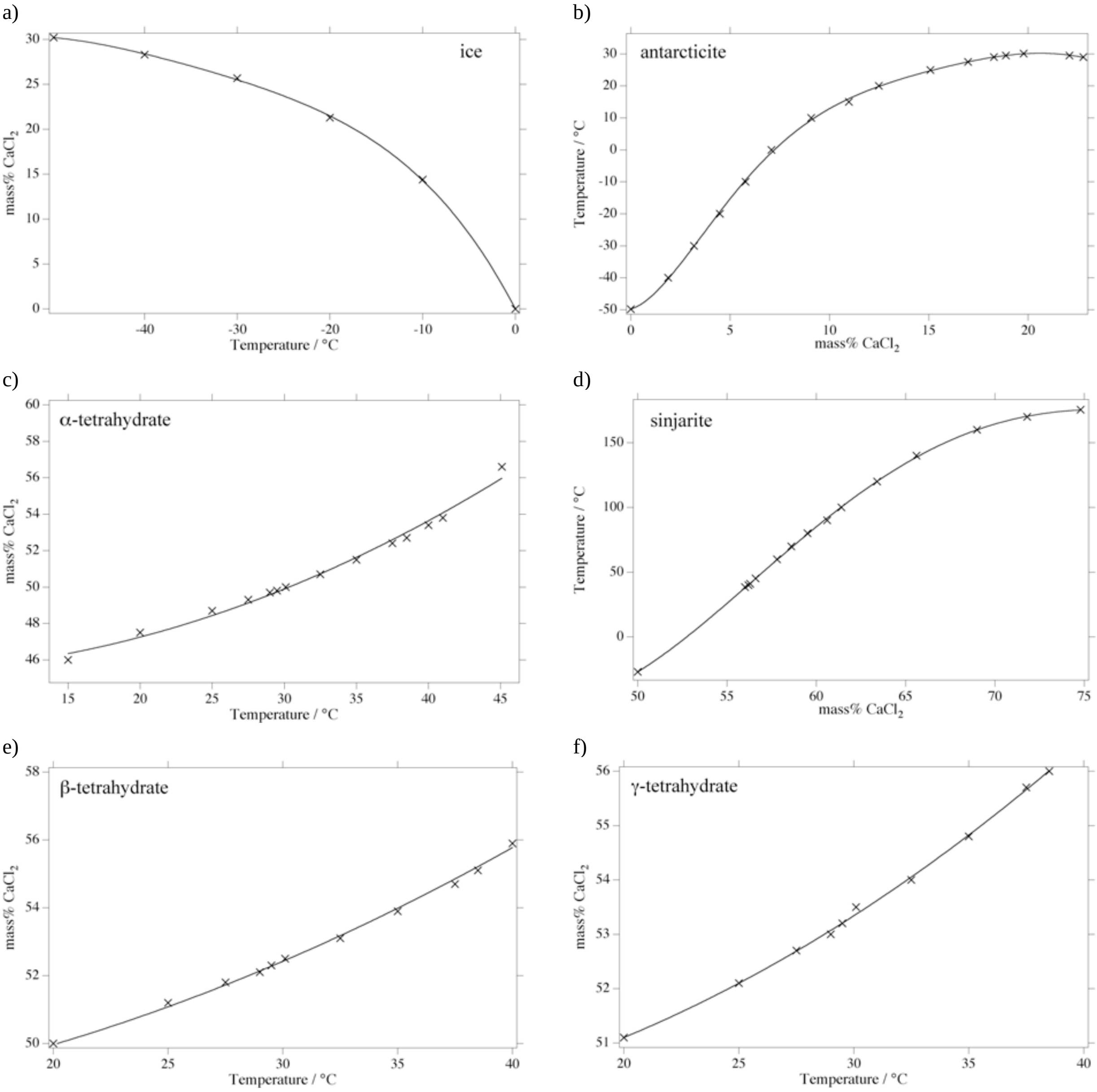

Fig. 4.1. Polynomial best fits through the solubility data (Linke, 1958) of a) ice, b) antarcticite, c) α-tetrahydrate, d) sinjarite, e) β-tetrahydrate and f) γ-tetrahydrate. An additional metastable reaction point is added to the solubility curve of sinjarite at -27 °C and 50 mass% CaCl$_2$, resulting from observations made in this study (see Chapter 5.1).

$$w = -1.9676 \cdot T - 0.064352 \cdot T^2 - 0.0011468 \cdot T^3 - 8.1 \cdot 10^{-6} \cdot T^4 \tag{4.1}$$

$$\begin{aligned} T = {} & -49.8 + 1.9995 \cdot wd + 2.1473 \cdot wd^2 - 0.31895 \cdot wd^3 \\ & + 0.01986 \cdot wd^4 - 0.00058197 \cdot wd^5 + 6.521 \cdot 10^{-6} \cdot wd^6 \end{aligned} \tag{4.2}$$

$$w = 45.291 - 0.01221 \cdot T + 0.0055249 \cdot T^2 \tag{4.3}$$

$$T = 8925.2 - 589.32 \cdot w + 13.956 \cdot w^2 - 0.14092 \cdot w^3 + 0.00051823 \cdot w^4 \tag{4.4}$$

$$w = 47.725 + 0.022852 \cdot T + 0.0044603 \cdot T^2 \tag{4.5}$$

$$w = 49.545 - 0.019602 \cdot T + 0.0048721 \cdot T^2 \tag{4.6}$$

where w is mass% $CaCl_2$, wd is the differential mass% (w-30.22) and T is the temperature in °C. Metastable extensions of the solubility curves are included in the equations 4.2, 4.3, 4.4, 4.5 and 4.6. The equations 4.1 and 4.3 are valid from 0 °C to -50 °C, and 15 °C to 46 °C, respectively. The equations 4.2 and 4.4 are valid, from 30 to 53 mass%, and from 49 to 75 mass% $CaCl_2$. The equations 4.5 and 4.6 are valid from 10 °C to 41 °C, and 10 °C to 38 °C, respectively. Polynomial fitting presented in equation 4.2 and 4.4 cannot be performed in the reversed manner, i.e. mass% as a function of temperature, due to mathematical restrictions.

The salt content of $MgCl_2$-H_2O containing inclusions was calculated with the software AqSo3e (Bakker, 2003; according to Dubois and Marignac, 1997). Salinity calculations based on metastable ice melting temperatures (ice melting below the eutectic; see Chapter 5.1, experiment 030) in the $MgCl_2$-H_2O system are performed with equation 4.7, resulting from a polynomial best fit through the solubility data of ice (Fig. 4.2; values given by Linke, 1965). Equation 4.7 is theoretically valid from 0 to 21 mass% $MgCl_2$ and from 0 to -33.6°C. Nevertheless, the equation can be extrapolated into the metastable field.

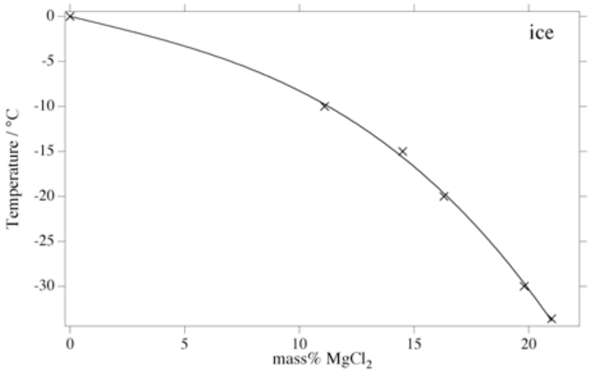

Fig. 4.2. Polynomial best fits through the solubility data of ice in the system $MgCl_2$-H_2O (Linke, 1965).

$$T = (-0.61557) \cdot w + (0.0027691) \cdot w^2 + (-0.0023922) \cdot w^3 \tag{4.7}$$

Salinity calculations, based on polynomial best fits through the solubility data of ice in the systems $FeCl_2$-H_2O, $FeCl_3$-H_2O, LiCl-H_2O and $ZnCl_2$-H_2O (Fig. 4.2; values given by Linke, 1958 and 1965), are given by equation 4.8, 4.9, 4.10 and 4.11. Equation 4.8 is valid from 0 to 30 mass% $FeCl_2$, equation 4.9 from 0 to 29 mass% $FeCl_3$, equation 4.10 from 0 to 26 mass% LiCl and equation 4.11 from 0 to 51 mass% $ZnCl_2$.

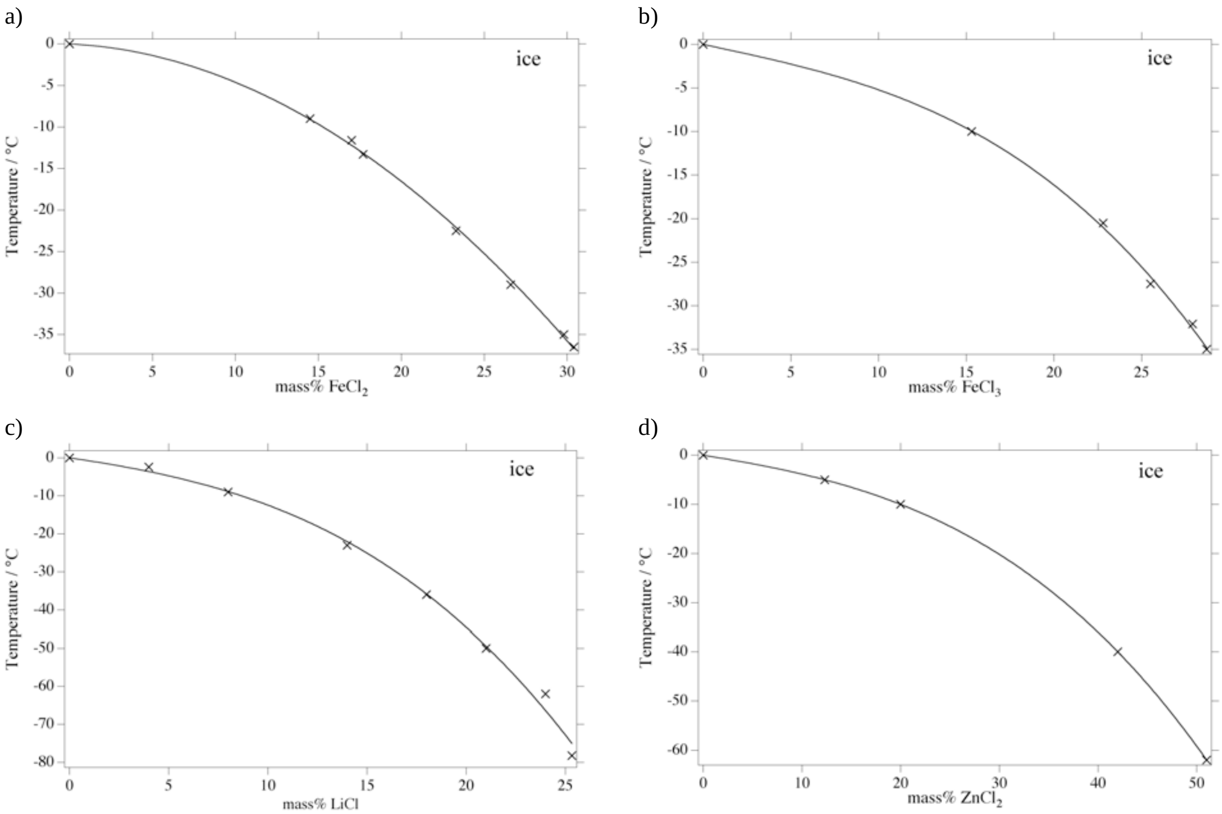

Fig. 4.3. Polynomial best fits through the solubility data for ice (Linke, 1958; Linke, 1965) in the system a) $FeCl_2$-H_2O, b) $FeCl_3$-H_2O, c) LiCl-H_2O and d) $ZnCl_2$-H_2O.

$$T = -0.095696 \cdot w - 0.036575 \cdot w^2 \qquad (4.8)$$

$$T = -0.43056 \cdot w + 0.00061394 \cdot w^2 - 0.00097176 \cdot w^3 \qquad (4.9)$$

$$T = -0.77838 \cdot w - 0.020768 \cdot w^2 - 0.002584 \cdot w^3 \qquad (4.10)$$

$$T = -0.32517 \cdot w - 0.0031321 \cdot w^2 - 0.00028097 \cdot w^3 \qquad (4.11)$$

Salinity calculations in the ternary NaCl-$CaCl_2$-H_2O and NaCl-$MgCl_2$-H_2O were performed with the software AqSo2e (Bakker, 2003; according to Naden, 1996) and AqSo3e (Bakker 2003; according to Dubois and Marignac, 1997), respectively. Salinity estimations from the melting temperatures of $MgCl_2 \cdot 12H_2O$ and ice in the ternary $CaCl_2$-$MgCl_2$-H_2O were based on Figure 2.15 (Chapter. 2). The salinity was approximated by purely geometrical means from the phase diagram. Table. 4.1 summarises the used software and/or references used for salinity calculations in this thesis.

Table 4.1 Software and/or related references used for salinity calculations.

Salt-system	Phase	Software*	Equation**	Reference
H_2O	ice	AqSo5e	-	Potter et al. (1978)
$NaCl-H_2O$	ice	BULK	-	Bodnar (1993)
$CaCl_2-H_2O$	ice	-	4.1	Linke (1958)
$CaCl_2-H_2O$	antarcticite	-	4.2	Linke (1958)
$CaCl_2-H_2O$	α-tetrahydrate	-	4.3	Linke (1958)
$CaCl_2-H_2O$	γ-tetrahydrate	-	4.6	Linke (1958)
$MgCl_2-H_2O$	ice	AqSo3e	-	Dubois and Marignac (1997)
$MgCl_2-H_2O$	ice (metastable)	-	4.7	Linke (1965)
$FeCl_2-H_2O$	ice	-	4.8	Linke (1958)
$FeCl_3-H_2O$	ice	-	4.9	Linke (1958)
$LiCl-H_2O$	ice	-	4.10	Linke (1965)
$ZnCl_2-H_2O$	ice	-	4.11	Linke (1965)
$NaCl-CaCl_2-H_2O$	ice	AqSo2e	-	Naden (1996)
$NaCl-CaCl_2-H_2O$	hydrohalite	AqSo2e	-	Naden (1996)
$NaCl-MgCl_2-H_2O$	Ice	AqSo3e	-	Dubois and Marignac (1997)
$NaCl-MgCl_2-H_2O$	hydrohalite	AqSo3e	-	Dubois and Marignac (1997)
$NaCl-MgCl_2-H_2O$	$MgCl_2 \cdot 12H_2O$	AqSo3e	-	Dubois and Marignac (1997)
$CaCl_2-MgCl_2-H_2O$	ice	-	-	Yanatieva (1946)
$CaCl_2-MgCl_2-H_2O$	$MgCl_2 \cdot 12H_2O$	-	-	Yanatieva (1946)

* used software refer to Bakker (2003)

** this study

4.3. Raman spectroscopy

Raman spectroscopy allows a non-destructive investigation of fluid inclusion composition. Identification of fluid and solid species were performed with a LABRAM (ISA Jobin Yvon) instrument using a frequency-doubled 120 mW Nd-YAG laser with an excitation wavelength of λ=532.6 nm. The polarisation state of the laser is consistent with the north-south direction (*y*-axis) of the microscope stage. All measurements were taken with an LMPlanFI 100x/0.80 n.a. (Olympus) objective lens. Measurements have a precision of 1.62 cm^{-1} at low $\Delta \nu$ (around 0 cm^{-1}) and 1.1 cm^{-1} at high $\Delta \nu$ (around 3000 cm^{-1}). For internal calibration, silicon (520 cm^{-1}), polyethylene (1062 cm^{-1}, 1128 cm^{-1}, 1169 cm^{-1}, 1295 cm^{-1}, 1487 cm^{-1}, 1439 cm^{-1}, 2848 cm^{-1}, 2881 cm^{-1}), calcite (156 cm^{-1}, 283 cm^{-1}, 713 cm^{-1}, 1087 cm^{-1}, 1437 cm^{-1}) and diamond (1332 cm^{-1}) were used. In general, Raman spectra were taken between 2900 and 3900 cm^{-1}, where aqueous solutions as well as salt hydrates have their prominent peaks.

4.3.1. Raman spectra adaptation and measurement conditions

Salt hydrates

Raman spectra of salt hydrates were taken by attaching a LINKAM MDS 600 heating-freezing stage to the Raman spectrometer. The method described by Dubessy et al. (1982) and Bakker (2004) was applied for those investigations. During heating and freezing of inclusions, hydrates nucleated and were measured subsequently at various temperatures. The method allows the identification of different phase assemblages, which cannot be characterised by optical means. Furthermore, the temperature of phase transition (i.e. eutectic, peritectic and melting points) was evaluated by changes in the Raman spectra. Measurement times varied in dependence of the signal intensity of the inclusion (dependent on the volume of the inclusions, respectively the volume of the hydrate crystal and depth of the inclusions in the quartz). Generally the integration time was chosen between 10 and 300 seconds.

Aqueous solutions

As the Raman measurement of liquid phases is very temperature sensitive, the spectra for the estimation of the salinity and the study of polarisation effects (see Chapter 5.6) were taken at a constant temperature (22 °C) with varying integration times depending on the signal intensity of the inclusion. A background correction was done, by subtracting the quartz host spectrum directly adjacent to the inclusions from the signal of the fluid (see also Bakker, 2004). In some cases, a second baseline correction was done with a straight-line correction. The latter was only performed in cases when the spectrum subtraction of the host mineral did not result in a straight horizontal background signal at zero intensity due to irregular fluorescence.

In contrast to the Raman measurement of homogeneous surfaces and pure solutions, measurements of fluid inclusions are more complicated. Inclusions with equal fluids may reveal significantly different Raman signals, i.e. amplitude intensity, due to the total inclusion volume, inclusion shape, and the depth of focus. To compensate these effects for direct comparison of individual fluid inclusions, the whole spectrum was normalised by scaling the maximum amplitude, at approximately 3500 cm^{-1} to equal intensities. Normalisation was not performed for the comparison of peak positions and peak intensity ratios of different saline aqueous solutions. All operations (background correction and normalisation) were enabled with *LABSPEC 2.09* (Horiba, Jobin Yvon) software.

The study of temperature dependent spectral evolution of pure H_2O inclusions was done with inclusions with the sample surface orientated perpendicular to the optical axis (c-axis) to avoid the influence of polarisation effects (see Chapter 5.6). Raman spectra of cooled liquids (below 20 °C) were taken by attaching a LINKAM MDS 600 heating-freezing stage to the Raman spectrometer.

4.3.2. Experimental setups and special features

Reference Raman spectra of pure water and saline solutions (up to 24 mass% NaCl) were taken in open plastic tubes with a volume of about 480 mm^3. The depth of focus was adjusted to obtain a maximum intensity of the spectrum. The deconvolved spectra were used to compare measurements made on “free drops” with measurements in fluid inclusions with similar salinities (see Chapter 5.6).

Correlations between the geometric properties of inclusions and contour modifications in the Raman bands were investigated with five fluid inclusions in experiment 019. The shape and size (including length and projected area) of these inclusions were defined according to the method of Bakker and Diamond (2006) by rotating the sample stepwise on a spindle stage. The spindle stage was adopted under the Raman spectrometer on the microscope stage.

To investigate the crystal orientation effects on the Raman spectra, samples were rotated over 180° in steps of 10° on the microscope stage. The rotation angles 0, 90, and 180° was defined as three extinction positions, where at 0° the *c*-axis is parallel to the north-south direction of the microscope stage, i.e. parallel to the laser polarisation plane. In these sets of measurements on the same inclusion, the liquid phase was always measured at the same location within the inclusion. For distinct orientations of the host crystal, quartz cores were drilled parallel to the *c*-axis, i.e. direction $\left[0001\right]$, perpendicular to the *c*-axis, i.e. direction $\left[10\bar{1}0\right]$ and parallel to the *a*-axis, i.e. direction $\left[10\bar{1}1\right]$. One orientation was drilled exactly perpendicular to one of the rhombohedral-planes $\left[2\bar{1}\bar{1}0\right]$. Figure 4.4 shows a schematic image of a quartz crystal with its optical properties.

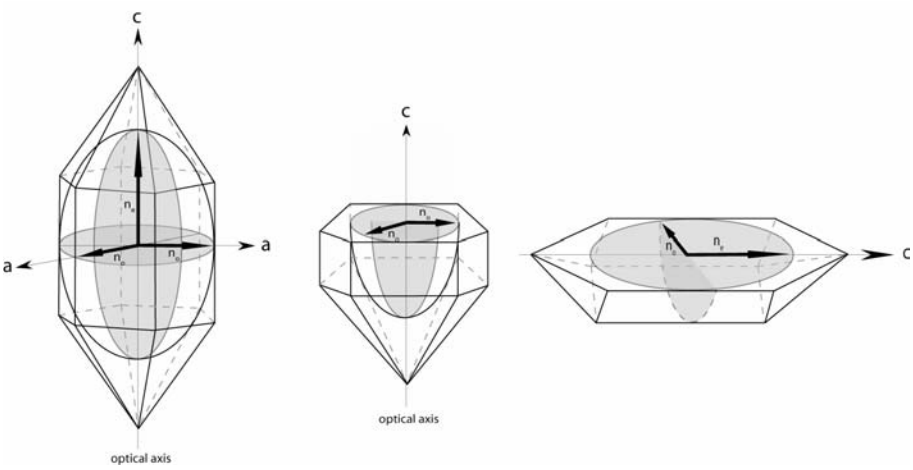

Fig. 4.4. Optical properties of a quartz crystal schematically illustrated with the indicatrix ellipsoid (n_o is the ordinary ray and n_e is the extraordinary of the ellipsoid) cut perpendicular and parallel to the optical axis.

Influences on the Raman spectra caused by the depth of the inclusions in the quartz host were investigated in experiments 027 and 029. Ten fluid inclusions at different depths in each sample were rotated through an angle of 90°, while spectra were taken every 10°.

The spectral effect of the inclusion shape (reflection polarisation effects), i.e. the orientation of the fluid-mineral interface where the laser beam enters, with respect to the laser's plane of polarisation, had been studied in a natural nearly negative-crystal-shaped inclusion (Fig. 4.5).

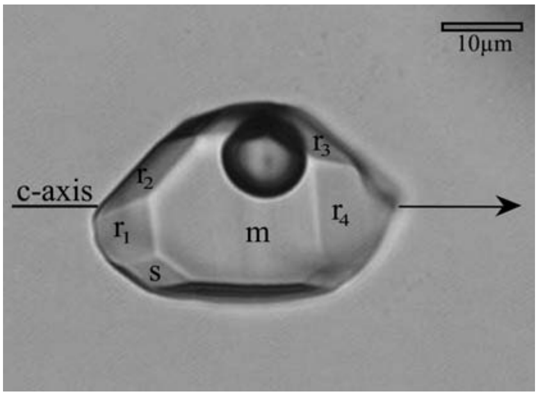

Fig. 4.5. Negative-crystal-shaped H_2O-N_2-CO_2-rich natural fluid inclusions with 9.23 mass% NaCl (*m* = prism-plane; *r* = rhombohedra-planes; *s* = dipyramid-plane). Ice melting point at -8.3°C and a clathrate melting point at 5.3°C. Raman spectral analysis reveals a composition of 5 mole% CO_2 and 95 mole% N_2. The volume fraction of the vapour phase is about 12% at room temperature.

This inclusion contains a H_2O-NaCl-N_2-CO_2-rich fluid mixture (composition of 5 mole% CO_2 and 95 mole% N_2 with a salt concentration of 9.23 equivalent mass% NaCl). Raman measurements were taken in steps of 10° rotation (up to 180°) with focus on the planes m, s, r_1, r_2, r_3, r_4 of the walls of the fluid inclusion (see Fig. 4.5). The angle between the incident laser beam and a specific fluid inclusion wall was determined by measuring the angle between the pole of the crystal faces in the wall and the pole of the plane in which the laser beam is polarised (the pole is the *x*-axis of the microscope stage), using a stereographic projection.

To quantify the effect of birefringence on the spectral contour independently from the relative orientation of inclusion the walls, a 5 mm diameter hole with a depth of about 1 mm was drilled in a natural quartz crystal (Fig. 4.6). The hole was completely filled with pure water and covered with doubly polished, orientated quartz plates (cut either parallel or perpendicular to the optical axis) of various thicknesses. This setup simulates: (1) a large fluid inclusion with a well-defined orientation of the inclusion wall (i.e. the quartz cover plate); (2) the inclination of the fluid inclusion wall; and (3) the thickness of host, through which the laser must pass. Raman spectra were again obtained over a total rotation of 180°.

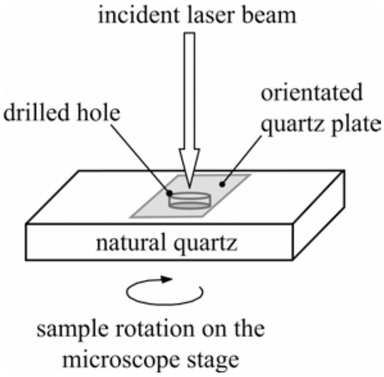

Fig. 4.6. The experimental setup of a fluid inclusion simulated by covering a hole (about 1 mm depth and 5 mm diameter) drilled in a quartz crystal and covered with a thin double polished quartz plate. The volume of the hole filled with solution is about 20 mm^3.

4.4. Deconvolution

Deconvolution is a mathematical procedure, which is often used to remove the smearing or broadening of peaks. Hidden peaks, which evidence no local maxima in the original data stream may do so once the data has been deconvolved and filtered (Peak Fit; User manual, 2002). The deconvolution is thought of as a peak separation procedure. Peaks are separated only if the overlap is modest enough that the deconvolution resolves the original data into a new data stream, where no peaks overlap. Fitting of spectroscopic data is nowadays a standard technique to best describe the obtained data. Each spectrum is a combination of separate curves. Some of them are visible, whereas some of them are hidden. A fitting procedure allows the separation of overlapping and hidden bands to determine the band position, half width and amplitude intensity.

The PeakFit program (© SYSTAT Software Inc.) for smoothing and fitting spectra, finding hidden peaks and calculating the derivatives and curve fitting had been used to deconvolve Raman spectra of aqueous solutions and salt hydrates. In this work spectra were deconvolved, by using a combination of Gaussian and Lorentzian functions. The best coefficient of determination, i.e. R^2 approaching 1, is obtained by these functions. The Gaussian contribution is defined by equation 4.12.

$$I_{Gauss} = a_o \cdot \exp\left[-4\ln(2) \cdot q^2\right] \qquad (4.12a)$$

$$q = \frac{x - a_1}{a_2} \qquad (4.12b)$$

where I_{Gauss} is the intensity, x is the relative wavenumber (cm^{-1}), a_0 is the amplitude, a_1 is the centre (cm^{-1}), i.e. the peak position, and a_2 is full width at half maximum (cm^{-1}). The Lorentzian contribution ($I_{Lorentz}$) is shown in equation 4.13.

$$I_{Lorentz} = a_0 \cdot \frac{1}{\left[1 + 4 \cdot q^2\right]} \qquad (4.13)$$

Raman spectra are best described by a combination of Gaussian and Lorentzian contributions (Eq. 4.14). This equation simply represents the intensity fractionation *(φ)*, such that φ=1 represents a purely Gaussian contribution and φ=0 a purely Lorentzian contribution. Equation 4.14b had been selected to describe individual deconvolved band contributions of the Raman spectra in this study (see Peak Fit v. 4.11).

$$I = \varphi \cdot I_{Gauss} + (1 - \varphi) \cdot I_{Lorentz} \qquad (4.14a)$$

$$I = a_0 \left[\frac{\varphi \cdot \frac{\sqrt{\ln 2}}{a_2 \sqrt{\ln \pi}} \cdot I_{Gauss} + (1 - \varphi) \cdot \frac{1}{\pi a_2} \cdot I_{Lorentz}}{\varphi \cdot \frac{\sqrt{\ln 2}}{a_2 \sqrt{\pi}} + (1 - \varphi) \cdot \frac{1}{\pi a_2}} \right] \qquad (4.14b)$$

4.4.1. Deconvolution of aqueous solutions

Spectra deconvolution of aqueous solutions was performed by a purely geometrical fit with three Gaussian-Lorentzian contributions (Bakker, 2004). Before fitting, baseline corrections were applied to the spectra by using a straight-line correction, performed with the PC-software PeakFit (© SYSTAT Software Inc.).

4.4.2. Deconvolution of salt hydrates

As the Raman spectra of hydrates are very complex and consist of overlapping bands, deconvolution was used to separate peaks or define hidden peaks. Gaussian-Lorentzian functions were used in the present work to deconvolve salt hydrate spectra at different temperature. The complexity of the spectra requires in some cases the use of additional contributions, so called “background” contributions ($\Delta\nu^{bg}$). The term is not used in the classical meaning. It defines hidden and overlapping peaks, where no local maxima in the raw spectra can be allocated. However, those contributions are necessary to balance the fitting procedure to allow the deconvolution of defined band positions for the main hydrate peaks. Prior fitting, baseline corrections were applied to the spectra by using a straight-line correction, performed with the PC-software PeakFit (© SYSTAT Software Inc.).

5. RESULTS

5.1. Microthermometry: Cooling experiments

Microthermometric studies at low temperatures (lower limit -190 °C) were carried out for all experiments. In the following, the results are discussed of individual salt-H_2O systems, due to the various phase assemblages, that may occur. The full data set of microthermometrical results, including final melting temperatures of solid phases and the results of the calculated salinities, are given in Chapter 5.3.

5.1.1. H_2O inclusions

Aqueous fluid inclusions nucleate ice at about -40 °C during cooling experiments (Fig. 5.1a/b). The nucleation is noticeable by a sudden shrinkage of the vapour bubble. Ice appears glassy and is optically not distinguishable from liquid water. The vapour bubble deforms due to re-crystallisation of ice during heating (Fig. 5.1c). First liquid is generated just before the final melting of ice at about 0.0 °C. Various synthesis were performed in the pure H_2O system, which all reveal the same freezing and melting behaviour. The final ice melting temperatures vary from 0.1 to -0.4 °C (see Table 5.1 in Chapter 5.3).

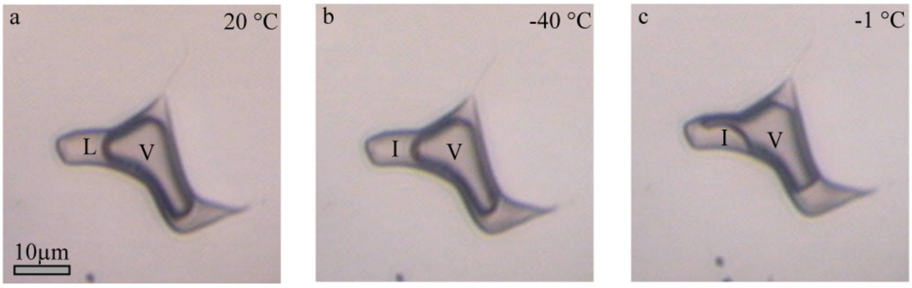

Fig. 5.1. Freezing and melting behaviour of a pure H_2O inclusion. a) Inclusion at 20 °C containing liquid and vapour. b) Freezing of the inclusions with the nucleation of ice at -40 °C. c) Re-crystallised ice and vapour at -1.0 °C. V=vapour; L=liquid; I=ice.

5.1.2. NaCl-H_2O inclusions

NaCl-containing fluid inclusions nucleate ice and hydrohalite during cooling experiments ($NaCl\cdot 2H_2O$). Figure 5.2 illustrates the typical freezing and melting behaviour of such inclusions. Freezing of a 23 mass% $NaCl_2$ inclusions is observed at about -80°C, which is mainly noticeable by the deformation of the vapour bubble (Fig. 5.2a/b). Initially, frozen inclusions contain a glass-like substance, composed of hydrohalite and ice. The solid phase assemblage remains stable down to temperatures of -190 °. The glass-like material re-crystallise at about -30 °C to a randomly orientated mixture of ice and hydrohalite, which has a granular texture and brownish colour (Fig. 5.2c). Slow heating promote the re-crystallisation and thereby crystal enlargement (Fig. 5.2d/e). First melt (eutectic melting) is produced at about -23 °C. Single crystals of hydrohalite (greenish/yellowish colour) and ice can be obtained in a saline aqueous liquid at -22 °C (Fig. 5.2f). Hydrohalite and ice dissolve at -21.1 (±0.1) °C. The melting temperature corresponds to a calculated salinity of 23.1 mass% NaCl in the solution (eutectic composition).

Fluid inclusions with lower salt contents (less than 23 mass% NaCl) show a similar freezing behaviour. The initial nucleation temperature is increasing with lower salinities, but still vary in a wide temperature range (between -40 to -100 °C). First liquid is generated again at about -23 °C. At the eutectic temperature (-21.1 °C), hydrohalite dissolves, whereas ice remains stable with the vapour and a high saline solution at higher temperatures. Cooling of the phase assemblage (ice, brine and vapour) results in the growth of ice crystals in the metastable brine. A retrial nucleation of hydrohalite occurs at related temperatures as observed for the initial freezing. Final melting in those inclusions is observed by the dissolution of ice. The melting temperature is dedicated by the salt content of the enclosed fluid and vary from -2.7 to -21.1 °C, corresponding to salinities between 4.5 and 23.2 mass% NaCl. Detailed microthermometrical results and salinity calculations for each experiment are given in Table 5.2 in Chapter 5.3.

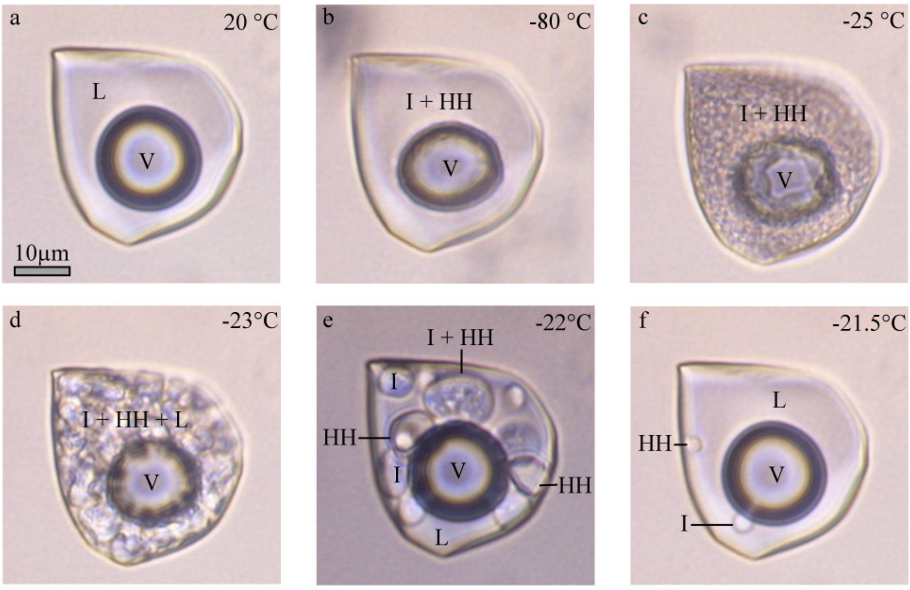

Fig. 5.2. Freezing and melting behaviour of an inclusion in experiment 019. a) Inclusion containing brine and vapour at 20 °C. b) Nucleation of a glassy substance at -80 °C. c) Micro-crystalline mixture of hydrohalite and ice at -25 °C. d) Re-crystallised hydrohalite and ice crystals at -23 °C. e) Hydrohalite and ice stable with liquid at -22 °C. f) Single hydrohalite and ice crystals in the presence of brine and vapour at -21.5 °C. V=vapour; L=liquid; I=ice, HH=hydrohalite.

5.1.3. $CaCl_2$-H_2O inclusions

Experiment 005: 30 mass% $CaCl_2$

The synthesis of sample 005 is defective due to difficulties during the sample preparation. Some inclusions were formed during the synthesis, which contain various solid phases (Fig. 5.3). However, microthermometric studies were not performed, because the trapping was not homogeneous.

Fig. 5.3. Inclusions and unhealed cracks containing various solid phases, formed in experiment 005.

Experiment 020: 30 mass% $CaCl_2$

Inclusions from this experiment do not freeze during subsequential heating and freezing. A supersaturated saline liquid remains present with the vapour phase down to -190 °C. A relative increase in the volume fraction of vapour (about 6%) is observed during cooling (Fig.5.4). The application of different cooling and heating parameters do not promote any nucleation in those inclusions. The intended salinity cannot be verified because of the lack of ice and hydrate melting temperatures.

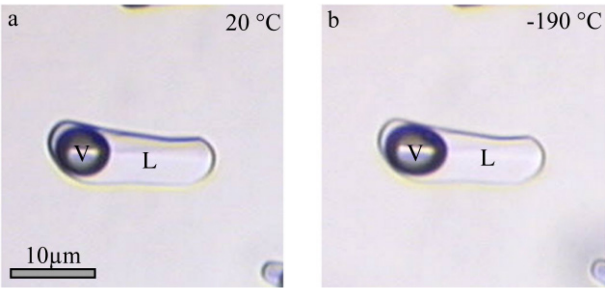

Fig. 5.4. Fluid inclusion in experiment 020, containing brine and vapour at a) 20 °C and b) -190 °C. V=vapour; L=liquid.

Experiment 021: 45 mass% $CaCl_2$

Minor variations in salinity and unpredictable metastabilities result in different types of hydrate nucleation in high saline synthetic inclusions. Four types of hydrate nucleation are observed in fluid inclusions from this experiment.

Antarcticite ($CaCl_2 \cdot 6H_2O$): Nucleation of antarcticite occurs in a temperature range between -40 °C and -65 °C during cooling (Fig. 5.5a/b). The vapour bubble deform intensely due to the nucleation. The hydrate is glassy at this temperature and has a similar refraction index as quartz (Fig. 5.5b). The bulk salinity of the inclusion is close to the composition of antarcticite, therefore, the amount of liquid (or rather ice) is expected to be very small. The phase assemblage (i.e. antarcticite, vapour and potentially a small amount of liquid or ice) remains stable down to -190 °C. During heating, reactions (including phase changes) are not obtainable in the inclusions. Little movements of the “deformed” vapour phase may occur due to re-crystallisation, but melting processes are not provable (Fig. 5.5b/c). First optical visible melting takes place at about 28 °C. Thereby, single antarcticite crystals are formed (Fig. 5.5d), which dissolve in a small temperature range. The last melting is observed at about 29.4 (±0.3) °C, which corresponds to a calculated salinity of 49.0 (±0.5) mass% $CaCl_2$

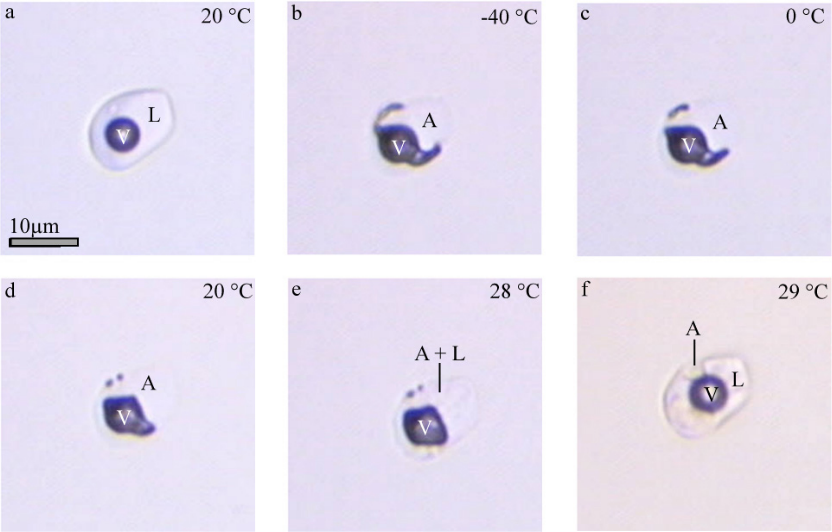

Fig. 5.5. Freezing and melting behaviour of an inclusion in experiment 021. a) Inclusion containing brine and vapour at 20 °C. b) Nucleation of antarcticite at about -40 °C. c-d) Re-crystallisation of antarcticite during heating to 20 °C. e) First melting of antarctite at 28 °C. f) Antarcticite in the presence of liquid and vapour at 29 °C. V=vapour; L=liquid; A=antarcticite.

Antarcticte ($CaCl_2{\cdot}6H_2O$) and α-Tetrahydrate (α-$CaCl_2{\cdot}4H_2O$): Similar to the previously described freezing behaviour, antarcticite nucleates in the temperature range between -40 °C and -65 °C (Fig. 5.6a/b). The vapour bubble deforms due to the nucleation. Antarcticite is stable between -190 and 28 °C. At about 29 °C the peritectic reaction takes place and thereby α-tetrahydrate is formed (Fig. 5.6d/e). Figure 5.7 illustrates in detail the peritectic reaction in the temperature range between 28.0 and 29.5 °C. α-tetrahydrate, brine and vapour represent a stable phase assemblage at 30 °C, whereas antarcticite is completely consumed by the peritectic reaction (Fig. 5.6e/f; Fig. 5.7). Cooling of this phase assemblage results in the growth of α-tetrahydrate crystals, whereas antarcticite is metastable absent. Final melting of α-tetrahydrate is observed at 32.5 (±0.4) °C, which corresponds to a calculated salinity of 50.7 (±0.1) mass% $CaCl_2$.

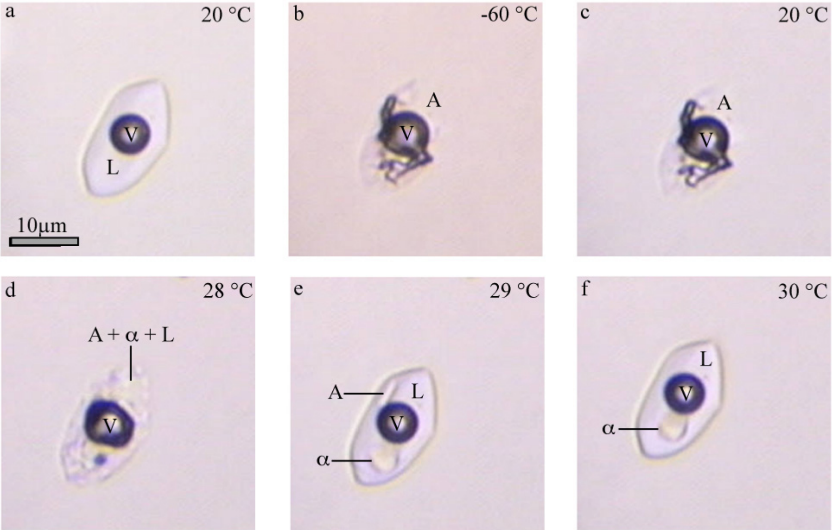

Fig. 5.6. Freezing and melting behaviour of an inclusion in experiment 021. a) Inclusion containing brine and vapour at 20 °C. b) Nucleation of antarcticite at about -60 °C. c) Antarcticite and vapour at 20 °C. d) Incongruent melting of antarcticite resulting in the formation of α-tetrahydrate at about 28 °C. e) Antarcticite and α-tetrahydrate in the presence of liquid and vapour. f) α-tetrahydrate stable with the liquid and vapour. V=vapour; L=liquid; A=antarcticite; α=α-tetrahydrate.

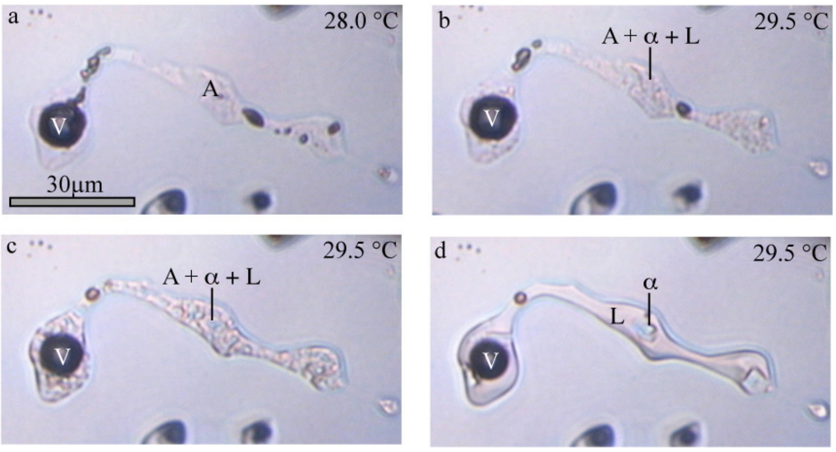

Fig. 5.7. Peritectic reaction observed experiment in experiment 021. a) Antarcticite in the presence of vapour at 28 °C. b) Antarcticite start to melt incongruently and first optical obsverable liquid is generated. c) Antarcticite, α-tetrahydrate, liquid and vapour are co-existing at 29.5 °C. d) α-tetrahydrate, liquid and vapour at 29.5 °C, whereas antarcticite is already consumed by the peritectic reaction. V=vapour; L=liquid; A=antarcticite; α=α-tetrahydrate.

<u>γ-Tetrahydrate (γ-$CaCl_2$·$4H_2O$):</u> Hydrate crystals nucleate at temperatures of about -30 °C and grow slowly at a constant low temperature (Fig. 5.8a-c). The phase assemblage, including the hydrate, brine and vapour, remains present down to -190 °C. The final melting of the hydrate is observed at 11.5 (±0.2) °C, by a slow dissolution of the crystals (Fig. 5.8d), which corresponds to a calculated salinity of 50.0 (±0.0) mass% $CaCl_2$ in the solution. The melting temperature of the hydrate phase corresponds to the metastable extension of the γ-tetrahydrate liquidus (see Chapter 7).

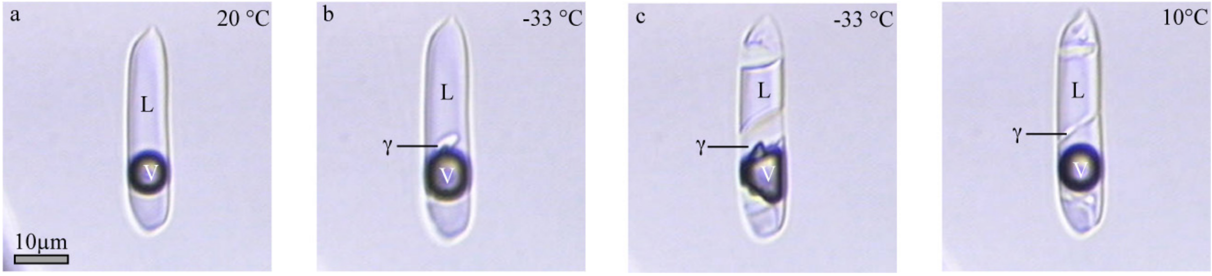

Fig. 5.8. Freezing and melting behaviour of an inclusion in experiment 021. a) Inclusion containing brine and vapour at 20 °C. b) Nucleation of γ-tetrahydrate at -33 °C. c) Growing of the hydrate crystals by holding a constant temperature. d) γ-tetrahydrate in the presence of liquid and vapour at 10 °C. V=vapour; L=liquid; γ=γ-tetrahydrate.

<u>Sinjarite ($CaCl_2$·$2H_2O$) and α-Tetrahydrate (α-$CaCl_2$·$4H_2O$):</u> A different freezing behaviour can be observed within the same fluid inclusion illustrated in Figure 5.8. A metastable hydrate nucleates at about -35 °C (Fig. 5.9a/b). The hydrate appears to replace completely the brine in the inclusion and deforms thereby the vapour bubble. A liquid phase is optical or spectroscopical not accurately verifiable, but a small amount of liquid cannot be excluded to be present as a thin film between the hydrate crystals. Further cooling does not promote any reaction or re-crystallisation and the phase assemblage is present down to -190 °C. During heating, the hydrate reacts into α-tetrahydrate at temperatures between -29 and -25 °C. The irreversible phase transition is accompanied with a slight coarsening in the crystal texture, without the formation of an (optical visible) aqueous liquid (Fig. 5.9b/c). Nevertheless, it is contingent that a liquid phase is present throughout the observed

temperature range. Optically the phase transition is difficult to observe, but it is evident by a change in the Raman spectra of the hydrate phase (see Chapter 5.4). Final melting of α-tetrahydrate is observed at about 32.5 (±0.4) °C. The first hydrate phase is assumed to be a sinjarite, because the temperature of phase transition (-29 to -25 °C) corresponds to the metastable extension of the liquidus of sinjarite at about 50 mass% $CaCl_2$.

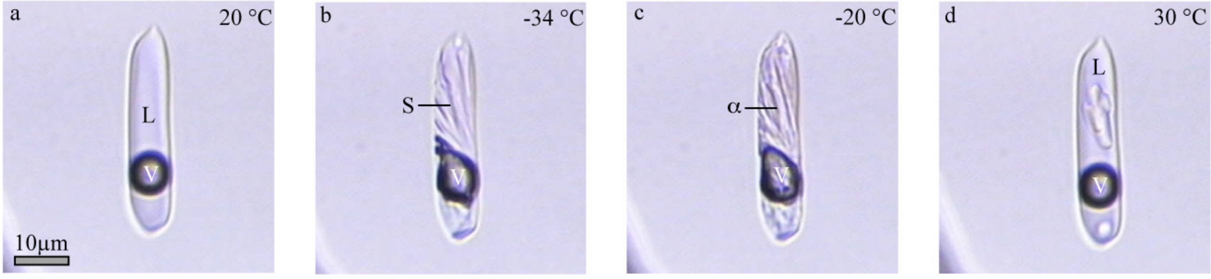

Fig 5.9. Freezing and melting behaviour of an inclusion in experiment 021. a) Inclusion containing brine and vapour at 20 °C. b) Nucleation of sinjarite at about -35 °C. c) α-tetrahydrate and vapour at -20 °C (after the phase transition between -29 and -25 °C). d) α-tetrahydrate in the presence of liquid and vapour at 30 °C. V=vapour; L=liquid; S=sinjarite; α=α-tetrahydrate.

It is interesting to note, that different freezing and melting behaviours are obtainable in the same inclusions. Which phase is preferred to nucleate is not indicated by the cooling rate. Inclusions next to each other show significant differences in the freezing and melting behaviour during the same path of cycling. The nucleation of the different hydrate phases seems to belong to spontaneous crystallisation processes.

Experiment 022: 15 mass% $CaCl_2$

Ice nucleation, in a granular, microcrystalline texture in the presence of a supersaturated film of brine, is observed at about -80 °C during cooling the inclusions (Fig. 5.10a/b). The phase assemblage remains metastable present during cooling to -190 °C. Heating of the inclusions induces the re-crystallisation of ice and thereby crystal enlargement (Fig. 5.10c). The final ice melting temperature is observed at -18.4 (±1.0), which corresponds to a calculated salinity of 20.6 (±0.5) mass % $CaCl_2$ in the solution. $CaCl_2 \cdot nH_2O$ hydrate nucleation could not be observed during repeated microthermometrical experiments.

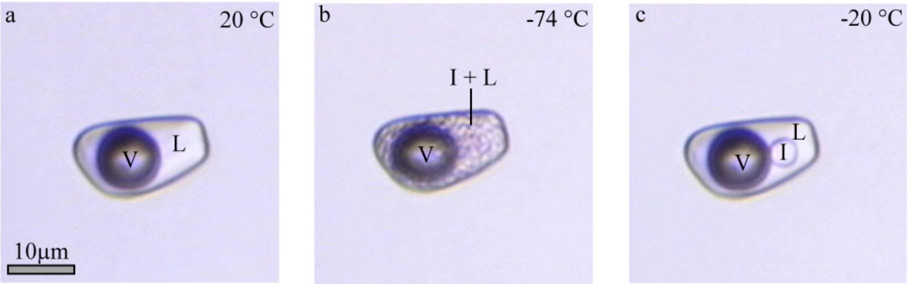

Fig. 5.10. Freezing and melting behaviour of an inclusion in experiment 022. a) Inclusion containing brine and vapour at 20 °C. b) Nucleation of ice at about -74 °C, whereas brine is present in the interstitial space between the ice crystals. c) Single ice crystal in the presence of brine and vapour at -20 °C. V=vapour; L=liquid; I=ice.

Experiment 044: 15 mass% $CaCl_2$

Ice nucleates at about -60 °C during cooling. The freezing and melting behaviour is similar as described for inclusions from experiment 022. The typical path of an inclusion during microthermometrical investigations is shown in Figure 5.11. Final ice melting temperatures are determined at -11.1 (±0.2), revealing a calculated salinity of -15.3 (±0.2) mass% $CaCl_2$ in the solution. Subsequential heating and cooling does not induce any hydrate nucleation in the inclusions.

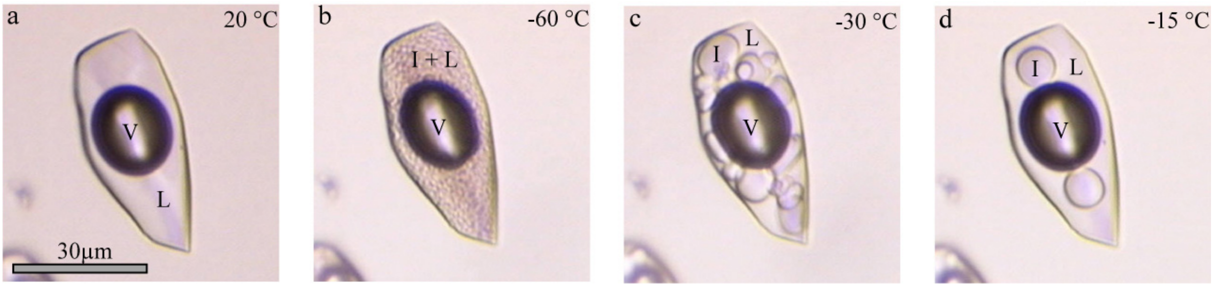

Fig. 5.11. Freezing and melting behaviour of an inclusion in experiment 044. a) Inclusion containing brine and vapour at 20 °C. b) Nucleation of ice at about -60 °C, whereas a high saline brine is present in the interstitial space between the multi-crystalline ice mixture. c) Ice re-crystallisation and melting during heating to -30 °C. d) Single ice crystals in the presence of brine and vapour at -15 °C. V=vapour; L=liquid; I=ice.

Antarcticite crystallisation is observable in partly healed fractures ("open cavities"). The final melting point at about -10 °C does not reflect the intended salinity. As the fractures are not completely isolated and still connected with fine channels to the quartz surface, the enclosed fluid may differ in salinity compared to the fluid trapped inclusions. Metastable hydrate nucleation occurs in inclusions adjacent to these fractures. It is assumed that these inclusions are affiliated to the fractures. The hydrate is present with liquid and vapour down to temperatures of -190 °C (Fig. 5.12a/b). Slow dissolution of the hydrate crystal starts at about 10 °C (Fig. 5.12c). Final melting is observed at about 13 °C. This phase most probably belongs to γ-tetrahydrate (similar optical occurrence as seen in experiment 021).

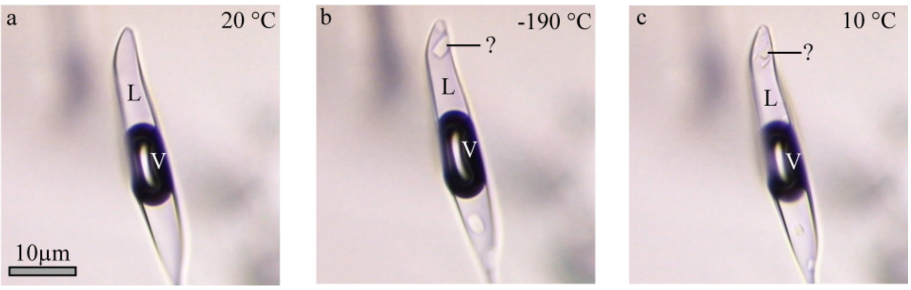

Fig. 5.12. Precipitation of a $CaCl_2$-phase (probably γ-tetrahydrate) in a partly healed inclusion (experiment 044). a) Brine and vapour at 20 °C. b) Single crystals of a hydrate crystal in the presence of liquid and vapour at -190 °C. c) Hydrate crystal in the presence of liquid and vapour at 10 °C. V=vapour; L=liquid; ?=γ-tetrahydrate.

Experiment 045: 30 mass% $CaCl_2$

In general, inclusions do not freeze during cooling studies. Instead of solidification a supersaturated brine remains present with the vapour phase down to -190 °C. Due to cooling, the volume fraction of the vapour phase slightly increases. Ice nucleation is rarely observed in some of the inclusions, but it is not reproducible. Final ice melting is observed at -46.5 (±0.3), which corresponds to a calculated salinity of 29.8 (±0.1) mass% $CaCl_2$.

Incomplete crack healing of quartz during the synthesis resulted in the formation of fluid inclusions, which are not completely isolated and still connected with fine channels (marked with arrows in Fig. 5.13 and 5.14) to the quartz surface. Capillary forces inhibit the complete loss of the fluid. Probably, water has been predominantly diffused through those channels, because the inclusions reveal a higher salinity than the imposed 30 mass% $CaCl_2$. Consequently, those inclusions reveal a similar freezing behaviour as inclusions from experiment 021. The nucleation of small hydrate crystals (γ-tetrahydrate) at about -35 °C (Fig. 5.13a) is observed. The final melting of γ-modification is obtained in a temperature range between 5 and 11 °C, similar to those temperatures observed in experiment 021. Antarcticite precipitates at various temperatures during heating and freezing in those inclusions (Fig. 5.13b). Optically it is not evident, if both hydrates occur in a phase assemblage, or γ-tetrahydrate is consumed by the reaction. Raman spectra reveal the stability of both hydrates at -190 °C (see Chapter 5.3.4). Heating induces intense re-crystallisation (Fig. 5.13c-e) and therefore the final melting of the γ-tetrahydrate in the presence of antarcticite cannot be observed accurately. Antarcticite is the last phase to melt at 25.4 (±0.6) °C. This temperature corresponds to a calculated salinity of 45.7 (±0.4) mass% $CaCl_2$ in the solution.

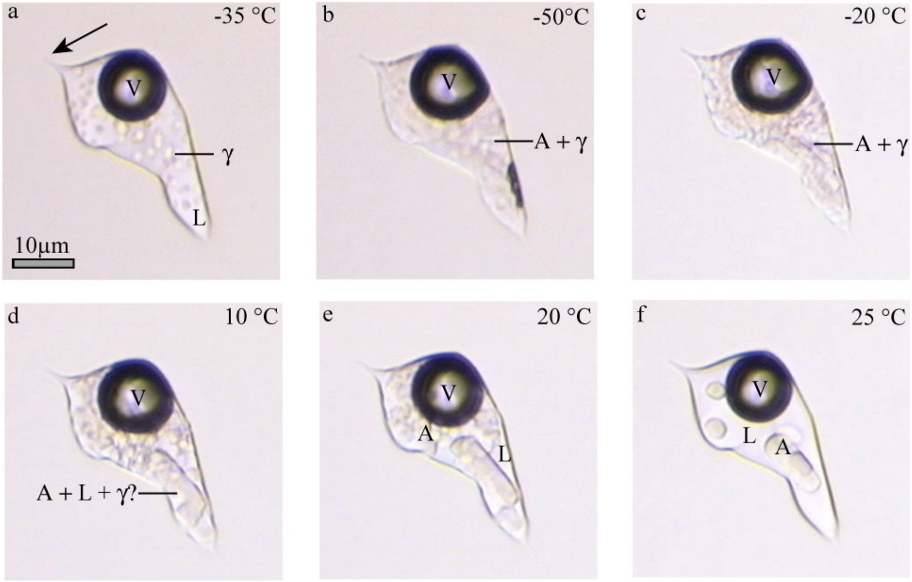

Fig. 5.13. Freezing and melting behaviour of an inclusion in experiment 45. a) Nucleation of *γ*-tetrahydrate in the presence of liquid and vapour at about -35 °C. b) Nucleation of antarcticite at about -50 °C. c-d) Re-crystallisation of antarcticite and *γ*-tetrahydrate. e) Antarcticite and liquid at 20 °C. f) Antarcticite in the presence of liquid and vapour at 25 °C. V=vapour; L=liquid; A=antarcticite; *γ*=*γ*-tetrahydrate.

Nucleation of a glassy phase at about -50 °C is also observed in those inclusions (Fig. 5.14a/b). This phase replaces completely the brine, which is evident by a strong deformation of the vapour bubble (Fig. 5.14b). The glassy phase re-crystallises during subsequently heating into a microcrystalline mixture (orange-skin texture) at -20 °C (Fig. 5.14c), and finally to larger single crystals of antarcticite (Fig. 5.14d). During cooling, these crystals grow constantly and are in equilibrium with an undersaturated brine at -190 °C (Fig. 5.14e/f). Final melting of antarcticite is again observed at about 25 °C.

Like mentioned before in experiment 021, the different freezing and melting behaviours occur in same inclusions during several microthermometric investigation. Additionally, inclusions next to each other show significant differences in the freezing and melting behaviour during the same path of cycling. The nucleation of the different hydrate phases seems to belong to spontaneous crystallisation processes.

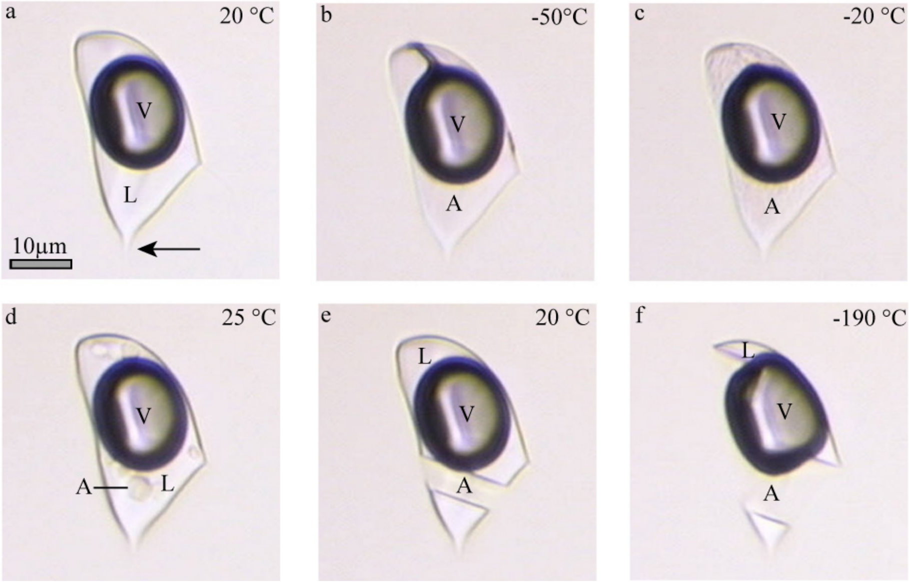

Fig. 5.14. Freezing and melting behaviour of an inclusion in experiment 45. a) Inclusion containing brine and vapour at 20 °C. b) Nucleation of antarcticite at about -50 °C. c) Re-crystallisation of antarcticite. d) Melting of antarcticite. e-f) Cooling and thereby growing of a single antarcticite crystal to -190 °C. Liquid is stable down to -190 °C. V=vapour; L=liquid; A=antarcticite.

5.1.4 $MgCl_2$-H_2O inclusions

Experiment 025: 15 mass% $MgCl_2$

Inclusions freeze in two different manners, i.e. (1) nucleation of ice and (2) nucleation of ice and $MgCl_2 \cdot 12H_2O$.

(1) Ice nucleates at temperatures between temperatures of -70 to -80 °C and appears in a granular, microcrystalline texture (1 in Fig. 5.15a/b). A supersaturated film of brine is in equilibrium with ice at the freezing temperature. The phase assemblage (ice, $MgCl_2$-rich brine and vapour) remains stable during cooling to -190 °C. Slow re-crystallisation into single ice crystals is induced during heating the inclusions (1 in Fig. 5.15c/d). Final melting of ice occurs at -23.1 (±1.3) °C, which reveals a calculated salinity of 17.7 (±0.5) mass% $MgCl_2$ in the solution.

(2) $MgCl_2$-hydrate ($MgCl_2 \cdot 12H_2O$) nucleation is observed in some of the inclusions. The crystallisation of the hydrates seems to go along with the ice precipitation. As ice and hydrate nucleate in a microcrystalline mixture, the solid phases cannot be distinguished by optical means (presence is confirmed by Raman spectroscopy; see Chapter 5.4). $MgCl_2 \cdot 12H_2O$, ice and vapour represent a stable phase assemblage during cooling to -190°. First re-crystallisation occurs at about -40 °C (2 in Fig. 5.15c), where multiple small crystals collect into several larger crystals (2 in Fig 5.15. d/e). Melting of $MgCl_2 \cdot 12H_2O$ (eutectic melting) is observed at about -33 °C (eutectic melting). Ice, brine and vapour are the stable phases above this temperature (2 in Fig 5.15. f). Final melting is again observed with the dissolution of ice at about -23 °C

The various phase equilibria are obtainable in inclusions during the same cooling run. Adjacent inclusions may nucleate those different phase assemblages simultaneously (see Fig. 5.15). As the final melting temperatures of ice are equal, the difference in crystallisation is not due to salinity variations between the inclusions.

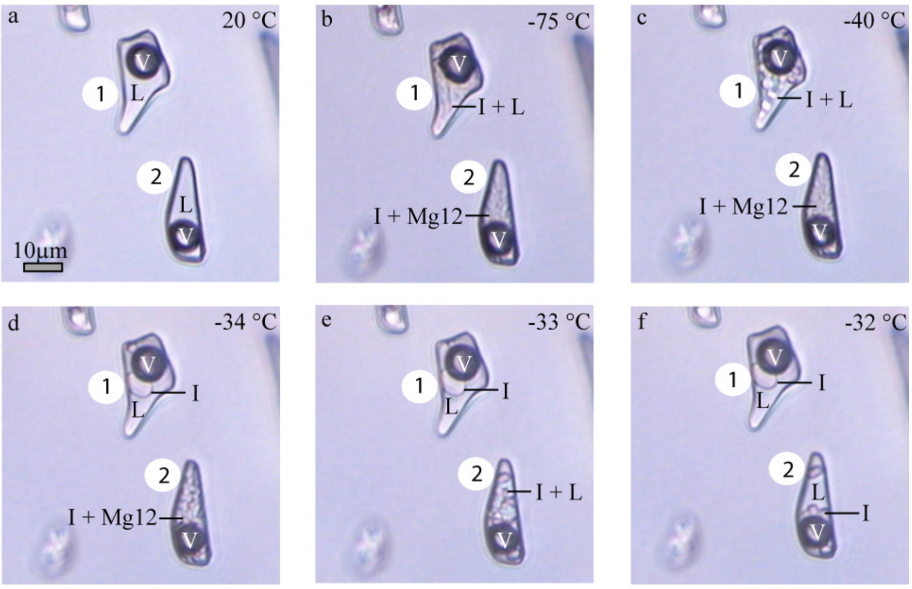

Fig. 5.15. Freezing and melting behaviour of inclusions in experiment 25. a) Inclusions containing brine and vapour at 20 °C. b) Nucleation of ice in inclusion 1, or rather nucleation of ice and $MgCl_2 \cdot 12H_2O$ in inclusion 2 at -77 °C. c) Re-crystallisation of ice in inclusion 1, whereas no reaction are obtainable in inclusion 2. d-e) Single ice crystal, liquid and vapour in inclusion 1 at -33 °C. Inclusion 2 undergo the eutectic reaction (melting of $MgCl_2 \cdot 12H_2O$). f) Inclusion 1 and 2 containing ice, brine and vapour at -32 °C. V=vapour; L=liquid; I=ice; Mg12=$MgCl_2 \cdot 12H_2O$.

Experiment 026: 30 mass% $MgCl_2$

Inclusions do not freeze during subsequential cooling and heating experiments. The saline liquid remains stable with the vapour bubble to -190 °C (Fig. 5.16). A relative increase in the volume fraction of vapour is observed with decreasing temperature. The intended salinity of 30 mass% $MgCl_2$ cannot be verified because of the lack of ice and hydrate melting temperatures.

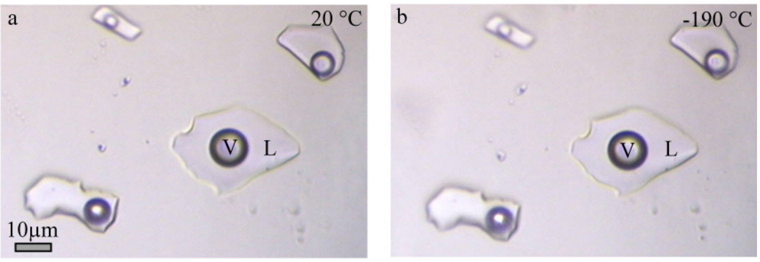

Fig. 5.16. Fluid inclusions in experiment 026, containing brine and vapour at a) 20 °C and b) -190 °C. V=vapour; L=liquid.

Experiment 030: 30 mass% $MgCl_2$

Two different types of freezing occur: (1) nucleation of ice and (2) nucleation of ice and $MgCl_2{\cdot}12H_2O$. The different freezing behaviors are obtainable in the inclusions during the same path of cooling.

(1) Ice nucleates between -60 and -100°C (Fig. 5.17) and is present with a $MgCl_2$-rich brine during cooling to -190 °C. Final melting of ice is observed at about -39.8 (±0.1) °C. As the melting temperature is below the eutectic (-33.6 °C), ice melts in a metastably state. Salinity calculations, based on the extended liquidus curve of ice (see Chapter. 4.2), results in 22.5 (±0.0) mass% $MgCl_2$ in the solution.

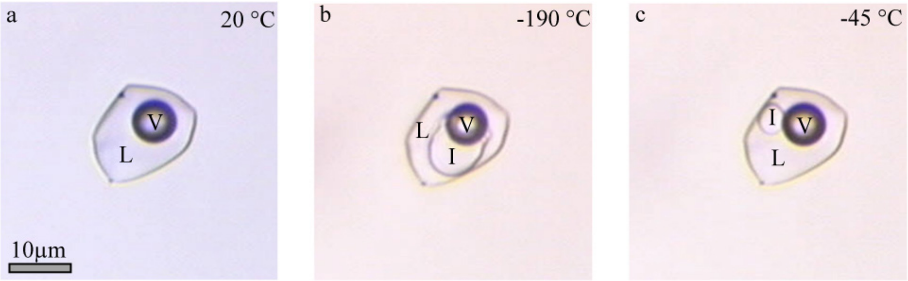

Fig. 5.17. Freezing and melting behaviour of an inclusion in experiment 030. a) Inclusion containing brine and vapour at 20 °C. b) Ice in equilibrium with brine and vapour at -190 °C. c) Single ice crystal in the presence of brine and vapour at -45 °C. V=vapour; L=liquid; I=ice.

(2) More common, ice and $MgCl_2{\cdot}12H_2O$ nucleation occurs in the inclusions during cooling. The nucleation temperature of the hydrate is difficult to obtain, as the refraction index of $MgCl_2{\cdot}12H_2O$ is similar to that of ice. Two different types of hydrate nucleation are observed. First, nucleation of $MgCl_2{\cdot}12H_2O$ is directly linked with the ice precipitation (both phases nucleate at the same temperature). Second, ice nucleates at a specific temperature and is stable with the brine and vapour. $MgCl_2{\cdot}12H_2O$ nucleates during further stepwise heating and freezing below the eutectic temperature. The temperature of hydrate nucleation cannot be qualified specifically. The phase assemblage ($MgCl_2{\cdot}12H_2O$, ice and vapour) is stable down to -190 °C. During heating, eutectic melting of the hydrate is observed at -32.8 (±0.2) °C, followed by the final melting of ice at -32.4 (±0.6) °C. Those melting temperatures are close to the theoretical eutectic temperature at -33.6 C and reveal a calculated salinity of 20.7 (±0.2) mass % $MgCl_2$. The typical path of hydrate melting is shown in Figure 5.18.

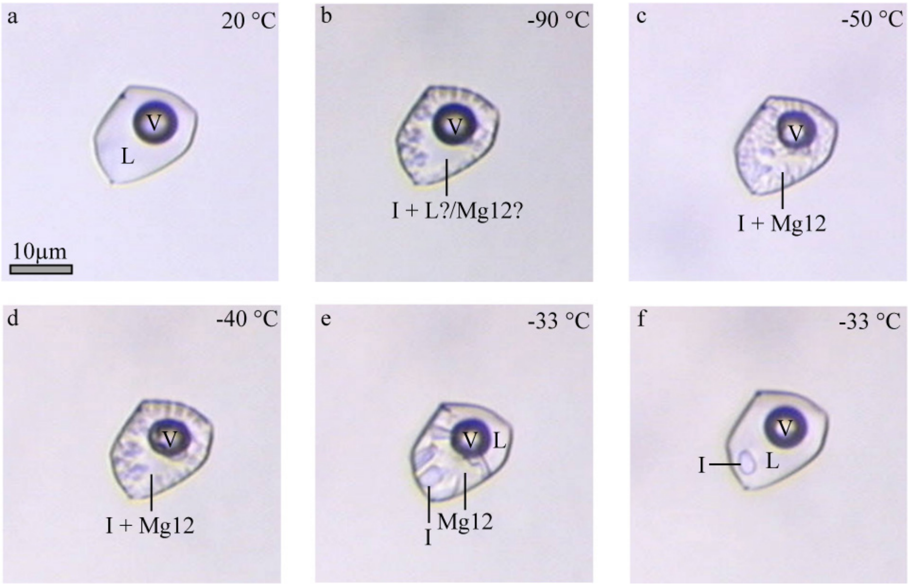

Fig. 5.18. Freezing and melting behaviour of an inclusion in experiment 030. a) Inclusion containing brine and vapour at 20 °C. b) Nucleation of ice at -90 °C, $MgCl_2 \cdot 12H_2O$ or brine is present. c/d) Ice, $MgCl_2 \cdot 12H_2O$ and vapour stable at -50 °C respectively at -40 °C. e) Melting of ice and Mg-hydrate at about -33 °C. f) Single ice crystal in the presence of brine and vapour at -33 °C. V=vapour; L=liquid; I=ice; Mg12= $MgCl_2 \cdot 12H_2O$.

Experiment 046: 15 mass% $MgCl_2$

The sample is defective due to difficulties during the sample preparation. No inclusions were found, which could be used for microthermometric investigations. The quartz section shows unhealed fractures without any fluid enclosed (Fig. 5.19).

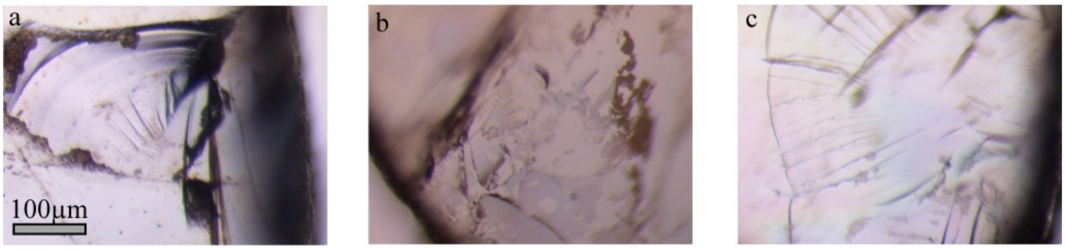

Fig. 5.19. Defective experiment 046. The cracks are not healed and thereby no inclusions are formed during the synthesis.

Experiment 047: 30 mass% $MgCl_2$

Inclusions do not freeze during microthermometrical studies. A supersaturated $MgCl_2$-rich brine is present with vapour down to temperatures of -190 °C (Fig. 5.20). An alight increase of the volume fraction of the vapour phase is observed during cooling. The intended salinity of 30 mass% $MgCl_2$ cannot be verified because of the lack of ice melting temperatures.

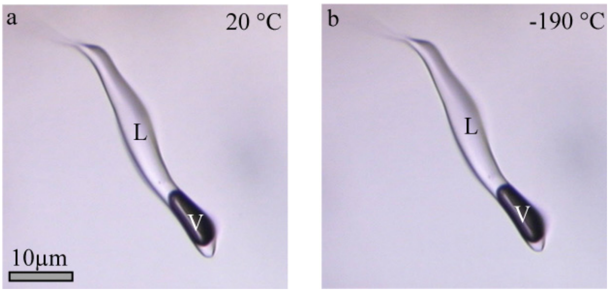

Fig. 5.20. Fluid inclusion in experiment 047, containing brine and vapour at a) 20 °C and b) -190 °C. V=vapour; L=liquid.

5.1.5 $FeCl_2$-H_2O inclusions

Experiment RJB 006: 11 mass% $FeCl_2$

The nucleation of ice is observed between -35 and -55 °C during cooling the inclusions (Fig. 5.21a/b). Ice nucleates in randomly orientated granular texture and re-crystallise to single crystals during heating (Fig. 5.21c). Final melting is observed at -5.9 (±0.3) °C, which implies a calculated salinity of about 11.5 (±0.3) mass% $FeCl_2$ in the solution. $FeCl_2$-hydrate precipitation cannot be induced during subsequential heating and cooling of those inclusions.

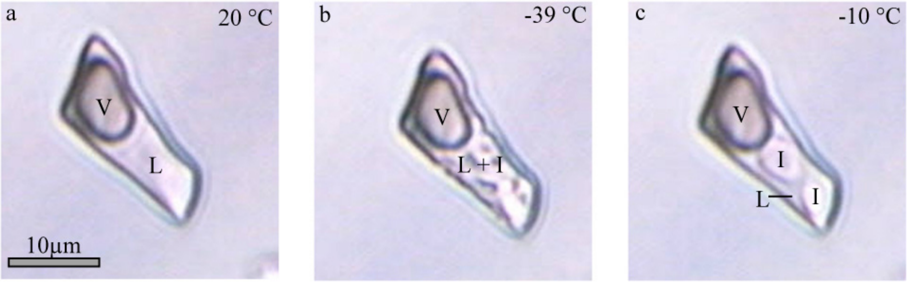

Fig. 5.21 Freezing and melting behaviour of an inclusion in experiment RJB 006. a) Inclusion containing brine and vapour at 20 °C. b) Nucleation of ice at about -39 C° in the presence of $FeCl_2$-rich brine. c) Re-crystallised ice in the presence of brine and vapour at -10 °C. V=vapour; L=liquid; I=ice.

Experiment RJB 007: 36 mass% $FeCl_2$

In general, inclusions precipitate ice between -45 and -60 °C during cooling. Freezing and melting occur similar as described for inclusions in experiment RJB 006. Final melting of ice is observed at -9.2 (±0.5) °C, which corresponds to a calculated salinity of about 14.6 (±0.4) mass% $FeCl_2$ in the solution.

$FeCl_2{\cdot}6H_2O$ nucleation is rarely observed in some of the inclusions. The temperature of nucleation cannot be defined, as the hydrate is optical barely distinguishable from ice. The presence of the hydrate is confirmed by Raman spectroscopy (see Chapter 5.5). $FeCl_2{\cdot}6H_2O$, ice and vapour represent a stable phase assemblage down to -190 °C. The melting of $FeCl_2{\cdot}6H_2O$ is observed at about -33 °C, close to the eutectic temperature of the system at -36.5 °C. Final melting is again observed with the dissolution of ice at about -9 °C. In general, hydrate crystallisation is very difficult to induce and is rarely observed.

Experiment RJB 011: 30 mass% $FeCl_2$

Ice nucleation occurs between -50 and -65 °C in the inclusions during cooling (Fig. 5.22a/b). Freezing and melting behave similar as described for inclusions in experiment RJB 006. Final melting of ice is observed at -14.4 (±0.2) °C, which corresponds to a calculated salinity of about 18.6 (±0.1) mass% $FeCl_2$. $FeCl_2$-hydrate precipitation cannot be induced during subsequent heating and cooling the inclusions.

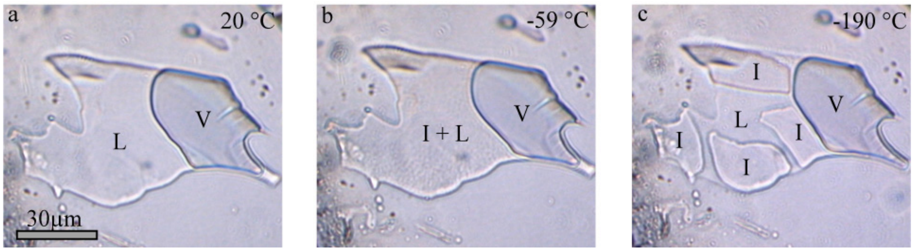

Fig. 5.22. Freezing and melting behaviour of an inclusion in experiment RJB 011. a) Inclusion containing brine and vapour at 20 °C. b) Nucleation of ice at about -59 °C. c) Re-crystallised ice in the presence of brine and vapour at -190 °C. V=vapour; L=liquid; I=ice.

5.1.6 $FeCl_3$-H_2O inclusions

Experiment RJB 008: 25 mass% $FeCl_3$

During cooling, ice precipitates in the temperature range between -75 and -90 °C (Fig. 5.23a/b). A $FeCl_3$-rich brine is in equilibrium with ice down to -190 °C (Fig. 5.23c). Ice nucleates in a randomly orientated granular texture and re-crystallise into single ice crystals during heating. Final melting is observed at -31.1 (±0.1) °C. This melting temperature corresponds to a calculated salinity of about 27.3 (±0.4) mass% $FeCl_3$. $FeCl_3$-hydrate precipitation cannot be induced during subsequential heating and cooling the inclusions.

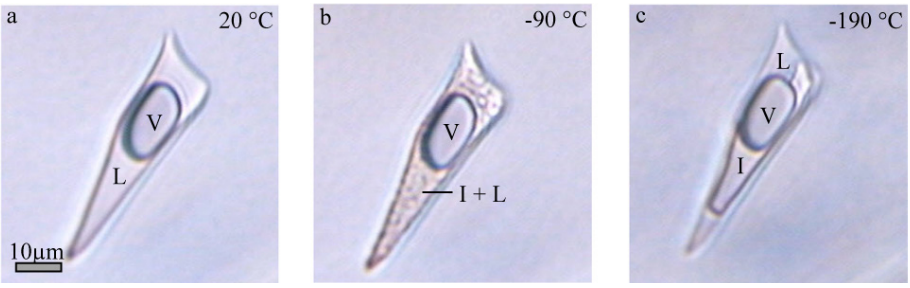

Fig. 5.23 Freezing and melting behaviour of an inclusion in experiment RJB 008. a) Inclusion containing brine and vapour at 20 °C. b) Nucleation of ice at about -90 °C. c) Re-crystallised ice in the presence of brine and vapour at -190 °C. V=vapour; L=liquid; I=ice.

Experiment RJB 016: 15 mass% $FeCl_3$

Ice nucleates between -45 and -55 °C during cooling the inclusions (Fig. 5.24a/b). Brine is in equilibrium with ice down to -190 °C (Fig. 5.24c). Freezing and melting behave similar as described for inclusions in experiment RJB 008. Final ice melting temperature is obtained at -11.2 (±0.2) °C and corresponds to a calculated salinity of about 16.4 (±0.2) mass% $FeCl_3$. Like in experiment RJB 008 $FeCl_3$-hydrate nucleation is not observed during cooling and heating sequences.

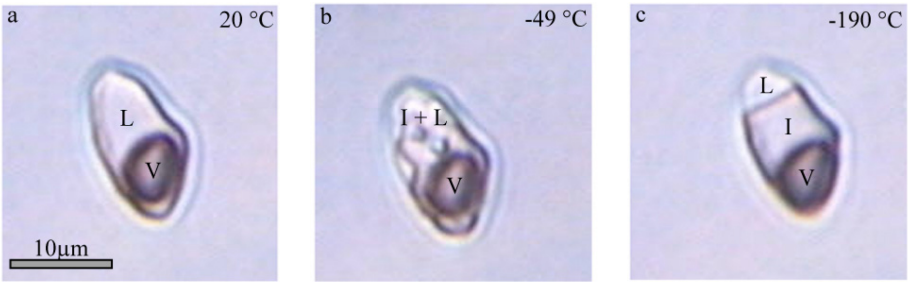

Fig. 5.24. Freezing and melting behaviour of an inclusion in experiment RJB 016. a) Inclusion containing brine and vapour at 20 °C. b) Nucleation of ice at about -90 °C. c) Re-crystallised ice crystals in the presence of brine and vapour stable at -190 °C. V=vapour; L=liquid; I=ice.

5.1.7. LiCl-H_2O inclusions

Experiment 053: 10 mass% LiCl

Inclusions freeze at between temperatures from -50 to -60 °C during cooling (Fig. 5.25a/b). Ice precipitates in a granular mixture of crystals, remaining a LiCl-rich brine. Re-crystallisation of ice occurs during heating the inclusions (Fig. 5.25c). Hydrates do not occur during subsequent cooling and heating. The brine is in equilibrium with ice and vapour down to -190 °C. Final ice melting is observed at -12.0 (±0.1) °C, which corresponds to a calculated salinity of 9.8 (±0.1) mass% LiCl.

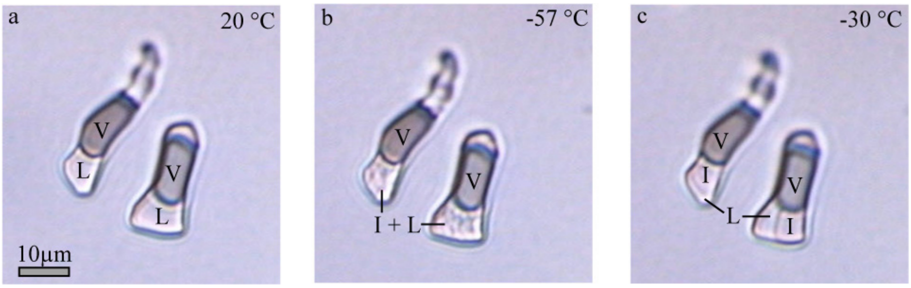

Fig. 5.25. Freezing and melting behaviour of an inclusion in experiment RJB 053. a) Inclusion containing brine and vapour at 20 °C. b) Nucleation of ice at about -57 °C. c) Single ice crystal, brine and vapour at -30 °C. V=vapour; L=liquid; I=ice.

Experiment 056: 25 mass% LiCl

Generally, inclusions do not freeze. The use of different cooling and heating parameters do not promote any nucleation. The saline brine is stable with the vapour down to -190 °C. A relative increase in the volume fraction of vapour is observed during cooling. Ice nucleation is seldomly observed in the sample. Final melting occurs at about -70 °C. The salinity calculation reveals about 25 mass% LiCl.

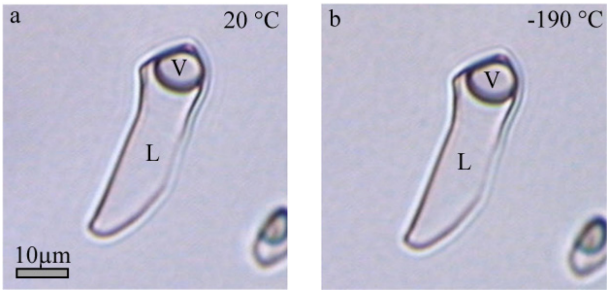

Fig. 5.26. . Fluid inclusion in experiment 056, containing brine and vapour at a) 20 °C and b) -190 °C. V=vapour; L=liquid.

Incompletely healed cracks in the sample (see also experiment 044 with H_2O-$CaCl_2$ solutions) contain multiple vapour bubbles separated by liquid. The enclosed fluid may not reflect the salinity of the synthesised fluid inclusions. Nucleation of an unknown solid phase is observed at about 20 °C. It cannot be excluded that the precipitation is induced by use of the Raman laser. This phase is stable between -190 and 104 °C (final melting temperature). Further melting points are observed at about 75 °C and at about -5 °C during different microthermometric runs. The variable melting temperatures belong to the same unknown solid phase, which is verified with Raman spectroscopy (see Chapter 5.4). As the crack is not completely sealed, it is assumed that repeated heating and cooling induces leakage of H_2O thereby the salinity may have changed. This would explain the strong variation in the observed melting temperature. The unknown phase is not identified, most probably the solid belongs to a $LiCl^{\cdot}nH_2O$ modification.

5.1.8. $ZnCl_2$-H_2O inclusions

Experiment 048: 40 mass% $ZnCl_2$

Inclusions freeze at about -80 °C during cooling. Due to the nucleation of ice, the vapour bubble slightly deforms (Fig. 5.27a/b). Ice appears in a glassy way and start to re-crystallise to a granular ice-mixture during heating (Fig. 5.27c-e). A $ZnCl_2$-rich brine remain stable with ice and vapour to temperatures of -190 °C (Fig. 5.27f). The final melting of ice is observed at -17.3 (±0.1) °C, corresponding to 27.6 (±0.1) mass% $ZnCl_2$. $ZnCl_2$-hydrates do not nucleate in the inclusions.

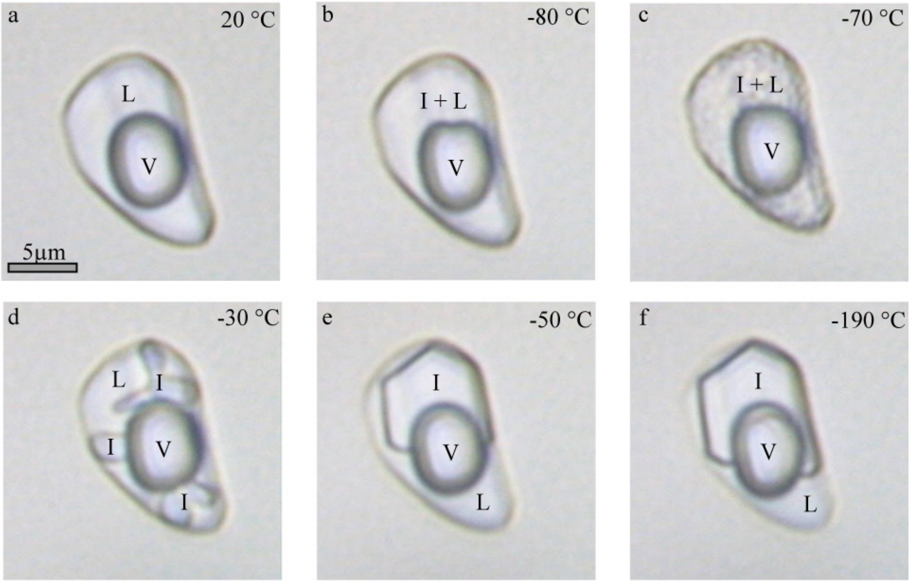

Fig. 5.27. Freezing and melting behaviour of an inclusion in experiment 048. a) Inclusion containing brine and vapour at 20 °C. b) Nucleation of ice at about -80 °C. c-d) Re-crystallisation and melting of ice between -70 and -30 °C. e-f) Single ice crystal in the presence of brine during cooling to -190 °C. V=vapour; L=liquid; I=ice.

Experiment 049: 30 mass% $ZnCl_2$

Generally, inclusions do not freeze during cooling experiments. The saline liquid is in present with vapour down to -190 °C (Fig. 5.28). A relative increase in the volume fraction of vapour is observed during cooling. Ice crystallisation is rarely observed in some inclusions. Ice, brine and vapour are present to -190 °C (Fig. 5.29a/b). Final melting of ice is observed at about -32.1 (±0.3) °C (Fig. 5.29c). This melting temperature corresponds to

37.9 (±0.2) mass% $ZnCl_2$. As the nucleation is difficult to reproduce, the observed melting has to be considered carefully. It cannot be excluded that the enclosed fluid from those inclusions may differ slightly in salinity from the majority of the trapped inclusions.

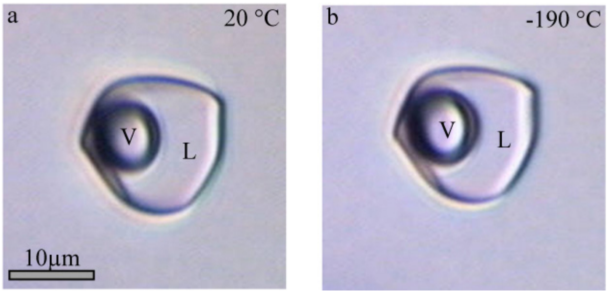

Fig. 5.28. Fluid inclusion in experiment 049, containing brine and vapour at a) 20 °C and b) -190 °C. V=vapour; L=liquid.

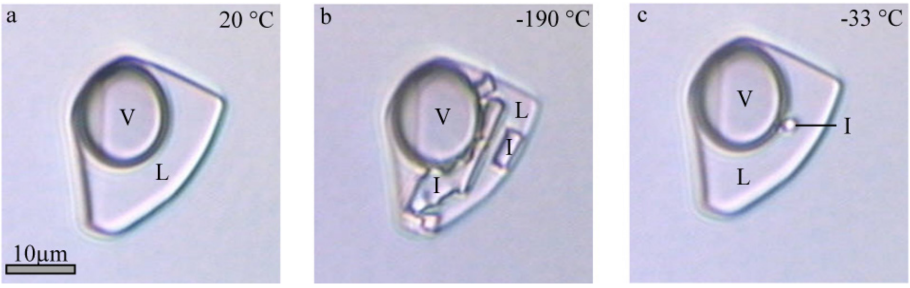

Fig. 5.29. Freezing and melting behaviour of an inclusion in experiment 049. a) Inclusion containing brine and vapour at 20 °C. b) Ice, brine and vapour in equilibrium at -190 °C. c) Single ice crystal in the presence of brine and vapour at -33 °C. V=vapour; L=liquid; I=ice.

Experiment 052: 10 mass% $ZnCl_2$

Inclusions freeze between -40 and -50 °C into a microcrystalline textured mass (Fig. 5.30a/b). Ice, brine and vapour remain present down to -190 °C. Heating results in the re-crystallisation and crystal enlargement of ice (Fig. 5.30c). Final melting of ice is observed at -4.2 (±0.1) °C, which corresponds to a calculated salinity of 10.7 (±0.2) mass% $ZnCl_2$ in the solution.

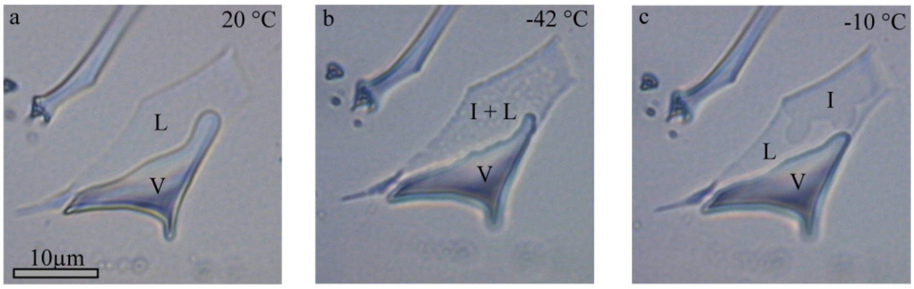

Fig. 5.30. Freezing and melting behaviour of an inclusion in experiment 052. a) Inclusion containing brine and vapour at 20 °C b) Nucleation of ice at about -42 °C. c) Re-crystallised Ice in the presence of brine and vapour at -10 °C. V=vapour; L=liquid; I=ice.

5.1.9. NaCl-$CaCl_2$-H_2O inclusions

Experiment 006: 12 mass% NaCl / 12 mass% $CaCl_2$

Two different types of freezing occur in the inclusions: (1) nucleation of ice and (2) nucleation of ice and hydrohalite. The eutectic temperature of this fluid system was not detected, due to the absence of a stable phase assemblage, i.e. hydrohalite, antarcticite and ice.

(1) Freezing of inclusions is observed by as sudden shrinkage and deformation of the vapour bubble at about -100 °C (Fig. 5.31a/b). Ice appears glassy at the freezing temperature. A supersaturated brine remain present with ice and vapour down to temperatures of -190 °C (Fig. 5.31f). Heating causes slow re-crystallisation of ice, resulting in a randomly oriented mixture of small ice crystals (Fig. 5.31c-e). Further heating promotes crystal enlargement. Final melting of ice is observed at -34.2 (±1.1) °C. This temperature does not correspond to stable thermodynamic properties for solutions with a NaCl/$CaCl_2$ ratio of 1/1 (intended salt ratio). It is assumed that ice melts metastably and therefore salinity calculations are not practical (see Chapter 7).

(2) A second type of freezing, illustrated in Figure 5.32, arises with the nucleation of ice and hydrohalite at temperatures about -100 °C. Ice and hydrohalite are present with a $CaCl_2$-rich brine in a temperature range from -190 to -28 °C. Heating of inclusions induces slow re-crystallisation. Final ice melting is observed at -27.6 (±0.4) °C, remaining hydrohalite, brine and vapour. Subsequent cooling of this phase assemblage (hydrohalite, brine and vapour) results in the growth of hydrohalite. Ice precipitation is again observed at about -80 °C, whereas a $CaCl_2$-rich brine remains present. $CaCl_2$ cannot be fixed in a hydrate phase during microthermometry. The final melting in those inclusions is observed by the dissolution of hydrohalite at -0.1 (±0.1) °C. The melting temperature allows a salinity calculation, which reveals 13.2 (±0.7) mass% NaCl and 15.1 (±0.6) mass% $CaCl_2$ in the solution. In some cases the melting of hydrohalite is observed at -4.6 (±1.4). Salinity calculations based on lower hydrohalite melting temperature result in 13.4 (±1.2) mass% NaCl and 14.6 (±1.2) mass% $CaCl_2$.

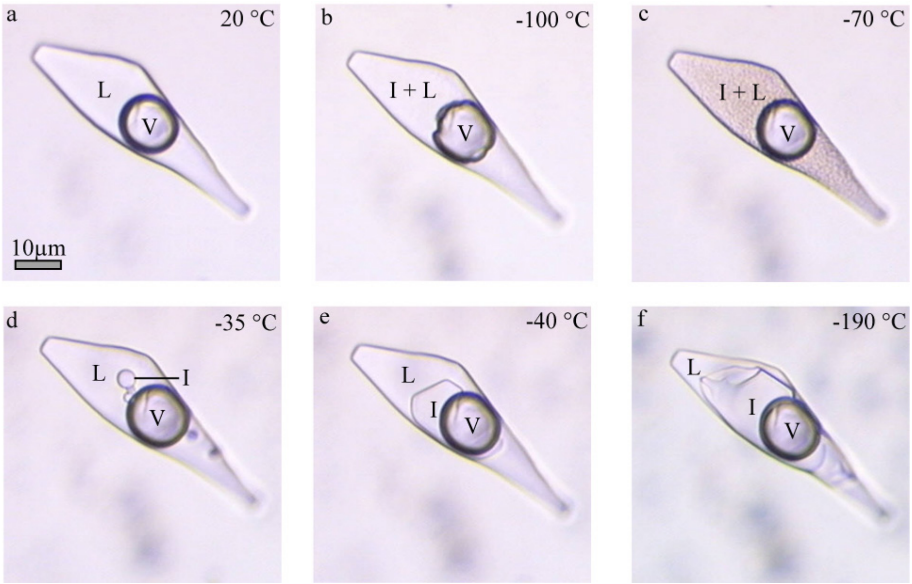

Fig. 5.31. Freezing and melting behaviour of an inclusion in experiment 006. a) Inclusion containing brine and vapour at 20 °C. b) Nucleation of ice at -100 °C. c) Re-crystallisation of ice at -70 °C. d) Single ice crystals and brine at -35 °C. e-f) Growing of ice during cooling to -190 °C. V=vapour; L=liquid; I=ice.

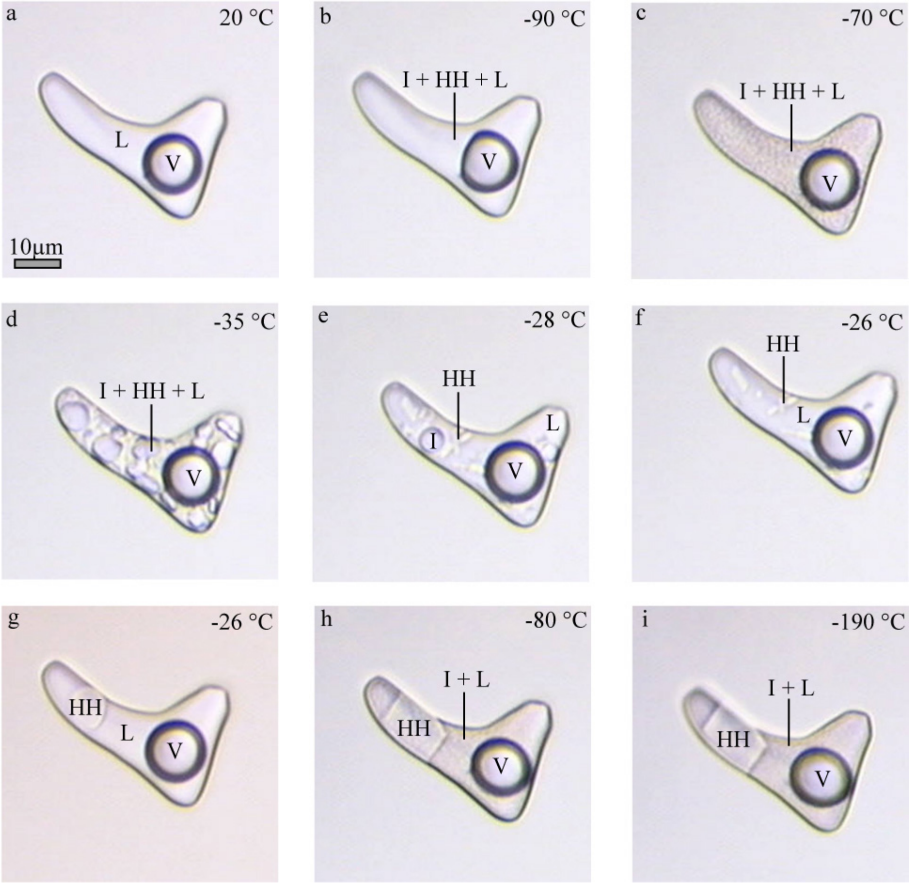

Fig. 5.32. Freezing and melting behaviour of an inclusion in experiment 006. a) Inclusion containing brine and vapour at 20 °C b) Nucleation of ice and hydrohalite at -90 °C. c) Re-crystallisation of ice and hydrohalite at -70 °C. d) Ice, hydrohalite and brine at -35 °C. e) Dissolution of ice at about -28 °C. f) Hydrohalite and $CaCl_2$-rich brine in the presence of vapour g/h) Cooling of a single hydrohalite crystal and thereby growing of the crystal. Ice precipitate again at about -80 °C. i) Hydrohalite crystal surrounded by microcrystalline textured ice, stable with a Ca-rich brine and vapour at -190 °C. V=vapour; L=liquid; I=ice; HH=hydrohalite.

Experiment 007: 1 mass% NaCl / 30 mass% $CaCl_2$

Inclusions from experiment 007 contain various solid phases at room temperature (Fig. 5.33). The sample is defective due to difficulties during the sample preparation and cannot be used for microthermometric and Raman spectroscopic studies.

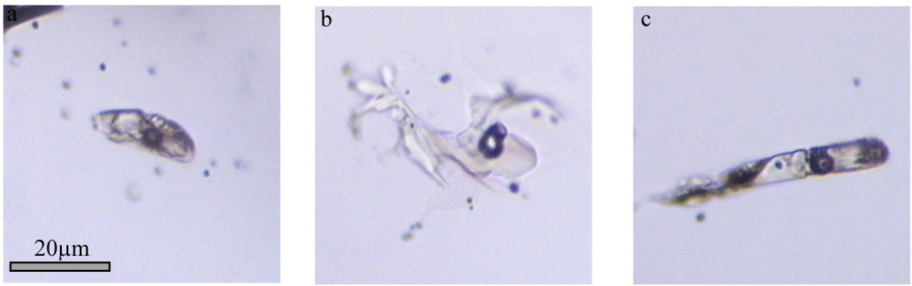

Fig. 5.33. Inclusions containing various solid phases and vapour formed in experiment 007.

Experiment 023: 1 mass% NaCl / 30 mass% $CaCl_2$

The synthesis of sample 023 with an intended salinity of 1.4 mass% NaCl and 29.8 mass% $CaCl_2$ is defective due to difficulties during the sample preparation. The quartz section shows unhealed cracks with various solid and vapour phases (Fig. 5.34). No fluid inclusions were generated, which can be used for microthermometric investigations.

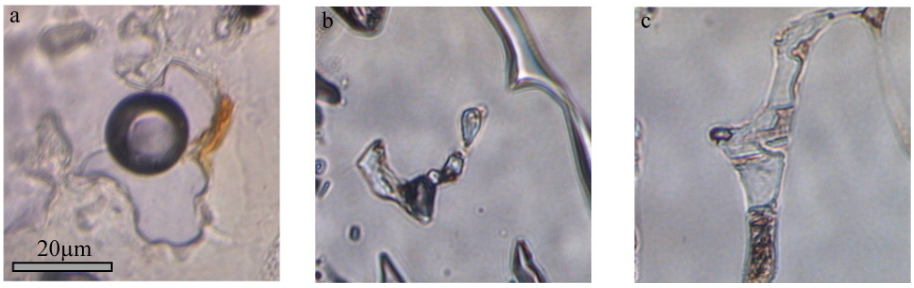

Fig. 5.34. Unhealed cracks in experiment 023, containing solid and vapour phases.

Experiment 024: 10 mass% NaCl / 30 mass% $CaCl_2$

Three different behaviours can be distinguished during cooling experiments in the inclusions: (1) absence of nucleation, (2) nucleation of hydrohalite and (3) nucleation of hydrohalite and ice.

> (1) Predominantly, inclusions do not show any nucleation during cooling experiments. A supercooled brine is present down to -190 °C.
>
> (2) Hydrohalite precipitates in some of the inclusions between -40 and 50 °C (Fig. 5.35a/b). No further nucleation occurs in those inclusions and hydrohalite is present with a $CaCl_2$-rich brine at low temperatures. During heating, hydrohalite reacts to halite between -12 and 6 °C (Fig. 5.35c/d). Subsequent cooling (halite and liquid) do not induce further nucleation and halite is present with brine down to -190 °C (Fig. 5.35e). Halite dissolves at temperatures between 140 and 170 °C and is afterwards metastably absent at room temperature (Fig. 5.35f).
>
> (3) Hydrohalite nucleates between -40 and -50 °C (Fig. 5.36a/b). During further cooling ice precipitates at about -100 °C (Fig. 5.36c) and is present with hydrohalite and a $CaCl_2$-rich brine at -190 °C (Fig. 5.36d). Ice melting is observed at -42.2 (±0.3) °C (Fig. 5.36e). Hydrohalite reacts again to halite between temperatures of 10 to 30 °C (Fig. 5.36f/g). Cooling of the phase assemblage (halite and liquid) again causes ice nucleation at about -100 °C. Halite, ice and a $CaCl_2$-rich brine is present down to -190 °C (Fig. 5.36h). Ice melting is observed at -40.6 (±0.5) °C, i.e. at slightly higher temperatures than observed for the phase assemblage ice and hydrohalite. Halite itself melts between 160 and 180 °C (Fig. 5.36i) and does not nucleate again during cooling to room temperature.

Salinity calculations are not performable with the observed melting and phase transition temperatures. Fluid inclusions from this experiment react in a highly metastable way during cooling and heating experiments.

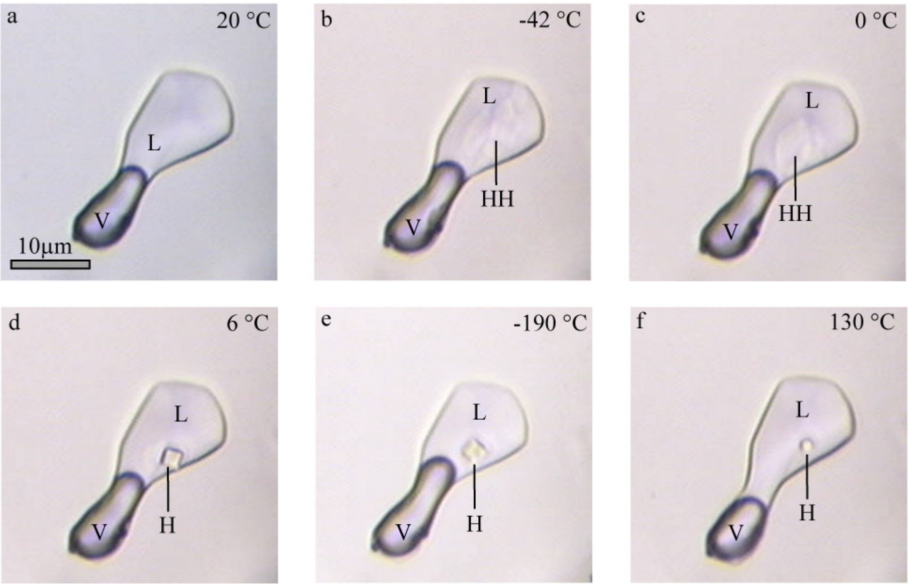

Fig. 5.35. Freezing and melting behaviour of an inclusion in experiment. 024. a) Inclusion containing brine and vapour at 20 °C. b) Nucleation of hydrohalite at about -42 °C. c) Hydrohalite, brine and vapour present at 0 °C. d) Phase transition of hydrohalite into halite at about 6 °C. e) Halite, brine and vapour present at -190 °C. f) Halite crystal, just before final melting at about 140 °C. V=vapour; L=liquid; HH=hydrohalite; H=halite.

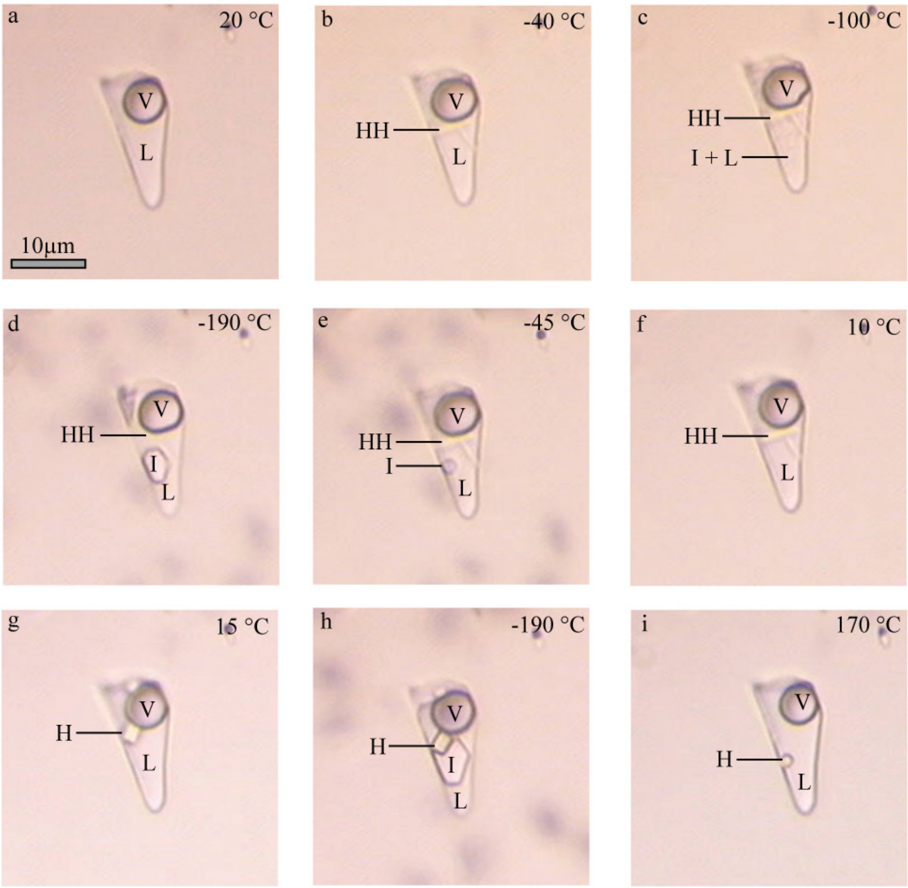

Fig. 5.36. Freezing and melting behaviour of an inclusion in experiment 024. a) Inclusion containing brine and vapour at 20 °C. b) Nucleation of hydrohalite at about -40 °C. c) Nucleation of ice at about -100 °C. d) Hydrohalite, ice, brine and vapour present at -190 °C. e) Hydrohalite, ice, brine and vapour present at -45 °C, just before the final melting of ice. f) Hydrohalite, brine and vapour at 10 °C. g) Phase transition of hydrohalite into halite at about 15 °C. h) Halite, ice, brine and vapour at -190 °C. i) Halite crystal, just before final melting at about 180 °C. V=vapour; L=liquid; HH=hydrohalite; H=halite.

Experiment 031: 1 mass% NaCl / 30 mass% $CaCl_2$

Inclusions from experiment 031 show various solid phases at room temperature (Fig. 5.35). Four phases are distinguished in those inclusions by Raman spectroscopic means. The opaque phases and cubic crystals found in the inclusions are Raman inactive. The cubic crystals most probably belong to NaCl. The presence of two other phases was confirmed by Raman spectroscopy. Both show vibrational modes in the stretching region of water. The Raman spectra do not correspond to hydrohalite or $CaCl_2$-hydrates. Nevertheless, it is suggested that the phases are $CaCl_2.nH_2O$ modifications. The trapping of the inclusions was strongly inhomogeneous and therefore the sample was not used for microthermometric studies.

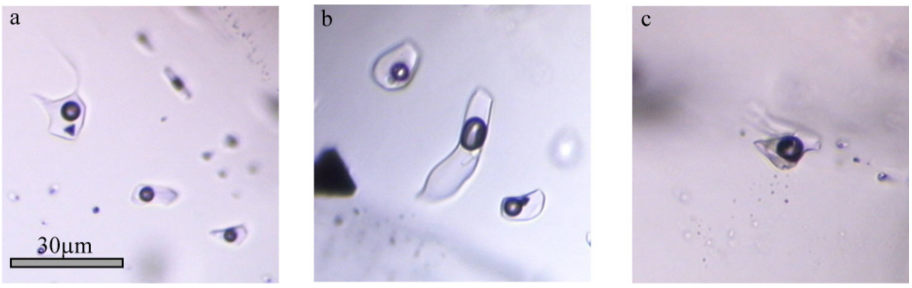

Fig. 5.35. Inclusions containing various solid phases in the presence of liquid and vapour formed in experiment 031.

5.1.10. NaCl-$MgCl_2$-H_2O inclusions

Experiment 032: 10 mass% NaCl / 20 mass% $MgCl_2$

The experiment is defective, although inclusions were formed during the synthesis, which contain solid phases (Fig. 5.36). This remains an oversaturated solution at room temperature, which does not correspond to the intended salinity. The crystals could not be identified by optical means. The solid phases are Raman inactive, therefore it is suggested, that the crystals most probably belong to NaCl and $MgCl_2$. Microthermometric studies were not performed with those inclusions.

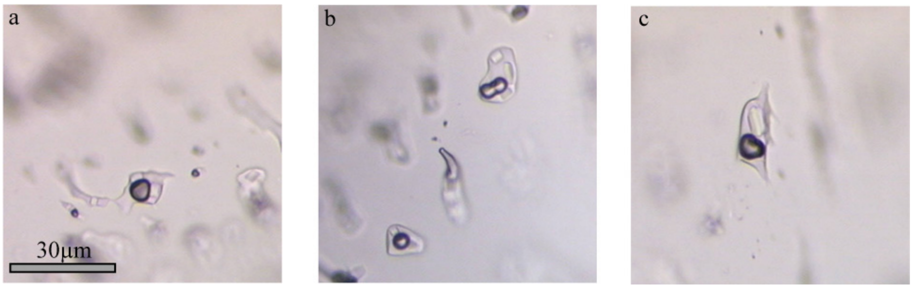

Fig. 5.36. Inclusions containing various solid phases (probably NaCl and $MgCl_2$) in experiment 032.

Experiment 033: 10 mass% NaCl / 13 mass% $MgCl_2$

Ice and hydrohalite nucleation is observed during microthermometrical runs at low temperature in the inclusions. Freezing of the inclusions occurs with a randomly orientated mixture of ice and hydrohalite crystals at -70 °C (Fig.5.37a/b). A $MgCl_2$-rich brine is still present at the freezing temperature, which forms a film of brine between the crystal mixture. Re-crystallisation and crystal enlargement is induced during heating (Fig. 5.37c). Ice, hydrohalite, $MgCl_2$-rich brine and vapour represent the phase assemblage at -190 °C (Fig. 5.37d). Melting of hydrohalite is observed at about -25.1 (± 0.4) °C (Fig. 5.37e/f), followed by the melting of ice at -20.5 (±0.1) °C. Those melting temperatures corresponds to a calculated salinities of 12.5 (±0.7) mass% NaCl and 9.3 (±0.5) mass% $MgCl_2$. All inclusions in this system freeze and melt in the same manner. Nucleation of Mg-hydrates is not induced during subsequential heating and freezing in those inclusions.

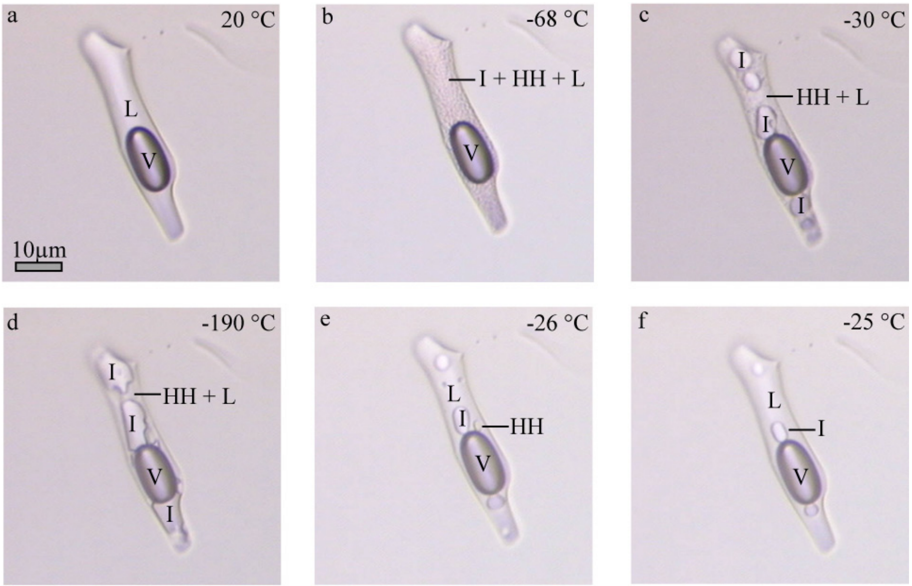

Fig. 5.37. Freezing and melting behaviour of an inclusion in experiment 033. a) Inclusion containing brine and vapour at 20 °C. b) Nucleation of ice and hydrohalite at about -68 °C. c) Re-crystallised of ice and hydrohalite at -30 °C. d) Ice and hydrohalite in the presence of brine and vapour at -190 °C. e) Single ice and hydrohalite crystals stable with the brine just before final melting of hydrohalite f) Ice crystals, brine and vapour at -25 °C. V=vapour; L=liquid; I=ice; HH=hydrohalite.

Experiment 035: 2 mass% NaCl / 24 mass% $MgCl_2$

Two different types of freezing occur: (1) nucleation of ice and (2) nucleation of ice and salt hydrates.

(1) Nucleation of ice occurs at temperatures about -80 °C (Fig. 5.38a/b). Ice precipitates fine-grained and re-crystallises during heating. No other phase precipitation occurs during further cooling (Fig. 5.38c-e). A super-cooled brine (NaCl-$MgCl_2$-rich), ice and vapour are present down to -190 °C (Fig. 5.38f). Final melting of ice is observed at temperatures -26.4 (±0.2) °C. The salinity can be approximated from the phase diagram (Fig. 2.14) by taking into account the intended NaCl/$MgCl_2$ ratio for synthesis (2 mass% NaCl and 24% $MgCl_2$; ratio 1/12). 1.7 mass% NaCl and 17.5 mass% $MgCl_2$ can be appreciated in the solution.

(2) In some inclusions $MgCl_2$-hydrate ($MgCl_2 \cdot 12H_2O$) and NaCl-hydrate ($NaCl \cdot 2H_2O$) nucleate together with ice. It may occur in the same inclusions as described in (1) during different cycling modes (compare Fig. 5.38 and Fig. 5.39). Microthermometric conditions (e.g. cooling rates) have not been changed, therefore the crystallisation occurs spontaneously with an unpredictable outcome. Freezing of the inclusion occurs in the same manner as described before at temperatures at about -80 °C. Optically there is no difference between the both freezing performances. Nevertheless, Raman spectroscopy verifies the stability of the $MgCl_2 \cdot 12H_2O$ and $NaCl \cdot 2H_2O$ (see Chapter 5.4). Eutectic melting of both, $MgCl_2 \cdot 12H_2O$ and $NaCl \cdot 2H_2O$, is observed at about -35.6 (±0.3) °C, remaining ice and liquid is stable above this temperature. Final melting is again observed with the dissolution of ice at about -26.0 °C. The obtained melting temperatures correspond to a calculated salinity of 5.2 (±0.7) mass% NaCl and

16.4 (±0.4) mass% $MgCl_2$. It is assumed, that the calculated salinity, based on the melting temperatures of the hydrates and ice, reveal the true values. More details are given in Chapter 7.

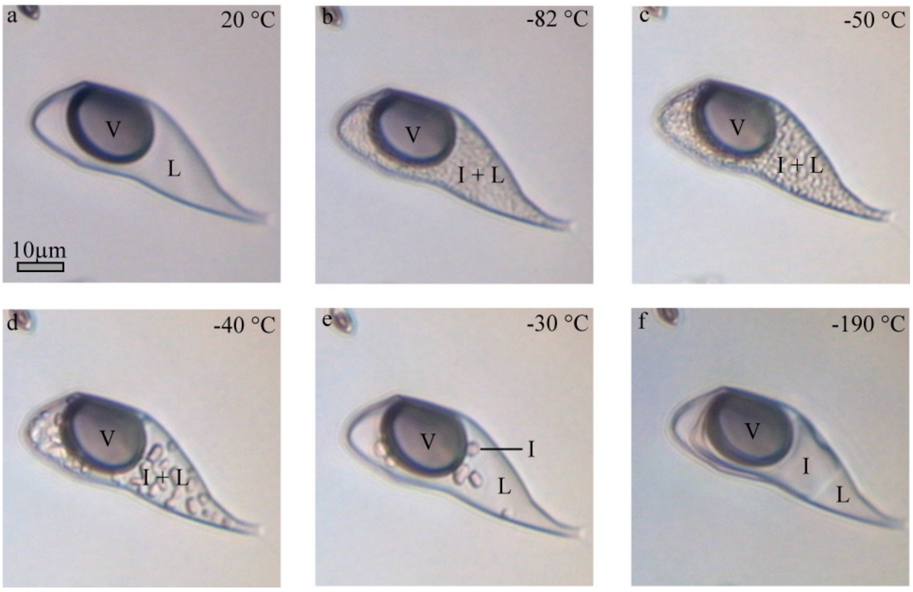

Fig. 5.38. Freezing and melting behaviour of an inclusion in experiment 035. a) Inclusion containing brine and vapour at 20 °C. b) Freezing of the inclusion at -80 °C with the nucleation of ice. c) Re-crystallisation of ice during heating. d-e) Melting of ice crystals between -40 and -30 °C. f) Ice in the presence of brine and vapour at -190 °C. V=vapour; L=liquid; I=ice.

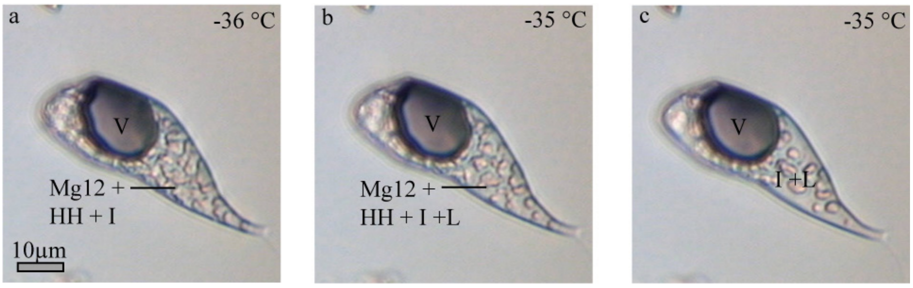

Fig. 5.39. Freezing and melting behaviour of an inclusion in experiment 035. The freezing occur similar to Fig. 5.38. Besides, the nucleation of ice also $MgCl_2 \cdot 12H_2O$ and $NaCl \cdot 2H_2O$ precipitate at about -80 °C. a) $MgCl_2 \cdot 12H_2O$, hydrohalite, and ice in the presence of vapour at -36 °C. b) Melting of $MgCl_2 \cdot 12H_2O$ and hydrohalite at about -35.5 °C. c) At -35 °C $MgCl_2 \cdot 12H_2O$ is completely molten. Ice is present with brine at this temperature. V=vapour; L=liquid; I=ice; HH=hydrohalite; Mg12=$MgCl_2 \cdot 12H_2O$.

Experiment 038: 10 mass% NaCl / 13 mass% $MgCl_2$

Freezing of inclusions occur in general either with the nucleation of (1) ice or (2) ice and hydrohalite.

(1) The nucleation of ice occurs at temperatures around -100 °C, where small crystals start to grow in the liquid. Ice, a NaCl-$MgCl_2$-rich brine and vapour are present down to -190 °C. Final melting of ice is observed at -39.9 (±0.4). Ice melts metastably below the eutectic temperature (-35.3 °C). Therefore salinity calculations based in this temperature cannot be performed.

(2) Freezing of the inclusions behaves optically similar as described before (Fig. 5.40a-c). During heating, re-crystallisation into single crystals occurs, which allow the optical discrimination of ice and hydrohalite (Fig. 5.40d). Cooling of the phase assemblage results in the growth of the crystals. At -190 °C, ice, hydrohalite, a $MgCl_2$-rich brine and vapour is present (Fig. 5.40e). Melting of ice is observed at

-39.0 (±0.4) (Fig. 5.40f). Subsequent cooling (after the melting of ice), results in the growth of hydrohalite. Ice again nucleates at about -90 °C. $MgCl_2$-hydrate nucleation does not occur during further heating or cooling the inclusion. The last melting is observed by the dissolution of hydrohalite at about -33.2 (±0.8) °C. Again, those estimated melting temperatures do not allow a salinity calculation, because ice as well as hydrohalite melts metastably (see Chapter 7).

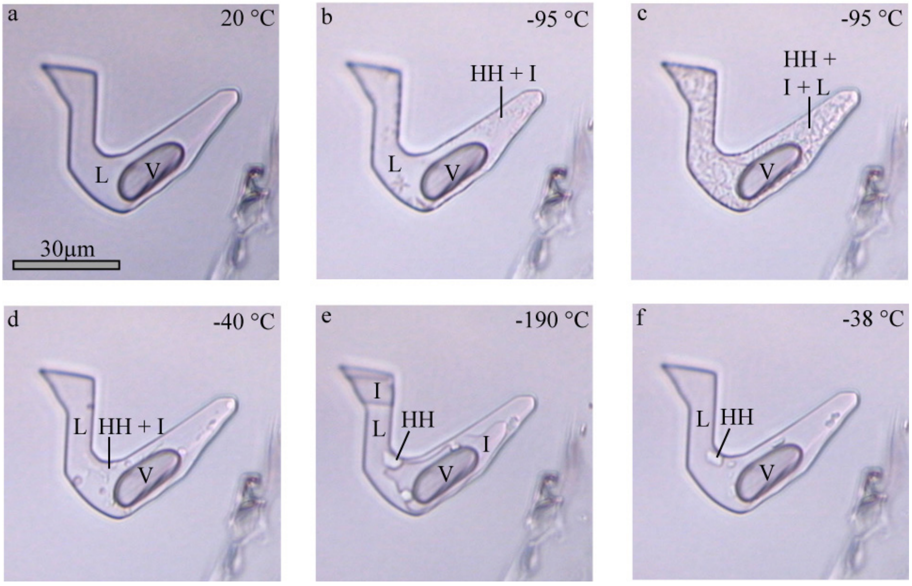

Fig. 5.40. Freezing and melting behaviour of an inclusion in experiment 038. a) Inclusion containing brine and vapour at 20 °C. b) Freezing of the inclusion at -95 °C with the nucleation of ice. c) Crystal growing by holding a constant temperature at -95 °C. Hydrohalite also nucleate around this temperature. d) Ice, hydrohalite, Mg-rich brine and vapour at -40 °C. e) Phase assemblage of ice, hydrohalite, super-cooled brine in the presence of vapour at -190 °C. f) Hydrohalite crystals, brine and vapour at -38 °C, after final ice melting at about -38 °C. V=vapour; L=liquid; I=ice; HH=hydrohalite.

The precipitation of an unknown solid phase, most probably a $MgCl_2 \cdot nH_2O$ modification, is rarely observed in some inclusion (Fig. 5.41a/b). It is not possible to distinguish between the different nucleation processes by optical means. Nevertheless, during heating a different melting attitude is observed compared to (1) and (2). First melt is generated in a temperature range from -60 to -50 °C (Fig. 5.40c-e). After melting a significant amount of liquid is present, which is equilibrium with ice and hydrohalite. If hydrohalite is a product of the reaction, or if it is already stable before the melting process, could not be confirmed. Therefore, the first optical melt process may not accord to eutectic melting and liquid may still be present at temperatures below -60 °C. The melting behaviour during further heating of such inclusion is the same as described in (2), and includes the melting of ice at about -40 °C followed by the melting of hydrohalite at about -33 °C. (Fig. 5.40f). Subsequent cooling does not induce the nucleation of the previously described phase again. Generally a reproduction of such nucleation procedures is very difficult and usually not possible.

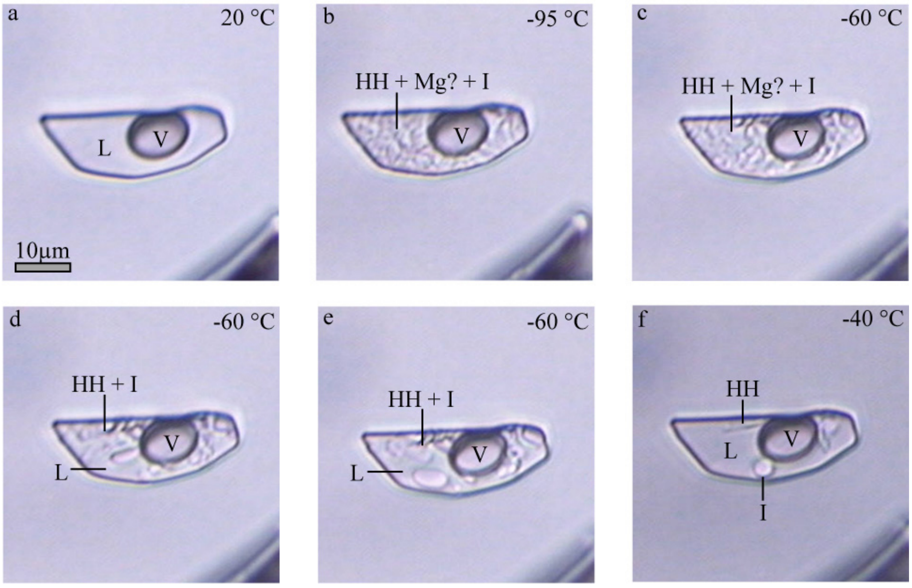

Fig. 5.41. Freezing and melting behaviour of an inclusion in experiment 038. a) Inclusion containing brine and vapour at 20 °C. b) Freezing of the inclusion at -95 °C. c) Stable phase assemblage of ice, Mg-hydrate, probably liquid or hydrohalite in the presence of vapour at -60 °C. d-e) Melting of Mg-Hydrate, remaining ice, hydrohalite, liquid and vapour. f) Single ice and hydrohalite crystals stable with vapour at -40 °C. V=vapour; L=liquid; I=ice; HH=hydrohalite; Mg?=$MgCl_2$-hydrate?

5.1.11. $CaCl_2$-$MgCl_2$-H_2O inclusions

Experiment 050: 10 mass% $CaCl_2$ / 10 mass% $MgCl_2$

Freezing of inclusions occur with the nucleation of: (1) ice, (2) ice and antarcticite or (3) ice and $MgCl_2 \cdot 12H_2O$.

(1) Ice nucleates at about -75 °C (Fig. 5.42a/b) into a microcrystalline texture, which show a greyish/brownish colour. At the freezing temperature, small amounts of brine remain present in the interstitial space between the ice crystals. Ice, brine and vapour remain down to -190 °C (Fig. 5.42e). Re-crystallisation into single ice crystals takes place during heating. Final melting is observed at -22.7 (±0.3) °C (Fig. c/d/f). The salinity can be approximated from the phase diagram (Fig. 2.2.15) by taking into account the intended NaCl/$MgCl_2$ ratio for synthesis (10 mass% $MgCl_2$ and 10% $CaCl_2$; ratio 1/1). About 10 mass% NaCl and 10 mass% $MgCl_2$ can be appreciated for the solution, which coincide with the intended salinity of synthesis.

(2) Ice and antarcticite precipitate in some of the inclusions. The melting of the hydrate is not observable because the hydrate occurs in a fine-grained mass together with ice and re-crystallisation to larger single hydrate crystals does not occur (the identification of the hydrate was only possible with Raman spectroscopy). Ice is the last phase to melt in those inclusions at temperatures about -23 °C. One inclusion contains a solid phase at temperatures above 0°. The last melting of this unknown phase is observed at about 13.5 °C. Most probably this phase belong to a $CaCl_2 \cdot nH_2O$ modification (γ-$CaCl_2 \cdot 4H_2O$, see results of experiment 021 in the binary $CaCl_2$-H_2O system).

(3) Ice and $MgCl_2 \cdot 12H_2O$ nucleation is observed in some of the inclusions. The hydrate crystals are optically not distinguishable from the ice crystals as both show a similar refraction index. The identification of the hydrate is only possible with Raman spectroscopy. The melting temperature of $MgCl_2 \cdot 12H_2O$ is observed between -40 and -35 °C. Last melting is again observed with the dissolution of ice at about -22 °C. The salinity can be approximated from the phase diagram shown in Fig. 2.14.

The salinity is approximated between 7 to 9 mass% $CaCl_2$ and 12 to 13 mass% $MgCl_2$. It is assumed, that the salinity approximation, based on the melting temperatures of the hydrates and ice, reveal the true values (compare with salinity approximation from the melting temperatures obtained in (1). More details are given in Chapter 7.

In the cases (2) and (3), hydrates (antarcticite or rather $MgCl_2 \cdot 12H_2O$) form together with ice, brine and vapour a phase assemblage down to temperatures of -190 °C. A precipitation of antarcticite together with $MgCl_2 \cdot 12H_2O$ is not observed. In general, replications of the precipitation of those hydrates in the inclusions were mostly not successful.

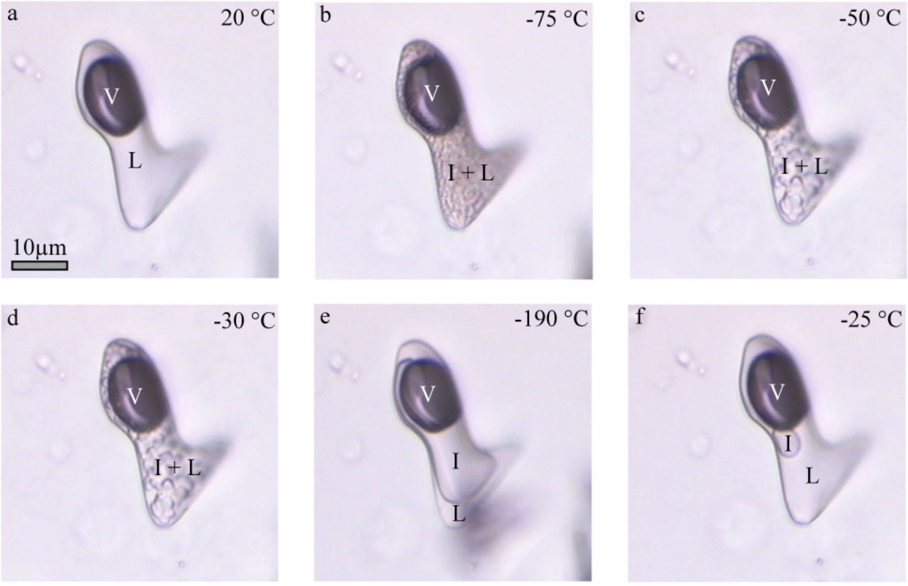

Fig. 5.42. Freezing and melting behaviour of an inclusion in experiment 050. a) Inclusion containing brine and vapour at 20 °C b) Nucleation of ice at -75 °C. c/d) Re-crystallisation of ice during heating. e) Single ice crystal, brine and vapour at -190 °C. f) Single ice crystal in the presence of brine and vapour at -25 °C. V=vapour; L=liquid; I=ice.

Experiment 051: 10 mass% $CaCl_2$ / 20 mass% $MgCl_2$

Inclusions, with an intended salinity of 10 mass% $CaCl_2$ and 20 mass% $MgCl_2$, do not freeze during subsequent heating and freezing. In only one inclusion ice nucleation at about -80 °C was observed. The relative volume of the ice crystal was very small did not change during further cooling. The last melting is observed at about -60 °C. As the eutectic is defined at about -55 °C, the melting of ice occurs in a metastable state. Hydrates do not nucleate in the inclusions.

5.2. Microthermometry: Heating experiments

Synthesised fluid inclusions with known composition are trapped in quartz at defined temperatures and pressures (see Chapter 3). From those parameters the homogenisation temperature as well as the type of homogenisation, i.e. homogenisation into vapour respectively liquid or rather critical homogenisation, can be predicted. Homogenisation data for all experiments are listed in Chapter 5.3/Table 5.13.

Experimental parameters of pure water experiments (see Table 5.13) were chosen to reach critical homogenisation at 374 °C. Figure 5.43 displays an inclusion during heating from room temperature up to the critical homogenisation. With increasing temperature the volume fraction liquid/vapour does not change significantly (Fig. 5.43a-c). Inclusions homogenise neither by evaporation of the liquid nor by condensation of the vapour phase. The density of the vapour increases towards the critical value, whereas the density of the liquid decreases, until both phases occupy an equal volume in the inclusion. The meniscus between liquid and vapour disappears exactly at the critical point liquid and vapour is transferred into a supercritical fluid (Fig. 5.43d-f). During further heating the inclusion will follow the critical isochore. The supercritical fluid separates again during cooling just below the critical point again into a liquid and vapour phase.

Salt containing inclusions homogenise throughout into the liquid phase during heating experiments. Figure 5.44 illustrates the typical path of such inclusions during heating. At room temperature (Fig. 5.44a) the inclusion contains liquid and vapour, whereas the corresponding volume fractions depend on the fluid density at trapping (desired temperature and pressure of synthesis). The volume fraction of vapour decreases significantly during heating to 400 °C (Fig. 5.44c-d). At 403 °C the inclusion homogenise into liquid phase (Fig. 5.44e). Subsequent cooling does not immediately result again in the separation of the liquid, as observed for inclusions with critical density. The separation is delayed and occurs at 381 °C (Fig. 5.44f). Such a delay is observed for all synthesised saline inclusions, whereas the temperature interval of supercooling may differ in the diverse experiments.

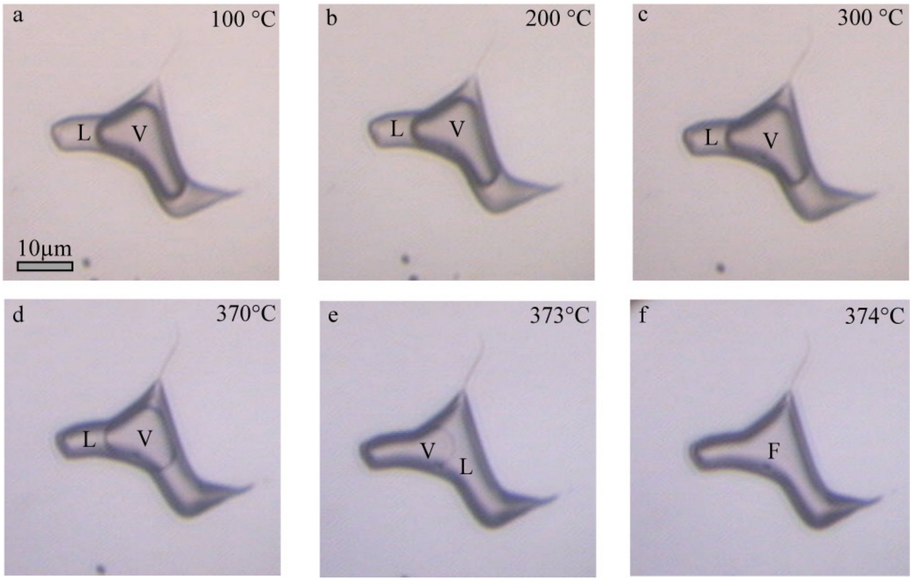

Fig. 5.43. Critical homogenisation of H_2O fluid inclusion. a-c) Fluid inclusions containing liquid and vapour during heating from 100 °C to 300 °C. The volume fraction remains nearly constant during heating. d) The volume fraction of the vapour is reduced at 370 °C. e) The meniscus between liquid and vapour start to disappear at 373 °C. f) The inclusion contain a supercritical fluid at 374 °C. L=liquid; V=vapour; F=supercritical fluid.

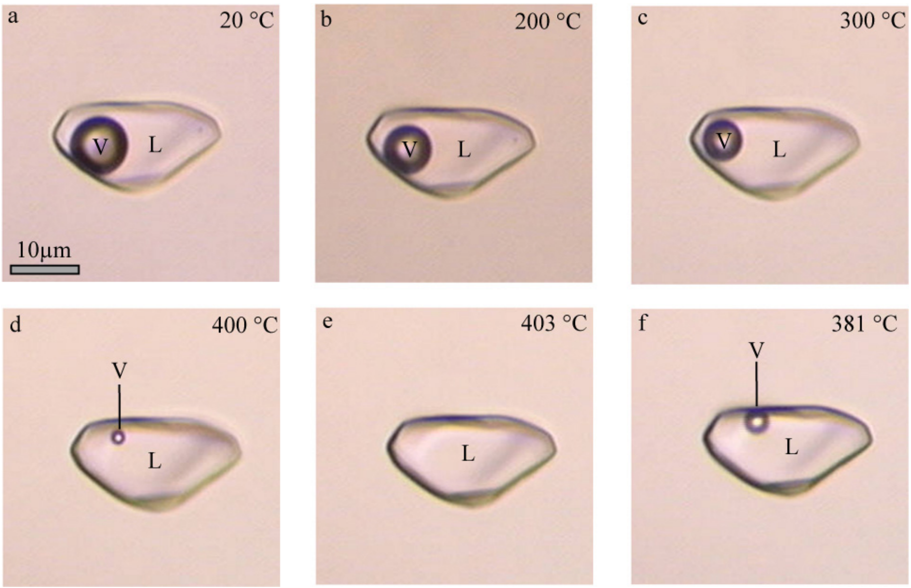

Fig. 5.43. Homogenisation into the liquid phase of a NaCl-$CaCl_2$-H_2O fluid inclusion (experiment 024). a-d) Fluid inclusion containing liquid and vapour during heating from 20 °C to 400°C. e) At 403 °C the inclusion homogenise into liquid. f) Separation of the liquid phase into liquid and vapour at 381 °C. L=liquid; V=vapour.

5.3. Microthermometry – Results

Table 5.1. Ice melting temperatures ($T_{m(ice)}$) of pure H_2O fluid inclusions. The salinity calculations are based on ice melting temperatures according to the equation of state of Potter et al. (1978) using the software AqSo5e (Bakker 2003). Calculations are based on equivalent mass% NaCl. *n* represents the number of measured inclusions. Temperatures are given in °C.

Experiment	$T_{m(ice)}$	n	mass% NaCl
001	-0.4 (±0.2)	20	0.6 (±0.3)
003	-0.1 (±0.1)	28	0.3 (±0.2)
027	0.1 (±0.0)	20	0.0 (±0.0)
028	0.1 (±0.1)	20	0.0 (±0.0)
029	0.1 (±0.1)	20	0.0 (±0.0)
041	-0.4 (±0.1)	20	0.7 (±0.2)
042	0.1 (±0.1)	20	0.0 (±0.0)

Table 5.2 Ice and hydrohalite melting temperatures ($T_{m(ice)}$; $T_{m(HH)}$) of NaCl-H_2O fluid inclusions. The salinity calculations are based on ice melting temperatures accord to the equation of state of Bodnar (1993) using the software BULK (Bakker, 2003). *n* represents the number of measured inclusions. Temperatures are given in °C.

Experiment	$T_{m\ (ice)}$	$T_{m(HH)}$	n	mass% NaCl
002	-21.0 (±0.3)	-21.1	18	23.1 (±0.2)
004	-21.1 (±0.1)	-21.1	40	23.1 (±0.1)
008	-2.7 (±0.1)	-21.1	30	4.5 (±0.2)
009	-3.6 (±0.1)	-21.1	30	5.9 (±0.2)
010	-4.8 (±0.0)	-21.1	10	7.6 (±0.0)
011	-6.4 (±0.4)	-21.1	30	9.7 (±0.6)
012	-8.3 (±0.0)	-21.1	10	12.1 (±0.0)
013	-9.8 (±0.1)	-21.1	10	13.8 (±0.1)
015	-14.2 (±0.0)	-21.1	10	17.9 (±0.0)
016	-16.8 (±0.1)	-21.1	10	20.0 (±0.0)
017	-12.0 (±0.1)	-21.1	40	15.9 (±0.1)
018	-20.3 (±0.1)	-21.1	30	22.6 (±0.1)
019	-21.1 (±0.1)	-21.1	10	23.2 (±0.0)

Table 5.3. Ice melting temperatures ($T_{m(ice)}$) of $CaCl_2$-H_2O fluid inclusions. Salinity calculations are based on equation 4.1 (see Chapter 4.2). n represents the number of measured inclusions. Temperatures are given in °C.

Experiment	$T_{m(ice)}$	n	mass% $CaCl_2$
020	-	-	-
021	-	-	-
022	-18.4 (±1.0)	17	20.6 (±0.5)
044	-11.1 (±0.2)	7	15.3 (±0.2)
045	-46.5 (±0.3)	3	29.8 (±0.1)

Table 5.4. Melting temperatures of $CaCl_2$-hydrates (T_m) observed from experiment 021 and 045. Salinity calculations are based on equations. 4.2, 4.3, 4.5 and 4.6 (see Chapter 4.2). Temperatures are given in °C.

Experiment	Phase	T_m	n	mass% $CaCl_2$
021	$CaCl_2 \cdot 6H_2O$	29.4 (±0.3) °C	5	49.0 (±0.5)
021	$CaCl_2 \cdot 6H_2O$	29.7 °C (±0.7)*	16	-
021	α-$CaCl_2 \cdot 4H_2O$	32.5 (±0.4) °C	28	50.7(±0.1)
021	γ-$CaCl_2 \cdot 4H_2O$	11.5 (±0.2) °C	7	50.0 (±0.0)
021	$CaCl_2 \cdot 2H_2O$	-29 to -26 °C **	4	~ 50
044	γ-$CaCl_2 \cdot 4H_2O$	~ 13.0	2	~ 50
045	$CaCl_2 \cdot 6H_2O$	25.4 (±0.6) °C	8	45.7 (±0.4)
045	γ-$CaCl_2 \cdot 4H_2O$	5 to 10 °C	2	49.9 (±0.4)

* peritectic melting

** phase transition into α-$CaCl_2 \cdot 4H_2O$

Table 5.5. Ice and $MgCl_2 \cdot 12H_2O$ melting temperatures ($T_{m(ice)}$; $T_{m(Mg12)}$) of $MgCl_2$-H_2O fluid inclusions. The salinity calculations are based on ice melting temperatures according to empirical best fits after Dubois & Marignac (1997) using the software AqSo3e (Bakker, 2003). Salinity calculations according to metastable ice melting (experiment 030) are performed with equation 4.7 (see Chapter 4.2). n represents the number of measured inclusions. Temperatures are given in °C.

Experiment	$T_{m(ice)}$	$T_{m(Mg12)}$	n	mass% $MgCl_2$
025	-23.1 (±1.3)	~ -33.0 *	17 / 3 *	17.7 (±0.5)
026	-	-	-`	-
030	-32.4 (±0.6)	-32.8 (±0.2) *	13 / 5 *	20.7 (±0.2)
	-39.8 (±0.1)**	-	6	22.5 (±0.0)
047	-	-	-	-

* eutectic melting

** metastable melting; only observed when $MgCl_2 \cdot 12H_2O$ nucleation was absent

Table 5.6. Ice and $FeCl_2 \cdot 6H_2O$ melting temperatures ($T_{m(ice)}$; $T_{m(Fe6)}$) of $FeCl_2$-H_2O fluid inclusions. Salinity calculations are based on equation 4.8 (see Chapter 4.2). n represents the number of measured inclusions. Temperatures are given in °C.

Experiment	$T_{m(ice)}$	$T_{m(Fe6)}$	n	mass% $FeCl_2$
RJB 006	-5.9 (±0.3)	-	26	11.5 (±0.3)
RJB 007	-9.2 (±0.5)	-33*	20 / 2*	14.6 (±0.4)
RJB 011	-14.4 (±0.2)	-	19	18.6 (±0.1)

* eutectic melting

Table 5.7. Ice melting temperatures ($T_{m(ice)}$) of $FeCl_3$-H_2O fluid inclusions. Salinity calculations are based on equation 4.9 (see Chapter 4.2). n represents the number of measured inclusions. Temperatures are given in °C.

Experiment	$T_{m(ice)}$	n	mass% $FeCl_3$
RJB 008	-31.1 (±1.0)	11	27.3 (±0.4)
RJB 016	-11.1 (±0.2)	20	16.4 (±0.2)

Table 5.8. Ice melting temperatures ($T_{m(ice)}$) of LiCl-H_2O fluid inclusions. Salinity calculations are based on equation 4.10 (see Chapter 4.2). n represents the number of measured inclusions. Temperatures are given in °C.

Experiment	$T_{m(ice)}$	n	mass% LiCl
053	-12.0 (±0.1)	20	9.8 (±0.1)
056	~ -70	1	~ 25.0

Table 5.9. Ice melting temperatures ($T_{m(ice)}$) of $ZnCl_2$-H_2O fluid inclusions. Salinity calculations are based on equation 4.11 (see Chapter 4.2). n represents the number of measured inclusions. Temperatures are given in °C.

Experiment	$T_{m(ice)}$	n	mass% $ZnCl_2$
048	-17.3 (±0.1)	13	27.6 (±0.1)
049	-32.1 (±0.3)	3	37.9 (±0.2)
052	-4.2 (±0.1)	11	10.7 (±0.2)

Table 5.10. Ice and hydrohalite melting temperatures ($T_{m(ice)}$, $T_{m(HH)}$) of NaCl-$CaCl_2$-H_2O fluid inclusions. Salinity calculations accord to empirical best fits after Naden (1996) using the software AqSo2e (Bakker, 2003). *n* represents the number of measured inclusions. Temperatures are given in °C.

Experiment	$T_{m(ice)}$	n	$T_{m(HH)}$	n	$T_{m(H)}$	n	mass% NaCl	mass% $CaCl_2$
006	-34.2 (±1.1)*	6	-	-	-	-	-	-
	-27.6 (±0.4)	9	-0.1 (±0.1)	9	-	-	13.2 (±0.7)	15.1 (±0.6)
	-27.3 (±0.8)	2	-4.6 (±1.4)	2	-	-	13.4 (±1.2)	14.6 (±1.2)
024	-42.2 (±0.3)**	3	-12 to 30	6	-	-	-	-
	-40.6 (±0.5)***	5	-	-	140 to 187	9	-	-

* metastable melting; only observed when hydrohalite nucleation was absent

** phase assemblage: hydrohalite, ice and liquid

*** phase assemblage: halite ice and liquid

Table 5.11. Ice, hydrohalite and $MgCl_2 \cdot 12H_2O$ melting temperatures ($T_{m(ice)}$, $T_{m(HH)}$, $T_{m(Mg12)}$) of NaCl-$MgCl_2$-H_2O fluid inclusions. $T_{m(Mg?)}$ corresponds to the melting of an undefined phase (most probably $MgCl_2 \cdot nH_2O$). Salinity calculations accord to empirical best fits after after Dubois & Marignac (1997) using the software AqSo3e (Bakker, 2003). Salinities given for experiment 035 (according to ice melting only) are approximated from the phase diagram shown in Fig. 2.14. Salinity calculations for experiment 038 could not be performed, due to metastable melting. *n* represents the number of measured inclusions. Temperatures are given in °C.

Experiment	$T_{m(ice)}$	n	$T_{m(HH)}$	n	$T_{m(Mg12)}$	n	$T_{m(Mg?)}$	n	mass% NaCl	mass% $MgCl_2$
033	-20.5 (±0.1)	7	-25.1 (±0.4)	7	-	-	-	-	12.5 (±0.7)	9.3 (±0.5)
035	-26.4 (±0.2)	8	-	-	-	-	-	-	1.7	17.5
	-26.2 (±0.3)	5	-35.6 (±0.3)	5	-35.6 (±0.3)	5	-	-	5.2 (±0.7)	16.4 (±0.4)
038	39.9 (±0.4)	13	-	-	-	-	-50 to	3	-	-
	-39.0 (±0.4)*	14	-33.2 (±0.8)*	?	-33.2 (±0.8)*	14	-60**	?	-	-

* metastable melting

** metastable eutectic melting

Table 5.12. Ice and $MgCl_2 \cdot 12H_2O$ melting temperatures ($T_{m(ice)}$, $T_{m(Mg12)}$) $CaCl_2$-$MgCl_2$-H_2O fluid inclusions. $T_{m(?)}$ corresponds to the melting of an undefined phase (most probably γ-$CaCl_2 \cdot 4H_2O$). The salinity is approximated from ice and $MgCl_2 \cdot 12H_2O$ melting temperatures according to Fig. 2.15. n represents the number of measured inclusions. Temperatures are given in °C.

Experiment	$T_{m(ice)}$	n	$T_{m(Mg12)}$	n	$T_{m(?)}$	n	mass% $CaCl_2$	mass% $MgCl_2$
050	-22.7 (±0.3)	10	-	-	-	-	-	-
	-22.1 (±0.1)	3	-40 to -35 °C	3	-	-	6.8 to 8.8	11.6 to 13.2
	-	-	-	-	13.5	1	-	-
051	-60	1	-	-	-	-	-	-

Table 5.13. Homogenisation temperatures (T_h) of synthesised inclusions. Pure H_2O inclusions homogenise critical (L + V → F), whereas all other inclusions showed homogenisation into the liquid phase (L + V → L). *n* represents the number of measured inclusions. Temperatures are given in °C.

Experiment	Composition	T_h (L + V → L)	n	T_h (L +V → F)	n
001	H_2O	-	-	370.3 (±0.9)	20
003	H_2O	-	-	373.0 (±0.5)	28
027	H_2O	-	-	374.6 (±0.5)	20
028	H_2O	-	-	374.1 (±0.4)	20
029	H_2O	-	-	374.1 (±0.2)	20
041	H_2O	-	-	366.8 (±2.0)	20
042	H_2O	-	-	374.1 (±0.4)	20
054	H_2O	-	-	372.9 (±2.3)	20
002	$NaCl$-H_2O	390.9 (±7.3)	20	-	-
004	$NaCl$-H_2O	392.2 (±0.2)	22	-	-
008	$NaCl$-H_2O	417.9 (±2.3)	18	-	-
009	$NaCl$-H_2O	397.4 (±3.2)	30	-	-
010	$NaCl$-H_2O	401.7 (±3.7)	30	-	-
011	$NaCl$-H_2O	402.7 (±0.4)	10	-	-
012	$NaCl$-H_2O	402.0 (±1.5)	30	-	-
013	$NaCl$-H_2O	406.9 (±0.7)	10	-	-
015	$NaCl$-H_2O	407.3 (±1.1)	10	-	-
016	$NaCl$-H_2O	398.3 (±0.2)	10	-	-
017	$NaCl$-H_2O	397.1 (±0.6)	10	-	-
018	$NaCl$-H_2O	403.0 (±1.0)	40	-	-
019	$NaCl$-H_2O	391.7 (±1.2)	30	-	-
055	$NaCl$-H_2O	388.5 (±0.5)	10	-	-
020	$CaCl_2$-H_2O	465.4 (±5.1)	18	-	-
020	$CaCl_2$-H_2O	494.6 (±2.3)	2	-	-
021	$CaCl_2$-H_2O	436.6 (±6.5)	20	-	-
022	$CaCl_2$-H_2O	401.5 (±7.2)	7	-	-
022	$CaCl_2$-H_2O	486.6 (±5.5)	13	-	-
044	$CaCl_2$-H_2O	448.3 (±1.7)	20	-	-
045	$CaCl_2$-H_2O	445.0 (±2.4)	20	-	-
025	$MgCl_2$-H_2O	430.1 (±5.1)	20	-	-

Table 5.13. Continued

Experiment	Composition	T_h (L + V → L)	n	T_h (L +V → F)	n
026	$MgCl_2$-H_2O	408.5 (±6.0)	14	-	-
026	$MgCl_2$-H_2O	450.5 (±5.6)	6	-	-
030	$MgCl_2$-H_2O	390.8 (±2.9)	16	-	-
030	$MgCl_2$-H_2O	436.6 (±13.2)	4	-	-
047	$MgCl_2$-H_2O	404.2 (±1.0)	18	-	-
047	$MgCl_2$-H_2O	439.9 (±0.1)	2	-	-
RJB 006	$FeCl_2$-H_2O	334.4 (±7.5)	20	-	-
RJB 007	$FeCl_2$-H_2O	380.8 (±7.1)	10	-	-
RJB 007	$FeCl_2$-H_2O	359.1 (±9.7)	10	-	-
RJB 011	$FeCl_2$-H_2O	367.8 (±3.4)	20	-	-
RJB 018	$FeCl_3$-H_2O	377.9 (±5.2)	20	-	-
RJB 016	$FeCl_3$-H_2O	365.4 (±1.3)	20	-	-
053	LiCl-H_2O	449.8 (±0.4)	12	-	-
053	LiCl-H_2O	480.3 (3.2)	2	-	-
056	LiCl-H_2O	443.0 (±23.9)	15	-	-
056	LiCl-H_2O	495.9 (±4.4)	5	-	-
048	$ZnCl_2$-H_2O	383.3 (±2.5)	20	-	-
049	$ZnCl_2$-H_2O	349.9 (±1.7)	20	-	-
052	$ZnCl_2$-H_2O	402.9 (±3.9)	15	-	-
006	NaCl-$CaCl_2$-H_2O	406.5 (±5.6)	20	-	-
024	NaCl-$CaCl_2$-H_2O	407.0 (±7.0)	20	-	-
033	NaCl-$MgCl_2$-H_2O	441.1 (±10.4)	17	-	-
033	NaCl-$MgCl_2$-H_2O	364.1 (±0.7)	3	-	-
035	NaCl-$MgCl_2$-H_2O	510.8 (±1.4)	20	-	-
038	NaCl-$MgCl_2$-H_2O	419.7 (±6.6)	17	-	-
038	NaCl-$MgCl_2$-H_2O	371.0 (0.2)	3	-	-
050	$CaCl_2$-$MgCl_2$-H_2O	455.1 (±1.6)	20	-	-
051	$CaCl_2$-$MgCl_2$-H_2O	492.5 (±8.0)	19	-	-
051	$CaCl_2$-$MgCl_2$-H_2O	433.8	1	-	-

5.4. Raman spectroscopy of inclusions at low temperatures

Raman spectroscopy of fluid inclusions at low temperatures was performed, by attaching a heating-freezing stage to the Raman spectrometer (see Chapter 4). During the microthermometric runs, Raman spectra were taken at different temperatures on the various phase assemblages, which occurred during freezing and heating of the inclusions (see Chapter 5.2).

5.4.1. H_2O inclusions

Ice nucleates in pure H_2O inclusions during cooling experiments. The Raman spectrum of ice shows two main peak positions at 3091 (±3) and 3218 (±3) at -190 °C. Additionally a broad band with a maximum at about 3321 (±4) cm^{-1} can be defined. At higher temperatures, peaks shift to higher wavenumbers and peak broadening occur (Fig. 5.44a). A fitting procedure can be applied to analyse the Raman spectra. Deconvolution of the ice spectrum results in six Gaussian-Lorentzian contributions with major peak positions at 3090 ($\Delta\nu_2^{ice}$) and 3215 ($\Delta\nu_4^{ice}$) cm^{-1}. Peak positions of hidden peaks are positioned at 3000 ($\Delta\nu_1^{ice}$), 3125 ($\Delta\nu_3^{ice}$), 3310 ($\Delta\nu_5^{ice}$), and 3408 ($\Delta\nu_6^{ice}$) cm^{-1} (Fig. 5.44b). Main peak positions obtained from the fitted contributions are in a good agreement with the maxima obtained from the raw spectra. In addition, the fitting procedure allows the estimation of three additional band positions, which cannot accurately defined from the raw spectra.

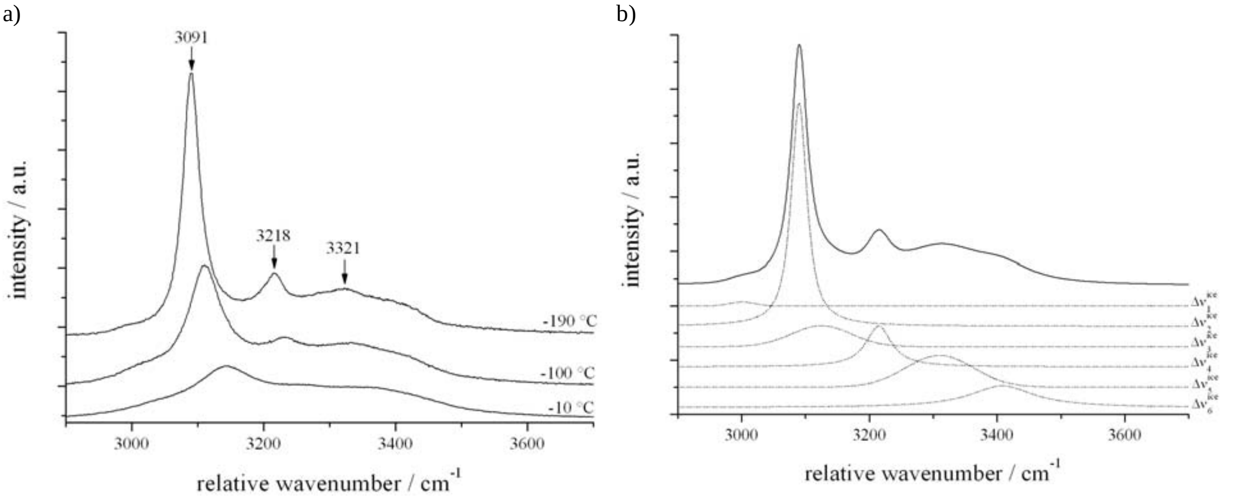

Fig. 5.44 a) Raman spectra of ice at -190 °C, -100 °C and -10 °C. b) Raman spectrum of ice at -190 °C (solid line). Dotted lines represent the Gaussian-Lorentzian deconvolution of the spectra resulting in six contributions ($\Delta\nu_1^{ice}$ - $\Delta\nu_6^{ice}$). The properties of the fits are given in Table A-1(APPENDIX).

A general trend of peak shift to higher wavenumbers with increasing temperature can be correlated from the deconvolved parameters (Fig. 5.45). A polynomial best fit through the observed main peak positions of $\Delta\nu_2^{ice}$ and $\Delta\nu_4^{ice}$ results in equation 5.1 and 5.3, respectively. Supplementary, the full width at half maximum is increasing. A polynomial best fit results in equation 5.2 and 5.4 for $\Delta\nu_2^{ice}$ and $\Delta\nu_4^{ice}$, respectively.

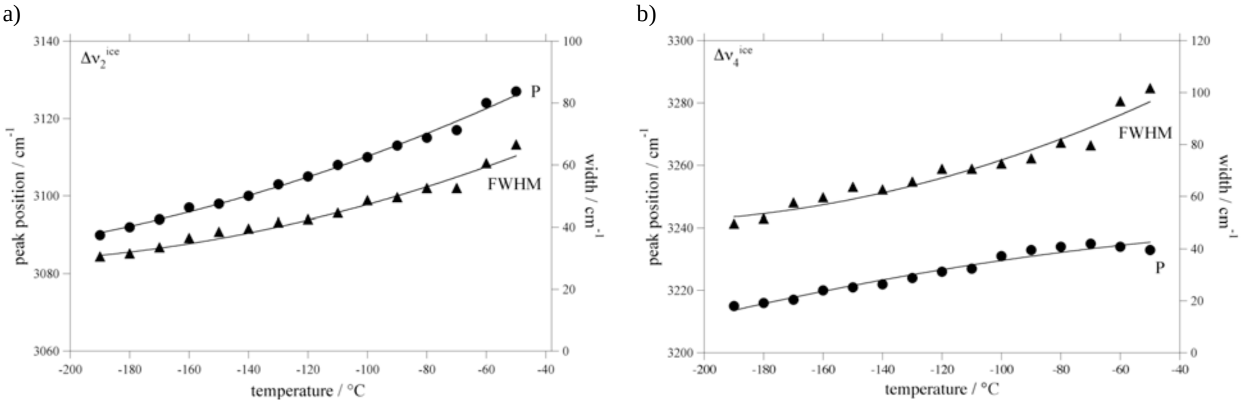

Fig. 5.45. Deconvolved peak position (*P*) and full width at half maxima (FWHM) of ice a) $\Delta\nu_2^{ice}$ and b) $\Delta\nu_4^{ice}$ as a function of temperature obtained from pure water fluid inclusion (experiment 027).

$$P_{(\Delta\nu_2^{ice})} = 3145.4 + 0.42157 \cdot T + 0.00070297 \cdot T^2 \tag{5.1}$$

$$FWHM_{(\Delta\nu_2^{ice})} = 83.311 + 0.4553 \cdot T + 0.00094619 \cdot T^2 \tag{5.2}$$

$$P_{(\Delta\nu_4^{ice})} = 3239.2 + 0.05271 \cdot T - 0.00043067 \cdot T^2 \tag{5.3}$$

$$FWHM_{(\Delta\nu_4^{ice})} = 126.29 + 0.66976 \cdot T + 0.0014722 \cdot T^2 \tag{5.4}$$

5.4.2. NaCl-H$_2$O inclusions

Hydrohalite and ice precipitate in inclusions synthesised in the NaCl-H$_2$O system during cooling experiments. Raman spectra at -190 °C reveal four main peaks for hydrohalite centred at about 3401 (±2) $\Delta\nu_3^{HH}$, 3418 (±1) $\Delta\nu_4^{HH}$, 3432 (±2) $\Delta\nu_5^{HH}$ and 3536 (±4) $\Delta\nu_6^{HH}$ cm^{-1}. Additionally, two small peaks are located at about 3299 (±1) $\Delta\nu_1^{HH}$ and 3320 (±2) $\Delta\nu_2^{HH}$ cm^{-1}. Raman spectra recorded on hydrohalite crystals in different inclusions show a variation in relative peak intensities, which is a consequence of the relative crystal orientation of the hydrate (Fig. 5.46). As the spectra were not always recorded on single crystals respectively the crystal orientation was not known, the relative intensity has only a limited significance.

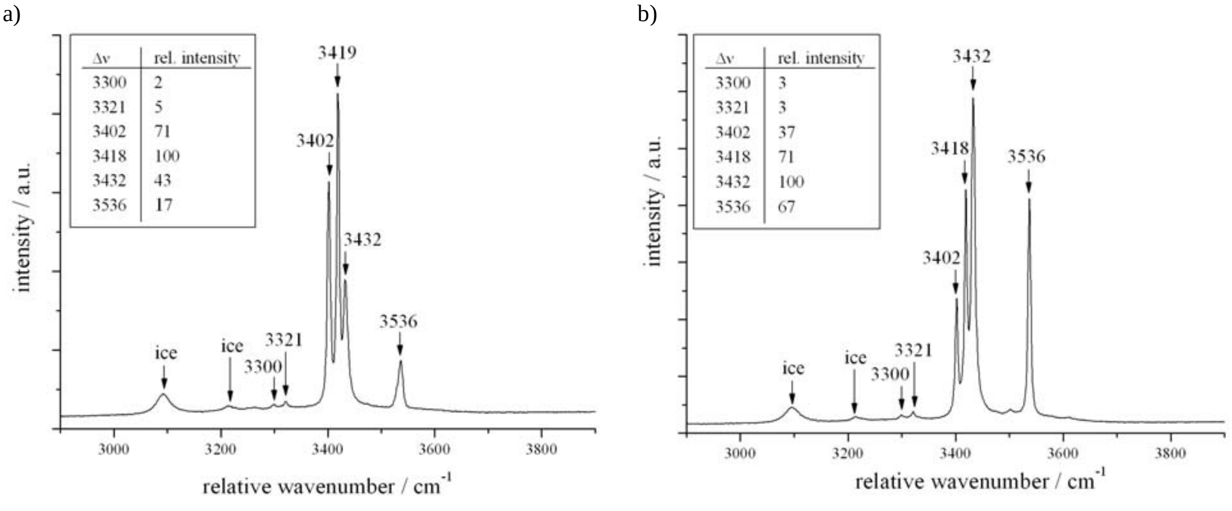

a)

Δv	rel. intensity
3300	2
3321	5
3402	71
3418	100
3432	43
3536	17

b)

Δv	rel. intensity
3300	3
3321	3
3402	37
3418	71
3432	100
3536	67

Fig. 5.46 Raman spectra of hydrohalite at -190 °C taken from two different inclusions from experiment a) 009 and b) 010. Variable relative peak intensities are caused by different crystallographic orientation of the measured hydrate crystals.

The Raman bands of hydrohalite are broadening with increasing temperature and thereby spectroscopic information is lost (Fig. 5.47). At -190 °C six peaks can be obtained, whereas at -100 °C the band position at 3432 cm^{-1} ($\Delta\nu_5^{HH}$) is hidden due to peak broadening. Only two bands ($\Delta\nu_4^{HH}$, $\Delta\nu_6^{HH}$) are recorded at -30 °C.

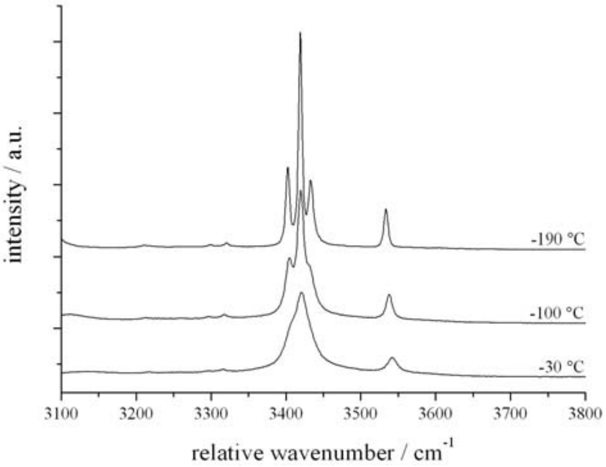

Fig. 5.47. Raman spectra of hydrohalite at -190 °C, -100°C and -30°C.

To analyse Raman spectra of ice-hydrohalite mixtures at higher temperatures, a deconvolution using Gaussian-Lorentzian functions is required. A hydrohalite/ice spectrum at -190 °C can be deconvolved into nine Gaussian-Lorentzian contributions (see Fig. 5.48). The contribution $\Delta\nu^{bg}$ is necessary to compensate background effects of the raw spectrum. After fitting the spectra at different temperatures the shift in band position and full width at half maximum can be obtained (Fig. 5.49). Peak positions of $\Delta\nu_5^{HH}$ shift to lower wavenumbers with decreasing temperature, whereas $\Delta\nu_3^{HH}$ and $\Delta\nu_6^{HH}$ shift to higher wavenumbers. The position of $\Delta\nu_4^{HH}$, which represents the most characteristic maxima of the spectra, is nearly constant in the observed temperature range. In general, the full width at half maximum is increasing with rising temperature (see Fig. 5.49). Polynomial best fits through the main peak positions as well as through the peak width are given in equations 5.5. to 5.12.

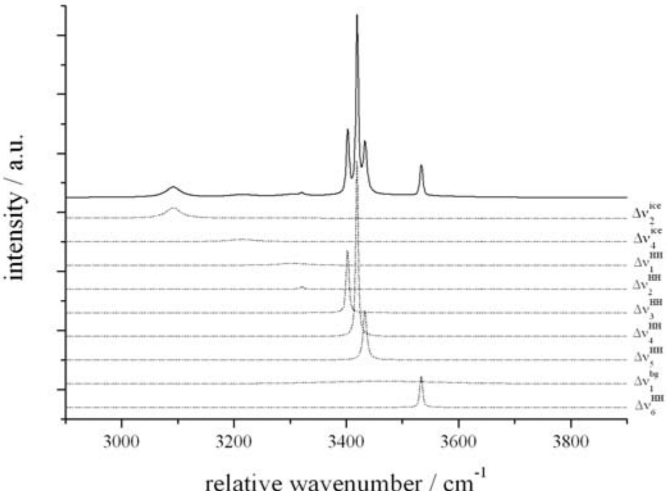

Fig. 5.48. Raman spectrum of hydrohalite and ice at -190 °C. Dotted lines represent the Gaussian-Lorentzian deconvolution of the spectrum resulting in nine contributions, whereas band positions centred at 3092 and 3214 cm^{-1} ($\Delta\nu_{2-4}^{ice}$) belongs to the Raman modes of ice. Band positions at 3304, 3321, 3402, 3419, 3433, 3535 cm^{-1} ($\Delta\nu_{1-6}^{HH}$) belongs to the Raman modes of hydrohalite. $\Delta\nu^{bg}$ with a band positions centred at 3462 cm^{-1} compensate background effects. The properties of the fit are given in Table A-2 (APPENDIX).

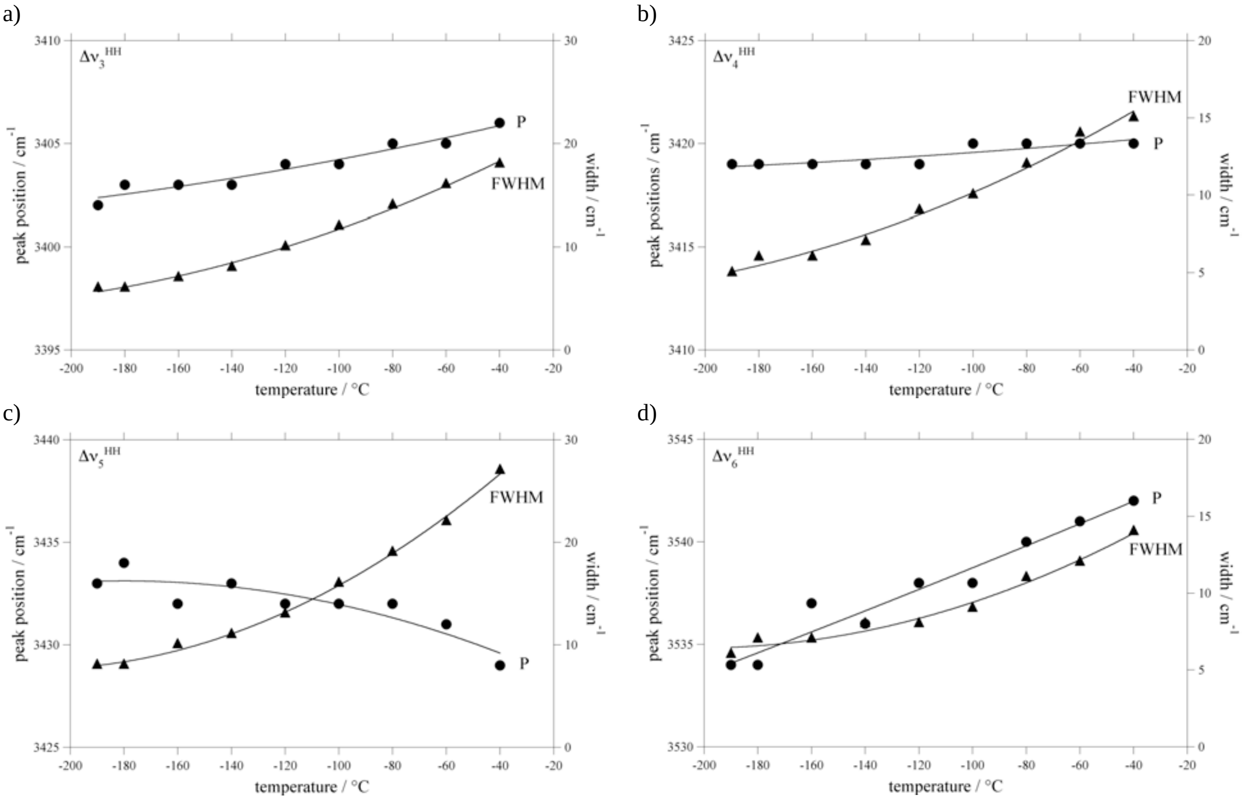

Fig. 5.49 Peak positions (*P*) and half width at full maximum (*FWHM*) for the Gaussian-Lorentzian contribution as a function of a) $\Delta\nu_3^{HH}$ and b) $\Delta\nu_4^{HH}$, c) $\Delta\nu_5^{HH}$, and d) $\Delta\nu_6^{HH}$ as a function of temperature.

$$P_{(\Delta\nu_3^{HH})} = 3407.1 + 0.033691 \cdot T + 4.5029 \cdot 10^{-5} \cdot T^2 \qquad (5.5)$$

$$FWHM_{(\Delta\nu_3^{HH})} = 23.779 + 0.14835 \cdot T + 0.00027866 \cdot T^2 \qquad (5.6)$$

$$P_{(\Delta\nu_4^{HH})} = 3420.7 + 0.013157 \cdot T + 1.9098 \cdot 10^{-5} \cdot T^2 \qquad (5.7)$$

$$FWHM_{(\Delta\nu_4^{HH})} = 19.807 + 0.11761 \cdot T + 0.00021095 \cdot T^2 \qquad (5.8)$$

$$P_{(\Delta\nu_5^{HH})} = 3427.3 - 0.064642 \cdot T - 0.00017964 \cdot T^2 \qquad (5.9)$$

$$FWHM_{(\Delta\nu_5^{HH})} = 36.426 + 0.26899 \cdot T + 0.00062782 \cdot T^2 \qquad (5.10)$$

$$P_{(\Delta\nu_6^{HH})} = 3544.2 - 0.056328 \cdot T - 1.609 \cdot 10^{-5} \cdot T^2 \qquad (5.11)$$

$$FWHM_{(\Delta\nu_6^{HH})} = 18.004 + 0.1142 \cdot T + 0.00028162 \cdot T^2 \qquad (5.12)$$

5.4.3. $CaCl_2$-H_2O inclusions

Cooling of inclusions in the $CaCl_2$-H_2O system may lead to the precipitation of various solid phases (see Chapter 5.1). In general, ice and brine are present in low salinity inclusions, whereas high saline inclusions form $CaCl_2$-hydrates (i.e. antarcticite, tetrahydrate-modifications and sinjarite) during cooling experiments.

Ice and brine

Raman spectra confirm the presence of brine or rather ice and brine at -190 °C in inclusions with relatively low salinities. $CaCl_2$-rich brine reveals a broad signal (Fig. 5.50a), which can be assigned to a typical liquid aqueous solution spectrum. The presence of ice is confirmed by Raman bands, centred at about 3090 and 3216 cm^{-1} (Fig. 5.50b).

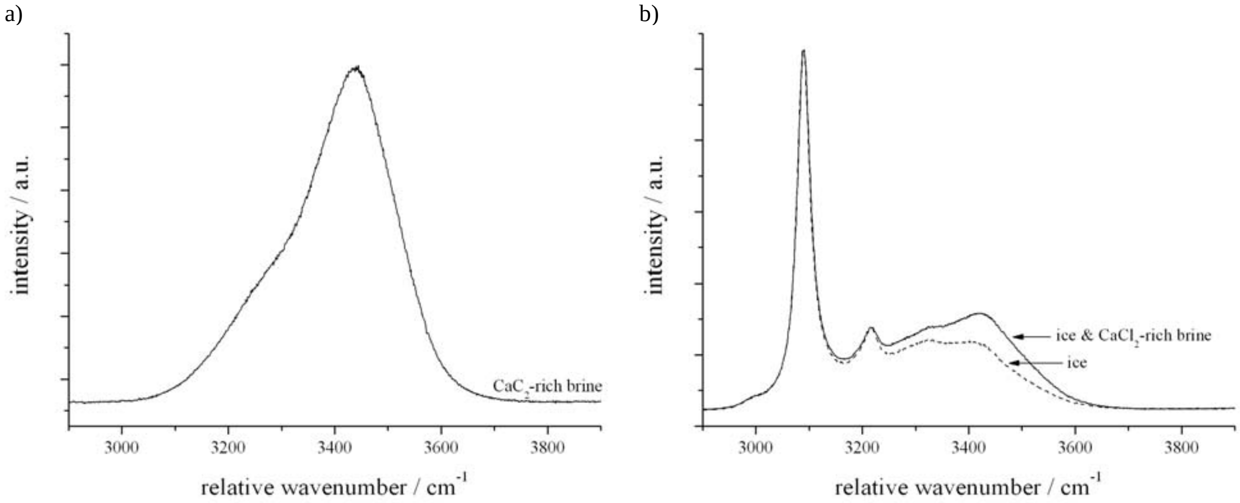

Fig. 5.50. Raman spectra of a) 30 mass% $CaCl_2^{\cdot}$-rich brine and b) ice and $CaCl_2$-rich brine at -190 °C.

Antarcticite ($CaCl_2{\cdot}6H_2O$)

The Raman spectrum of antarcticite is defined with four main peak positions at about 3240 (±2) $\Delta\nu_1^{an}$, 3387 (±2) $\Delta\nu_2^{an}$, 3402 (±2) $\Delta\nu_3^{an}$ and 3430 (±1) $\Delta\nu_4^{an}$ cm^{-1} at -190 °C. Spectra of antarcticite are gained, which show variations in peak positions and relative intensities, which correspond to different orientations of the measured hydrate crystals (Fig. 5.51). Depending on the crystallographic orientation, Raman bands could be absent or are poorly recognisable. For example, the peak centred at about 3387 cm^{-1} in Figure 5.51a is only evident as a shoulder in Figure 5.51b.

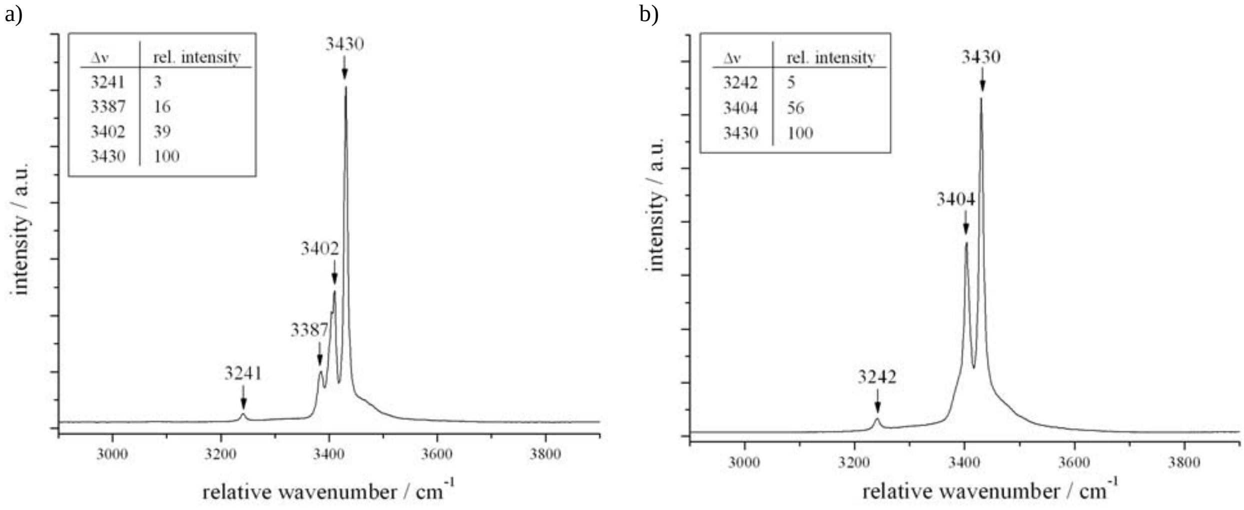

Fig. 5.51. Raman spectra of antarcticite at -190 °C (experiment 021). Variable relative peak intensities are caused by different crystallographic orientations of the measured hydrate crystals.

As well as for other hydrates, peak broadening is obtained with increasing temperatures. The Raman bands become less defined at higher temperatures as shown in Figure 5.52. At -190° C the four main peaks are observable, whereas at 20 °C only two peaks define the spectrum.

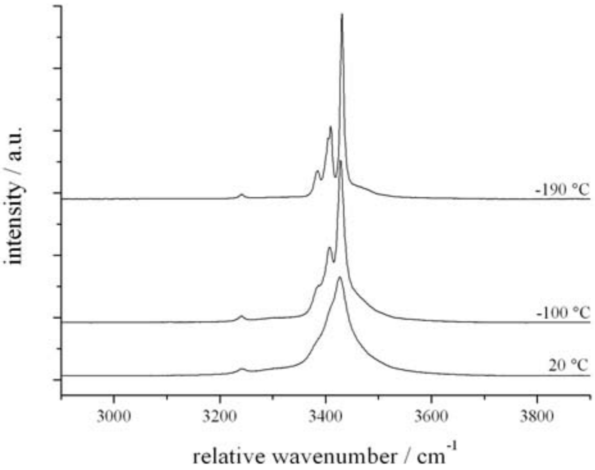

Fig. 5.52. Raman spectra of antarcticite at -190 °C, -100°C and 20°C.

To analyse the spectra at higher temperatures, a deconvolution using Gaussian-Lorentzian functions is applied to each spectrum. Six contributions are needed to describe the spectrum at -190 °C (Fig. 5.53). The additional band $\Delta\nu^{bg}$ is necessary to compensate background effects of the raw spectrum. Due to the fitting, an additional band for antarcticite ($\Delta\nu_5^{ant}$) can be centred at 3431 cm^{-1}, which appears in the Raman spectrum as a shoulder only (between 3450 and 3500 cm^{-1}). Figure 5.54 illustrates the deconvolved band positions and the half width at full maximum as a function of temperature. The positions of the main peaks and the full width at half maximum remain nearly constant for the four main peaks ($\Delta\nu_1^{an}$, $\Delta\nu_2^{an}$, $\Delta\nu_3^{an}$, $\Delta\nu_4^{an}$) with increasing temperature (see Fig. 5.54). Polynomial best fits through the main peak positions as well as through the peak width are given in equations 5.13. to 5.20.

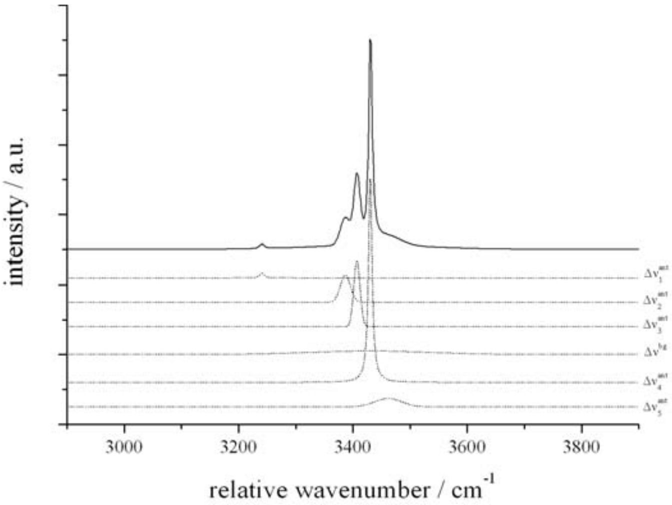

Fig. 50.53. Raman spectrum of antarcticite at -190 °C (solid line). Dotted curves represent the Gaussian-Lorentzian deconvolution of the spectrum resulting in six contributions ($\Delta\nu_{1\text{-}5}^{ant}$ and $\Delta\nu^{bg}$) with peak positions centred at 3242, 3387, 3407, 3429, 3431 and 3462 cm^{-1}. The properties of the deconvolved peaks at various temperatures are given in Table A-3 (APPENDIX).

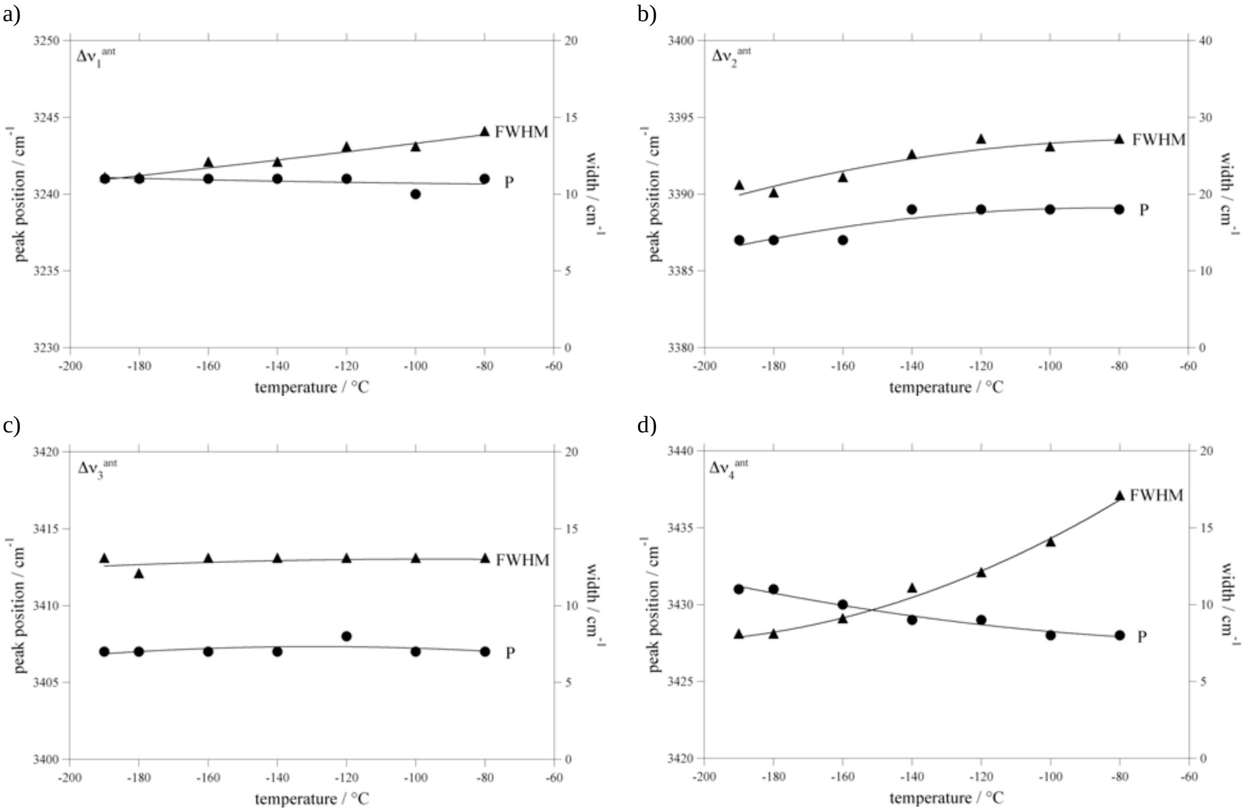

Fig. 5.54. Relative peak positions (*P*) and half width at full maximum (*FWHM*) for the Gaussian-Lorentzian contributions a) $\Delta\nu_1^{ant}$, b) $\Delta\nu_2^{ant}$, c) $\Delta\nu_3^{ant}$ and d) $\Delta\nu_4^{ant}$ as a function of temperature.

$$P_{(\Delta\nu_1^{ant})} = 3240.6 + 0.000068317\cdot T + 1.429\cdot 10^{-5}\cdot T^2 \tag{5.13}$$

$$FWHM_{(\Delta\nu_1^{ant})} = 16.291 + 0.031826\cdot T + 1.96\cdot 10^{-5}\cdot T^2 \tag{5.14}$$

$$P_{(\Delta\nu_2^{ant})} = 3387.5 - 0.036954\cdot T - 0.00021885\cdot T^2 \tag{5.15}$$

$$FWHM_{(\Delta\nu_2^{ant})} = 24.943 - 0.065148\cdot T - 0.00048302\cdot T^2 \tag{5.16}$$

$$P_{(\Delta\nu_3^{ant})} = 3405.3 - 0.03212\cdot T - 0.00012467\cdot T^2 \tag{5.17}$$

$$FWHM_{(\Delta\nu_3^{ant})} = 12.577 - 0.0094233\cdot T - 4.9672\cdot 10^{-5}\cdot T^2 \tag{5.18}$$

$$P_{(\Delta\nu_4^{ant})} = 3427.7 + 0.0094638\cdot T + 0.00014549\cdot T^2 \tag{5.19}$$

$$FWHM_{(\Delta\nu_4^{ant})} = 30.817 + 0.21447\cdot T + 0.00049352\cdot T^2 \tag{5.20}$$

α-Tetrahydrate (α-$CaCl_2 \cdot 4H_2O$)

Raman spectra of α-tetrahydrate display a complex contour at -190 °C with main peak positions centred at about 3197 (±2) $\Delta\nu_1^{\alpha}$, 3369 (±6) $\Delta\nu_3^{\alpha}$, 3425 (±3) $\Delta\nu_4^{\alpha}$ and 3446 (±2) $\Delta\nu_5^{\alpha}$ cm^{-1} (Fig. 5.55). Shoulders can be defined at 3215 (±64) $\Delta\nu_2^{\alpha}$, 3472 (±5) $\Delta\nu_6^{\alpha}$, and 3519 (±2) $\Delta\nu_7^{\alpha}$ cm^{-1}. Different spectra of α-$CaCl_2 \cdot 4H_2O$ with varying peaks positions and relative intensities are shown in Figure 5.55, which corresponds to different crystallographic orientations.

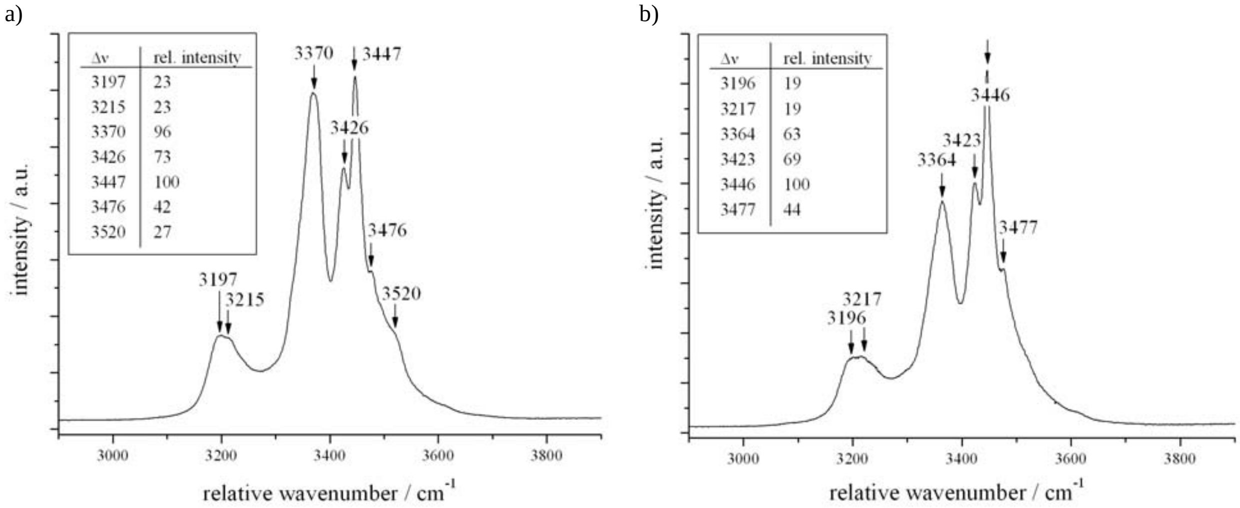

a)

Δν	rel. intensity
3197	23
3215	23
3370	96
3426	73
3447	100
3476	42
3520	27

b)

Δν	rel. intensity
3196	19
3217	19
3364	63
3423	69
3446	100
3477	44

Fig. 5.55. Raman spectra of α-tetrahydrate at -190 °C (experiment 021). Variable relative peak intensities are caused by different crystallographic orientations of the measured hydrate crystals.

The Raman bands of the hydrate are broadening at higher temperature, resulting in a broad relatively undefined spectrum. At -190 °C α-tetrahydrate is characterised by seven peaks, whereas at higher temperatures only three maxima (smearing over a wide wavenumber range) can be seen (Fig. 5.56).

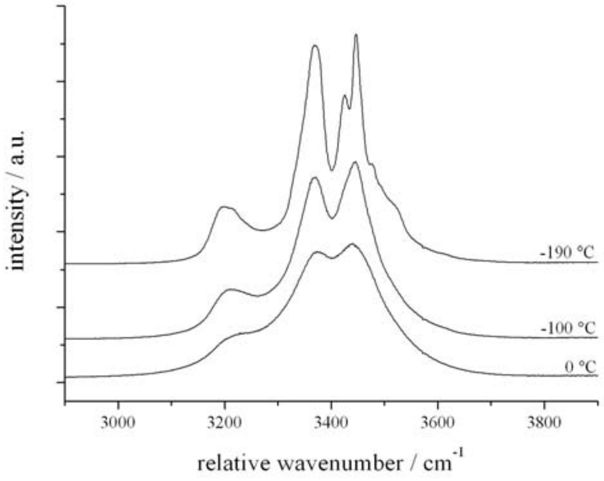

Fig. 5.56. Raman spectra of α-tetrahydrate at -190 °C, -100 °C and 0 °C.

The Raman spectrum can be analysed with Gaussian-Lorentzian functions, whereas nine contributions ($\Delta\nu_{1\text{-}7}^{\alpha}$ and $\Delta\nu^{bg}$) are required to describe the spectrum at -190 °C (Fig. 5.57). $\Delta\nu^{bg}$ centred at 3299 and 3543 cm^{-1} are necessary to compensate background effects of the raw spectrum. The deconvolved band positions (see Fig.

5.57) differ from the obtained positions of the raw spectrum due to the fitting procedure. This deviation reflects the complexity of the raw spectrum, which consists of overlapping bands and has a relatively high rise in the “background”.

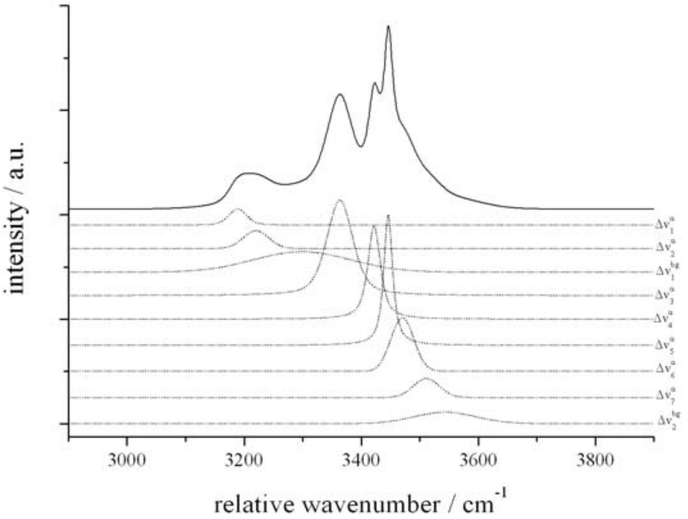

Fig. 5.57 Raman spectrum of α-tetrahydrate at -190 °C (solid line). Dotted curves represent the Gaussian-Lorentzian deconvolution of the spectrum resulting in nine contributions. The peak positions for $\Delta\nu_{1\text{-}7}^{\alpha}$ are centred at 3189, 3220, 3364, 3422, 3446, 3470 and 3511 cm^{-1}. $\Delta\nu^{bg}$ are centred at 3299 and 3543 cm^{-1}.The properties of the fit are given in Table A-4 (APPENDIX).

γ-Tetrahydrate (γ-$CaCl_2 \cdot 4H_2O$)

The Raman spectrum of γ-tetrahydrate is defined by a relatively broad signal at -190 °C. It does not show sharp and defined peaks, which implies a poorly crystallised phase. A broad peak characterises the spectrum at about 3432 (±2) $\Delta\nu_3^{\gamma}$ cm^{-1}. Shoulders are defined at about 3260 $\Delta\nu_1^{\gamma}$, 3393 $\Delta\nu_2^{\gamma}$, 3463$\Delta\nu_4^{\gamma}$ and 3575 $\Delta\nu_5^{\gamma}$ cm^{-1}. The effect of different crystal orientations on the Raman signal is shown in Figure 5.58. At higher temperatures the Raman spectrum of the hydrate may easily confused with a spectrum of a liquid aqueous solution, due to the lack of characteristic intensity maxima (Fig. 5.59).

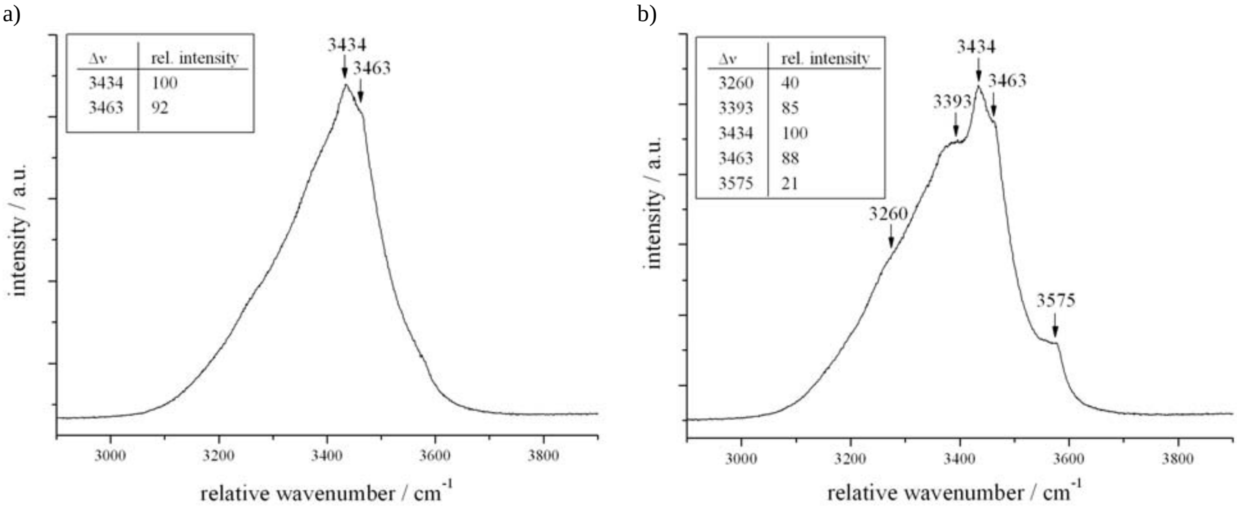

Fig. 5.58. Raman spectra of γ-$CaCl_2 \cdot 4H_2O$ at -190 °C (experiment 021). Variable relative peak intensities are caused by different crystallographic orientations of the measured hydrate crystals.

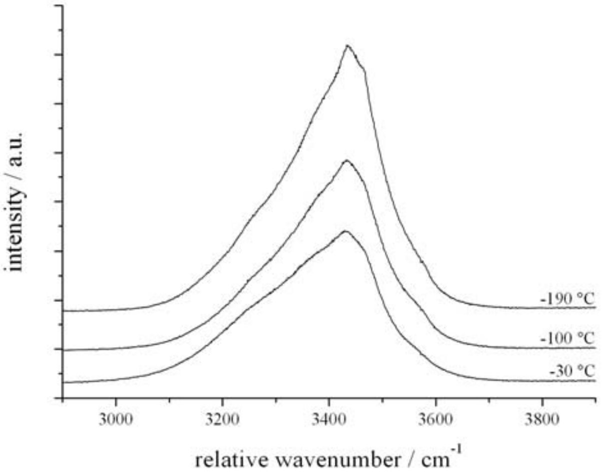

Fig. 5.59. Raman spectra of γ-$CaCl_2 \cdot 4H_2O$ at -190 °C, -100 °C and -27 °C.

Due to the use of Gaussian-Lorentzian deconvolution, the spectrum can be analysed at -190 °C (Fig. 5.60). Five contributions describe the spectrum, with main peak positions centred at 3339, 3403, 3431, 3458 and 3532 cm^{-1} ($\Delta\nu_{1\text{-}5}^{\gamma}$). The deconvolved band positions differ from the obtained positions of the raw spectrum due to the fitting procedure. This deviation is due to absence of well-defined peaks in the raw spectrum.

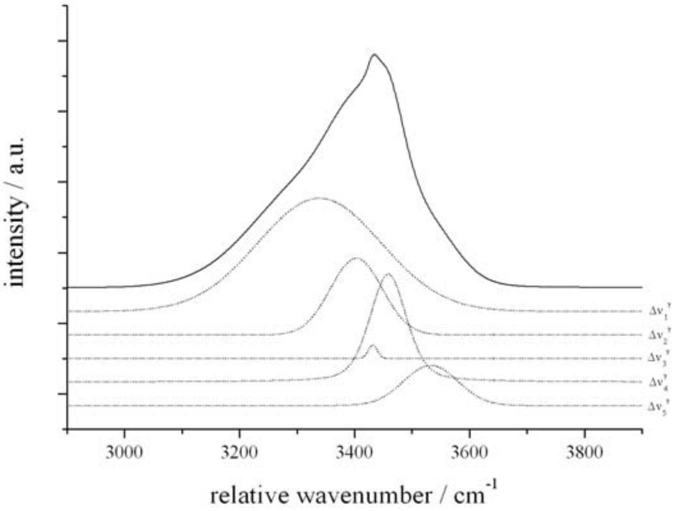

Fig. 5.60. Raman spectrum of γ-$CaCl_2 \cdot 4H_2O$ at -190 °C (solid line). Dotted curves represent the Gaussian-Lorentzian deconvolution of the spectrum resulting in five contributions with peak positions centred at 3339, 3403, 3431, 3458 and 3532 cm^{-1} ($\Delta\nu_{1\text{-}5}^{\gamma}$). The properties of the deconvolved peaks are given in Table A-5 (APPENDIX).

Sinjarite ($CaCl_2 \cdot 2H_2O$)

Raman spectra of sinjarite display a complex contour at -190 °C, with main peak positions at 3377 (±1) $\Delta\nu_6^{sin}$, 3405 (±3) $\Delta\nu_7^{sin}$, 3424 (±2) $\Delta\nu_8^{sin}$, 3464 (±2) $\Delta\nu_9^{sin}$, 3559 (±2) $\Delta\nu_{10}^{sin}$ cm^{-1} and shoulders at about 3190 (±2) $\Delta\nu_1^{sin}$, 3249 (±9) $\Delta\nu_2^{sin}$, 3281 (±4) $\Delta\nu_3^{sin}$, 3315 (±5) $\Delta\nu_4^{sin}$ and 3351 (±4) $\Delta\nu_5^{sin}$ cm^{-1}. The effect of relative crystal orientation on the relative intensities of the Raman bands is shown in Figure 5.61. Depending on the crystallographic orientation some Raman bands may get hidden. For example the main peak position at about 3406 cm^{-1} in Figure 5.61b, is missing in the spectrum obtained from another crystal shown in Figure 5.61a. Also some peaks in the front shoulder of the spectra (between 3100 and 3400 cm^{-1}) may be camouflaged.

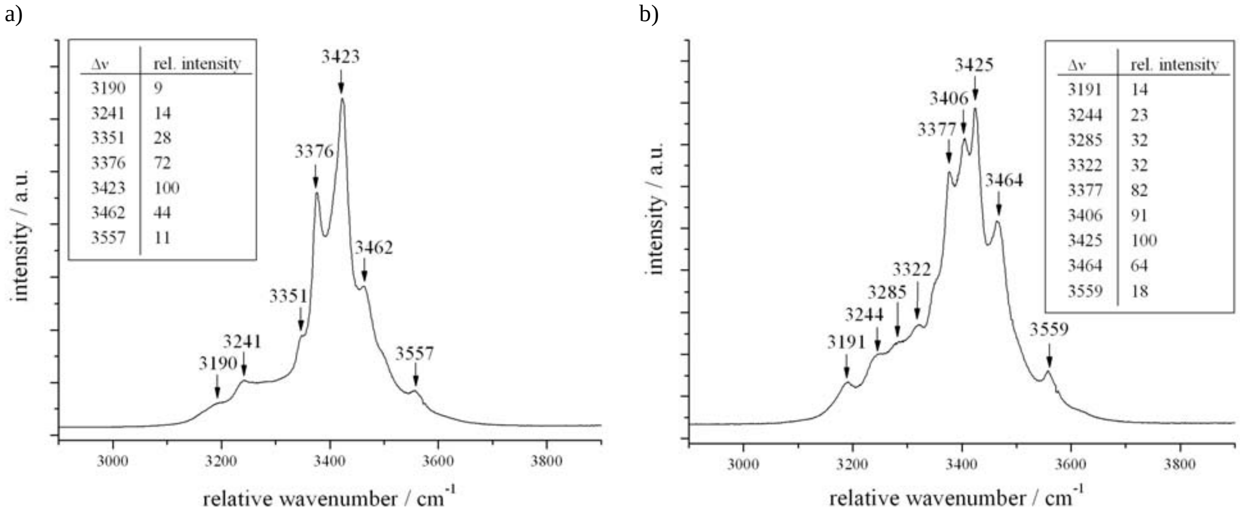

Fig. 5.61. Raman spectra of sinjarite (CaCl$_2$·2H$_2$O) at -190 °C (experiment 021). Variable relative peak intensities are caused by different crystallographic orientations of the measured hydrate crystals.

The evolution of the Raman spectrum with increasing temperature is shown in Figure 5.62. The obtained peaks at -190 °C broaden during heating. At -100 °C, only a very broad peak centered at 3401 cm^{-1} defines the spectra. The same as for γ-tetrahydrate, the spectrum can be easily confused with a spectrum of a liquid aqueous solution at higher temperatures.

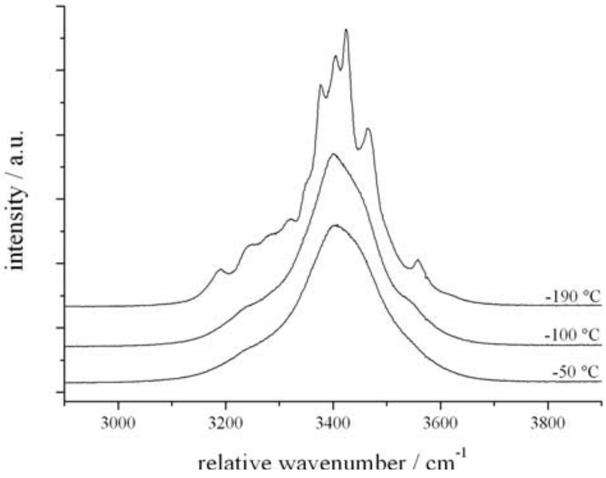

Fig. 5.62. Raman spectra of sinjarite at -190 °C, -100 °C and -50 °C.

As the Raman spectrum is consisting of many overlapping bands, a Gaussian-Lorentzian deconvolution results in a great number of evaluated contributions. The best fit to obtain hidden bands consists of about eleven functions (see Fig. 5.63). The deconvolved band positions differ slightly from the obtained positions of the raw spectrum, due to the complexity of the raw spectrum.

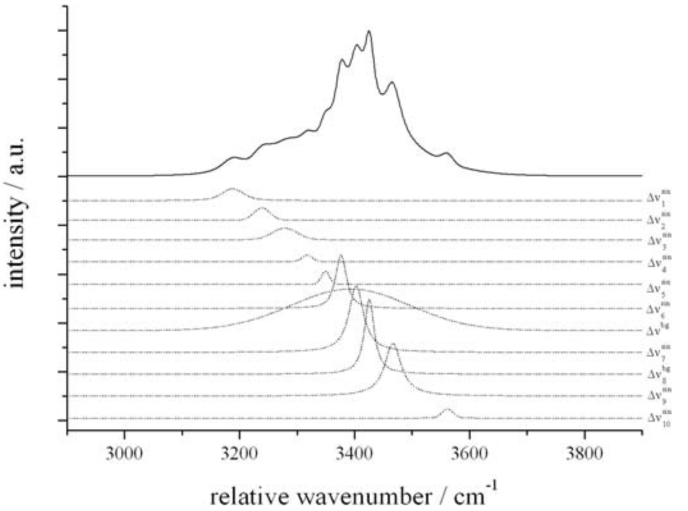

Fig. 5.63. Raman spectrum of sinjarite at -190 °C (solid line). Dotted curves represent the Gaussian-Lorentzian deconvolution of the spectrum resulting in eleven contributions. The peak positions for $\Delta\nu_{1\text{-}10}^{sin}$ are centred at 3188, 3240, 3278, 3318, 3350 3378, 3403, 3426, 3467, 3562 cm^{-1} and $\Delta\nu^{bg}$ at 3393 cm^{-1}. The properties of the deconvolved peaks are given in Table A-6 (APPENDIX).

Antarcticite & γ-Tetrahydrate

Raman spectroscopy verifies the stability antarcticite and γ-tetrahydrate at low temperatures (see Chapter 5.2.). Antarcticite is identified with peak maxima centred at about 3240, 3387, 3402 and 343 cm^{-1} at -190 °C, whereas γ-tetrahydrate is identified by a high rise in the background and two additional peaks, which occur at about 3463 and 3575 cm^{-1} (Fig. 5.64).

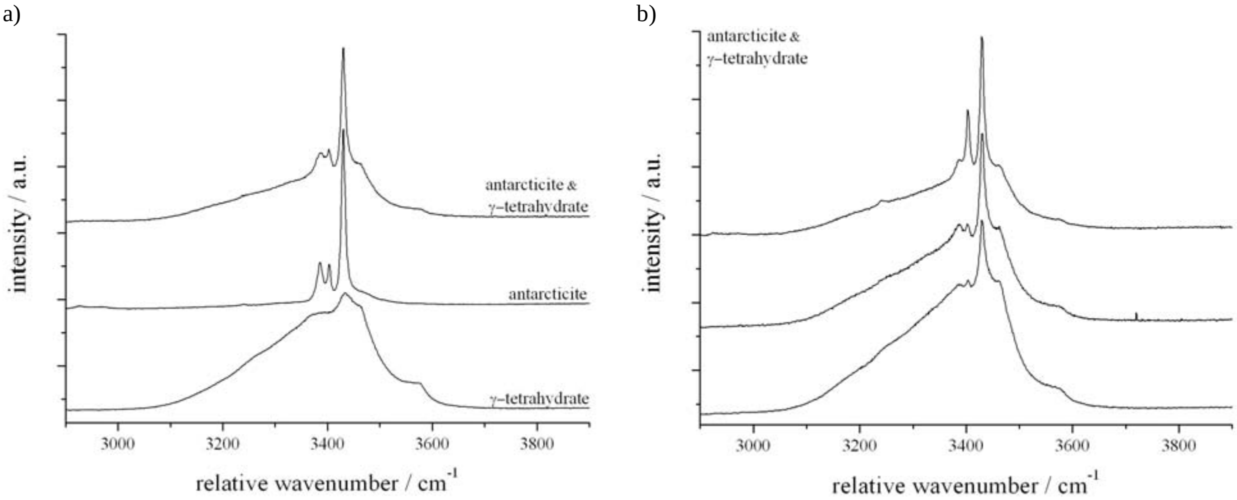

Fig. 5.64. a) Raman spectra of γ-tetrahydrate, antarcticite and γ-$CaCl_2 \cdot 4H_2O$ and antarcticite at -190 °C (experiment 045). b) Raman spectra of γ-tetrahydrate and antarcticite at -190 °C (experiment 045).

Phase transition: Sinjarite into α-Tetrahydrate

Sinjarite may react to α-tetrahydrate at temperatures between -29 and -25 °C in high saline inclusions (see Chapter 5.2). The transition is evident by a change in the Raman spectrum of the hydrate phase. At -30 °C the Raman spectrum is characterised by a broad peak. Heating to -26 °C results in a spectrum with slightly more pronounced peaks and shoulders (Fig. 5.65). This behaviour is not expected for hydrates, because increasing temperatures are usually smoothing spectra. Figure 5.66 illustrates the Raman spectra taken at -190 °C before (spectrum of sinjarite) and after the phase transition (spectrum of α-tetrahydrate). This phase transition is metastably irreversible. It is contingent that a liquid phase is present throughout the observed temperature range. As both, the spectra of α-tetrahydrate and sinjarite are very complex and show a high rise in the background, the Raman signal of the liquid is may be camouflaged.

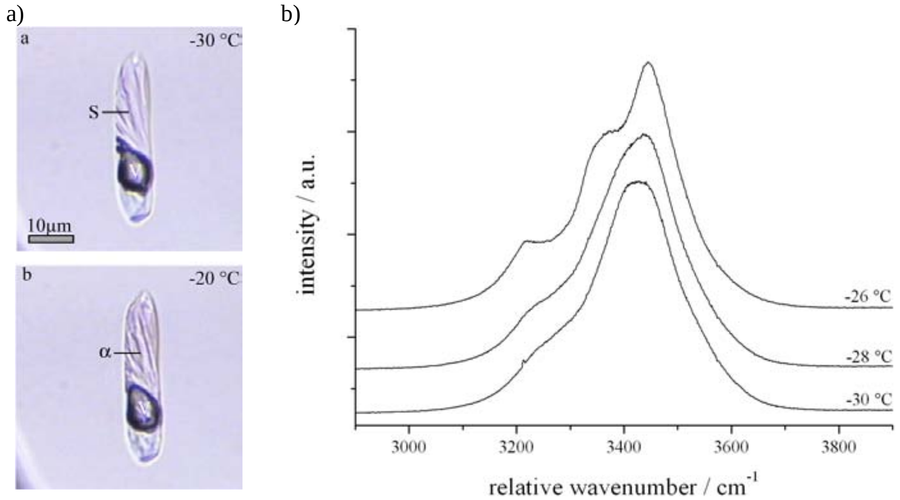

Fig. 5.65. a) Fluid inclusion with sinjarite at -30 °C and α-tetrahydrate at -20 °C. b) Raman spectra taken in a temperature range between -30 and -26 °C, whereas sinjarite react to α-tetrahydrate (experiment 021).

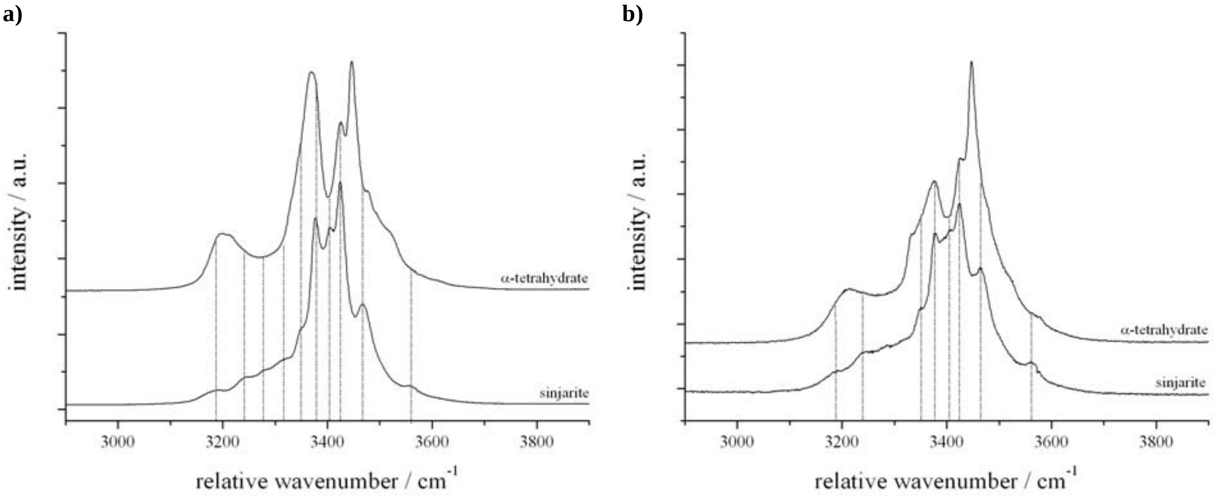

Fig. 5.66 Raman spectra of sinjarite and α-tetrahydrate measured in fluid inclusions at -190 °C at the same relative position before and after the phase transition (experiment 021). Dotted lines illustrate the relative peak positions obtained for sinjarite.

5.4.4. $MgCl_2$-H_2O inclusions

Dependent on the salinity, different phase assemblages occur during cooling experiments in fluid inclusions containing $MgCl_2$. Raman spectra verify the stability of: (1) brine, (2) ice and brine and (3) $MgCl_2 \cdot 12H_2O$ and ice -190 °C (see Chapter 5.3.). The $MgCl_2$-rich brine shows a broad signal (Fig. 5.67a), which can be assigned to a typical liquid aqueous solution spectrum. In addition to the broad Raman signal of the liquid brine, Raman bands of ice are obtained at about 3090 and 3218 cm^{-1} (Fig. 5.67b).

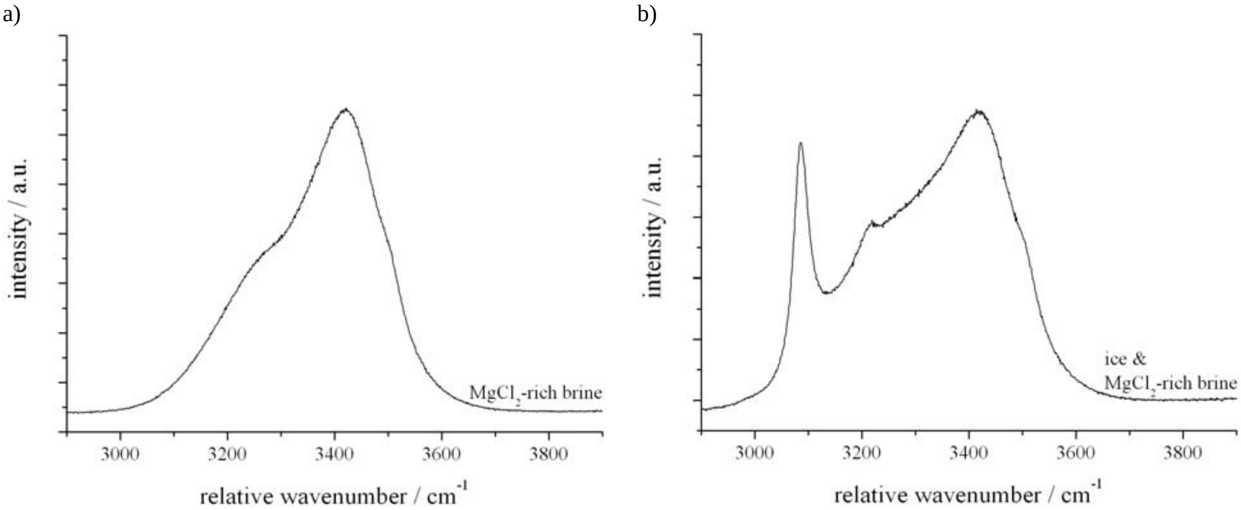

Fig. 5.67. a) Raman spectrum of 30mass% $MgCl_2{}^{\cdot}$-rich brine at -190 °C (experiment 047). b) Raman spectrum of and ice and $MgCl_2{}^{\cdot}$-rich brine at -190 °C (experiment 025).

$MgCl_2{}^{\cdot}12H_2O$ is defined by a complex Raman spectrum a low temperatures. Main peak positions of the Raman bands ($\Delta\nu_{1\text{-}8}{}^{Mg12}$) are assigned at about 3191 (±5), 3252 (±4), 3322 (±5), 3397 (±5), 3428 (±5), 3459 (±2), 3479 (±4) and 3512 (±2) cm^{-1} at -190 °C. Due to the effect of the crystallographic orientation of the measured hydrate crystals, some of these peaks may disappear or be hidden beyond "shoulders" of other main peaks. For example, the peak positions at about 3250 cm^{-1} shown in the spectrum in Figure 5.68a, is not detectable in the spectrum shown in Figure 5.68b. In addition, The relative peak intensity is influenced by the crystallographic orientation. The peak centred at 3401 cm^{-1}, shows the highest relative intensity (Fig. 5.68a, whereas the highest peak intensity is observed at 3512 cm^{-1} in (Fig. 5.68b). A good deal of the spectroscopic information is lost at higher temperatures. At -190 °C up to eight Raman bands are observable, whereas only three bands define the spectrum at -50 °C (Fig. 5.69).

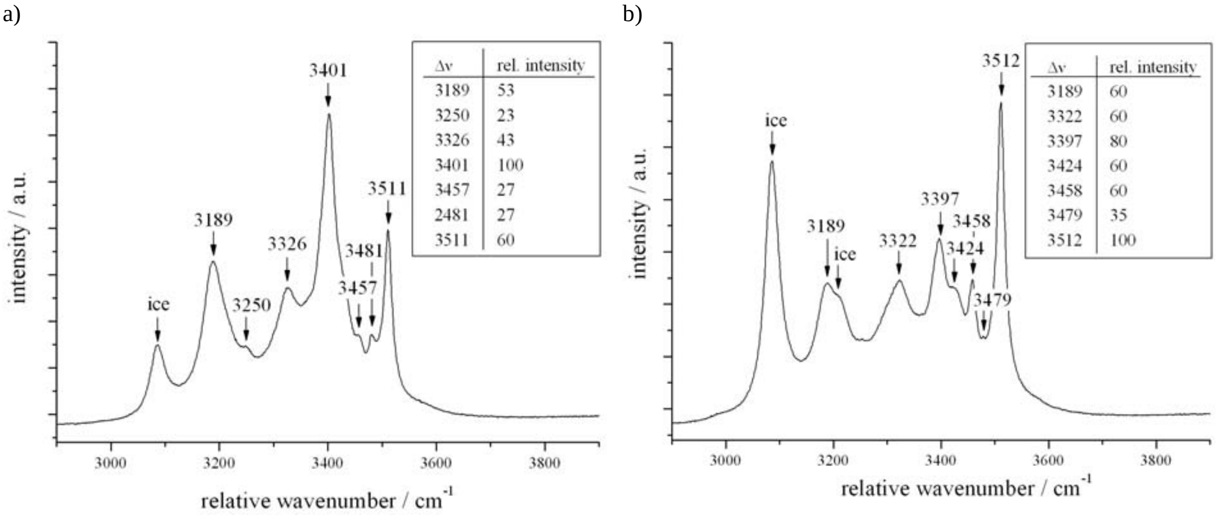

Δv	rel. intensity
3189	53
3250	23
3326	43
3401	100
3457	27
2481	27
3511	60

Δv	rel. intensity
3189	60
3322	60
3397	80
3424	60
3458	60
3479	35
3512	100

Fig. 5.68. Raman spectra of ice and $MgCl_2{}^{\cdot}12H_2O$ at -190 °C (experiment 030). Variable relative peak intensities are caused by different crystallographic orientations of the measured hydrate crystals.

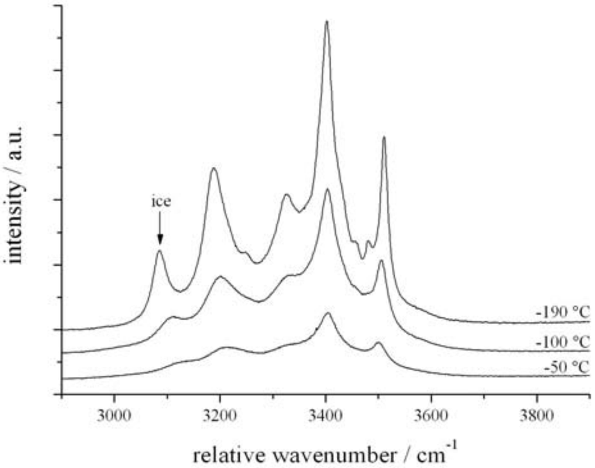

Fig. 5.69 Raman spectra of $MgCl_2 \cdot 12H_2O$ (and ice) at -190 °C, -100 °C and -50 °C.

A deconvolution of the hydrate spectra can be applied to the Raman spectrum, with the use of Gaussian-Lorentzian functions. At -190 °C the Mg-hydrate/ice spectrum (at -190 °C) can be deconvolved into eleven Gaussian-Lorentzian contributions (see Fig. 5.70). $\Delta\nu^{bg}$ is added to the fitting procedure to compensate background effects.

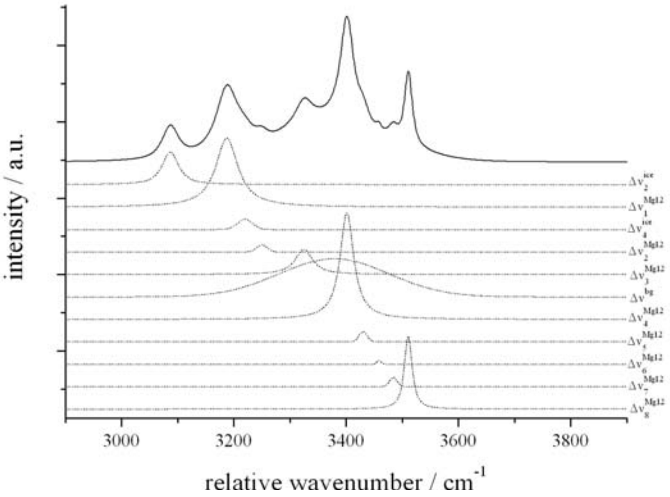

Fig. 5.70. Raman spectrum of $MgCl_2 \cdot 12H_2O$ and ice at -190 °C. Dotted lines represent the Gaussian-Lorentzian deconvolution of the spectrum resulting in eleven contributions, whereas band positions centred at 3087 and 3220 cm^{-1} belongs to the Raman modes of ice. Band positions at 3188, 3249, 3325, 3402, 3430, 3458, 3484, 3511 cm^{-1} ($\Delta\nu_{1\text{-}8}^{Mg12}$) belongs to the Raman modes of the Mg-hydrate. $\Delta\nu^{bg}$ is defined at 3378 cm^{-1} and is required to compensate background effects. The properties of the deconvolved peaks are given in Table A-7 (APPENDIX).

5.4.5. $FeCl_2$-H_2O inclusions

During cooling experiments two different phase assemblages may occur. Raman spectra verify the stability of: (1) ice and brine and (2) ice and $FeCl_2 \cdot 6H_2O$ at -190 °C (see Chapter 5.3). The $FeCl_2$-rich brine is characterised by a broad signal (Fig. 5.71a), which can be assigned to a typical liquid aqueous solution spectrum. Raman bands about 3089 and 3216 cm^{-1} verify the presence of ice at -190 °C (Fig. 5.71b).

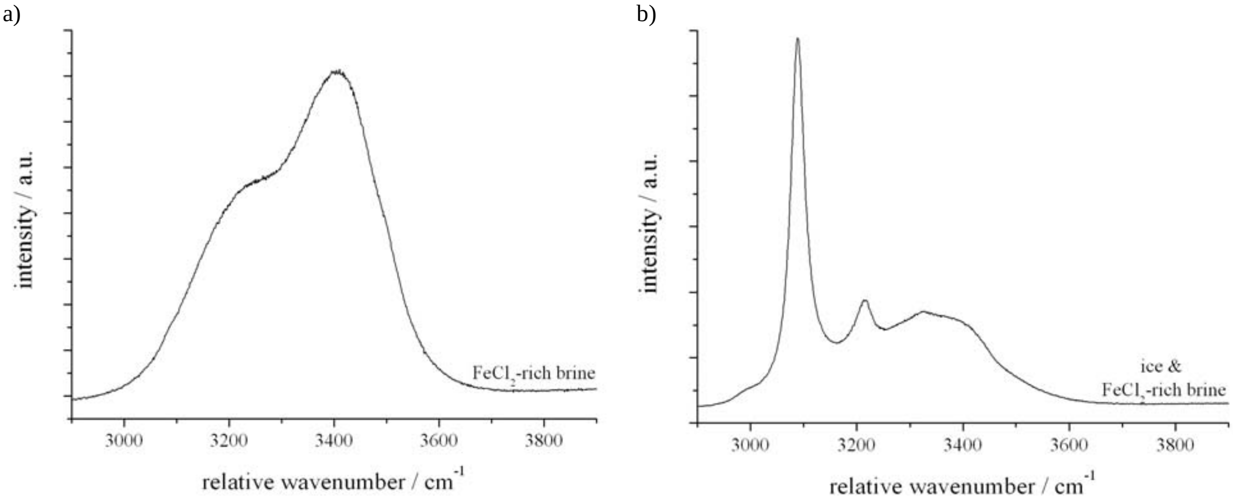

Fig. 5.71. a) Raman spectrum of $FeCl_2$-rich·-rich brine at -190 °C (experiment RJB 006). b) Raman spectrum of and ice and $FeCl_2$-rich rich brine at -190 °C (experiment RJB 006).

$FeCl_2$-hydrate nucleation ($FeCl_2 \cdot 6H_2O$) rarely occurs in inclusions containing $FeCl_2$. Raman spectra taken at -190 °C on the solid phases in the inclusions reveal main peak positions at 3086 (±1) and 3213 (±1), which belong Raman modes of ice. Additionally, four Raman bands ($\Delta\nu_{1-4}^{Fe6}$) centred at 3372 (±2), 3390 (±2), 3411(±2) and 3426 (±2) cm^{-1} occur, which refer to the $FeCl_2 \cdot 6H_2O$ (Fig 5.72). Different crystallographic orientation of the measured hydrate crystals may influence the relative intensities and the occurrence of peaks. As shown in Figure 5.72a, the peak at about 3388 cm-^{1}, is not detectable in the Raman spectrum shown in Figure 5.72b. Additionally, the peak intensities vary significantly. At higher temperatures peak broadening occurs. Four main peaks can be located for $FeCl_2 \cdot 6H_2O$ at -190 °C, whereas at -100 °C only two peaks are observed. Only one main peak position characterises the spectra at -34 °C (Fig. 5.73).

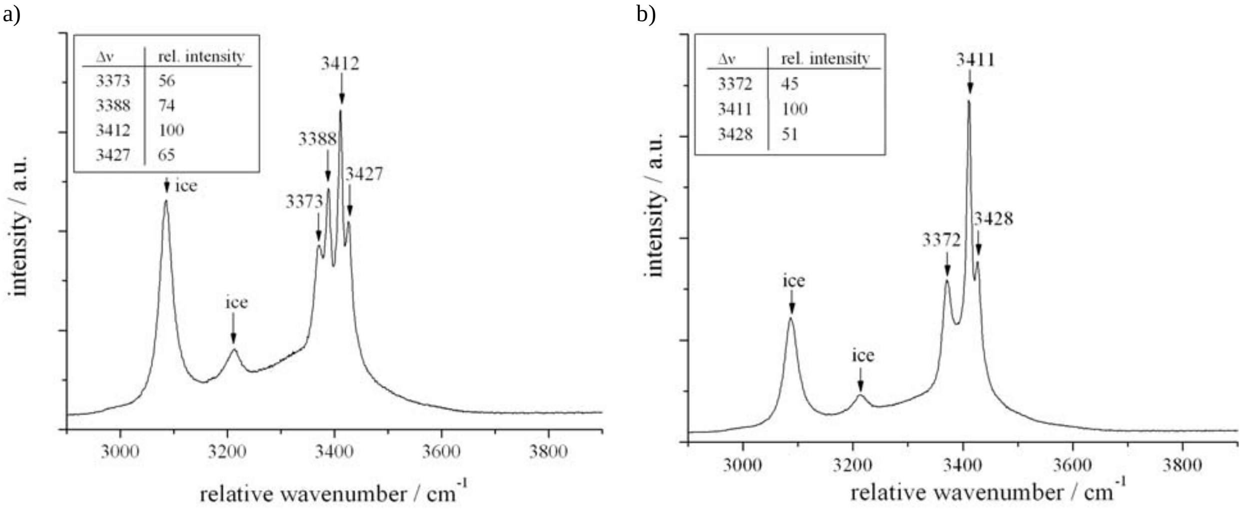

a)

Δv	rel. intensity
3373	56
3388	74
3412	100
3427	65

b)

Δv	rel. intensity
3372	45
3411	100
3428	51

Fig. 5.72 Raman spectra of $FeCl_2 \cdot 6H_2O$ at -190 °C (experiment RJB 007). Variable relative peak intensities are caused by different crystallographic orientations of the measured hydrate crystals.

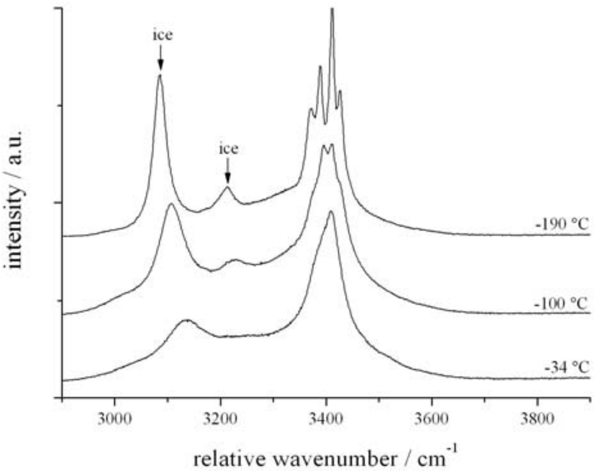

Fig. 5.73. Raman spectra of $FeCl_2 \cdot 6H_2O$/ice at 190 °C, -100 °C and -34 °C.

The $FeCl_2 \cdot 6H_2O$/ice Raman spectra can be analysed with using Gaussian-Lorentzian functions. Up to eight contributions fit the spectra taken at -190 °C (see Fig. 5.74). Two background contributions are added to the fitting procedure to compensate the background of the spectrum.

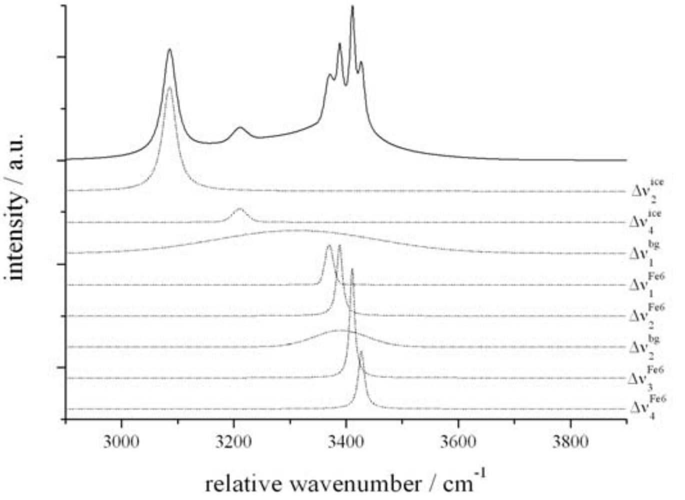

Fig. 5.74. Raman spectrum of $FeCl_2 \cdot 6H_2O$/ice at 190 °C (solid line). Dotted lines represent the Gaussian-Lorentzian deconvolution of the spectrum resulting in eight contributions. Band positions at 3086 and 3210 cm^{-1} belong to the Raman modes of ice ($\Delta\nu_{2-4}^{ice}$). Band positions at 3370, 3389, 3390 and 3411 cm^{-1} ($\Delta\nu_{1-4}^{Fe6}$) belong to the Raman modes of the Fe-hydrate. $\Delta\nu_{1-2}^{bg}$, positioned at 3427 and 3312 cm^{-1}, are required to compensate the background. The properties of the deconvolved peaks are given in Table A-8 (APPENDIX).

5.4.6. $FeCl_3$-H_2O inclusions

$FeCl_3$ containing fluid inclusions precipitate only ice during cooling experiments. Ice remains stable with $FeCl_3$-rich brine and vapour down to -190 °C. Raman spectra taken from this phase assemblage reveal band positions of ice at about 3088 and 3214 cm^{-1} and a broad undefined signal, which is characteristic for the presence of aqueous liquid (similar to the spectrum shown in Fig. 5.71a).

5.4.7. LiCl-H_2O inclusions

Different phase assemblages occur during cooling experiments in fluid inclusions containing LiCl. Raman spectra verify the stability ice in the presence of brine at -190 °C (see Chapter 5.3.). The LiCl-rich brine (Fig. 5.75a) shows a broad signal, which can be assigned to a liquid aqueous solution spectrum. In addition, to the broad band of the liquid phase, Raman bands of ice are obtained at about 3090 and 3218 cm^{-1} (Fig. 5.75b).

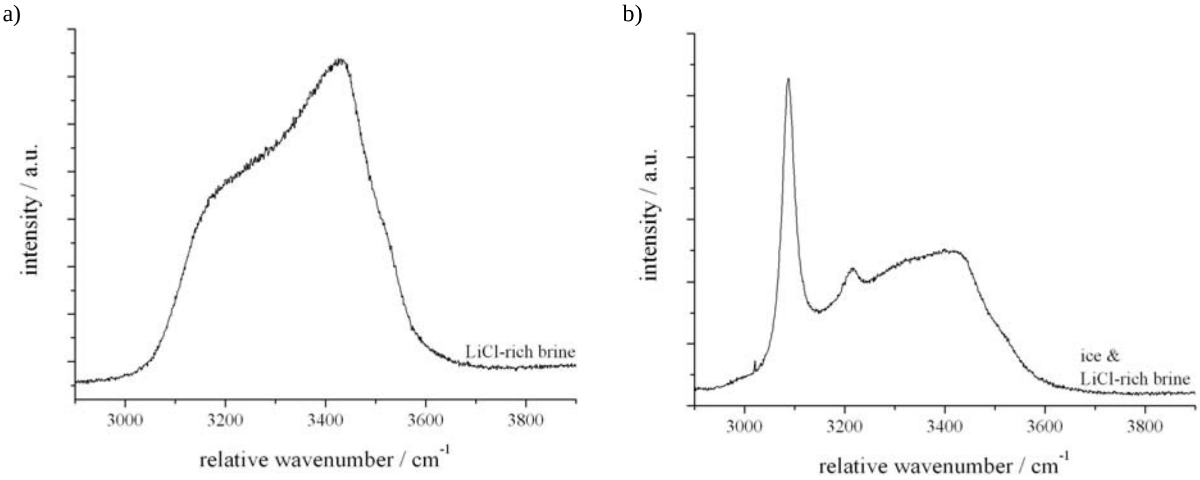

Fig. 5.75. a) Raman spectrum of LiCl -rich-rich brine at -190 °C (experiment 053). b) Raman spectrum of and ice and LiCl -rich rich brine at -190 °C (experiment 056).

Nucleation of a solid phase was observed in fluid inclusions that remain connected to the quartz surface along unhealed cracks. This phase shows strong vibrational modes in the stretching region of water. The Raman spectrum is characterised by two band positions centred at 3359 (±1) and 3376 (±1) cm^{-1} at -190 °C (Fig. 5.76a). Most probably this phase belongs to a Li-hydrate modification. Again, peak broadening occurs with increasing temperature as illustrated in Figure 5.76b. The double peaks obtained at -190 °C modify to a single broad band with a main peak positions at 3380 at -10 °C. The Raman spectrum can be analysed by using three Gaussian-Lorentzian contributions as shown in Figure 5.77. The contribution $\Delta\nu^{bg}$ is added to the fitting procedure to compensate the background of the spectra.

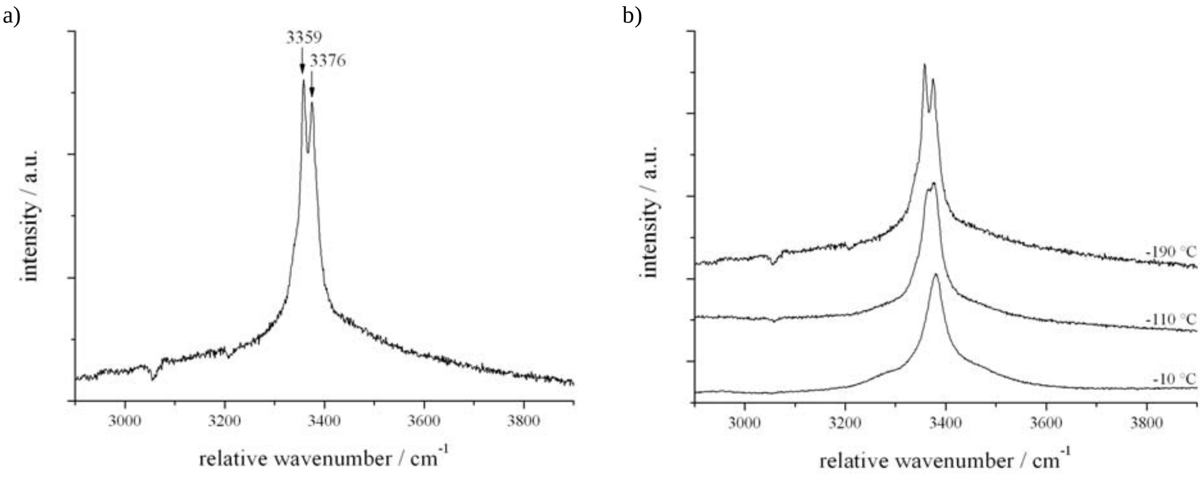

Fig. 5.76. a) Raman spectrum of Li-hydrate phase at -190 °C. b) Raman spectra of a Li-hydrate phase at -190 °C, -110 °C and -10 °C (experiment 056).

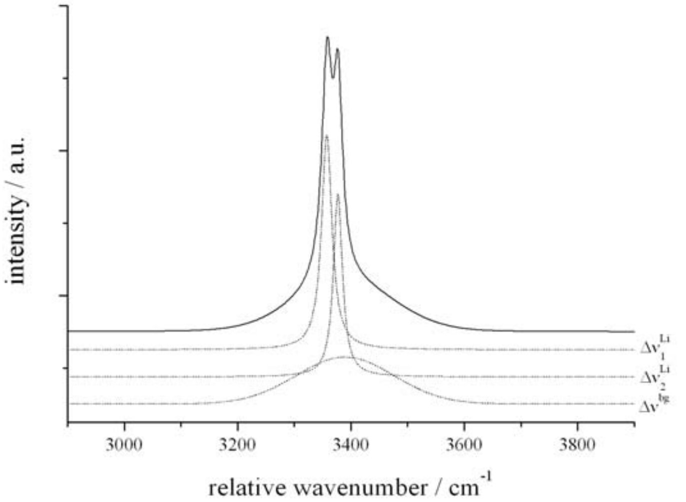

Fig. 5.77. Raman spectrum of a Li-hydrate phase at 190 °C (solid line). Dotted lines represent the Gaussian-Lorentzian deconvolution of the spectrum resulting in three contributions. Band positions at 3358 and 3377 cm^{-1} belong to the Raman modes of the solid ($\Delta\nu_{1\text{-}2}^{Li}$). $\Delta\nu_1^{bg}$, centered at 3389 cm^{-1}, is required to compensate the background. The properties of the deconvolved peaks are given in Table A-9 (APPENDIX).

5.4.8. $ZnCl_2$-H_2O inclusions

Ice precipitation occurs in the $ZnCl_2$-H_2O inclusions during cooling experiments. Raman spectra down to -190 °C show the two main peaks of ice at about 3090 and 3217 cm^{-1} (Fig. 5.78a). Additionally a broad signal, which attributes to the stretching vibrations of a liquid aqueous solution, is obtained (Fig. 5.78b). Remarkable modifications in the spectra may occur in the front interval (3000 to 3400 cm^{-1}). The band position at about 3200 cm^{-1} can be strongly pronounced for a $ZnCl_2$-rich brine at low temperatures.

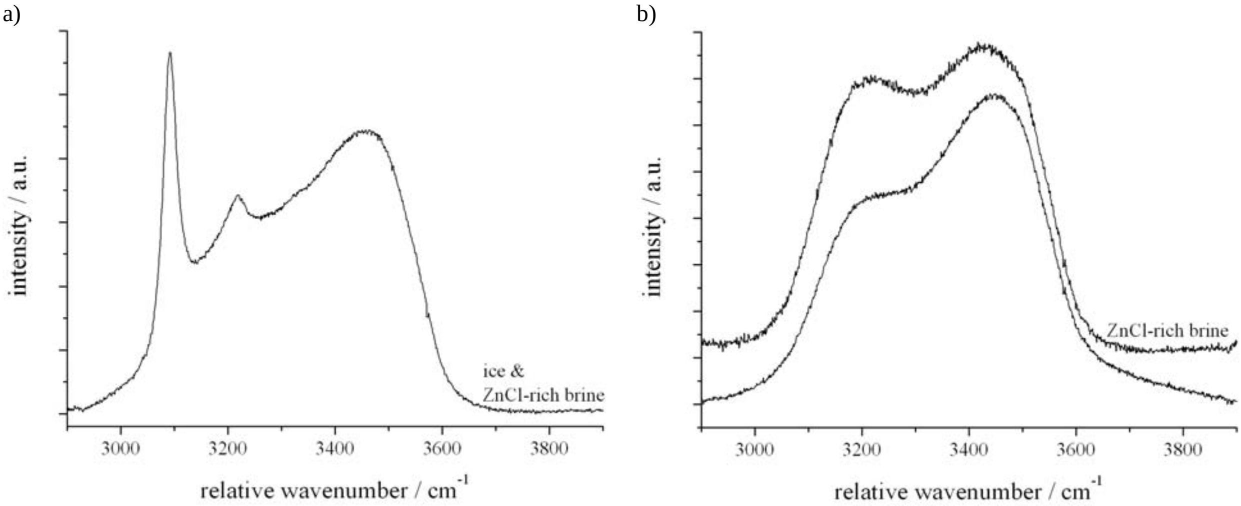

Fig. 5.78. Raman spectra of a) ice and ZnCl-rich brine (experiment 048) and b) ZnCl-rich brine at -190 °C (experiment 049).

5.4.9. NaCl-$CaCl_2$-H_2O inclusions

In the NaCl-$CaCl_2$ system ice and ice/hydrohalite precipitation is observed during cooling processes (Fig 5.79a). Raman spectra obtained at -190 °C show main peak positions at about 3088, 3216 cm^{-1}, which correspond to the characteristic Raman bands of ice, and at 3299, 3321, 3402, 3419, 3432 and 3534 cm^{-1}, which correspond to the Raman bands of hydrohalite (Fig 5.79b). $CaCl_2$ is dissolved in the liquid phase, which is stable down to -190 °C, representing a supersaturated brine at this temperature. Raman spectroscopy verifies the presence of brine (Fig. 5.79b). The presence of $CaCl_2$ does not influence the observed peak positions of neither ice nor hydrohalite. Therefore it is concluded that $CaCl_2$ does not integrate in the crystal structure.

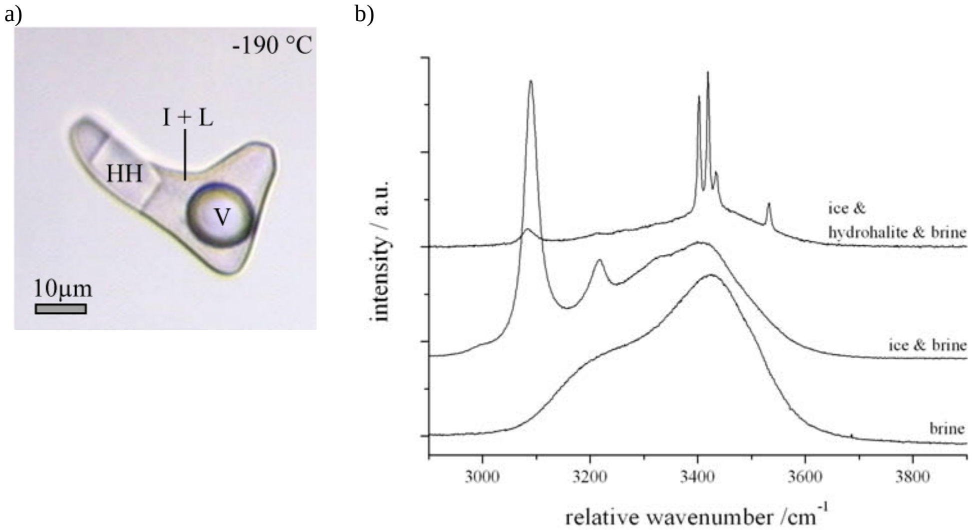

Fig. 5.79. a) Fluid inclusions at -190 °C containing ice, hydrohalite, $CaCl_2$-rich brine and vapour (experiment 006). b) Raman spectra of ice, hydrohalite and $CaCl_2$-rich brine at -190 °C (experiment 006).

5.4.10. NaCl-$MgCl_2$-H_2O inclusions

Different phase assemblages occur in NaCl-$MgCl_2$ fluid inclusions depending on the salinity. Ice and hydrohalite precipitation (Fig. 5.80a) occurs during cooling in inclusions in which the NaCl content exceeds the $MgCl_2$ content. Raman spectra (Fig. 5.80b) of the phase assemblage reveal Raman bands of ice (at about 3089, 3215 cm^{-1}), hydrohalite (at about 3322, 3401, 3419, 3433 and 3534 cm^{-1}) and brine (broad signal). The total amount of $MgCl_2$ is concentrated in the liquid phase, which is stable down to -190 °C, representing a supersaturated brine at this temperature.

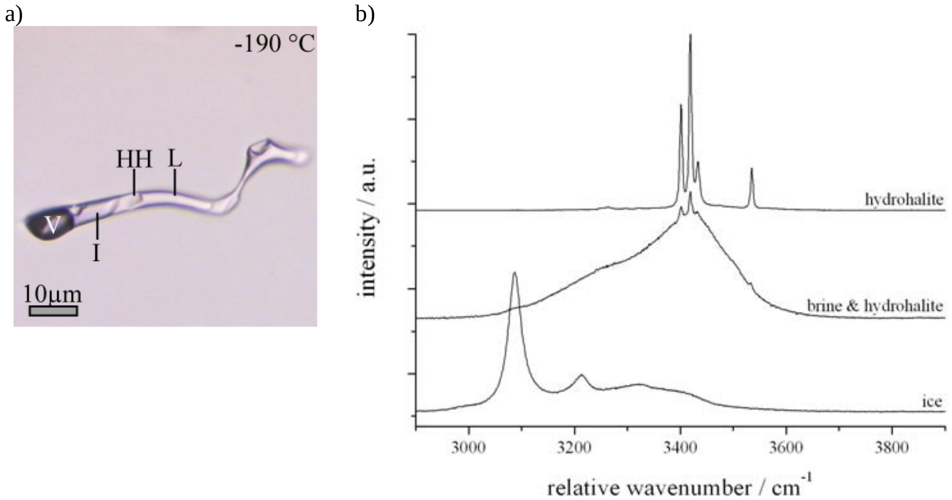

Fig. 5.80. a) Fluid inclusions at -190 °C containing ice, hydrohalite, $MgCl_2$-rich brine and vapour (experiment 033). b) Raman spectra of ice, hydrohalite and $MgCl_2$-rich brine at -190 °C (experiment 033).

Inclusions with 5 mass% NaCl and 16 mass% $MgCl_2$ (experiment 035), show Raman bands of ice, $MgCl_2 \cdot 12H_2O$ and hydrohalite at -190 °C (Fig. 5.81). Optically, hydrohalite is not verifiable in those inclusions. Main peaks of ice were defined at about 3089 and 3216 cm^{-1}. $MgCl_2 \cdot 12H_2O$ is characterised by peak positions at about 3188, 3248, 3323, 3399, 3430, 3459, 3482 and 3510 cm^{-1}. At 3418 and 3532 cm^{-1} two peaks occur, which belong to hydrohalite. Those peaks are relatively small and partly overlapped by the strong bands of $MgCl_2 \cdot 12H_2O$. The amount of precipitated hydrohalite is expected to be small due to the salinity of inclusions. Therefore, hydrohalite cannot no be identified by Raman spectroscopy in all frozen inclusions.

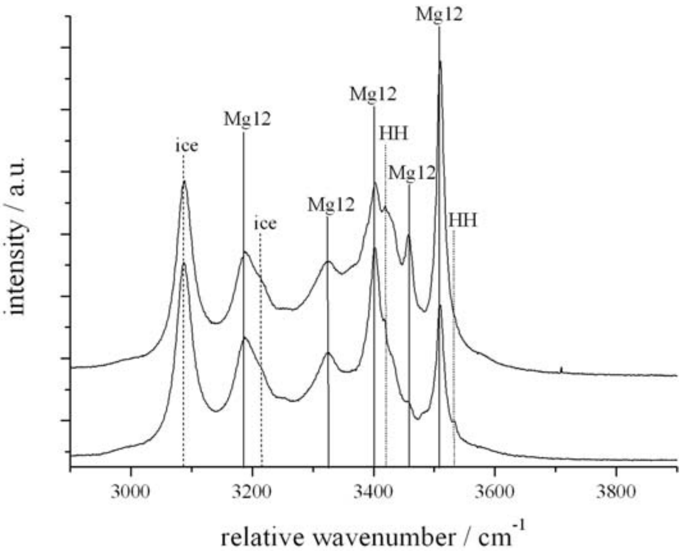

Fig 5.81. Raman spectra of the phase assemblage ice, $MgCl_2 \cdot 12H_2O$ (Mg12) and $NaCl \cdot 2H_2O$ (HH) obtained from experiment 035 (5 mass% NaCl and 16 mass% $MgCl_2$) at -190 °C.

Within inclusions from experiment 038, two different phase assemblages were observed during cooling experiments. The first phase assemblage consists of hydrohalite, ice and $MgCl_2$-rich brine. Raman spectra are similar to Fig. 5.81. A second assemblage includes an unknown phase, probably a modification of a $MgCl_2$-hydrate. Raman spectra obtained at -190 °C show the main Raman bands of ice. In addition, bands at about 3288, 3334, 3393, 3419 (shoulders), 3428, 3448, 3462, 3492 and 3520 cm^{-1} occur (Fig. 5.82a). A comparison with main peak positions obtained from $MgCl_2 \cdot 12H_2O$ and hydrohalite is given in Figure 5.83 and Table 5.14. Some peaks are overlapping, but not all can be allocated to one of those phases. At higher temperatures the vibrational modes become less defined. At -100 °C only four peaks characterise the spectra and show a slight decrease in relative peak positions (Fig. 5.82b).

Tab. 5.14. Comparison of main peak positions ($\Delta\nu$ in cm^{-1}) of $MgCl2 \cdot 12H_2O$, $NaCl \cdot 2H_2O$ and an unknown phase.

Phase	Δν	Δν	Δν	Δν	Δν	Δν	Δν	Δν	Δν	Δν	Δν
$MgCl2 \cdot 12H_2O$	3191	3252	-	3322	3397	-	3428	3459	3479	-	3512
$NaCl \cdot 2H_2O$	3299	-	-	3320	3401	3418	3432	-	-	-	3536
?	-	-	3288	3334	3393	3419	3428	3448	3462	3492	3520

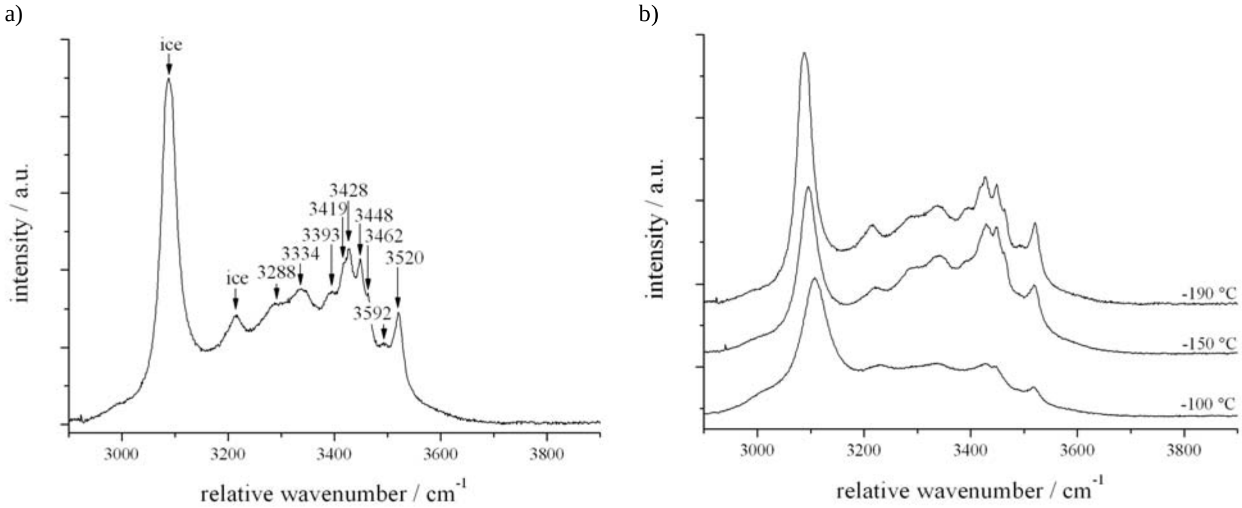

Fig. 5.82. a) Raman spectrum of an unknown hydrate phase at- 190 °C (experiment 038). b) Raman spectra of an unknown hydrate phase at -190, -150 and -100 °C (experiment 038)

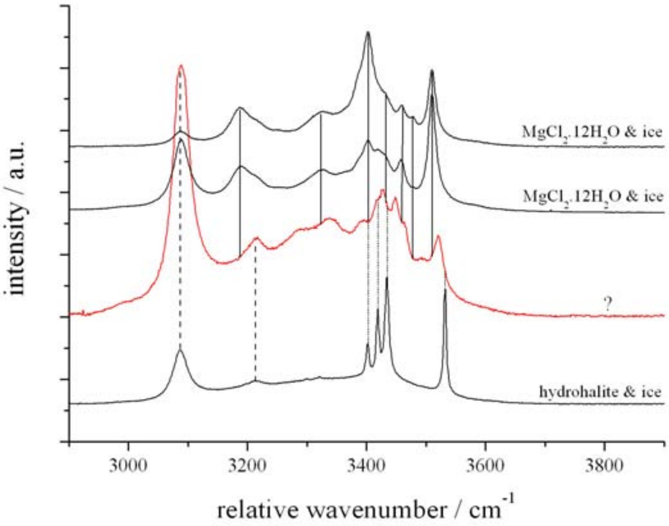

Fig. 5.83. Raman spectrum of ice and an undefined phase (?) obtained (experiment 038) in comparison with Raman spectra of MgCl2·12H_2O/ice and hydrohalite/ice. Solid lines illustrate the main peak positions of MgCl2·12H_2O, dashed lines the positions of ice and dotted lines the positions of hydrohalite.

5.4.11. $CaCl_2$-$MgCl_2$-H_2O inclusions

Three different phase assemblages occur in inclusions during cooling to -190 °C which can be identified with Raman spectroscopy, i.e. (1) ice and liquid; (2) $CaCl_2 \cdot 6H_2O$, ice and liquid; (3) $MgCl_2 \cdot 12H_2O$, ice and liquid. Ice peaks in the Raman spectra are positioned at about 3088 and 3204 cm^{-1}. The occurrence of peaks at about 3213, 3324, 3401, 3428, 3456, 3478 and 3510 cm^{-1} correspond to $MgCl_2 \cdot 12H_2O$. Peak positions of $CaCl_2 \cdot 6H_2O$ are centred at about 3241, 3389, 3404 and 3431 cm^{-1}. Raman spectra of the different phase assemblages are shown in Figure 5.84.

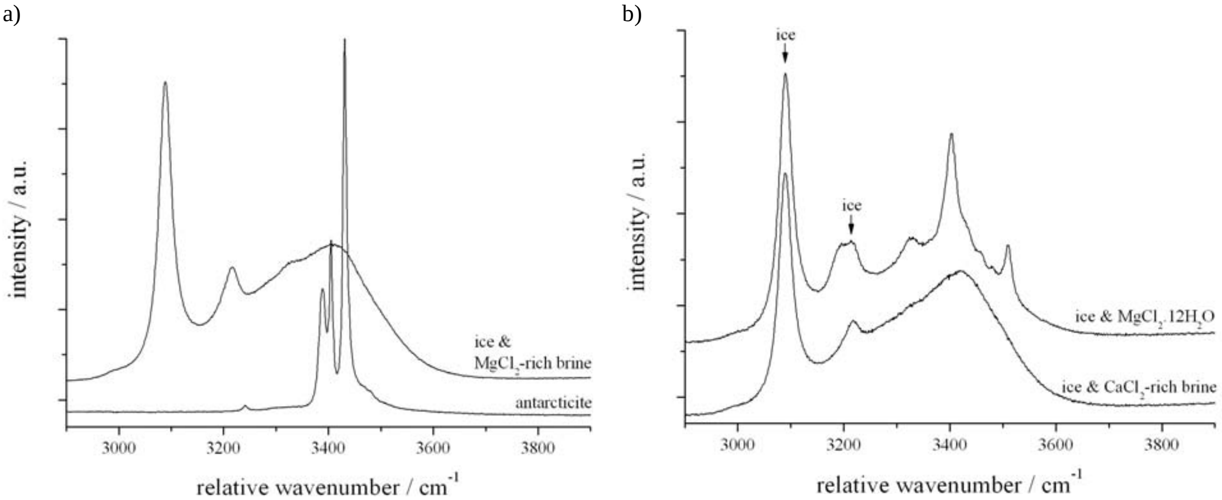

Fig. 5.84. a) Raman spectra of the phase assemblage antarcticite, ice and $MgCl_2$-rich brine (experiment 050). b) Raman spectra of the phase assemblage $MgCl_2 \cdot 12H_2O$, ice and $CaCl_2$-rich brine (experiment 050).

5.5. Raman spectroscopy of H_2O inclusions at high temperatures

The Raman stretching vibrations of warer show one broad signal in the range between 2900 and 3900 cm^{-1}, which consists of overlapping vibrational modes. The morphology of the Raman spectrum of pure water is strongly dependent upon temperature. Figure 5.85a illustrates the evolution of the spectra at different temperatures. The whole spectra shift to higher wavenumbers with increasing temperatures and the band signal becomes narrower. A Raman spectrum of aqueous solutions can be described by purely geometrical properties using three Gaussian-Lorentzian contributions (see Chapter 4 and 7). At 20 °C the spectra of pure water is defined by main peak positions at 3222 (*Peak1*), 3433 (*Peak2*) and 3617 (*Peak3)* cm^{-1} (Fig. 5.85b). Such contributions can be used to characterise the liquid water spectra up to 160 °C. A systematic trend in deconvolved main peak positions and in half width can be observed for all three functions (Fig. 5.86). Main peak positions (*P*) of *Peak1* (Eq. 5.21) and *Peak2* (Eq. 5.22) increase with higher temperatures, whereas the position of *Peak3* (Eq. 5.23) decreases. The full width at half maximum (*FWHM*) remains approximately constant (Eq. 5.24). Deconvolution parameters are given in the Table A-10 (APPENDIX). The intensity of the *Peak3* is decreasing drastically towards 160 °C. The intensity ratio *Peak2/Peak3* tend to zero (Fig. 5.86d). The shoulder at high wavenumber (characterised by *Peak3*) is not pronounced anymore (see spectra at 200 °C in Fig 5.85a). Raman spectra at higher temperatures (above 160 °C) are better described by using only two contributions (*Peak1* and *Peak2*)

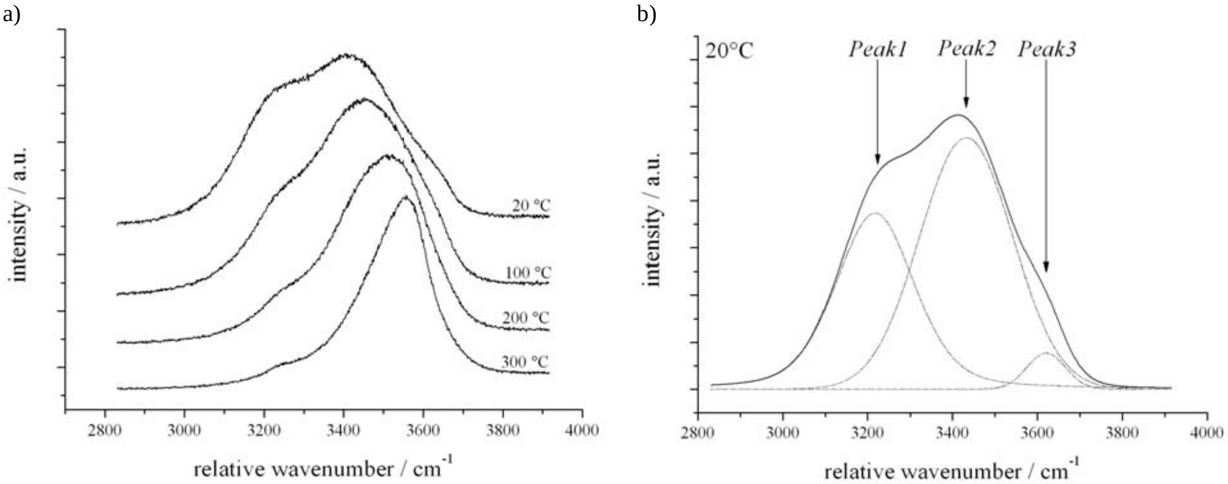

Fig. 5.85 a) Raman spectra of pure water obtained at 20, 100, 200 and 300 °C. b) Raman spectrum of pure water measured in a fluid inclusion at 20 °C deconvolved with three Gaussian-Lorentzian contributions.

$$P_{Peak1} = 3207.1 + 0.52232 \cdot T - 0.0016518 \cdot T^2 \qquad (5.21)$$

$$P_{Peak2} = 3421 + 0.59137 \cdot T + -0{,}224256 \cdot T^2 \qquad (5.22)$$

$$P_{Peak3} = 3619.3 + 0.069345 \cdot T - 0.0020387 \cdot T^2 \qquad (5.23)$$

$$FWHM_{Peak1} = 214.87 + 0.25208 \cdot T - 0.0024851 \cdot T^2 \qquad (5.24)$$

$$FWHM_{Peak2} = 258.58 + 0.017262 \cdot T - 0.0015774 \cdot T^2 \qquad (5.25)$$

$$FWHM_{Peak3} = 107.71 - 0.09375 \cdot T + 0.03497 \cdot T^2 \qquad (5.26)$$

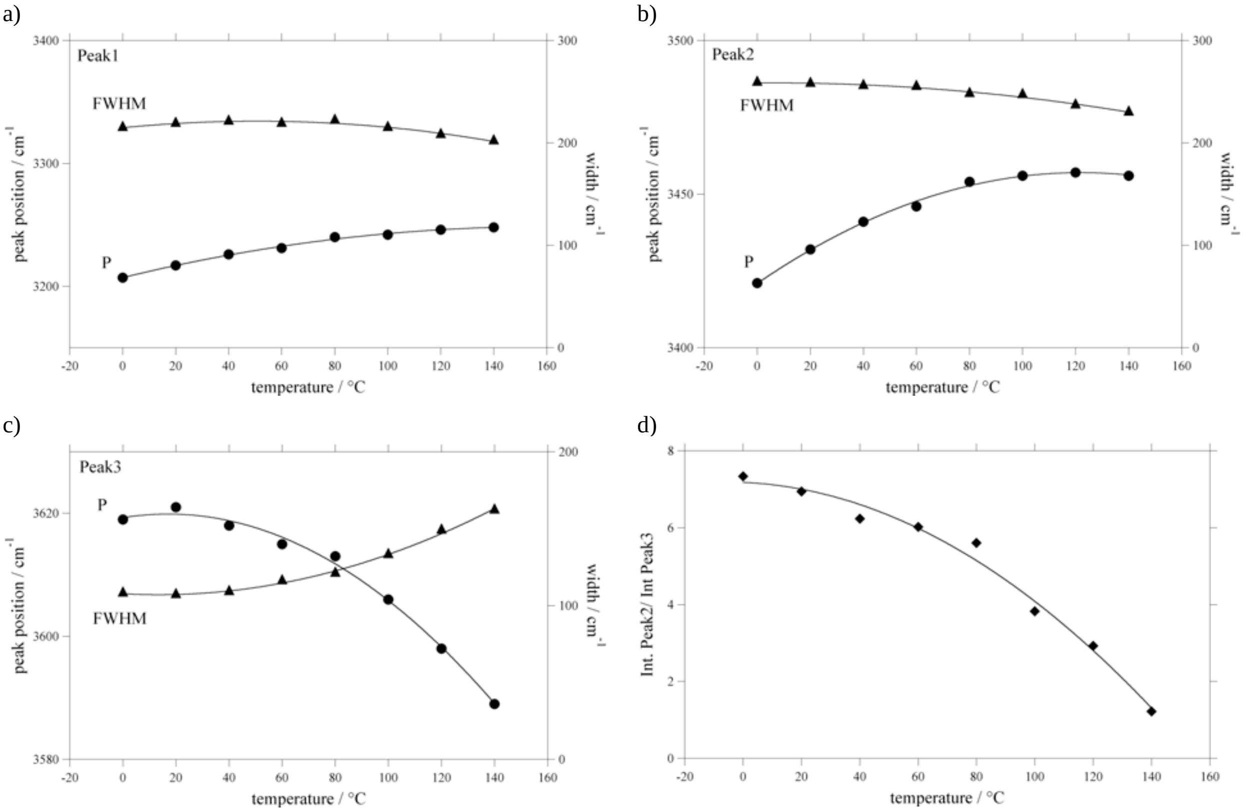

Fig. 5.86. Deconvolved peak position (*P*) and full width at half maximum (*FWHM*) for a) *Peak1*, b) *Peak2* and c) *Peak3* as a function of temperature obtained from pure water fluid inclusion (experiment 027). Solid line represents polynomial best fits (Eq. 5.21 to 5.26) through the data. d) Intensity (Int.) ratio of *Peak2/Peak3* as a function of temperature.

5.6. Salinity estimation using of the OH stretching bands of water

5.6.1. Method

This study provides a method to estimate the salinity of fluid inclusions by the analysis of Raman spectra of aqueous solutions in the OH stretching region (2800 to 3800 cm^{-1}). Raman spectra of pure water and saline fluid inclusions at room temperature are analysed by using Gaussian-Lorentzian functions that deconvolve the spectroscopic signal, i.e. the fitting of multiple spread functions to obtain hidden peaks (PeakFit 4.11, user manual, 2002; see Chapter 4). A deconvolution with three Gaussian-Lorentzian curves as illustrated in Figure 5.87 is preferred (see also Bakker, 2004). It can be applied to pure H_2O as well as to brines. The deconvolved spectra can be used for a spectroscopic methodology to determine the salinity of natural aqueous fluids.

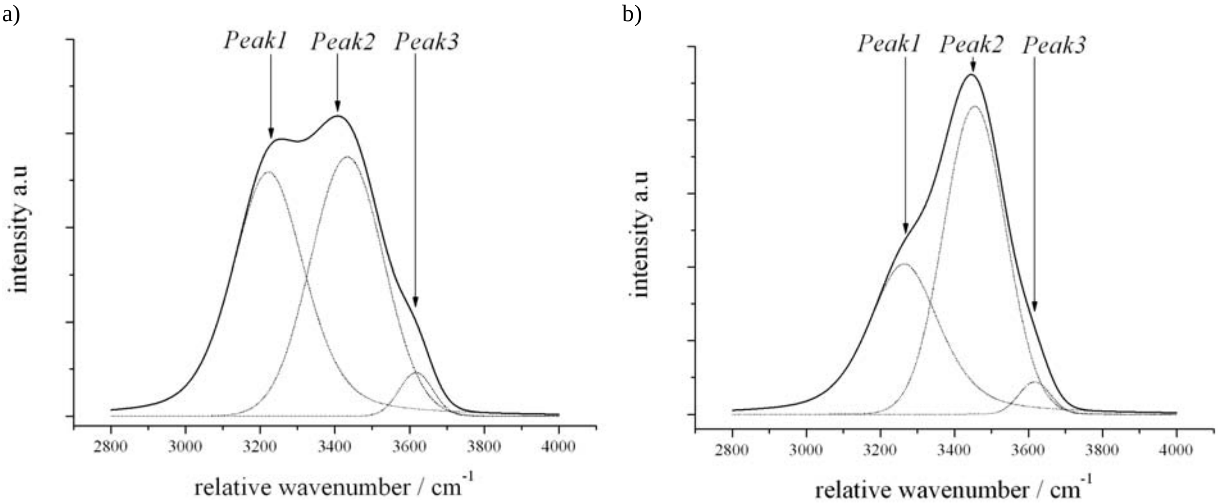

Fig. 5.87. Deconvolution of a Raman spectrum of a) pure water from experiment 003 and of a b) 23 mass% NaCl-H_2O solution from experiment 019 at room temperature by defining three Gaussian-Lorentzian components. Deconvolved peak positions for pure water are 3222 cm^{-1} (*Peak1*), 3433 cm^{-1} (*Peak2*) and 3617 cm^{-1} (*Peak3*), whereas the positions for the NaCl-H_2O solution are identified at 3266 cm^{-1} (*Peak1*), 3454 cm^{-1} (*Peak2*) and 3609 cm^{-1} (*Peak3*).

The most significant Raman spectral indicator for the estimation of the salinity of a free fluid (reference solutions; see Chapter 4.3) is the first deconvolved Gaussian-Lorentzian peak (*Peak1*, see Fig. 5.87). A full set of the experimental results, i.e. a_o, a_1, a_2 and φ values of all peaks, is given in the Table A-11 (APPENDIX). It is possible to determine the specific relative wavenumber of *Peak1* (peak position) for fluids of different salinities (Fig. 5.88 solid symbols). The data show a linear increase in relative wavenumber values with increasing salinity. A linear best fit through this data results in equation 5.27.

$$\Delta\nu_1 = a + b \cdot \mathrm{sal} \qquad (5.27)$$

where *sal* is the salinity in mass% NaCl, $\Delta\nu_1$ is the band position of *Peak1* in relative wavenumbers, *a* is 3222.8 (±0.3) cm^{-1}, and *b* is 1.69 (±0.02) cm^{-1}. Measurements of brines with similar salinities in fluid inclusions may reveal different Raman contours depending on the orientation of the host crystal and other factors. For essentially identical salinities, the deconvolved peak positions (*Peak1*) can be substantially different between the reference solutions, measured in open tubes and fluid in inclusions (Fig. 5.88, shaded bars). In general, *Peak1* values obtained from fluid inclusions are shifting to higher relative wavenumbers compared values obtained from reference solutions. The shift is illustrated with the dashed lines in Figure 5.82, corresponding to maximally +27 cm^{-1} for higher wavenumbers and a much smaller shift (about -6 cm^{-1}) for lower wavenumbers. This spectral effect may cause an incorrect estimation of salinity in fluid inclusions referring to equation 5.27. For example, *Peak1* measured at 3263 cm^{-1} in a fluid inclusion corresponds to 16 mass% NaCl, whereas the same band position correspond to 24 mass% NaCl in the reference solution (see Fig. 5.88). The variation of *Peak1* for a specific salinity of the fluid inclusions is caused by the rotation of the sample, i.e. a variation in crystal orientation (indicatrix) with respect to the plane of polarisation of the laser beam.

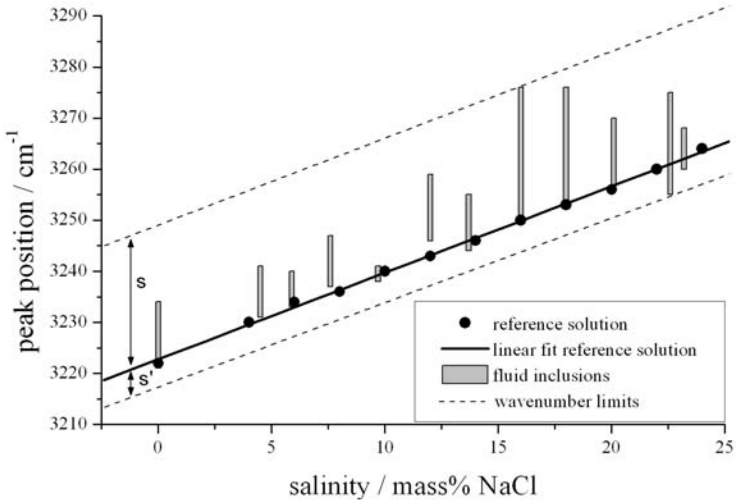

Fig. 5.88. Peak position of the first Gaussian-Lorentzian component (*Peak1*) as a function of salinity (mass% NaCl). Filled dots represent the peak positions measured in pure water and in saline reference solutions in open tubes. Shaded bars represent the range of peak positions measured in individual fluid inclusions in quartz over a sample rotation of 90°. *S* and *S´* represent the possible maximum offset in the band position estimation that is caused by rotation.

5.6.2. Polarisation effects

The Raman spectrum of H_2O can be substantially different between a free drop of water and a fluid inclusion as a result of polarisation effects (Dubessy et al., 2002). The Raman spectra of aqueous solutions in fluid inclusions may be influenced by the crystallographic orientation of the host mineral, due to the interaction between light (laser) and a birefringent mineral such as quartz (e.g. Turrell and Corset, 1996). The spectral slopes, in Figure 5.89a, in the range of 2800 to 3800 cm^{-1} relative wavenumbers ($\Delta\nu$) for the enclosed fluid compared to that of a free water drop of the same composition, depends on the orientation of the host quartz. Another polarisation effect is caused by the quartz-fluid interface, i.e. polarisation due to reflection. There are effects due to the angle between the plane of polarisation of the laser and the plane defined by the inclusion wall onto which the laser is incident (Fig. 5.89b). The slope of the Raman spectrum is much steeper for the fluid in an inclusion than for a free water drop. For the same crystallographic orientation of the quartz host, an approximately perpendicular interface, i.e. parallel to the sample surface (arrow "*b*" in Fig. 5.89b), results in a steeper spectral slope than for an inclined interface (arrow "*a*" in Fig. 5.89b). These two polarisation effects on a laser beam crossing the quartz host in order to characterise the fluid entrapped in inclusions were also experimentally examined and quantified.

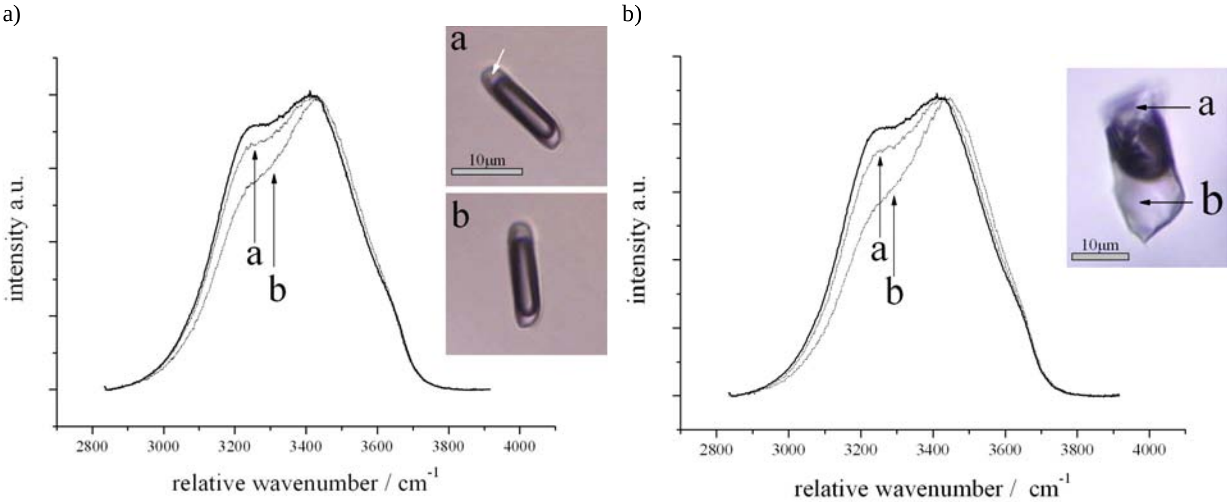

Fig. 5.89. a) Raman spectra of pure liquid water at 22 °C measured in a synthetic fluid inclusion with different crystallographic orientations of the host mineral compared to a liquid water spectrum (thick line) measured in a free water drop. The arrow illustrates the spot of measurement within the inclusion. The spectrum labeled "*a*" was measured at the location shown by the arrow in the inclusion in the image, whereas the spectrum labeled "*b*" was measured at the same point, but after 40° rotation of the sample. b) Raman spectra of pure liquid water at 22°C measured in a synthetic fluid inclusion in quartz at two different locations at the interface (marked with arrows "*a*" and "*b*", respectively) compared to the liquid water spectrum (thick line) measured in a free water drop. Measurements were taken at the same crystallographic orientation of the quartz host crystal.

Birefringence polarisation

The influence of birefringence on the H_2O Raman contour was studied with respect to the crystal orientation of quartz, i.e. variation of the angle between the polarisation plane of the laser beam and the axis of the ellipsoid, representing refraction indices. Pure H_2O fluid inclusions were synthesised in quartz cores orientated parallel to the *c*-axis (experiment 029) as well as perpendicular to the *c*-axis (experiment 027). Due to rotation, sample 029 (// *c*-axis) reveals a strong modification in the Raman bands, both in *Peak1* values and amplitude ratios belonging to *Peak2/Peak1* (open symbols in Fig. 5.90). Rotation results in an increase in relative wavenumbers compared to free water drops (Fig. 5.90a) with a maximum and minimum about every 45°. Rotation of the crystallographic axis of quartz (either the *a*-axis or *c*-axis) to about the 30° and 120° position orientates them parallel to the laser polarisation plane, i.e. *y*-direction on the microscope stage. The wavenumber value of *Peak1* varies between 3223 and 3239 cm^{-1} whereas the amplitude ratio varies between 1.18 and 1.72. These values are significantly different from those in the reference solution (3222 cm^{-1}, ratio of 1.06). In contrast, rotation of sample 027 does not result in significant modification of the Raman bands (solid symbols in Fig. 5.90). Both wavenumber of *Peak1* and the amplitude ratios are approximately the same as those of the reference solution. These variations were also observed in experiments 028, 041 and 042. However, this rotational effect does not always occur to a similar extent in a number of inclusions in these samples. It, therefore, appears that additional non-rotational effects influence the Raman spectra.

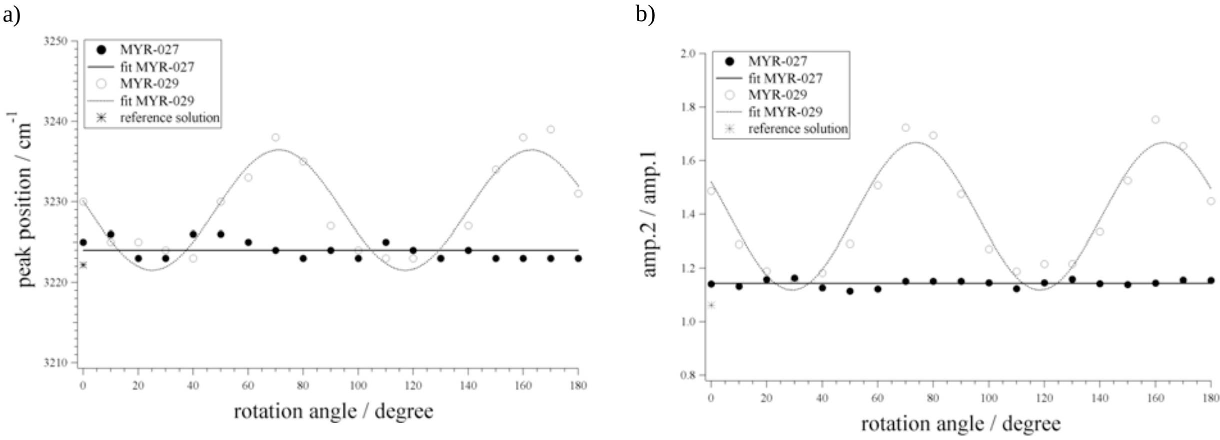

Fig. 5.90. a) Deconvolved values of *Peak1* and b) amplitude ratios of *Peak2/Peak1*, measured in synthetic fluid inclusions as a function of rotation in experiments, where the sample surface is orientated perpendicular (experiment 027) and parallel to the *c*-axis (experiment 029). The continuous solid line represents a linear best fit through the data points of experiment 027, whereas the data points of experiment 029 are best represented by a sinusoidal fit (dotted line). As a reference, the peak position and amplitude ratio of pure water (reference solution) is shown.

Inclusion depth

The depth of the inclusion in the quartz hardly affects *Peak1* (Fig. 5.91), observing synthetic pure water inclusions in quartz. However, the crystallographic orientation of the quartz matters. *Peak1* varies between 3218 and 3225 cm^{-1} in inclusions from experiment 027 (⊥ *c*-axis), whereas inclusions from experiment 029 (// *c*-axis) reveal a much larger variation, between 3218 and 3235 cm^{-1}, similar to the results illustrated in Figure 5.90. This rotational variability in peak positions is mainly caused by the effect of birefringence. Within sample 029 most inclusions display a large variation in peak position. However, two inclusions show a very small variation (fluid inclusions at 2 and 28 μm depth, Fig. 5.91b). This insensitivity to rotation is the result of additional effects such as interface orientation. There is no defined trend between inclusion depth and the position of the Raman bands.

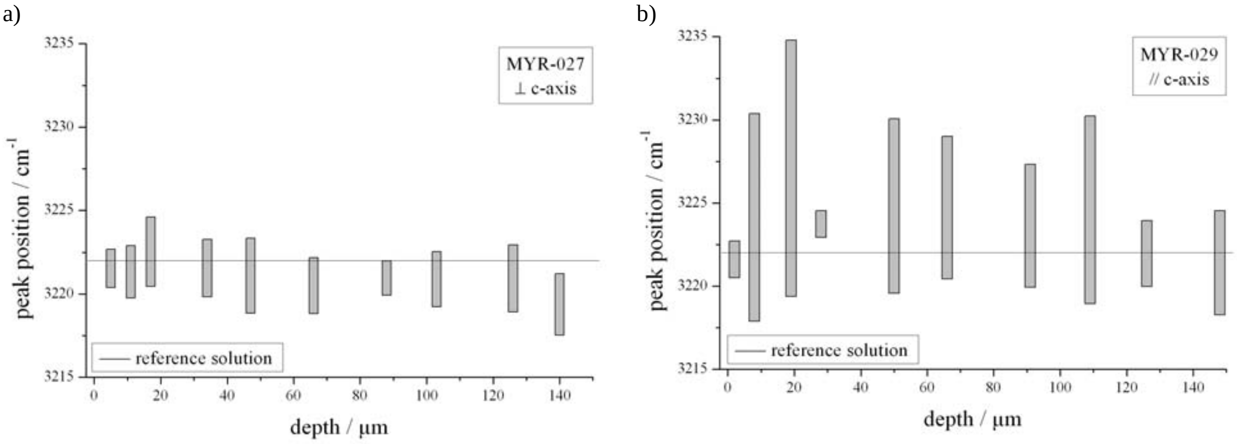

Fig. 5.91. Deconvolved values of *Peak1* of synthetic pure water fluid inclusions as a function of inclusion depth in the quartz host. The spectra were taken on inclusions for which the sample surface is orientated a) perpendicular (experiment 027) and b) parallel to the *c*-axis (experiment 029), with measurements made over a rotation of 90°. The continuous line represents the peak position of pure water (reference solution).

Inclusion size

The influences of the inclusion size, was studied with saline inclusions (23.2 mass% NaCl) in an inclined healed crack in experiment 019 (Table 5.15). The variation in the evaluated peak positions results from taking spectra at different locations in several inclusions, but at the same crystallographic orientation of the quartz (without any rotation of the sample). The scatter in the data does not reveal a clear relationship between the size (area and length of the inclusion) and the deconvolved *Peak1* position of the fluid. The variation in *Peak1*, measured in the same inclusion, indicates that another factor must affect the Raman spectra, which is not related to birefringence.

Table 5.15. Properties represented by the maximum areas and lengths of fluid inclusions in experiment 019. The melting temperatures of ice ($T_{m(ice)}$) and hydrohalite ($T_{m(HH)}$) as well as the homogenisation temperatures (T_h) were recorded with microthermometry. The variation in the evaluated peak positions results from measurements taken at different locations in the fluid inclusions at the same crystallographic orientation of the host mineral.

Inclusion	Peak position *(Peak1)* (cm^{-1})	Area (µm^2)	Length (µm)	$T_{m(ice)}$ (°C)	$T_{m(HH)}$ (°C)	T_h (°C)
FI2	3264 to 3266	177.0	23.8	-21.1	-18.9	390.8
FI4	3261 to 3269	284.2	29.7	-21.1	-19.0	391.5
FI5	3270 to 3273	234.3	32.5	-21.0	-19.0	391.3
FI7	3268 to 3282	117.2	16.9	-21.1	-19.1	390.3
FI9	3260 to 3261	132.1	14.8	-21.0	-18.9	393.0

Reflection polarisation

To investigate the impact of the orientation of quartz-fluid interfaces (polarisation due to reflection), a natural negative-crystal-shaped inclusion was studied (see Chapter 4). Orientation of this specific negative-crystal-shaped fluid inclusion implies, that it is orientated parallel to the c-axis of the host quartz. Raman measurements taken on different locations in the inclusion at the same crystallographic orientation show modifications in the spectra (Fig. 5.92). Parameters of the deconvolution are given in the Table A-12 (APPENDIX). Again, the magnitude of spectral modification depends on the rotation angle, with minima and maxima in relative wavenumbers and amplitude ratios every 45°. The axes of the indicatrix coincide with the laser beam polarisation plane at these extremes. The six locations show a variety of spectra (Fig. 5.92; Tab. A-12, APPENDIX). The horizontal interface (*m*) is more sensitive to the rotation angle (large modification in the Raman contour), whereas steeper interfaces (e.g. r_4) are less influenced. There is no clear relationship between the variability of the spectra and the angle between the interface plane and the polarisation plane of the laser beam. This interface-orientation effect was also seen in the synthetic inclusions in experiment 019 (Tab. 5.15), which have irregular morphologies. Note that this orientation phenomenon was not observed in inclusions where the sample surface is orientated perpendicular to the optical axis.

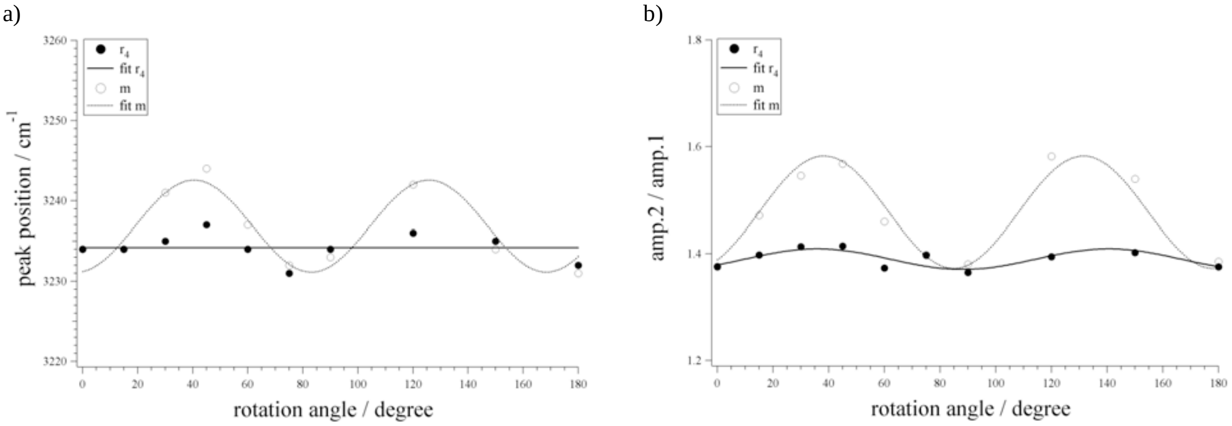

Fig. 5.92. a) Deconvolved values of *Peak1* and b) amplitude ratios of *Peak2/Peak1* as a function of rotation angle measured in the same negative-crystal-shaped inclusion (see Fig. 4.5) on two different planar interfaces (r_4= rhombohedra–plane; *m*=prism-plane). The continuous solid line represents the linear best fit through the data points of plane r_4 whereas the data points of plane *m* are best represented by a sinusoidal fit (dotted line).

Simulated inclusions

By analysing simulated inclusions (see Chapter 4; Fig. 4.6), the influence of birefringence was determined independently from the interface effects. The spectrum of pure liquid water was strongly influenced in the experiment where the quartz plate, covering the water drop in the quartz cavity, had an orientation parallel to the *c*-axis $[0001]$ and one *a*-axis $[10\bar{1}0]$. Figure 5.93 illustrates the systematic modifications of the Raman contour during the rotation of the sample from 0° to 45°.

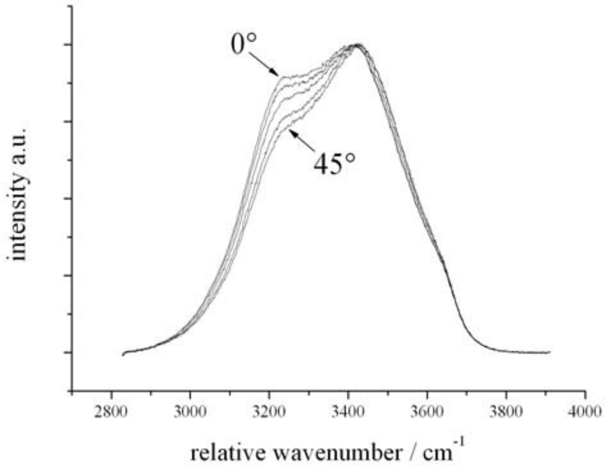

Fig. 5.93. Influence of the polarisation effect on the Raman stretching band of water due to the birefringence of quartz evidenced by the rotation of the quartz covering plate of simulated inclusions. At 0° the quartz plate was orientated parallel to the *c*-axis (north-south direction of the microscope stage, which is parallel to the laser polarisation plane) and was then stepwise rotated to 45°.

The typical Raman spectrum of pure water was only observed when the *c*-axis (shown with 0° in Fig. 5.93) or *a*-axis was orientated exactly parallel to the laser beam's polarisation plane, whereas in all other orientations spectral variations were recorded. The greatest modification in the deconvolved peak position and amplitude ratio was recorded at a rotation angle of 45° (see Fig. 5.93). Experiments where the quartz plate was orientated perpendicular to the *c*-axis did not show significant rotation-dependent modifications in the spectra. This observation confirms that birefringence is a major actuator of this variability in spectra contour, similar to the results with synthetic fluid inclusions.

The rotation-induced variation in Raman bands for pure H_2O with increasing depth in the simulated inclusion is illustrated in Figure 5.94. This set of analyses was done using quartz plates of different thickness and orientation (see Chapter 4; Fig. 4.6). The wavenumber value of *Peak1* decreases systematically with increasing depth in experiments with quartz plates perpendicular (experiment 027) and parallel (experiment 029) to the *c*-axis. As expected from the behaviour of the Raman spectra of synthetic fluid inclusions, the rotation-induced variation is small for quartz plates perpendicular to the *c*-axis (Fig. 5.94a). In experiments with quartz plates orientated parallel to the *c*-axis (Fig. 5.94b), the variation is much greater for shallow inclusions (3218 to 3233 cm^{-1}), and decreases drastically towards deeper levels. Therefore, the effect of birefringence is minimised with increasing depth. The behaviour, shown in Figure 5.94, is different from the results obtained on multiple natural fluid inclusions, but not in contrast because the additional effects such as reflection polarisation are constant for all measurements.

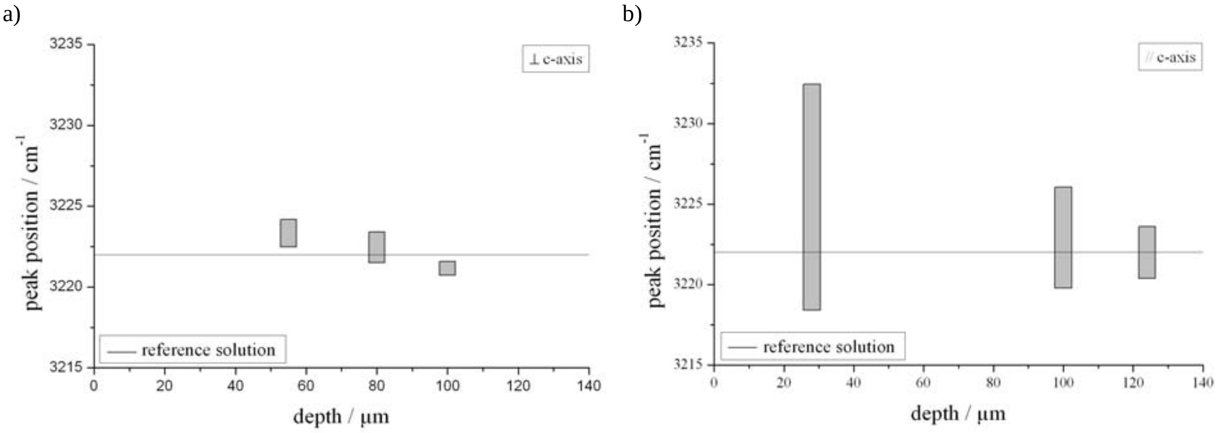

Fig. 5.94. Deconvolved values of *Peak1* of the simulated pure water fluid inclusions, as measured with different thickness of the quartz cover plates, orientated perpendicular to the *c*-axis (a) and parallel to the *c*-axis (b) with measurements made over a rotation of 90° (shaded bars). The continuous line represents the peak position of pure water (reference solution).

6. CASE STUDY ON NATURAL FLUID INCLUSIONS IN DOLOMITE (CANTABRIAN ZONE, NW-SPAIN)

Fluid inclusions were investigated from dolomites associated to the Barcaliente and Valdeteja Formation (Bodón Unit; Cantabrian Zone). Inclusions from those dolomites contain salt-rich aqueous solutions, in which the main compounds are Ca^{2+}, Mg^{2+}, Na^{+}, K^{+} and Cl^{-} (see Gasparrini, 2003). Microthermometric studies revealed the nucleation of complex phase assemblages at low temperatures. The precipitation of ice, hydrohalite and $MgCl_2$-hydrates was confirmed by Raman spectroscopy in those inclusions (Grimmer, 2000; Gasparrini, 2003). Nevertheless, Raman spectra at low temperatures show the coexistence of ice and a complex mixture of unknown salt hydrates (Gasparrini, 2003). Those spectra could not be interpreted until know. Further studies on those inclusions were done with cryogenic Raman spectroscopy to identify the type of salt hydrates by comparison with spectra obtained from synthetic fluid inclusions with known salinities (see Chapter 5.4).

6.1. Geological Setting

Carboniferous rocks are found as outcrops in the Iberian Massif. During the carboniferous period, sedimentation was coeval with the Variscan orogeny, in contrast to earlier Palaeozoic sedimentation in a rift to passive margin setting. The strong tectonic control on Variscan sedimentation resulted in mobile, unstable basins, with sedimentary successions, that show rapid temporal and spatial changes in lithofacies and thickness (Colmenero et al., 2002). The Cantabrian Zone in the north of Spain (Fig. 6.1), represents a foreland of the Iberian Massif and cuts into five tectonostratigraphic domains (see Fig. 6.2), i.e. the Fold and Nappe, Central Asturian Coalfield, Ponga Nappe, Picos de Europa and Pisuerga-Carrión provinces (Julivert, 1971).

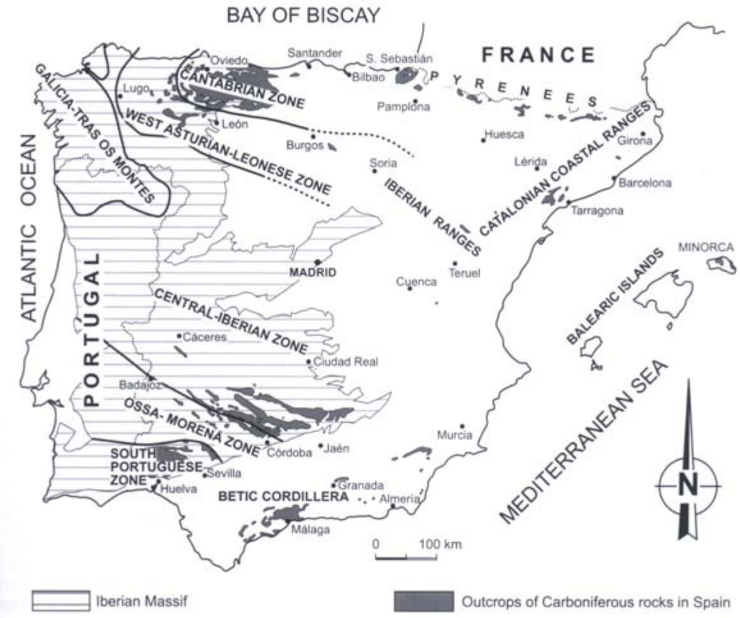

Fig. 6.1: The Iberian Massif with the locations of the Carboniferous outcrops (Colmenero et al., 2002).

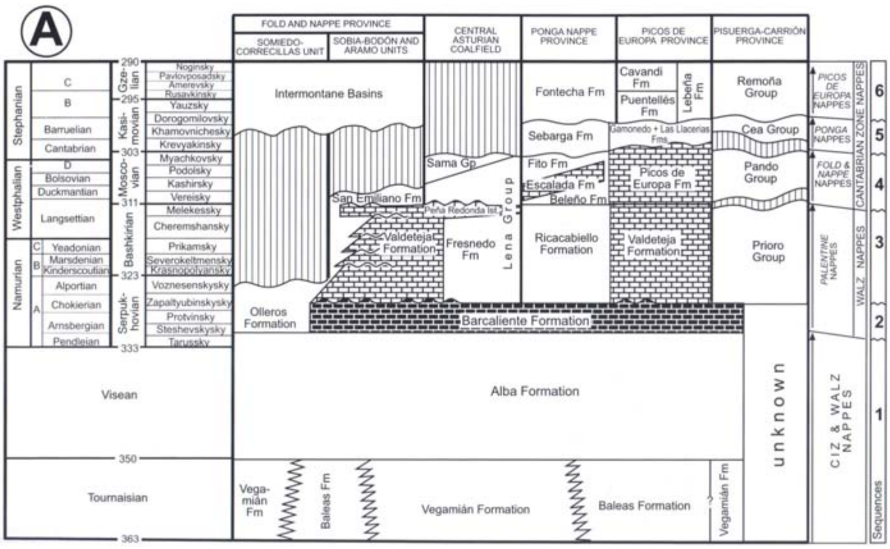

Figure 6.2. Stratigraphic correlation chart of the Cantabrian Zone (after Colmenero et al., 2002 and references therein).

The genesis of the Cantabrian Zone can be devided in six major sequences (Colmenero et al., 2002; see Fig. 6.2):

(1) The first sequence (upper Famennian/lower Tournaisian-Arnsbergian) overlies the upper Devonian terrigenous deposits and reflects the inversion from a passive continental margin to an active margin. Three units can be dissipated: the lateral Baleas and Vegamián formations and the overlying Alba Formation.

(2) The Barcalinete and Olleros Formation and a part of the Priori Group are comprises in the second sequence (Namurian A; Serpukhovian). During this period, the sedimentary basin is devided in a foredeep and a turbidite deposition. A shallow water realm was extended over the external part of the Fold and Nappe province and provides an uniform carbonate sedimentation (Barcaliente Formation).

(3) Siliclastic and carbonate lithologies can be found in sequence three (Namurian B-Langsettian). Thick limestone deposits (Valdeteja Formation) extend over the external part of the Fold and Nappe province. More siliclastic parts of the succession across the Fold and Nappe Province are represented by e.g. San Emilliano Formation.

(4) The sequence four (late Langsettian to Westphalian D) records the burial of the Valdeteja Formation. The succession is mainly dominated by terrigeneous deposits (frequently coal bearing).

(5) In sequence five (Westphalian D to Stephanian B), the sedimentary basin is reduced in size due to the advancement of the orogenic front. The inner sectors of the basin were thrust to the east and uplifted. Two successions can be devided, i.e. a succession accumulated in the foreland basin and a succession, which is deposited in an intermontane basis.

(6) Sequence six (middle Kasimovian to Gzelian) is characterised by the youngest carboniferous sediments. It can be divided of a foreland basin-fill succession, deposited during the southward emplacement of the Picos de Europa unit and the latest thrust of the Ponga Nappe unit. Intermontane basin-fill succession occurs in the Fold and Nappe province.

6.2. Sampling

Carbonian Outcrops (The Bodón Unit)

Sampling of the dolomites takes place in the Bodón Unit whereas extensive dolomitisation of carboniferous rocks can be found. The unit consists of the Alba Formation, Barcaliente Formation, Valdeteja Formation and the San Emillano Formation (Gasparrini, 2003).

Alba Formation: The formation is the most widespread lithostratigraphic unit in the Carboniferous of the Cantabrian Zone. It is made up of red limestones (pinkish or grey). The formation comprises red nodular limestones with red shale partings and beds and a red radiolite horizont (Colmenero et al., 2002). The dolomite is extremely thin developed in the study area and is imbedded with red shales.

Barcaliente Formation: The formation consists of a thickness between 300-350m and is mainly composed of laminated, thinly bedded, dark grey limestones and mudstones (Colmenero et al., 2002). The limestone is bedded in intervals from centimetre to decimetre laminations parallel to the bedding.

Valdeteja Formation: The formation has a variable thickness of 0 to 500 m (Gasparrini, 2003). The massive grey limestone occurs occasionally well bedded (see Fig. 6.7f). It is lateral inter-fingered with rocks of the San Emiliano Formation.

San Emilliano Formation: The formation consists of lutite and clastic carbontic sedimentary rocks. In addition, marls and shales can be found.

Devonian outcrops

Ermita Formation: The formation comprises a thin succession of cross-bedded, ferrigeneous, calcerous and microconglomeratic quartz sandstones, with layers of siltstones and shales (García-Alcalde et al., 2002).

La Vid Group: The group is devided into four members (García-Alcalde et al., 1979; Truyóls et al., 1990): sandy and argillaceous limestones, dolomitic marls and dolostones; argillaceous limestones and shales; dark brown shales with limestone lenses; red detritial limestones and marlstones interbedded with shales.

Table 6.1 gives the positions of the sampling localities “Las Salas” and “Villanueva de la Tercia”. Dolomites for fluid inclusion studies were collected from two different formations, i.e. Barcaliente Formation (B1, B2) and Valdeteja Formation (V2).

Table 6.1. Sampling localities. Formation (Fm.).

Locality	Position	Formation	Rock	Sample
Las Salas	N 42°/55.545 – W 005°/06.902	Alba Fm.	Dolomite	A1
	to	Barcaliente Fm.	Dolomite	B1, B2, B3, B4
	N 42°/55.655 – W 005°/06.842	Barcaliente Fm.	Calcite	C1
Villanueva de la Tercia	N 42°/58.678 –W 005°/38.799	La Vid Group	Limestone	E1
	N 42°/58.678 –W 005°/38.799	Ermita Fm.	Quarzite	Q1
	N 42°/58.655 – W 005°/38.833	Alba Fm.	Dolomite	A2
	N 42°/58.464 – W 005°/38.857	Barcaliente Fm.	Dolomite	B5
	N 42°/58.522 – W 005°/39.040	Valdeteja Fm.	Dolomite	V1, V2
	N 42°/58.243 – W 005°/39.468	San Emilliano Fm.	Lutite	E2

6.2.1. Las Salas

Dolomites from the Barcaliente Formation (sample B1 and B2) were sampled from an outcrop along the road from Las Salas to Cremenes (Fig. 6.3; Fig. 6.4a). The outcrop is centred in a fault zone (Fig. 6.4 b show the tectonically strained outcrop), where the dolomites of the Barcaliente Formation are strongly imbricated with rocks from the Alba Formation. Brecciated dolomites of the Barcaliente Formation with pink dolomitic interclastic fillings occur (Fig. 6.5a). In general, the pinkish colour may originate from the Alba Formation. Banded structures (zebra dolomites, Fig. 6.5.b) are common, which show a rhythmic repetition of mosaic and sparry dolomite sheets, which are interrupted by open cavities. Blocky calcite is found in cavities or respectively in veins, which crosscut the breccia (Fig. 6.5.c/d). The dolomite, corresponding to the Barcaliente Formation can be distinguished in two types by field observation; a grey-brow mosaic dolomite *(Dol A)* and a milky white to pinkish sparry dolomite (*Dol B*) (see also Fig. 6.3a). The mosaic dolomite is the most abundant and occurs massive, whereas the sparry dolomite is found along fractures and in cavities (pore filling).

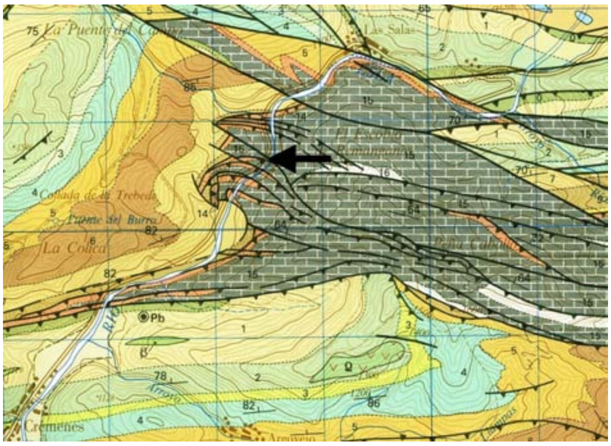

6.3. Geological map of sample locality "Las Salas" (samples B1 and B2) of dolomites from the Barcaliente Formation. The arrow marks the position of the outcrop. Mapa geologico de españa. Scale 1:50000, Sheet: Riano 15-7 (105). Detailed Legend in Fig. A-1 (APPENDIX).

🟧 Alba Formation

▦ Barcaliente Formation

a)

Fig. 6.4. a) Outcrop at "las Salas".

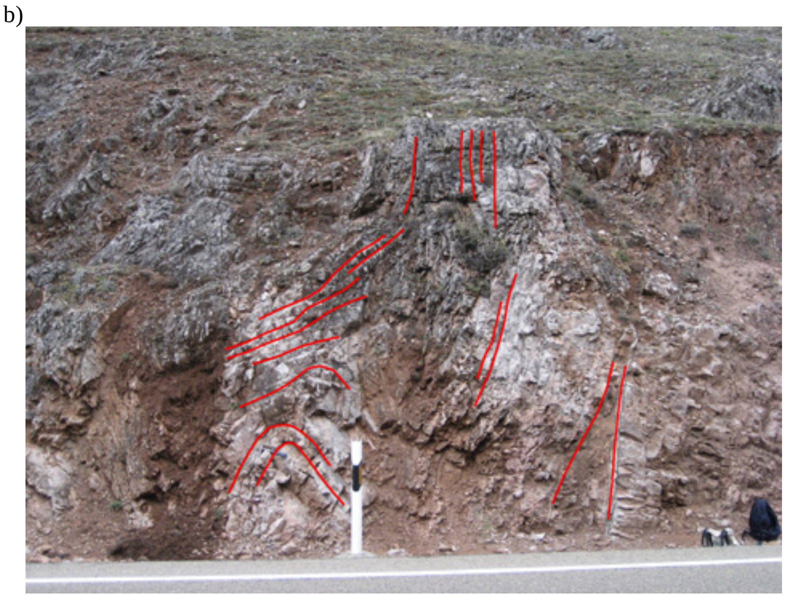

6.4. b) Tectonically strained outcrop.

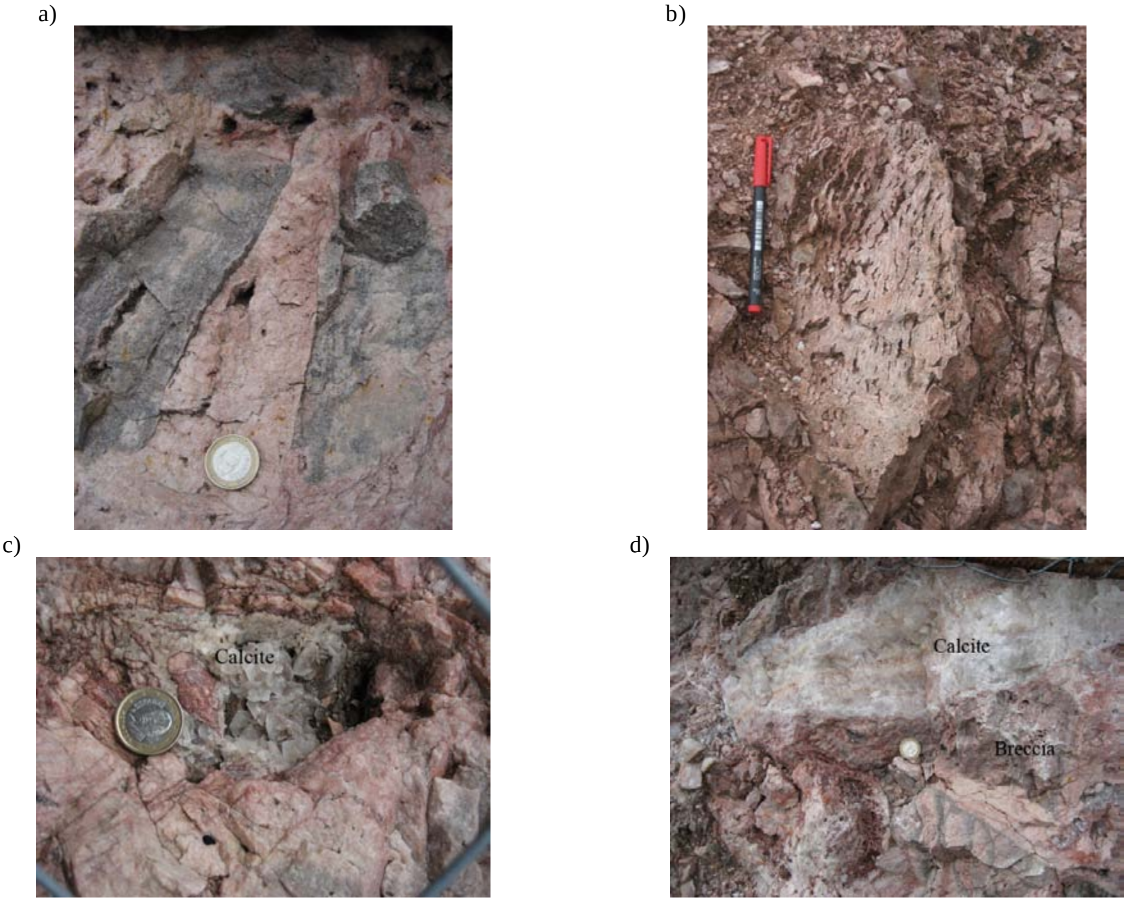

Fig. 6.5. a) Breccia from the Barcalienete Formation (grey) and pinkish dolomites between the rock fragments. b) Zebra dolomite. c) Calcite in cavities. d) Calcite veins, crossing the breccia.

6.2.2. Villanueva de la Tercia

Dolomite samples were collected at outcrops along the street from Millaro toVillanueva de la Tercia (Fig. 6.6a/b), which is positioned in the north flank of the “*Carmenes*” sinclinal and just south of the “*Leon Fault*”. Point 1 in the street profile (Fig. 6.6a) contains massive, grey to black Devonian limestone (La Vid Group; Fig. 6.7a). The nearly vertical bedded limestone alternates with clay layers. About 50 meters to the south, grey quarzite layers (Ermita Formation) are found (Fig. 6.7b), which are imbedded from partly oxidised clay rich layers. The transitions zone to the Alba Formation (2 in Fig. 6.3a) is dominated by black, fissured clay layers, which are strongly tectonically strained. The Alba Formation is characterised by massive pinkish limestone (Fig. 6.7c), which is partly interrupted by clay layers. The pinkish dolomite occurs undistributed, contrary to the brecciated occurrence in “Las Salas” (see Fig. 6.5a). The Alba Formation passes over into the Barcaliente Formation (3 in Fig. 6.6a). The grey dolomite of the Barcaliente Formation occurs massive and an characterised by nearly vertical bedding (Fig. 6.7d/e). Pinkish dolomites of the Valdeteja Formation continue the street profile (3 to 4 in Fig. 6.6a; Fig. 6.7f), which are interrupted by arenaceous and clay levels. The dolomite occurs partly as zebra-dolomite (Fig. 6.7g). The Valdeteja Formation crosses over into the mixed sedimentary rocks (siltstone, sandstones, mudstone, shales) of the San Emilliano Formation (4 in Fig. 6.6a)

Dolomites of the Barcaliente Formation (sample B5) and from the Valdeteja Formation (sample V2) were sampled in this area, which were used for fluid inclusion studies. In both formations, two types of dolomites can be distinguished by field observation (see Gasparrini, 2003), i.e. a massive grey to pinkish dolomite (*Dol A*) and a sparry white dolomite (*Dol B*).

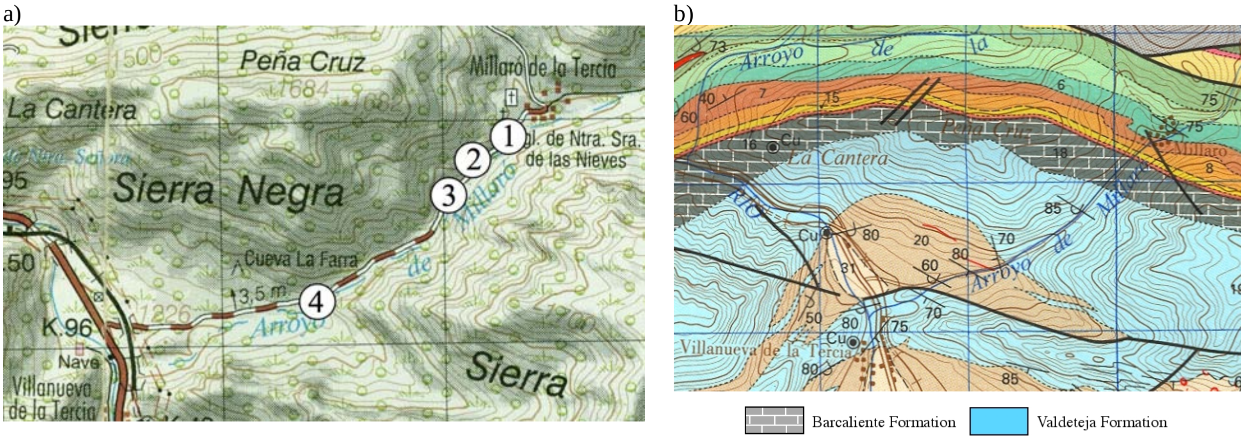
a)
b)

Fig. 6.6. a) Topographic map of the street profile “Villanueva de la Tercia”. b) Geological map of the sample locality “Villanueva de la Tercia”. Mapa geologico de españa. Scale 1:50000, Sheet: La pola de gordón 13-7 (103). Detailed Legend in Fig. A-2 (APPENDIX).

6.7. a) Outcrop of Devonian limestone (La Vid Group). b) Quarzit layer (Ermita Formation). c) Vertical bedded limestones of the Alba Formation. d) Vertical bedded limestones of the Barcaliente Formattion. e) Detail section of the limestone of the Barcalinete Formation. f) Outcrop of the Valdeteja Formation. g) Zebra-dolomite (Valdeteja Formation).

6.3. Dolomites of the Barcaliente Formation

In general, two different types of dolomites (*Dol A* and *Dol B*) can be distinguished in samples from the Barcaliente Formation (see Gasparrini, 2003). *Dol A* consists of a mosaic of fine grained crystals (Fig. 6.8a) and is characterised as a replacive dolomite. Due to the presence of many small fluid inclusions, the crystals occur cloudy in microscopical analyses. The contact between *Dol A* and *Dol B* is not well defined. A transitional zone, consisting of a medium to coarse crystalline *Dol B* (Fig. 6.8b), characterise the rocks. *Dol B* corresponds to a to a void filling event. The precipitated dolomite occurs coarse grained and fills cavities in the host rock (Fig. 6.8c/d). A detailed geological, petrological and mineralogical classification of the dolomites is given by Grimmer (2000) and Gasparrini (2003).

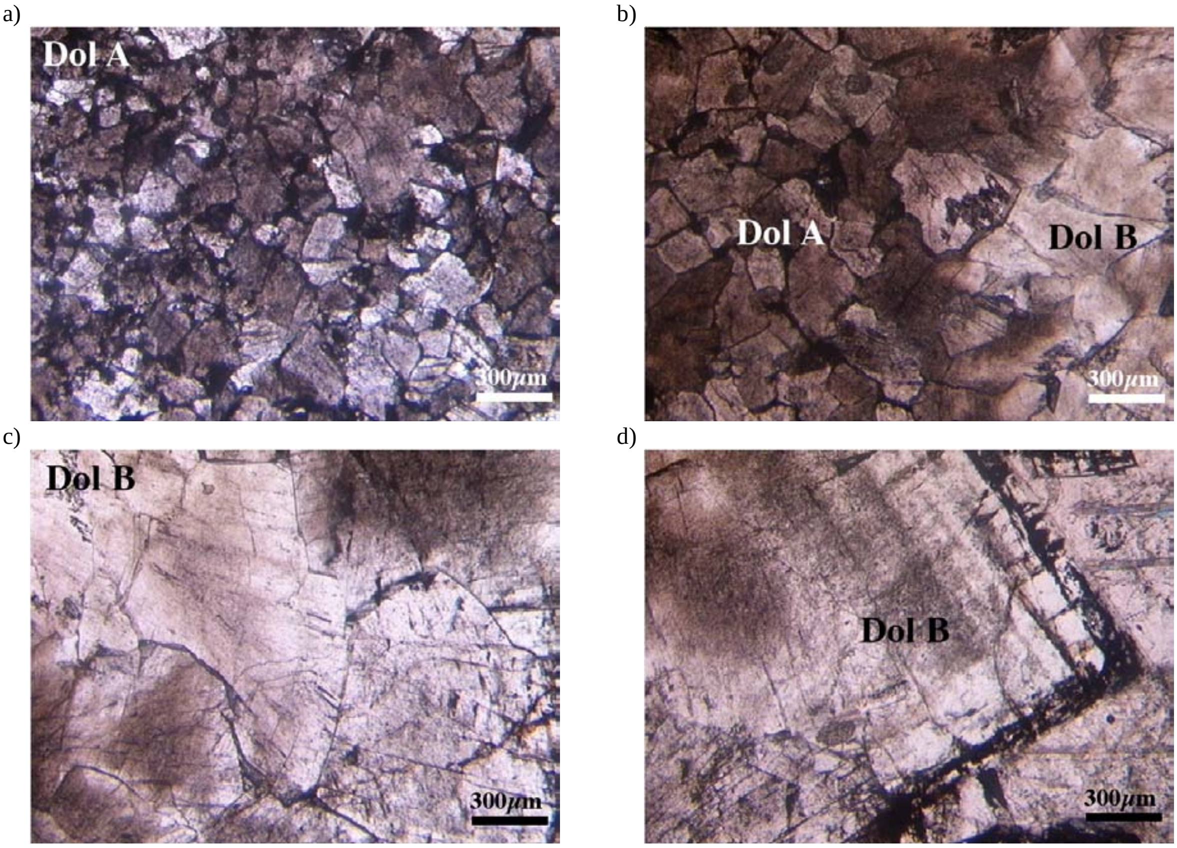

Fig. 6.8. Thin sections images of a) *Dol A*, b) the transitional zone between *Dol A* and *Dol B* and c-d) *Dol B* (sample B5).

6.3.1 Fluid inclusions in Dolomite A

The densely distributed inclusions (see Fig. 6.9) in the dolomite crystals show an irregular shape and are typically smaller than 5µm. The inclusions are filled with an aqueous solution and vapour. Due to the small size of the inclusion the degree of filling is not determined. Less common, inclusions contain a single-phase (all liquid).

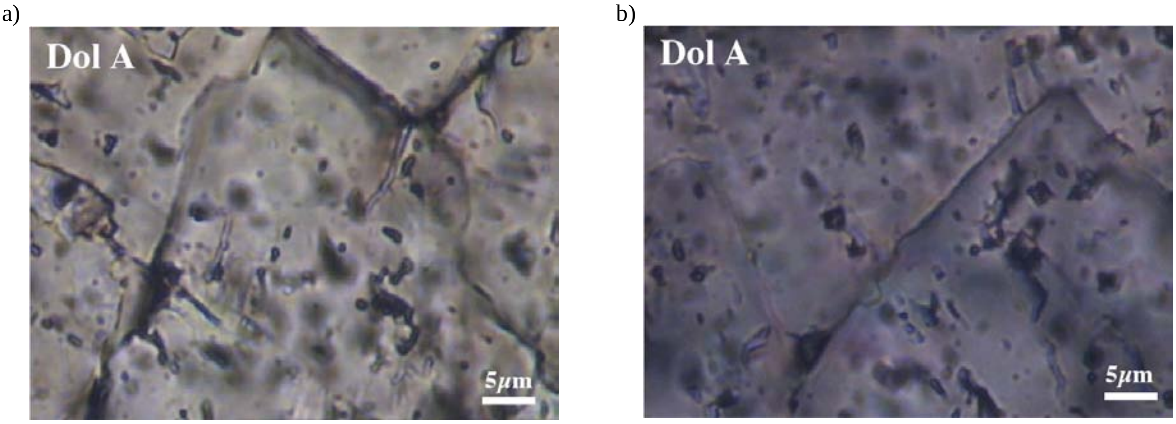

Fig. 6.9. a) Fluid inclusions in *Dol A* observed in sample B1. B) Fluid inclusions in *Dol A* observed in sample B2.

Microthermometric investigations at low temperatures are performed on those inclusions. In general, freezing is rarely observed in those inclusions during cooling. Due to the small size of the inclusions, the nucleation may also be camouflaged and cannot be observed optically as well as by spectroscopic means (Raman spectroscopy). Precipitation of salthydrates is observed in some of the inclusions. The small size of the inclusion mostly does not allow optical observation on nucleation or melting points. Nevertheless, the presence of hydrates was confirmed by Raman spectroscopy. Raman measurements taken at -190 °C (Fig. 6.10a/b), verifies the presence of ice (Raman bands at about 3089 and 3216 cm^{-1}) and hydrohalite (Raman bands at about 3403, 3420, 3430 and 3535 cm^{-1}). In addition the nucleation of antarcticite (Raman bands at about 3386, 3404 and 3431 cm^{-1}) in the absence of ice was observed. Additionally some inclusions show complex Raman spectra contours at -190 °C, which are interpreted as a mixture of salthydrates in the coexistence of ice (see Fig. 6.7c-e). Hydrohalite is present in most of the frozen inclusions (Raman bands at about 3403, 3420, 3430 and 3535 cm^{-1}). Nevertheless, a variety of additional peaks occur, which cannot be allocated easily to a specific salthydrate. Peak overlapping complicates the assignment of the Raman bands to specific salt hydrates. Some peaks fit with Raman bands observed from reference spectra of $MgCl_2$-modifications ($MgCl_2 \cdot 12H_2O$ and $MgCl_2 \cdot 6H_2O$; see Dubessy et al. 1982) and α-$CaCl_2 \cdot 4H_2O$. Final melting of ice is observed at about -38.0 °C, whereas hydrohalite dissolves at about -23.0 °C. As the inclusions are very small, the melting points of antarcticite as well as melting points of the undefined phase(s) are not observed.

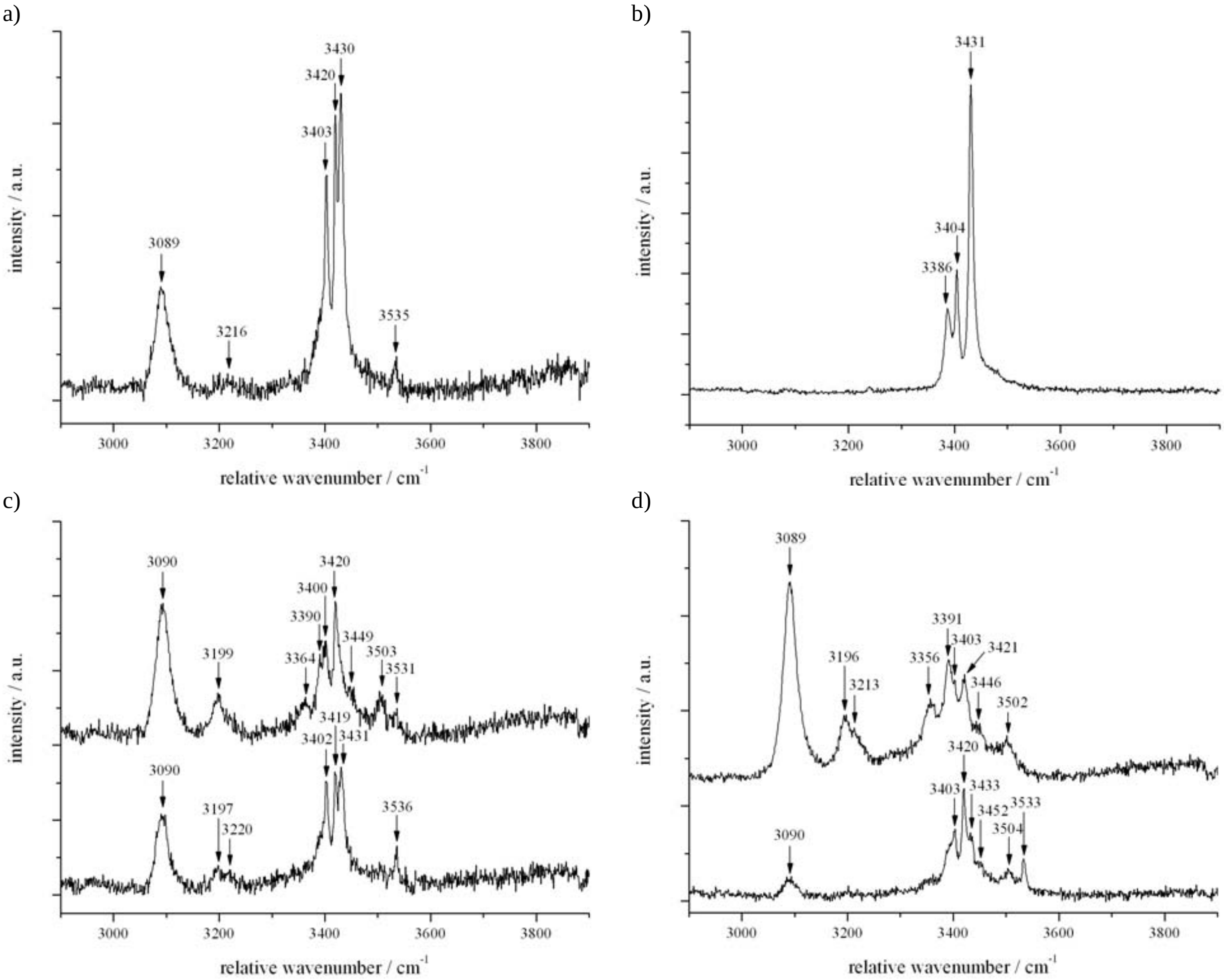

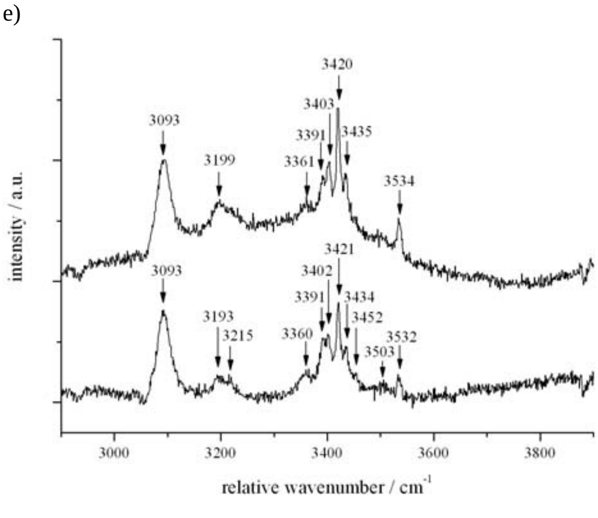

Fig. 6.10. a) Raman spectra of ice (3090 and 3216 cm-^{1}) and hydrohalite (3403, 3420, 3430 and 3535 cm^{-1}) measured at -190 in sample B1 (*Dol A*). b) Raman spectra of antarcticite (3386, 3404 and 3431 cm^{-1}) measured at -190 in sample B1 (*Dol A*). c-f) Raman spectra of a complex mixture of salthydrates in the coexistence of ice measured at -190 in sample B2 (*Dol A*).

6.3.2. Fluid inclusions in Dolomite B

Irregular shaped to crystallographic defined inclusions can be found uniformly distributed in the crystals of *Dol B*. Typically the inclusions are smaller than 10 µm (Fig. 6.11.). The inclusions contain aqueous liquid and vapour at room temperature. The volume fraction of vapour is between 6 to 11%.

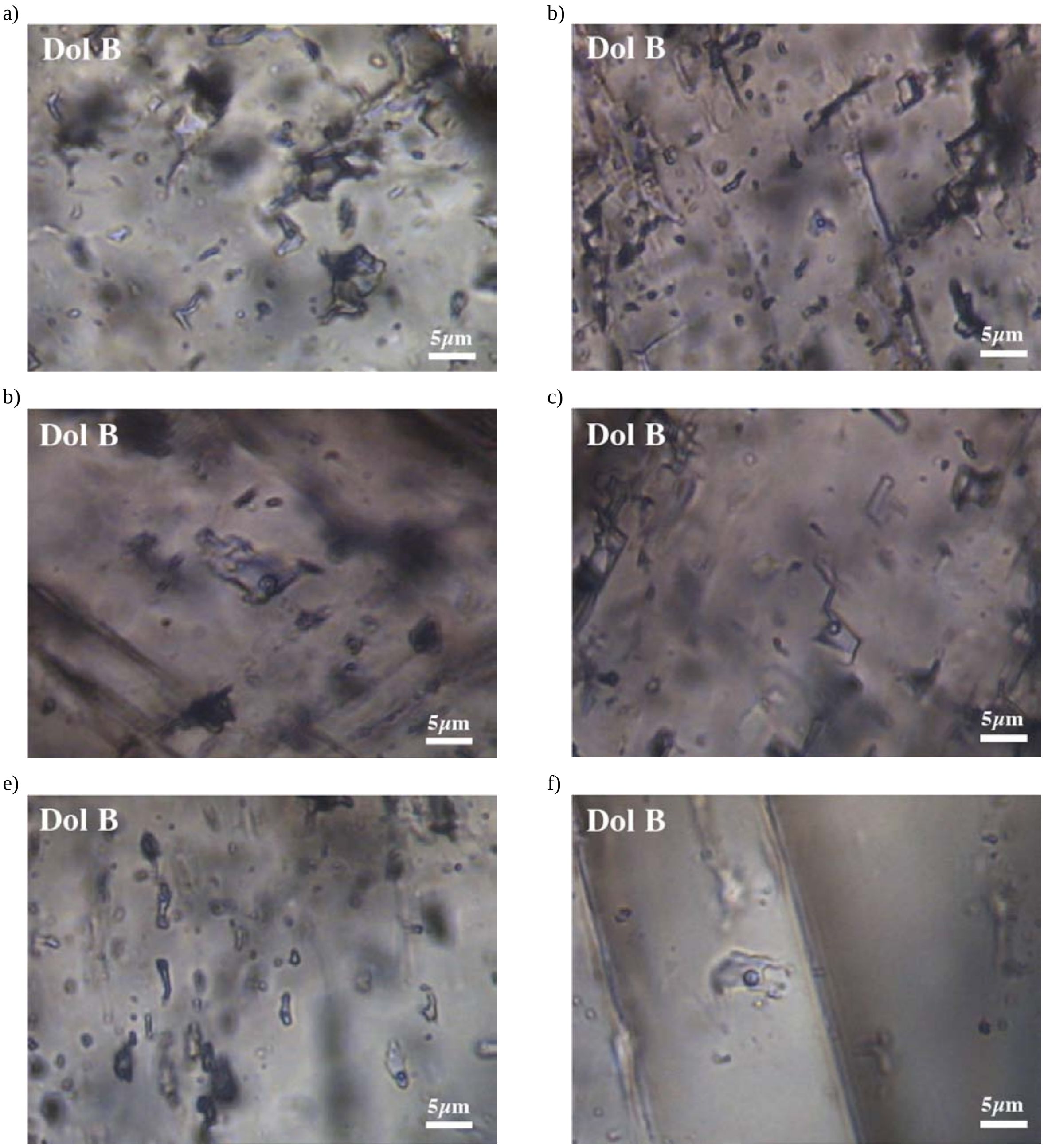

Fig. 6.11. a-b) Fluid inclusions in *Dol B* observed in sample B1. c-d) Fluid inclusions in *Dol B* observed in sample B2. e-f) Fluid inclusions in *Dol B* observed in sample B5

Complex phase assemblages are observed during cooling those inclusions. The precipitated phases cannot be distinguished by optical means. Raman spectra taken at -190 °C reveal the presence of ice (Raman bands at about 3092 and 3214 cm^{-1}) and a mixture of salthydrates (Fig. 6.12). Similar to inclusions from *Dol A*, hydrohalite may precipitate (Raman bands at about 3403, 3420, 3434 and 3532 cm^{-1}; see Fig. 6.12a) at low temperatures. Main peak positions at about 3389, 3404 and 3429 belong to the OH stretching modes of antarcticite (Fig. 6.12a). In addition, a variety of Raman bands occur (see Fig. 6.12). Peak overlapping complicates the assignment of the Raman bands to specific salt hydrates. It is assumed that the Raman bands belong to MgCl$_2$-hydrate or probably to CaCl$_2$-hydrate modifications (e.g. α-CaCl$_2$·4H$_2$O). An accurate identification of the hydrate(s) was not performed because of the lack of reference spectra.

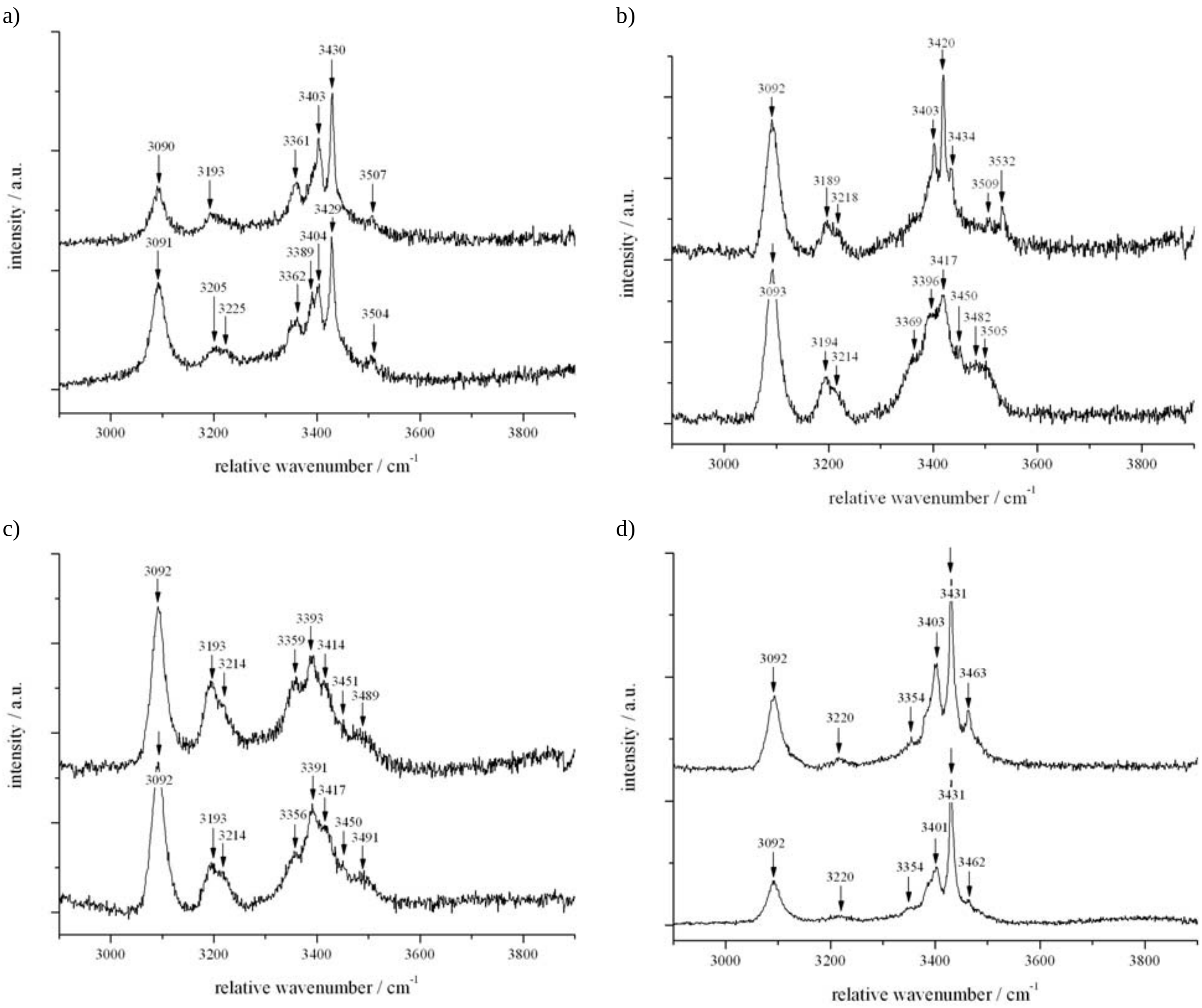

Fig. 6.12. Raman spectra of ice and a complex mixture of salt hydrates at -190 °C, measured in *Dol B* in a) sample B1 b-c) sample B2 and d) Sample B5.

6.3.3. Homogenisation Temperatures

Microthermometric measurements of the homogenisation temperature are performed on fluid inclusions from the different samples (see Fig. 6.13). Homogenisation of inclusions in *Dol A* is only observable in sample B1, whereas in the other samples the fluid inclusions are too small for optical investigations. The homogenisation temperatures of inclusions from *Dol A* are observed between 94 to 117 °C (mode 108 °C). Inclusions from *Dol B* homogenise between 91 to 110 °C (mode 109 °C) in sample B1, between 73 to 150 °C (mode 89 °C) in sample B2 and between 101 to 162 °C (mode 145 °C) in sample B5. Homogenisation occurs into the liquid phase for all inclusions.

Inclusions from sample B1 and B2 correspond to the dolomites observed by Grimmer (2000), who located homogenisation temperatures generally at higher temperatures: *Dol A* inclusions homogenise between 77 and 227 °C and *Dol B* between 75 and 236 °C. Gasparrini (2003) defined homogenisation temperatures for inclusions in *Dol A* between 100 and 140 °C (mode 130 and 140 °C) and in *Dol B* between 100 and 150 °C (mode 110 and 130 °C). Those observed values are in agreement with results obtained in this study.

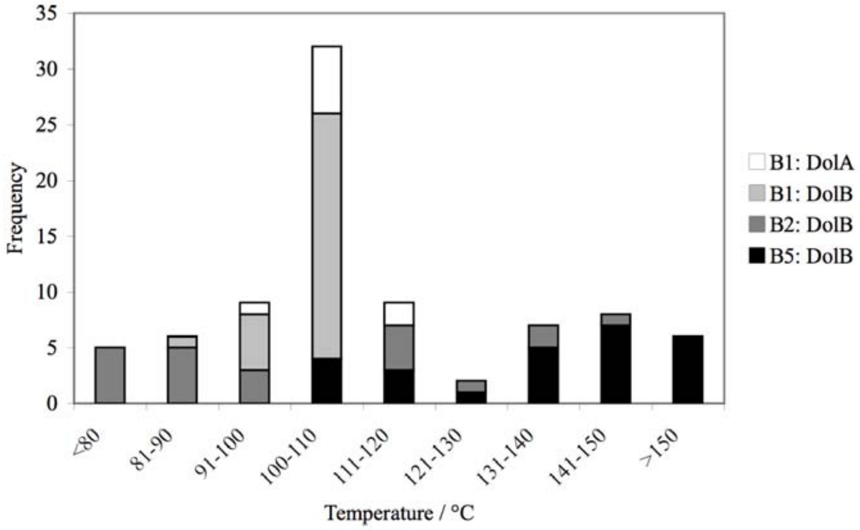

Fig. 6.13. Frequency of homogenisation temperatures, obtained from inclusions corresponding to dolomites of the Barcaliente Formation.

6.4. Dolomites of the Valdeteja Formation

In general, two different types of dolomites (*Dol A* and *Dol B*) can be distinguished in the sample from the Valdeteja Formation (similar to dolomites of the Barcaliente Formation). *Dol A* occur relatively fine crystallised and is defined as a replacive dolomite (Fig. 6.14a), whereas *Dol B* is coarse grained and occur as pore filling dolomite (Fig. 6.14b). Fluid inclusions are only studied in Dol B. The inclusion shape range from ellipsoidal, rectangular to irregular shaped forms (Fig. 6.15) The inclusions are uniformly distributed in the crystals and are up to 10 µm in size. They contain liquid and vapour (volume fraction of 8 to 16 %) at room temperature.

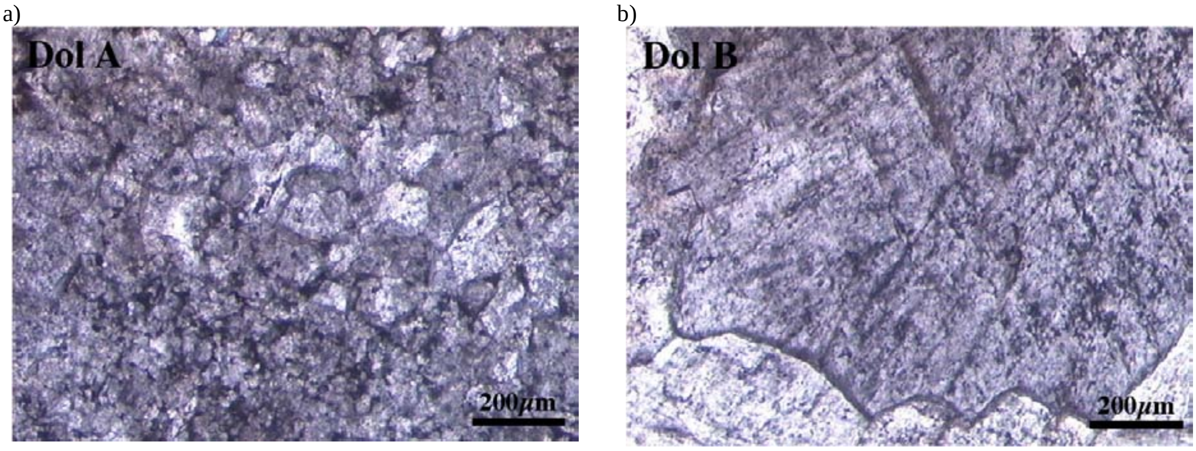

Fig. 6.14. Thin sections images (crossed nicols) of a) *Dol A*, b) *Dol B* (sample V2).

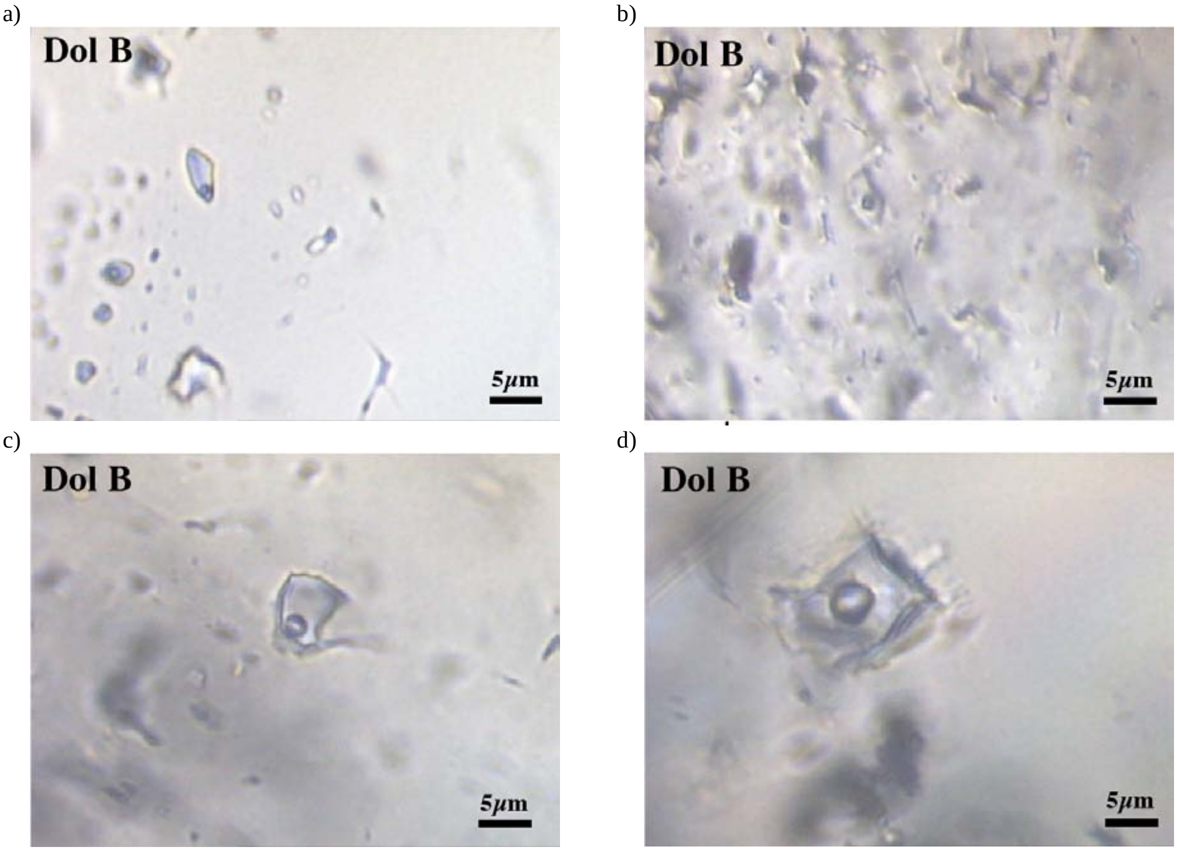

Fig. 6. 15. Fluid inclusions in *Dol B* observed in sample V2.

Complex phase assemblages are observed during cooling those inclusions (Fig. 6.16). The presence of ice is confirmed by the occurrence of Raman bands at about 3090 and 3214 cm^{-1} (at 190°C) in those inclusions. Additionally, various Raman bands occur (see Fig. 6.16), which can be allocated to hydrohalite (Raman bands at about 3403, 3420, 3434 and 3536 cm^{-1}) and to most probably antarcticite (Raman bands at about 3402 and 3428 cm^{-1}). However, some of the Raman bands cannot be assigned to a specific salthydrate. It is assumed that the Raman bands belong to $MgCl_2$-hydrate or probably to $CaCl_2$-hydrate modifications (e.g. α-$CaCl_2 \cdot 4H_2O$). Final melting of an unknown hydrate phase is observed at about -40 °C. Ice melting occurs as about -26 °C. Hydrohalite is the last phase to melt and dissolves at about -7 °C.

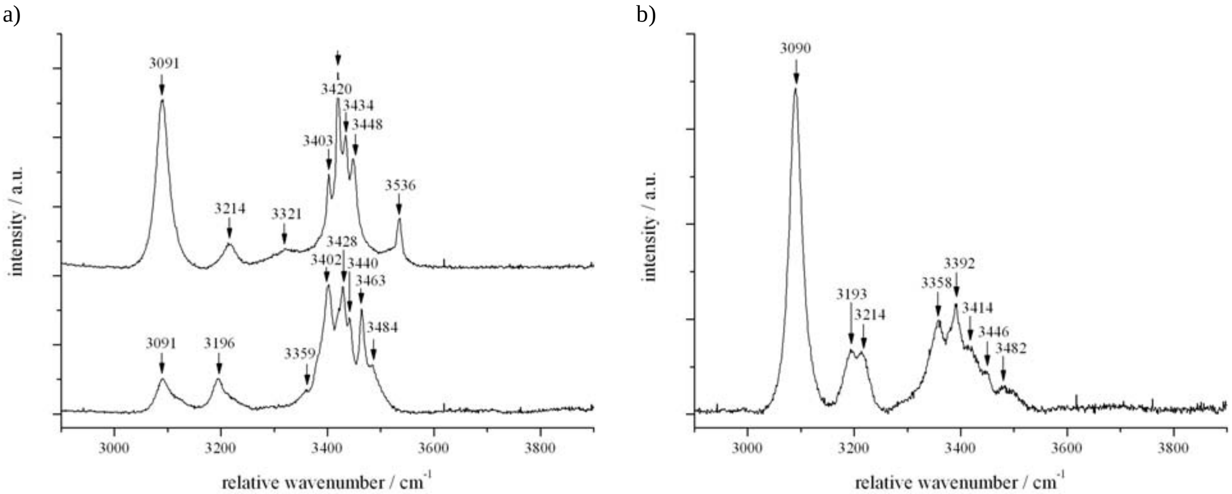

Fig. 6.16. Raman spectra of ice and a complex mixture of salt hydrates at -190 °C, measured in *Dol B* in sample V2.

6.5. Crush Leach Analysis

Crush-leach in combination with ion chromatography is a destructive method for analysing the chemical compositions of aqueous solutions released from fluid inclusions (see e.g. Roedder, 1984, Banks and Yardley, 1992). The method was used to determine the bulk composition of the inclusions.

The different types of dolomites (*Dol A* and *Dol B*) were separated (1 g) from sample B2, B5 and V2 and crushed under water (5 ml). The resulted solutions (fluid from inclusions plus leach water) were analysed by ion chromatography (DIONEX DX-500; DIONEX DX-120). *Dol A* and *Dol B* could not be separated accurately in sample B1, therefore the given values is an average concentration. The major anions and cations in the fluid are Mg^{2+}, Ca^{2+}, Na^+, K^+ and Cl^-. The full data set of crush leach analysis is given in Table 6.2. Bulk solutions should have a charge balance (CB), i.e. the number of positively charged ions should be equal with the number of negative charged ions. Shepherd (1985) suggested the calculation off the charge balance as follows:

$$\frac{\sum_c Z_c (C_c / A_c)}{\sum_a Z_a (C_a / A_a)} \qquad (6.1)$$

where *Z* is the number of charge of the individual cations (*c*) and anions (*a*), *C* is the concentration of the component and *A* the atomic mass. The overall balance should be 1, if the solution is balanced. A deviation of more than 0.3 indicates erroneous analyses (Shepherd, 1985). The calculation of the charge balance, with the results given in Table 6.2, shows an excess of positive charges in the leachate. Shepherd (1985) postulated the most likely causes by neglecting certain ions like e.g. HCO_3^-, Fe^{2+}, Al^{3+} in the analysis or by contamination from the host mineral. It is assumed, that the high amounts of Ca^{2+} and Mg^{2+} in leachate were affected by contamination of the host mineral (dolomite). In addition, HCO_3^- concentrations were not determined.

Tab. 6.2. Results of crush leach analysis (µg|l). CB is the charge balance (see text). bdl (below detection limit).

Sample	Dolomite	Li^+	Na^+	K^+	Mg^{2+}	Ca^{2+}	F^-	Cl^-	Br^-	I^-	NO_3^-	SO_4^{2-}	CB
B1	Dol AB	20.4	19077	18712	35513	32866	50	138281	2408	0.8	951	694	1.23
B2	Dol A	5.1	6715	2482	23954	13753	42	25249	239	0.5	624	1516	3.13
B2	Dol B	8.9	13801	3803	24392	15024	31	44790	297	0.7	962	1898	2.11
B5	Dol A	5.1	6883	2411	22961	11597	65	35233	504	0.6	430	414	2.17
B5	Dol B	15.4	14741	6264	26492	16438	108	78005	1050	0.8	264	836	1.37
V2	Dol A	21.8	20303	5552	31977	15141	39	58160	374	1.0	bdl	1069	2.12
V2	Dol B	21.9	20406	6015	27600	16410	36	79143	885	0.9	197	4560	1.44

Nevertheless, the ratio of certain cations can be used for direct comparison of the different dolomites and with results obtained by Gasparrini (2003). The cationic ratio relative to Na^+, are given in Table 6.2. In general the $Ca^{2+/}Na^+$ and the Mg^{2+}/Na^{2+} ratios are higher in dolomites of the Barcaliente Formation compared to dolomites of the Valdeteja Formation, whereas the K^-/Na^+ ratio is similar (except sample B1). Crush leach analysis of *Dol A* from Gasparrini (2003) values the cationic ratios of K^+/Na^+, Ca^{2+}/Na^+ and Mg^{2+}/Na^+ at 0.28, 0.83 and 2.03, respectively. The K^+/Na^+ ratio corresponds to the results of this study. Generally, the $Ca^{2+/}Na^+$ ratio is found at higher values in this study, whereas the Mg^{2+}/Na^+ is observed at lower values.

Table 6.3. Cationic ratios (relative to Na^+) from crush leach analysis.

Sample	Dolomite	K^+/Na^+	Ca^{2+}/Na^+	Mg^{2+}/Na^+
B1	Dol A and Dol B	0.98	1.72	1.86
B2	Dol A	0.37	2.05	3.57
B2	Dol B	0.28	1.09	1.77
B5	Dol A	0.35	1.68	3.34
B5	Dol B	0.42	1.12	1.80
V2	Dol A	0.27	0.75	1.57
V2	Dol B	0.29	0.80	1.35
Gasparrini (2003)	Dol B	0.28	0.83	2.03

6.6. Comparison with further studies

Grimmer (2000) classified the inclusions from the Barcaliente Formation (*Dol B*) as highly saline inclusions. He determined final melting temperatures between -30.7 and -9.7. Phase equilibria at low temperature are not discussed. By the use of Raman spectroscopy ice and hydrohalite was identified at low temperatures (Grimmer, 2000).

Gasparrini (2003) observed ice melting temperatures between -32 and -37 °C (mode value -40 °C) for inclusions in *Dol A*. Melting of ice in inclusions from *Dol A* was observed at similar temperatures (about -38 °C) in this study. In addition, hydrohalite melting was observed at about -23 °C (last phase to melt). Ice melting in *Dol B* was observed between -27 and -40 °C (mode value -34 °C) by Gasparrini (2003). This study reveal ice melting temperature (*Dol B*) at about -26 °C, i.e. in general at higher temperatures than observed by Gasparrini (2003). In addition, hydrate (unknown phase) melting was observed at about -40 °C, whereas final melting occurs at about -7 °C (hydrohalite melting).

Gasparrini (2003) presented Raman spectra of ice and complex hydrate mixtures at low temperatures. Main peak positions were located at about 3096 (ice), 3199-3205, 3220-3223 (ice), 3355-3367, 3396-3397, 3424-3426, 3451-3453 and 3505-3510 cm^{-1} at -190 °C. In general, those peaks are located at slightly higher wavenumbers but are comparable with results from this study (see Tab. 6.4). In addition, peaks at about 3400, 3428, 3446, 3463, 3482, 3531 cm^{-1} were identified in this study. Some of the peaks belong to hydrohalite and antarcticite. Nevertheless, still large number of peak positions (see Tab. 6.4) cannot be allocated to a specific hydrate phase due to the lack of reference spectra.

6.4. Comparison of main peak positions ($\Delta\nu$ in cm^{-1}) of ice-salt hydrate mixtures obtained from Gasparrini (2003) at -170°C with results from this study obtained at -190 °C.

This study	Gasparrini (2003)	Phase
3089-3093	3096	ice
3189-3205	3199-3205	unknown
3213-3225	3320-3223	ice
3354-3369	3355-3367	unknown
3386-3396	3396-3397	antarcticite
3400-3404	-	hydrohalite, antarcticite
3414-3421	3424-3426	hydrohalite
3428-3435	-	hydrohalite, antarcticite
3446-3452	3451-3453	unknown
3463	-	unknown
3482-3491	-	unknown
3502-3509	3505-3510	unknown
3531-3536	-	hydrohalite

6.7. Conclusions

The freezing behaviour of the inclusions from the different dolomite types is very complex. Hydrate nucleation is quite often inhibited in the inclusions and subsequential heating is necessary to induce precipitation. Additionally, the freezing behaviour is often not reproducible. Raman spectra taken from phase assemblages at -190 °C reveal the complex phase equilibria at low temperatures. Ice, hydrohalite and antarcticite can be identified in those inclusions by their characteristic Raman bands. Nevertheless, various Raman bands occur, which belong to other hydrate phases. The allocation to specific hydrate phases is not performable. The OH stretching modes of the specific hydrates occur in a relatively small wavenumber range and the discrimination between peaks is difficult due to peak overlapping. Additionally, the Raman bands may belong to hydrate phases (e.g. $MgCl_2{}^{\cdot}8H_2O$), where no reference Raman spectra are available now. Gasparrini (2003) showed very similar Raman spectra of salt mixtures. Those peaks fit with the results obtained in this study. Some additional peaks are allocated in this study. Due to crush leach analysis the composition of the fluid is determined. The main components are Ca^{2+}, Mg^{2+}, Na^{+}, K^{+} and Cl^{-}. Therefore it is assumed that the precipitated phases belong to $CaCl_2.nH_2O$, $MgCl_2.nH_2O$ or probably $CaCl_2MgCl_2.nH_2O$ modifications.

7. DISCUSSION

7.1. Phase equilibria at low temperature and Raman spectroscopy

Eutectic temperatures are normally used to define the salt system in natural fluid inclusions. The assumption for this application is the presence of stable phase assemblages and reliable data of phase relationships. Hydrate nucleation is often inhibited in inclusions as shown in this study. Therefore no eutectic melting occurs. Recrystallisation processes of ice or hydrate may be misinterpreted as eutectic reaction, specially, in low or high saline inclusions, where the volume fraction of ice or hydrates is relatively high. Small amounts of brine may be still present and thereby those systems are not representing a stable phase assemblage at low temperatures. If eutectic melting occurs, it is still difficult to obtain the temperature of first liquid produced. The temperature of first optically visible liquid may not reflect to eutectic (first) melting. Recrystallisation processes or simply poor microscopical resolution may lead to misinterpretation of eutectic processes. The eutectic points of multiple salt systems may occur in a relatively small temperature range (e.g. binary $CaCl_2$-H_2O -49.8 °C and ternary $CaCl_2$-KCl-H_2O -50.5 °C; Borisenko, 1977) and therefore accurate melting temperatures are necessary to avoid wrong interpretations of the salt compositions. Moreover, multiple salt systems complicate the investigation of reaction points (eutectic and peritectic reactions), due to the occurrence of various salt hydrates and still unavailable solubility data. Borisenko (1977) suggests the determination of eutectic temperatures by determining thawing temperatures. This presupposes subsequent heating and freezing of inclusions and the presumption of stable phase nucleation. As shown in this thesis, freezing of inclusions in the different salt systems generally leads to metastable phase assemblage. Stable phase relationships (e.g. binary NaCl-H_2O system) are only observed seldom compared to metastable ones. Melting occurs in general in a stable state and therefore, final melting temperatures of ice and salt hydrates are still reliable indicators of the salinity of those inclusions and can be used for salinity estimations. Raman spectroscopy is used to overcome the difficulties in identifying stable or metastable phase assemblages. The presence of brine, ice and salt hydrates in the inclusions can be verified by specific Raman bands, which occur in the stretching region of water (2900 to 3900 cm^{-1}). In addition, Raman spectroscopy is used to identify phase changes in inclusions, e.g. melting of hydrates or phase transitions, which cannot be identified by purely optical means.

H_2O System

Raman spectroscopy can be used to identify aqueous solutions in fluid inclusions. The most informative region of the Raman spectrum of water is the “stretching”[1] region between 2900 and 3900 cm^{-1} (e.g. Walrafen, 1962). This region shows a broad undulating elevated signal, which is a complex profile of overlapping bands. These bands can be defined according to a variety of theoretical vibrational modes such as unperturbed-, symmetric-, antisymmetric-, bending-vibrations and overtones. The presence of an aqueous solution in an inclusion can be confirmed by the occurrence of the typical “water hill”.

In addition, the presence of H_2O in fluid inclusions can be identified by the presence of ice at low temperature. Investigation on synthetic fluid inclusions containing pure water, show a delay in the nucleation of ice during

---

[1] The vibration modes of a water molecule, i.e. a nonlinear triatomic molecule, are always composites of simultaneous stretching and bending of bonds.

cooling. A supercooled liquid is stable to about -40 °C (see also Bakker, 2004). After freezing, ice is in equilibrium with vapour between -190 and 0°C. Ice is characterised by Raman spectroscopy by two main peaks, which are located at about 3090 and 3218 cm^{-1} at -190 ° C. Dubessy et al. (1982) centre those peaks at about 3090, 3150 and 3320 cm^{-1}. The second peak is located at much higher wavenumbers in this study (at about 3218 cm^{-1}). Due to Gaussian-Lorentzian analysis, the spectrum of ice can be deconvolved into six contributions. Bakker (2004) centres the main peak positions of ice at 3005, 3102, 3225, 3255, 3338 and 3414, by the use of deconvolution analysis. The values obtained form Gaussian-Lorentzian analysis in this study differ partly from the values given by Bakker (2004). Three peaks are located at comparable positions (i.e. at 3000, 3090 and 3408 cm^{-1}). The shift two lower wavenumber is caused due to use of an improved calibration method used in this study. The three additional peaks differ from the values given by Bakker (2004) and are centred at 3125, 3215 and 3310 cm^{-1}.

NaCl-H_2O System

Ice and hydrohalite represent a stable phase assemblage at low temperatures in synthesised fluid inclusions containing a dissolved NaCl content below the eutectic composition. Metastability is observed during initial freezing. A delay in precipitation is observed, whereas in general the initial freezing is lowered with increasing salinity. After the inclusions are frozen, ice and hydrohalite are the stable modifications in the temperature range between -190 and -23 °C. In theory, first melt occurs at the eutectic point at -21.1 °C (e.g. Linke 1965). In synthetic inclusions, first melt (eutectic liquid) is already generated at about -23 °C (see Fig. 5.2; Chapter 5). The eutectic reaction occurs in a temperature range of about 2°C in inclusions and is not defined by a specific temperature. Nevertheless, final melting of hydrohalite occurs at about -21.1 °C, at the theoretic eutectic (*X1* in Fig. 7.1). Therefore, the eutectic point in fluid inclusions is better defined by the disappearance of a phase than rather by the generation of first melt. Metastable eutectic melting, as described by e.g. Roedder (1984), was not observed in the inclusions. Ice is the last phase to melt in the inclusions and the melting temperature (*X2* in Fig. 7.1) is directly related to the amount of dissolved NaCl.

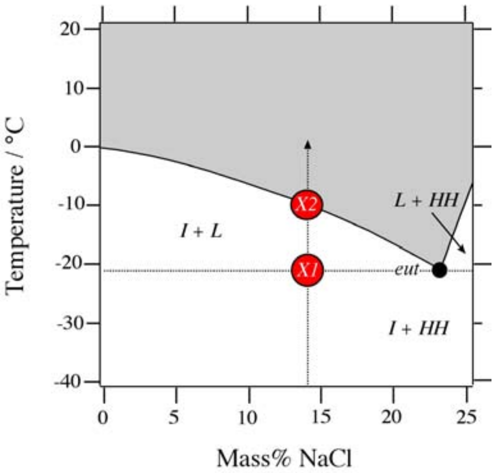

Fig. 7.1. Phase diagram of NaCl-H_2O (constructed after data given by Linke (1965)). The arrow marks the path of an 14 mass% NaCl-H_2O frozen inclusion during heating. First melt occur at *X1*, whereas hydrohalite dissolves. Ice and NaCl-rich brine is stable at temperatures above -21.1 °C. The ice melting temperature (*X2*) is directly related to the salinity of the inclusion. L=Liquid; I=ice; HH=hydrohalite; eut=eutectic.

Hydrohalite is identified by specific Raman bands, which occur in the OH stretching region. It is possible to identify hydrohalite in frozen inclusions with a low salt content of about 4.5 mass% NaCl. Previous Raman studies on frozen aqueous NaCl containing solutions reveal peak positions for hydrohalite at 3089, 3209, 3406, 3422, 3438 and 3536 cm^{-1} at -170 °C (Dubessy et al., 1982) and at 3403, 3420, 3435 and 3536 cm^{-1} at 175 to 185 °C (Samson and Walker, 2000). The first two peaks at 3089 and 3209 cm^{-1} observed by Dubessy et al. (1982) are in good agreement with values observed for pure ice (at about 3091, 3218 cm^{-1}). Therefore, those peaks most probably belong to the Raman bands of ice. In this study Measurements on single hydrohalite crystals were performable in the synthetic fluid inclusions, which centre those peaks at higher wavenumbers (at 3299 and 3320 cm^{-1}). Bakker (2004) defined five peak positions for hydrohalite at 3326, 3407, 3424, 3439 and 3539 cm^{-1} by analysing the spectra with Gaussian Lorentzian contributions. Those peaks are centred at higher wavenumbers compared to the results in this study. Due to improved calibration procedures, these values are shifted about 6 cm^{-1} to lower wavenumber in this study. The low intensity peak at 3299 cm^{-1} is not described in the article of Bakker (2004), Dubessy et al. (1982) and Samson and Walker (2000).

$CaCl_2$-H_2O System

Various freezing and melting behaviours are observed in synthetic fluid inclusions depending on the salinity. A variety of phase transitions and metastabilities occur within the inclusions during microthermometrical experiments. The experiments reveal, that metastable phase assemblages and transitions occur more often than stable conditions in inclusions containing a H_2O-$CaCl_2$ fluid mixture.

At relative low salinities, i.e. lower than the eutectic composition, ice and brine reflect a metastable phase assemblage below the eutectic temperature. Consequently, the brine is highly oversaturated in $CaCl_2$ at -190 °C. Different behaviour is observed in inclusions with eutectic composition: Nucleation of both ice and antarcticite is inhibited even down to -190 °C. Therefore a liquid phase may be present at extreme low temperatures (c.f. H_2O-$MgCl_2$ brines in Bakker, 2004) in inclusions and in small pores. Only in rarely cases (experiment 045), ice nucleation is observed. The lack of the stable presence of antarcticite at low temperatures in inclusions from experiments 021, leads to a variety of metastable behaviour. Repression of antarcticite nucleation in high saline inclusions may result in the formation of other $CaCl_2$ hydrates such as γ-tetrahydrate and sinjarite (see Chapter 5.1). These phases have distinctively different Raman spectra compared to antarcticite and α-tetrahydrate (see Chapter 5.4). The identification of the hydrates was obtained from the metastable extensions of the liquidus, given by equations 4.4 and 4.6 (see Chapter 4.2) and the observed temperature of phase transitions in the inclusions.

The γ-tetrahydrate and an undersaturated brine may represent a metastable phase assemblage down to -190 °C. It melts at about 11 °C in a bulk fluid composition of about 50 mass% $CaCl_2$ (X in Fig. 7.2a). Antarcticite was not produced after melting of the γ-tetrahydrate, therefore the phase assemblage altered into another metastability, i.e. only an undercooled brine. Secondly, the presence of sinjarite was also inferred from the metastable extensions of the liquidus (Y in Fig. 7.2b). Theoretically, the stability of sinjarite is limited within 60.63 to 86.06 mass% $CaCl_2$ bulk composition. However, at 50 mass% $CaCl_2$ the metastable extended liquidus of sinjarite occurs at the observed phase transition temperature between -29 and -25 °C. Most likely sinjarite is present with brine at -190 °C, but also a co-existence with γ-tetrahydrate cannot be excluded. Brine and the poorly crystallised γ-tetrahydrate are not easily to distinguish by the use of Raman spectroscopy, even in the presence of a hydrate (sinjarite), which shows intense and complex vibrational modes. After melting of sinjarite, α-tetrahydrate is produced instead of a brine along the metastable liquidus, whereas antarcticite remains metastable absent. Theoretically, antarcticite/brine or α-tetrahydrate/antarcticite represents a stable phase assemblage in this temperature range. It can be concluded that the system move from a "strongly" metastable arrangement (sinjarite) into a "lesser" metastable one (α-tetrahydrate). The presence of sinjarite is extended to a temperature range between -190 to about -30 °C.

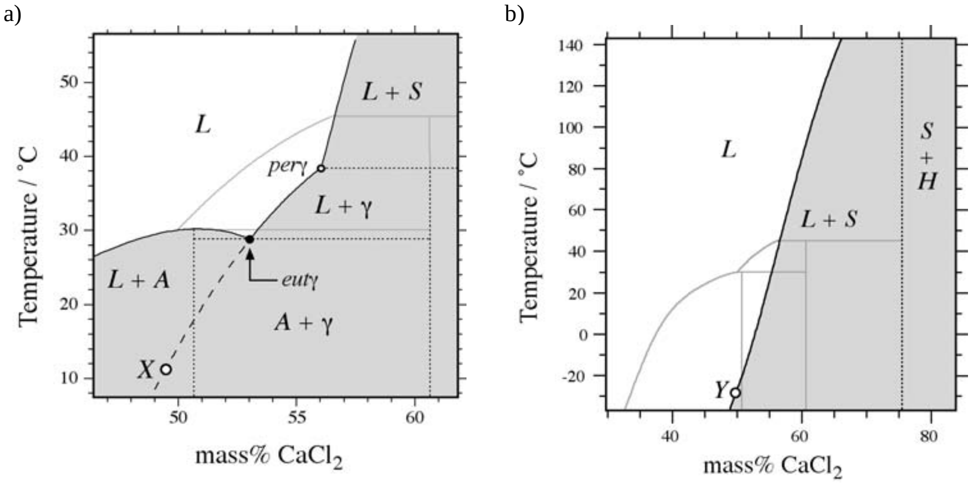

Fig. 7.2. Metastable phase relationship in the system $CaCl_2$-H_2O. a) Detail section with γ-tetrahydrate. The dotted line illustrates the metastable extensions of the liquidus, which intersect with the observed melting temperature of γ-tetrahydrate (*X*). b) Detail section with sinjarite. The metastable extensions of the liquidus intersect the temperature range, where the phase transition sinjarite into α-tetrahydrate was observed (*Y*). Gray lines correspond to the stable phase assemblage illustrated in Fig. 2.6. L=liquid; A=antarcticite; γ=γ-tetrahydrate; S=sinjarite; H=$CaCl_2 \cdot H_2O$; eut=eutectic; per=peritectic.

In H_2O-$CaCl_2$ bearing fluid inclusions, stable phase assemblages occur only close to the final melting temperatures either of ice, antarcticite, or α-tetrahydrate. Therefore, those temperatures can be used to calculate the salinity if the melting phase can be identified. The salinity of the brine in experiment 021 is close to the composition of antarcticite, and therefore small variations in experimental conditions that affect fluid composition may lead to different behaviours. Only small amounts of ice or tetrahydrate are produced at low temperatures and eutectic melting cannot be observed. Therefore, it is not possible to verify the existence of stable and metastable phase assemblages at low temperatures. Typically, these inclusions undergo the peritectic reaction and α-tetrahydrate is formed (see also Schiffries, 1990). From the data of Linke (1958) the peritectic reaction is anticipated at 30.1 °C. However, it occurs in a temperature interval between 29 and 31 °C in the synthetic fluid inclusions and it may occur slightly prematurely or rather slightly delayed. In few cases antarcticite melts just below the peritectic temperature, which indicate slight variances in salinity in the synthesised inclusions or rather the peritectic reaction is inhibited.

Previous works already illustrate, that $CaCl_2$ containing inclusions are strongly dedicated by metastable processes, i.e. expected phase nucleation is absent and rather metastable phase assemblages are present. Synthetic fluid inclusions containing H_2O-NaCl-$CaCl_2$ (Vanko et al., 1988) have revealed metastable phase behaviour at low temperature, similar to our results with binary H_2O-$CaCl_2$ fluids. Schiffries (1990) has identified antarcticite crystals in liquid-absent natural fluid inclusions from mafic pegmatites (Bushveld) by Raman spectroscopy. Furthermore, halite was identified by optical methods at room temperatures. Theoretically, these inclusions should also contain tetrahydrate, however, metastabilities among the α-, β- and γ-modifications did not allow an unequivocal interpretation of the Raman spectra obtained in the range of 1600 to 1700 cm^{-1}, whereas only antarcticite was identified in the range of 2800 to 3800 cm^{-1}. Samson and Walker (2000) prepared standard solutions of H_2O-NaCl-$CaCl_2$ fluids to obtain reference Raman spectra of hydrates at low temperatures in dependence of the NaCl/$CaCl_2$ mass ratio. In contrast to our synthetic fluid inclusions samples, antarcticite crystallised in those solutions below the eutectic composition (20 mass% $CaCl_2$). Our experimental work has illustrated that antarcticite only nucleates in highly saline inclusions.

Raman spectra of antarcticite gained from the synthesised inclusions, reveal characteristic peak positions at about 3240, 3387, 3402 and 3430 cm^{-1} at -190 °C in the OH stretching region. A previous study on frozen aqueous solutions containing $CaCl_2$, centre the Raman bands of antarcticite at 3090, 3242, 3384, 3401, 3407, 3433, 3448 and 3513 cm^{-1} at -170 °C. (Dubessy et al. 1982), The peak positions centred at 3090 cm^{-1} overlap with the main peak position of ice. Most probably, ice precipitated during the experimental cooling of the aqueous solutions. The four main Raman modes of antarcticite (3240, 3387, 3402 and 3430 cm^{-1}) correlate with the values given by Dubessy et al. (1992). Small variances in positions may be caused to the difference in temperature. Measurements in this study are taken at -190 °C, whereas the spectrum in the previous study correspond to a temperature of -170 °C. The occurrence of additional Raman bands at 3242 and 3513 cm^{-1} (Dubessy et al., 1982) could not be confirmed in this study. Nevertheless, the four main peaks are the characteristic ones and are sufficient for mineralogical identification of the hydrate. Samson and Walker (2000) confirmed the values given in this study. They obtained three main peak positions for antarcticite at 3386, 3406 and 3432 cm^{-1} at temperatures between -175 and -185 °C. Raman spectra of $CaCl_2$-hydrate modifications, i.e. α-tetrahydrate, γ-tetrahydrate and sinjarite, are not described in previous studies.

$MgCl_2$-H_2O System

Different behaviour in crystallisation may occur in synthetic inclusions in the $MgCl_2$-H_2O system during cooling. Stable as well as metastable phase equilibria are observed in inclusions with $MgCl_2$ content less than the eutectic composition (arrow *1* in Fig. 7.3). Inclusions may nucleate ice during cooling, which is metastable present with a supersaturated brine at low temperatures. The stable phase assemblage is represented by the crystallisation of ice and $MgCl_2 \cdot 12H_2O$. Such inclusions undergo eutectic melting at about -33 °C during heating (*X1* arrow *1* in Fig. 7.3). Ice melting occurs in both scenarios in a stable state at about -23 °C and is therefore a reliable indicator for the salinity (*X2* arrow *1* in Fig. 7.3).

Inclusions close to the eutectic composition (arrow *2* in Fig. 7.3) generally generate ice and $MgCl_2 \cdot 12H_2O$ during cooling. Both, ice and $MgCl_2 \cdot 12H_2O$ melt in a stable state at the eutectic temperature (*X1* arrow *2* in Fig. 7.3). Inhibition of $MgCl_2 \cdot 12H_2O$ nucleation, results in ice melting at about -40 °C. i.e. below the temperature of eutectic (*X1* arrow *2´* in Fig. 7.3). Salinity calculations based on the metastable extensions of the ice liquidus reveal a salinity of about 22.5 mass% $MgCl_2$, which is higher than obtained from the stable phase assemblage (20.7 mass% $MgCl_2$). As stable as well as metastable equilibria are observed within the same inclusion, the difference is not caused due to variations in salinity. The cause of the different melting behaviour of ice cannot be explained yet. In theory, melting of ice below the eutectic composition would not be expected for binary $MgCl_2$-H_2O inclusions. Observations of such temperatures in natural inclusions would indicate the presence of a different salt system, e.g. $CaCl_2$-H_2O or ternary salt-H_2O system, which are defined by a lower eutectic temperature.

A complete inhibition of nucleation is observed in inclusions containing an aqueous solution with $MgCl_2$ content close to stability of $MgCl_2 \cdot 12H_2O$ (30 mass% $MgCl_2$). A supercooled brine, which is stable down to -190 °C is characteristic for those inclusions (arrow *3* in Fig. 7.3).

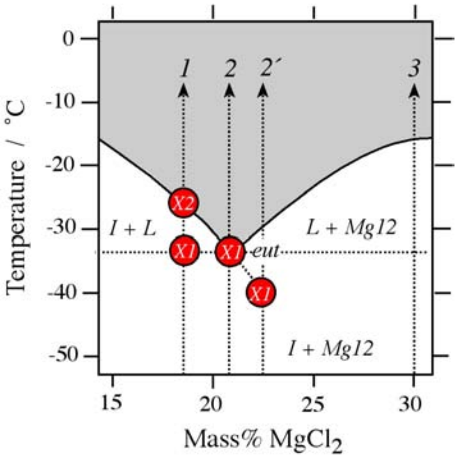

Fig. 7.3. Phase diagram of $MgCl_2$-H_2O constructed after data given by Linke (1965). The arrows marks the different path of melting behaviour observed in fluid inclusions depending on the salt content. The X mark reaction points (see text). L=Liquid; I=ice; Mg12=$MgCl_2.12H_2O$; eut=eutectic

Studies on synthetic fluid inclusions with a composition of 20.2 mass% $MgCl_2$ in the aqueous solutions was performed by Bakker (2004). He confirms the inhibition of $MgCl_2 \cdot 12H_2O$ nucleation during rapid cooling of inclusions. The inclusions only precipitated $MgCl_2 \cdot 12H_2O$ by initial slow cooling. This study reveals, that initial slow cooling does not always result in hydrate precipitation. Inclusions with metastable phase assemblages, consisting of ice and brine, were still found after slow cooling. More often hydrate precipitation was observed during subsequent heating and cooling of inclusions after the nucleation of ice. The eutectic point observed at -32.8 (±0.2) correlate with values given in literature (e.g. -33.0 °C given by Spencer et al., 1990; -33.1 °C; given by Bakker, 2004).

Dubessy et al. (1982) centred the main Raman bands at 3091, 3110, 3328, 3401, 3426, 3462, 3483 and 3511 cm^{-1} (at -170 °C). The peaks at low relative wavenumbers (at about 3091, 3218 cm^{-1}) probably belong to ice. Nevertheless, the peak positions at higher wavenumbers are in good correlation with the observed values given in this study (c.f. 3322, 3397, 3428, 3459, 3479 and 3512 cm^{-1}). Small variances are may caused to the difference in measurement conditions, i.e. temperature. The occurrence of the Raman band at about 3252 cm^{-1} is not described in previous studies. An additional peak is observed in this study at about 3191 cm^{-1}. Bakker (2004) confirm the presence of the Raman band (3199 cm^{-1}) by study synthetic fluid inclusions in quartz. Furthermore, he centred main peak positions at 3324, 3404, 3437, 3465, 3483 and 3517 cm^{-1}. Those peaks are centred at higher values due to the use of a different calibration method.

$FeCl_2$-H_2O System

In general, inclusions containing a $FeCl_2$-rich solution below the eutectic composition nucleate ice during cooling. This metastable phase assemblage (ice and brine) is characteristic for those inclusions at low temperatures. Stable phase assemblages occur above the eutectic temperature close to the final melting of ice (*X1* arrow *1* and *3* in Fig. 7.4). In rarely cases, stable phase assemblages were observed in inclusions containing about 15 mass% $FeCl_2$ in the solution. $FeCl_2 \cdot 6H_2O$ nucleates and is in equilibrium with ice between -190 and -33 °C. Eutectic melting occurs delayed at about -33 °C (*X1* arrow *2* in Fig. 7.4), compared to the value given in literature (-36.5 °C). Ice always melts in a stable state (*X2* arrow *2* in Fig. 7.4).

Hydrate nucleation is completely inhibited in inclusions with a salinity at about 11 mass% and a salinity about 20 mass% $FeCl_2$. As the variances in salinities are less than 5 mass%, the different behaviour is not yet allegeable.

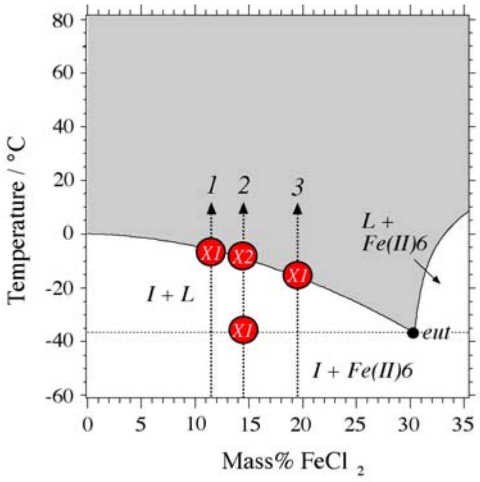

Fig. 7.4. Phase diagram of $FeCl_2$-H_2O costructed after data given by Linke (1958) and Kirgincev et al. (1972). The arrows marks the different path of melting behaviour observed in fluid inclusions depending on the salt content. The X mark reaction points (see text). L=liquid; I=ice; Fe(II)6=$FeCl_2.6H_2O$; eut=eutectic.

Investigations on synthetic NaCl-$FeCl_2$-rich inclusions performed by Baldassaro (1998) confirm the metastable behaviour of fluid inclusions during freezing, i.e. ice nucleation in the presence of a metastable brine. Hydrate precipitation was not observed in the study. As indicated in Chapter 2.2.5, the presence of $FeCl_2$-hydrates in fluid inclusions in generally interpreted from the observation of phase reactions. Direct qualitative analysis, for the verification of the stability $FeCl_2 \cdot nH_2O$ hydrates in natural fluid inclusions are still missing in literature.

The crystallisation of $FeCl_2 \cdot 6H_2O$ in the synthesised inclusions was verified by the use of Raman spectroscopy. Four Raman bands centred at about 3372, 3390, 3411 and 3426 cm^{-1} reveal the presence a hydrate phase. Due to the observed eutectic temperature, those bands can be assigned to the vibrational modes of $FeCl_2 \cdot 6H_2O$.

$FeCl_3$-H_2O System

$FeCl_3$-H_2O inclusions (composition below the eutectic) reveal highly metastable phase equilibria at low temperatures. Ice nucleates in the presence of a brine and the absence of a hydrate phase. The phase assemblage (ice and brine) is present between -190 °C and the final ice melting temperature (*X* in Fig. 7.5). The eutectic reaction is not observable, due to the absence of stable phase equilibria (inhibition of hydrate nucleation). In frozen aqueous solutions (Dubessy et al. 1982), the Raman spectrum of $FeCl_3 \cdot 6H_2O$ consists of three main bands at 3321, 3421 and 3533 cm^{-1} at -170 °C. Due to the lack of hydrate precipitation, those results cannot be confirmed in this study.

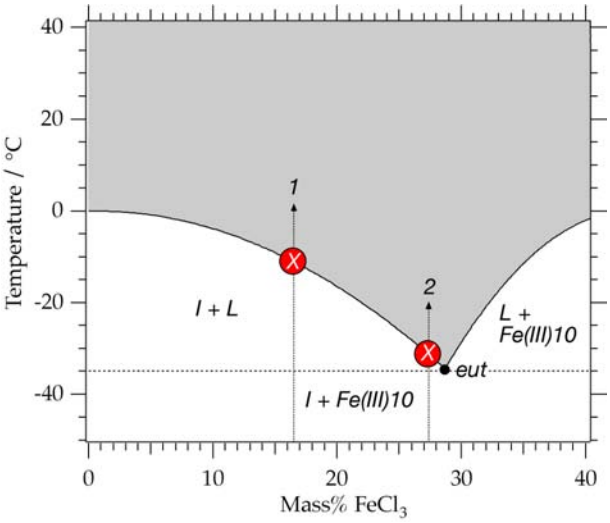

Fig. 7.5. Phase diagram of $FeCl_3$-H_2O costructed after data given by Linke (1958). The arrows marks the different path of melting behaviour observed in fluid inclusions depending on the salt content. The *X* marks the final ice melting.L=liquid; I=ice; Fe(II))10=$FeCl_3 \cdot 10H_20$; eut=eutectic;

LiCl-H_2O System

Low salinity inclusions (about 10 mass% LiCl) have metastable phase assemblages at low temperature. Ice and a LiCl-rich brine is present and the expected hydrate nucleation is inhibited in the inclusions. Inclusions near to the eutectic composition (25 mass% LiCl) only rarely freeze and reveal typically a highly metastable brine at -190 °C. Ice melting (*X* in Fig. 7.6) occurs in a stable state in the inclusions and the temperature reveals the salinity of the inclusions. As described in Chapter 5.1.8, crystallisation of an unknown phase may occur in partly healed fractures. The Raman spectrum of $LiCl \cdot 5H_2O$ displays a broad band at about 3430 cm^{-1} (Dubessy et al., 1992), that belongs to a poorly crystalline phase. Raman spectra of the unknown phase reveal vibrational modes in the OH-stretching region at about 3359 and 3376 cm^{-1} at -190. Those peaks are sharp and well defined and do not correspond to the obtained spectra presented by Dubessy et al. 1992. Due to the occurrence of Raman bands in the stretching region, it is assumed that the precipitated phase corresponds to a LiCl-hydrate phase. A clear identification of the phase is not performable due to the observation of different melting temperatures. As the highest melting temperature is observed above 100 °C, the phase probably belong to $LiCl \cdot 2H_2O$ or $LiCl \cdot H_2O$.

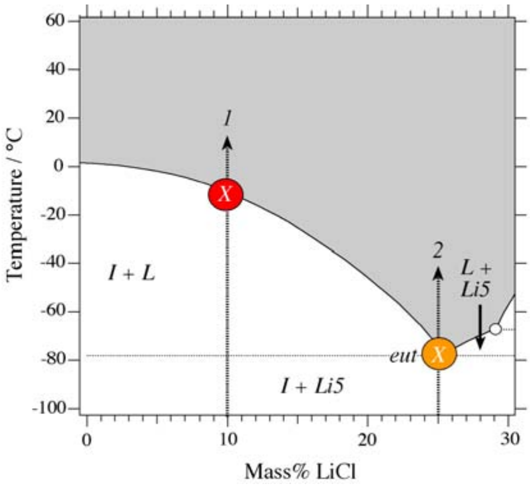

Fig. 7.6. Phase diagram of LiCl-H_2O constructed after data given by Yanatieva (1934) and Pátek and Klomfar (2006). The arrows marks the different path of melting behaviour observed in fluid inclusions depending of the salt content. The X mark the final ice melting. L=liquid; I=ice; Li5=$LiCl \cdot 5H_20$; eut=eutectic;

$ZnCl_2$-H_2O System

$ZnCl_2$-H_2O inclusions reveal highly metastable phase equilibrium at low temperatures. Ice nucleates in the presence of a metastable brine in the inclusions. The eutectic reaction is not observable, due to the absence of stable phase equilibria, i.e. absence of hydrates. Ice and brine are in equilibrium between -190 °C and the final ice melting temperature (*X* in arrow *1*,*2* and *3* in Fig. 7.7). With increasing salinity, freezing of inclusions is more inhibited. Inclusions with a salinity of about 38 mass% $ZnCl_2$ seldomly freeze. Those inclusions are generally characterised by supercooled brine at low temperatures.

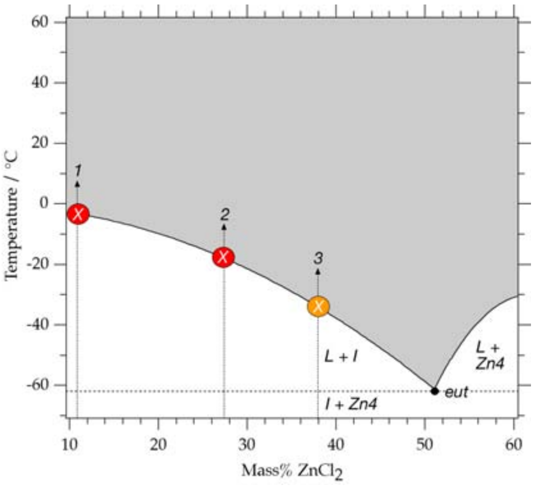

Fig. 7.7. Phase diagram of $ZnCl_2$-H_2O constructed after data given by Linke (1965) and Kirginzec et al. (1972). The arrows marks the different path of melting behaviour observed in fluid inclusions depending of the salt content. The *X* mark the final ice melting. L=liquid; I=ice; Zn4=$ZnCl_2.4H_2O$; eut=eutectic.

NaCl-$CaCl_2$-H_2O System

The synthesised inclusions in the ternary NaCl-$CaCl_2$-H_2O system reveal strongly metastable phase equilibria at low temperatures. Due to the absence of antarcticite nucleation, the ternary eutectic is not observed. Inclusions with an intended salt ratio of 1/1 (12 mass% NaCl and 12 mass% $CaCl_2$; experiment 006) react to two different phase equilibria.

> (1) Ice nucleation occurs in the absence of hydrate precipitation. Final melting is observed at about -34 °C, whereas this melting temperature does not correspond to stable thermodynamic properties with this salt content. The observed melting temperature reveal a much higher salinity than the inclusions really contain. Ice melts in a metastable state and the melting temperature is therefore not indicative for the salinity. However, the metastable extensions of the isotherm intersect the cotectic at the salt ratio 1/1 (*X* in Fig. 7.8a), corresponding to a salinity of about 13 mass% NaCl and 15 mass% $CaCl_2$.
>
> (2) Ice and hydrohalite (in the presence of brine) represent the second metastable phase assemblage in those inclusions. Ice melting occurs at about -28 °C, i.e. at much higher temperature than observed in (1) (*X1* in Fig. 7.8b). Final melting (*X2* in Fig. 7.8b) occurs with the dissolution of hydrohalite at -0.1 °C (respectively at -4.6; see Chapter 5. 2) in those inclusions. Salinity calculations based on those temperatures reveal the true composition of the inclusions, with a salt ratio of 0.8/1 (final melting -0.1) and 0.9/1 (final melting -4.6) NaCl/$CaCl_2$, respectively, i.e. close to the intended salinity ratio.

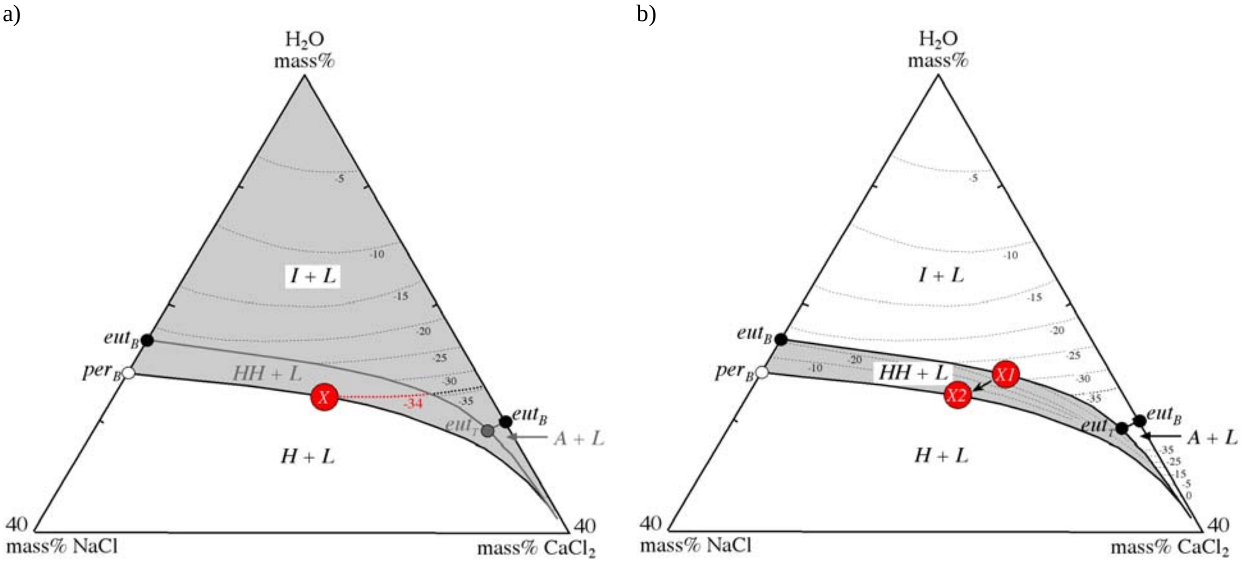

Fig. 7. 8. Melting path of inclusions from experiment 006. The diagram of the phase relationships in the ternary NaCl-CaCl$_2$-H$_2$O system is modified after Shepherd et al. (1985). See text for details. L=liquid; I=ice; HH=hydrohalite; A=antarcticite; eut$_T$=ternary eutectic; eut$_B$=binary eutectic; per$_B$=binary peritectic.

Inclusions with an intended salt ratio of 1/2 (10 mass% NaCl and 20 mass% CaCl$_2$; experiment 024) are characterised by three different metastable phase equilibria.

(1) Nucleation may be completely inhibited in those inclusions and only supercooled brine is present at low temperatures.

(2) Hydrohalite precipitate in the absence of ice and antarcticite. A phase transition from hydrohalite into halite occur in a temperature range between -12 and 6 °C. The transition is observed in a temperature interval and may occur metastable at temperature above 0°C. After final melting (halite melting at about 170 °C), halite is metastable absent in the inclusions.

(3) Ice and hydrohalite in the absence of antarcticite nucleate during cooling those inclusions. Ice melts at about -42 °C (*X1* in Fig. 7.9). Hydrohalite react to halite at temperatures above 0 °C (metastable) (*X2* in Fig 7.9). Again, after final melting of halite between 160 and 180 °C (*X3* in Fig. 7.9), halite is metastable absent in the inclusions.

Halite melting at temperatures between 160 and 180 °C indicate, that the inclusions may reveal a higher salinity as prearranged. 12 mass% NaCl and 27 mass% CaCl$_2$ can be derived from the phase diagram (see Fig. 7.9). The inclusions are therefore characterised by oversaturated brine at room temperature. As the reactions in those inclusions are highly metastable, the salinity of the inclusion can be assessed from the melting temperatures, whereas eutectic processes are absent.

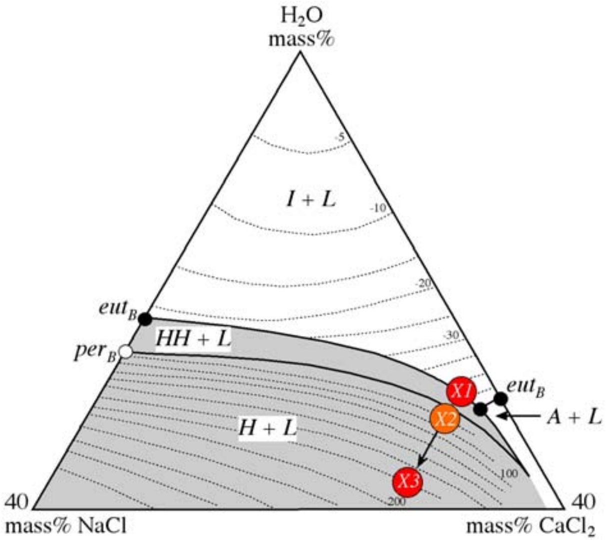

Fig. 7.9. Melting path of inclusions from experiment 024. The diagram of the phase relationships in the ternary NaCl-$CaCl_2$-H_2O system is modified after Williams-Jones and Samson (1990). See text for details. L=liquid; I=ice; HH=hydrohalite; A=antarcticite; eut$_T$=ternary eutectic; eut$_B$=binary eutectic; per$_B$=binary peritectic.

Davis et al. (1990) reported phase equilibria in experimental inclusion in halite. Metastable eutectic melting at approximately -52 °C was observed for inclusions with relatively low salinities. Those inclusions are characterised by a phase assemblage of halite, antarcticite and ice at low temperatures. In high saline inclusions, eutectic melting was observed at lower temperatures. Davis et al. (1990) interpreted the lowered eutectic melting with the presence of metastable $CaCl_2$-hydrate modification ($CaCl_2 \cdot 4H_2O$). Schiffries (1990) reported the presence of $CaCl_2$-hydrate ($CaCl_2 \cdot 4H_2O$ modification) in liquid absent aqueous natural inclusions in quartz from the Bushveld Complex. The subsolidus assemblage in those inclusions is reported to consist of antarcticite, a not specified $CaCl_2 \cdot 4H_2O$ modification and halite. Vanko et al. (1988) reported of metastable phase equilibria in high saline inclusions. Antarcticite is failed to nucleate is those inclusions and a $CaCl_2$-rich brine is present at low temperatures. Hydrohalite melting is reported to occur metastable, i.e. several degrees above cero (see also Zwart and Touret 1994). The hydrate may persist metastable to temperatures above the expected equilibrium (e.g. Roedder, 1984; Vanko et al., 1988). Samson and Walker (2000) investigated frozen aqueous solution in the ternary NaCl-$CaCl_2$-H_2O system by Raman spectroscopy. They identified hydrohalite and antarcticite as well as mixtures of both solids in Raman spectra and compared them with spectra taken from natural inclusions. The Raman bands of those two hydrates partly overlap. In addition, the relative orientation of the hydrate crystal to the incident Raman laser beam has an important effect on the intensity of individual Raman peaks (see Bakker, 2004), and these variable intensities may have an important effect on the morphology (the visibility of peaks) of Raman spectra of mixtures of hydrohalite ad antarcticite.

The nucleation of a stable phase equilibria including ice, hydrohalite and antarcticite could not be observed in this study. The nucleation of $CaCl_2$-hydrates in ternary system is in general inhibited. $CaCl_2$-hydrate nucleation is observed to be absent in the synthesised inclusions. Zwart and Touret (1994) reported of the inhibition of $CaCl_2$-hydrate nucleation in inclusions in the ternary NaCl-$CaCl_2$-H_2O system. $CaCl_2$ is reported to be concentrated in the brine at low temperatures. A phase transition from hydrohalite into halite is described by Zwart and Touret (1994), which is also observed in high saline inclusions in this study.

NaCl-$MgCl_2$-H_2O System

The ternary NaCl-$MgCl_2$-H_2O system is characterised by stable as well as metastable phase equilibria at low temperatures depending on the intended salinity.

Inclusions with an intended salt ratio of 1/1.3 NaCl-$MgCl_2$ (10 mass% NaCl and 13 mass% $CaCl_2$, experiment 033) react to a metastable phase assemblage during cooling. Ice and hydrohalite precipitate in the absence of $MgCl_2{\cdot}12H_2O$. The total amount of $MgCl_2$ is dissolved in the aqueous liquid phase, which remains present to -190 °C. Stable phase equilibria occur above the ternary eutectic temperature (-35.2). Hydrohalite melting (*X1* in Fig. 7.10) as well as ice melting (*X2* in Fig. 7.10) occur in a stable state and the observed temperatures are reliable parameter for salinity calculations.

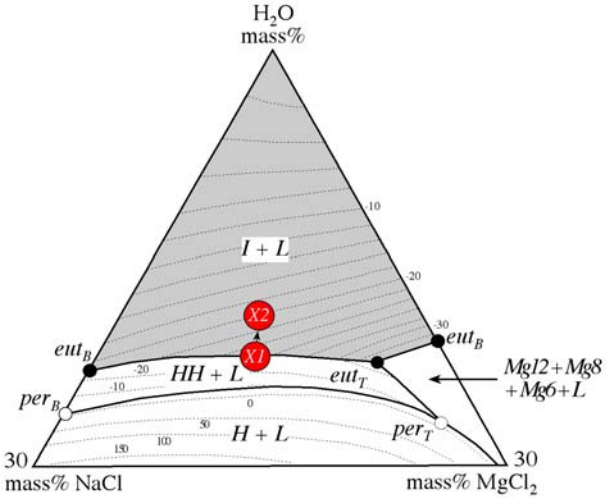

Fig. 7.10. Melting path of inclusions from experiment 024. The diagram of the phase relationships in the ternary NaCl-$MgCl_2$-H_2O system is modified after Borisenko (1977). See text for details. I=ice; L=liquid; HH=hydrohalite; Mg12=$MgCl_2{\cdot}12H_2O$; Mg8=$MgCl_2{\cdot}8H_2O$; Mg6=$MgCl_2{\cdot}6H_2O$; eut_T=ternary eutectic; per_T=ternary peritectic; eut_B=binary eutectic; per_B=binary peritectic.

Inclusions with a salt ratio of 1/12 NaCl/$MgCl_2$ (2 mass% NaCl and 24 mass% $MgCl_2$; experiment 035) reveal both stable as well as metastable phase equilibria at low temperatures.

(1) The metastable phase equilibrium is characterised by ice precipitation in the absence of hydrate nucleation. The total amount of salt is dissolved in the aqueous liquid, which is present in a metastable state down to -190 °C. The melting temperature of ice is observed at about -26 °C. With the knowledge of the intended salt ratio, the salinity can be estimated from the phase diagram. The dotted line in Figure 7.11a represents the composition of the intended fluid. It intersect the isotherm at -26 °C (final ice melting temperature; *X1* in Fig. 7.11a) at a composition of about 1.4 mass% NaCl and 17.7 mass% $MgCl_2$.

(2) The stable phase equilibrium is characterised by the stability of $MgCl_2{\cdot}12H_2O$, hydrohalite and ice below -36 °C. The ternary eutectic is observed at about -35.6 °C, whereas $MgCl_2.12H_2O$ and hydrohalite dissolves (*X1* in Fig. 7.11b). Final melting is observed at about -26 °C, by the melting of ice. Salinity estimations corresponding to the eutectic and ice melting reveal about 5.2 mass% NaCl and 16.4 mass% $MgCl_2$. This salinity differs from the intended and from the salinity estimation shown in (1). The real salt ratio in the inclusions is about 1/3.2 NaCl/$MgCl_2$.

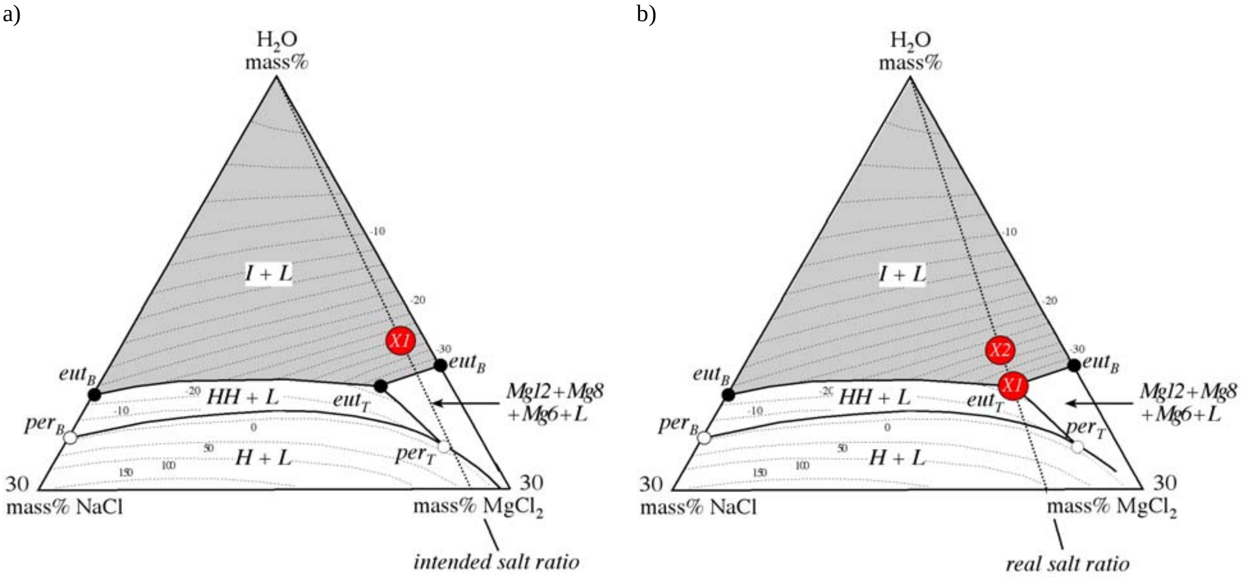

Fig. 7.11. Melting path of inclusions from experiment 035. The diagram of the phase relationships in the ternary NaCl-$MgCl_2$-H_2O system is modified after Borisenko (1977). See text for details. I=ice; L=liquid; HH=hydrohalite; Mg12=$MgCl_2 \cdot 12H_2O$; Mg8=$MgCl_2 \cdot 8H_2O$; Mg6=$MgCl_2 \cdot 6H_2O$; eut_T=ternary eutectic; per_T=ternary peritectic; eut_B=binary eutectic; per_B=binary peritectic.

Inclusions with a salt ratio of 1/1.3 NaCl/$MgCl_2$ (experiment 038; intended salinity 10 mass% NaCl and 13 mass% $CaCl_2$) reveal highly metastable phase relationships at low temperature.

(1) Ice and an oversaturated brine represent the phase assemblage at low temperatures. Final melting in the inclusions is observed at -39.9 °C, i.e. at temperatures lower than the ternary eutectic (-35.2 °C). Therefore, ice melts in a metastable state and the melting temperature is not indicative for the salinity.

. (2) A second, metastable phase equilibrium is observed by the presence of hydrohalite and ice at low temperatures. The total amount of $MgCl_2$ is dissolved in the brine. Ice and hydrohalite melt metastably at about -39 °C (*X1* on the metastable extensions on the cotectic; Fig. 7.12) and at about -33 °C (*X2* on the metastable extensions of the isotherm; Fig. 7.12), respectively. Salinity estimations are not executable because the system reacts highly metastable.

Rarely inclusions reveal a phase assemblage consisting of ice, probably hydrohalite and $MgCl_2.nH_2O$. First melt process was observed between -60 and -50 °C. It is not convenient if the melting correspond to a (metastable) eutectic or peritectic reaction, because the presence of hydrohalite or halite below –60 °C could not be confirmed. The presence of halite in the inclusion was optically not provable. After initial melting, ice and hydrohalite are present, whereas both melt during further heating in a metastably state as described in (2). Metastable eutectic melting at about -55 °C among the phases halite $MgCl_2.8H_2O$ and ice is described by Davis et al. (1990).

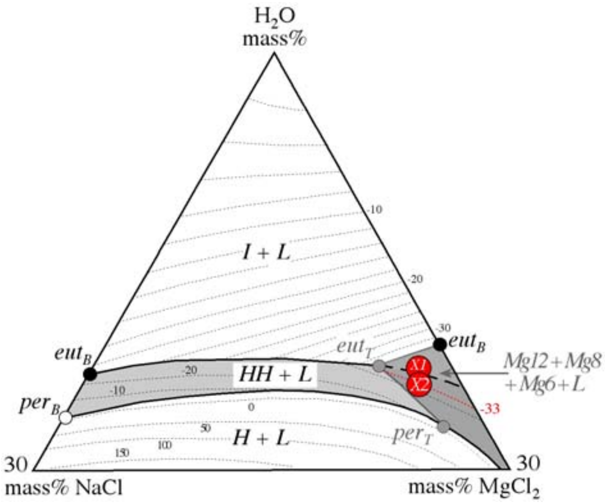

Fig. 7.12. Melting path of inclusions from experiment 038. The diagram of the phase relationships in the ternary NaCl-$CaCl_2$-H_2O system is modified after Borisenko (1977). See text for details. I=ice; L=liquid; HH=hydrohalite; Mg12=$MgCl_2{\cdot}12H_2O$; Mg8=$MgCl_2{\cdot}8H_2O$; Mg6=$MgCl_2{\cdot}6H_2O$; eut_T=ternary eutectic; per_T=ternary peritectic; eut_B=binary eutectic; per_B=binary peritectic.

Davis et al. (1990) observed the melting behaviour in experimentally grown halite crystals in the ternary NaCl-$MgCl_2$-H_2O system. They confirm the presence of stable salt hydrates ($MgCl_2.12H_2O$ and hydrohalite) during freezing. In addition, metastable eutectic melting at temperatures about -80 °C was observed, indicating the presence of metastable salt hydrates (presumably $MgCl_2.8H_2O$ and $MgCl_2.6H_2O$).

$CaCl_2$-$MgCl_2$-H_2O System

Inclusions in the ternary $CaCl_2$-$MgCl_2$-H_2O system are generally characterised by metastable phase assemblages at low temperatures. Due to the absence of complete solidification, the ternary eutectic could not be observed.

Inclusions with an intended salt ratio of 1/1 $CaCl_2$/$MgCl_2$ (10 mass% $CaCl_2$ and 10 mass% $MgCl_2$; experiment 050) may reveal three different metastable phase equilibria during cooling.

> (1) Ice may be the only solid phase, which precipitate during cooling. A $CaCl_2$-$MgCl_2$-rich brine is present down to -190 °C. Final melting is observed at about -23 °C (*X* in Fig. 7.12a). From the intended salt ratio the salinity can be estimated from the phase diagram. The melting temperature corresponds to the intended salinity.
>
> (2) Antarcticte and ice nucleates in the presence of a $MgCl_2$-rich brine in the inclusions during cooling. The final antarcticite melting was not observed. Ice melts at about -23 °C.
>
> (3) $MgCl_2.12H_2O$ and ice nucleates in the absence of antarcticite. The total amount of $CaCl_2$ remains dissolved in the brine, which is present down to -190 °C. $MgCl_2$-hydrate melting is observed between -40 and -35 °C (*X1* in Fig. 7.12b), whereas ice melts at about -22 °C (*X2* in Fig. 7.12b). The determination of the salinity with the observed melting points reveals a slightly lower content for $CaCl_2$ (7 to 9 mass%) and a slightly higher content for $MgCl_2$ (12 to 13 mass%). As the phase assemblage present a more stable than observed in (1), the approximated salinity is assumed to be the true value.

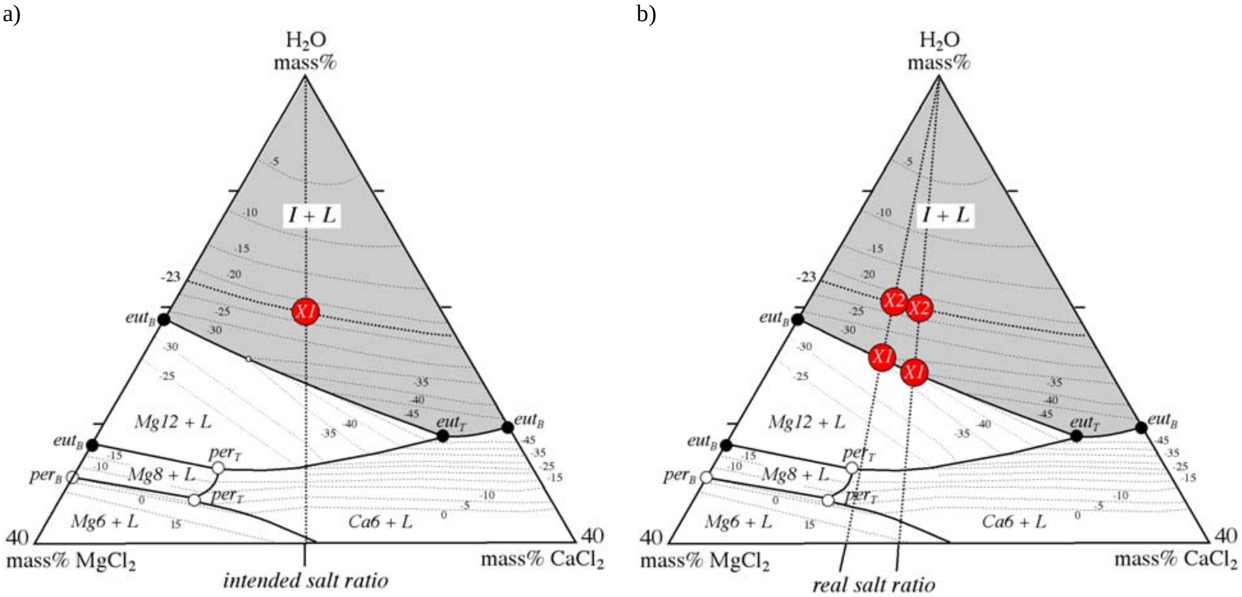

Fig. 7.12. Melting path of inclusions from experiment 050. The diagram of the phase relationships in the ternary NaCl-$CaCl_2$-H_2O system is constructed after data given by Yanatieva (1946), Prutton and Tower (1932) and Linke (1958, 1965)). See text for details. L=liquid; I=ice; Mg12=$MgCl_2 \cdot 12H_2O$; Mg8=$MgCl_2 \cdot 8H_2O$; Mg6=$MgCl_2 \cdot 6H_2O$; Ca6=$CaCl_2 \cdot 6H_2O$; eut_B=binary eutectic; eut_T=ternary eutectic; per_B=binary peritectic; per_T=ternary peritectic.

7.2. Synthesis of fluid inclusions

Salinities calculated from observed melting temperatures of solids (i.e. ice or hydrates) in the synthesised inclusions may differ from the intended salinities. As microthermometry offers reliable data for salinity calculations, the deviation must be caused due to difficulties during sample preparation. Calculated salinities of NaCl containing inclusions are generally in good agreement with the intended salinity. Large deviations are observed if other salts are used in experimentation, e.g.$CaCl_2$. The salts used for synthesis, e.g. $CaCl_2$ and $MgCl_2$, are highly hygroscopic and thereby the initial mass can be affected by adsorption of H_2O. This explains the generation of inclusions with lower salinities as expected from the synthesis. Higher salt amounts are probably caused due to the welding of the gold capsules used for synthesis. The filled tubes were partly immersed into cold water during the welding to prevent heating of the capsule and thereby evaporation of the solution. Within some experiments the cooling was not efficient enough and during the welding process, water may have escaped. Thereby the salt content in the solution increased. Evaporation of H_2O explains the presence of an oversaturated brine at room temperature (solid phases are present at room temperature) and completely failed experiments, where no inclusions were formed (absence of fluid.)

7.3. Salinity estimation using the OH stretching bands of water and Polarisation effects

Deconvolution of H_2O spectra

Multiple Gaussian-Lorentzian functions can be used to deconvolve the composite H_2O spectrum. However, many possibilities for fitting this “stretching” region are published in the literature: five deconvolved Gaussian components are defined by e.g. Carey and Korenowski (1998), Furić et al. (2000), Li et al. (2004), and Chumaevskii et al. (2001); four components are defined by e.g. Rull (2002); and three components are defined by e.g. Gopalakrishnan et al. (2005). Therefore, the spectral analyses of the "stretching" region are far from straightforward.

The contour of the Raman spectrum can be described by purely geometrical properties, such as amplitude (intensity), area, and slope (first derivate) in a wavenumber vs. intensity diagram (e.g. Mernagh and Wilde, 1989; Furić et al., 2000). Bakker (2004) recommends a purely geometrical fit of the Raman water spectrum with three Gaussian-Lorentzian contributions. This approach is an unambiguous procedure for fitting spectra and allows a relative easy comparison of peak positions and changes in spectrum morphology among aqueous solutions of different salinities or aqueous solutions of different temperatures. Analysis of Raman spectra from pure water inclusions, centre the main peak positions at 3222, 3433, 3617 cm^{-1}, which correspond to the values given by Bakker (2004).

Normalisation of Raman spectra and the use of ratios

Spectra obtained on different objects of similar material can be compared on the basis of band position and intensity. The intensity of the Raman signal depends on a variety of factors, such as the instrumental setup, surface irregularities, material densities, crystal orientation, volume of matter, and the inherent Raman scattering cross-section. However, for identical materials, the relative wavenumber position of peaks remains approximately constant. Because fluid inclusions are detected below the surface of the host, a change in depth results in a change in intensity of the Raman signal. In order to compare visually the Raman spectra among a series of fluid inclusions, the spectra have, therefore, to be normalised. Subsequently, the normalised spectra can be used to analyse salinity effects and properties of the host crystal that may influence the morphology of the spectra. For the analysis of peak positions and amplitude ratios, this normalisation is not required. In contrast, fluids that are directly measured in standard solutions with the same apparatus do not need to be normalised. Those spectra reveal directly both intensity and wavenumber shifts as a result of a variable salinity (see Fig. 5.88).

Three purely geometrical methods have been proposed in literature to analyse the Raman spectra of aqueous solutions at room temperatures: 1. Skewing parameter (Mernagh and Wilde 1989); 2. Raman difference spectroscopy (Furić et al., 2000; Dubessy et al., 2002); 3. Deconvolution (Bakker 2004). The method of Mernagh and Wilde (1989) does not require normalisation of the obtained spectra, because it is based on ratios of the geometrically defined properties of individual spectra (Fig. 7.13a). The skewing parameter is relatively easy to obtain from raw spectra, i.e. directly obtained from the instrument. The accuracy of the salinity calculation based on this method is about 3 mass% and it was tested for the binary H_2O-NaCl fluid system. Normalisation of spectra is required in the method of Dubessy et al. (2002) because the spectrum of the sample has to be compared to a reference spectrum (see Furić et al., 2000). This normalisation is obtained by dividing the intensity at each wavenumber position by the total area of the spectrum in order to obtain one unit area (Fig.

7.13b). Additionally, this method includes the possibility to estimate the type of dissolved salts from “isobestic points”. However, the wavenumber “equivalent” for specific one-component salts may coincide or be within a few cm^{-1} (within the accuracy) of each other, and the “isobestic points” of aqueous solutions with multiple salt components are unknown.

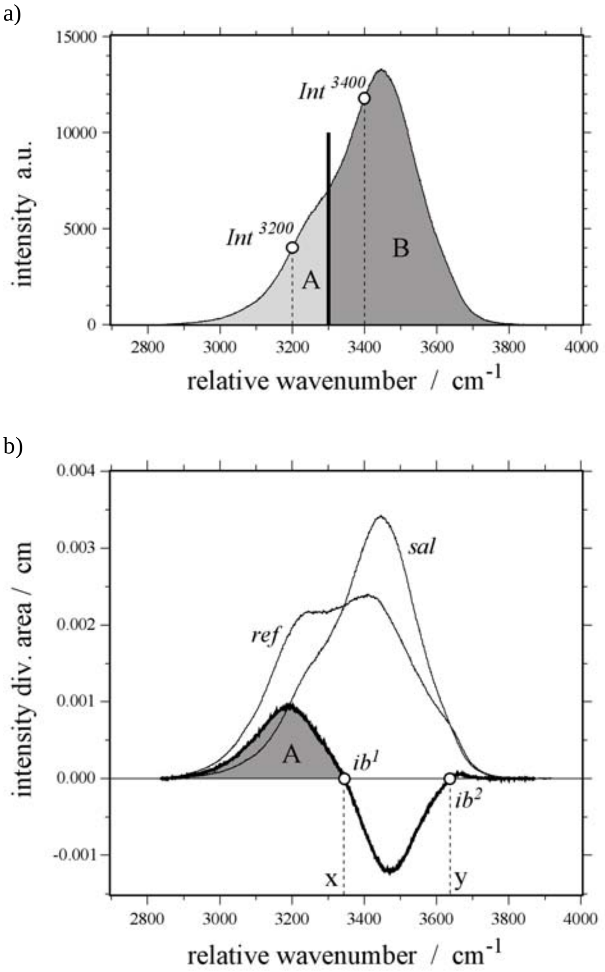

Fig. 7.13. (a) The method described by Mernagh and Wilde (1989), i.e. by dividing the O-H Raman profile into two halves at 3300 cm^{-1} (thick solid vertical line). The ratio of the area *A* (between 2800 and 3300 cm^{-1}) over area *B* (between 3300 and 3800 cm^{-1}) is used to express symmetric and anti-symmetric components of the spectra. The ratio of the intensity at 3200 cm^{-1} (int^{3200}) over intensity at 3400 cm^{-1} (int^{3400}) is used to calculate the cation effect. See Mernagh and Wilde (1989) for further details. (b) The method described by Dubessy et al. (2002) using Raman difference spectroscopy. The *y*-axis represents an “intensity div area” variable, which expresses the normalised values of the spectra (in cm). The normalised spectra of a fluid inclusion (sal) are subtracted from that of the H_2O reference solution (ref). The area *A* of the resulting curve is a measure for the salinity. The “isobestic points” (ib^1 and ib^2) may reveal the type of dissolved salt, corresponding to the wavenumber equivalent *x* and *y* . See Dubessy et al. (2002) for further details.

In this study, the normalisation of maximum intensity was only applied to visualise the changes in morphology of the Raman spectra due to host mineral properties. The deconvolved Raman spectra, according to the method of Bakker (2004), are not normalised for the analysis of peak positions and amplitude ratios. Reference fluids can be directly compared to the analysis of natural fluid inclusions. Similar to the method of Mernagh and Wilde (1989), the method can be applied to raw spectra and is also limited to the binary H_2O-NaCl system.

Birefringence polarisation

The most obvious explanation of variation in the Raman spectra of fluid in inclusions is the effect on the polarisation of the incident laser beam caused by the orientation of the host crystal (see also Dubessy et al., 2002). The Raman spectrum of fluid phases in inclusions is defined not only by the fluid phase itself: the laser light has to cross the host mineral, which causes additional polarisation effects in birefringent minerals.

Mernagh and Wilde (1989) did not consider the optical properties of birefringent materials in their study of salinity effects on the Raman spectrum of aqueous fluids. Consequently, their linear regression with the “skewing parameter” has limited application to the determination of the salinity of natural inclusions in quartz.

Dubessy et al. (2002) suggested to minimise these effects by using a depolarised laser or to orientate an axis of the indicatrix of birefringent host minerals parallel to the spectrometer slit. Our results (Fig. 5.90) have confirmed that Raman spectra that are influenced only by the birefringence of the host mineral are preferably analysed such that the host crystal has its optical axis orientated parallel to the polarisation plane of the laser. Our results also reveal that the lowest value of *Peak1* obtained from the rotation-controlled variation in the spectrum of a fluid inclusion (Fig. 5.90) best matches the *Peak1* in the reference solution. Peak positions of experiment 027 (sample surface is orientated perpendicular to the optical axis) are comparable to those of the reference solution of pure water. The minimum in the periodic function for experiment 029 (sample surface is orientated parallel to the optical axis) approaches the *Peak1* of the reference fluid (see Fig. 5.90a)

Reflection polarisation

Previous studies have paid little attention to polarisation effects of the laser beam due to the orientation of the quartz-fluid interface. The results of this study demonstrate that this factor cannot be ignored in the interpretation of salinities from Raman spectra of aqueous solutions in natural fluid inclusions. Reflection of the incoming light (laser beam) at the quartz-fluid interface induces polarisation effects as well (e.g. Tipler 1991). Figure 5.90 also illustrates that the orientation of the quartz host is a factor in the over-all effect. The rotation angle 0°, 90°, and 180° correspond to three extinction positions of quartz. Therefore, the reflection polarisation is partly coupled to the birefringence polarisation. According to equation 5.27, the wavenumber of *Peak1* measured in a fluid with about 9 mass% NaCl is 3238±1 cm^{-1}. Figure 5.92a illustrates for a natural inclusion of this composition a range in wavenumber values of 3232 to 3244 cm^{-1} that can be derived from the *m*-interface, and a smaller range for the r_4-interface (3231 to 3237 cm^{-1}). Figure 5.88 indicates that in such an inclusion with 9 mass% NaCl wavenumbers can vary between 3232 to 3265 cm^{-1}, depending on the orientation of the host crystal. Therefore, the true salinity of this inclusion could not be directly estimated from the Raman spectrum of the aqueous solution simply by reference to values obtained on standard solutions. Gases dissolved in the aqueous solution have an additional effect on the variety of the Raman stretching band morphology.

Inclusion depth

Quantification of the variation in Raman band morphology due solely to the depth of an inclusion in the quartz host is complicated (Fig. 5.91) by additional polarisation phenomena that may camouflage this effect. However, the results from simulated inclusions (Fig. 5.94) illustrate a correlation between the depth of the inclusion and modifications in the Raman bands. Higher *Peak1* values are obtained from shallow inclusions when compared to deeper inclusions of the same composition, regardless of whether the quartz cover was cut parallel or perpendicular to the *c*-axis. In the experiment in which the cover plate was cut parallel to the c-axis the rotation-induced variation caused by birefringence (Fig. 5.94b) decreases with increasing depth. Consequently, the deeper simulated inclusions reveal *Peak1* values that approach the value of the reference solution, independent of crystal orientation.

Applications for fluid inclusion studies

This study has shown that a large variety of salinities may give Raman spectra with similar band morphologies in the 2800 to 3800 cm^{-1} region. Therefore, the application of Raman spectral analysis to aqueous solutions containing a salt in natural fluid inclusions is still limited. As already indicated by Dubessy et al. (2002), an independent method is necessary to obtain the cation ratios before the salinity of natural inclusions can be determined via Raman spectroscopy. For example, the Raman spectra of salt hydrates in frozen inclusions reveal the major cations dissolved in the aqueous solution (e.g. Dubessy et al. 1982; Bakker 2004).

Microthermometry remains the main tool for analysing the salinity of natural fluid inclusions. Raman spectroscopy may be used to verify microthermometric results or to specify in more detail the analysed phase changes (e.g. Bakker 2004; Gasparrini et al. 2006). Furthermore, inclusions that are too small for optical microthermometric analysis (smaller than 2 μm diameter) can be investigated with Raman spectroscopy. For these inclusions, Raman spectroscopy offers a tool to specify the phases that are present within the inclusions. The aqueous phase can be analysed with Raman spectroscopy to obtain its salinity according to the method.

Natural fluid inclusions may be hosted in birefringent minerals such as quartz. The orientation of the sample and the shape of the inclusion itself will influence the morphology of the Raman band contour. For this reason, the orientation of the host should be controlled during measurements. In optically uniaxial minerals like quartz the best way to operate is to orientate the sample surface perpendicular to the *c*-axis, where birefringence and reflection polarisation do not influence the spectra. Another possibility would be to orientate the sample surface in an extinction position, such that the *c*-axis or *a*-axis is orientated parallel to the laser polarisation plane, to obtain the typical spectrum. The orientation of quartz grains can only be evaluated with Raman spectrometers equipped with an integrated optical microscope that has the option to use crossed polarisers. The orientation of the crystal in natural samples is often very difficult to determine due to the absence of this experimental setup. When the orientation of the host mineral cannot be determined or optimised, the inclusions under analysis have to be rotated through at least 90° and spectra obtained at regular intervals. The spectra must be deconvolved into three bands using Gaussian-Lorentzian functions. The lowest position derived for the first (*Peak1*) of the three bands can be referenced to a Raman calibration curve for salinity of standard solutions. If neither optimal orientation of the sample nor multiple analysis through 90° of rotation is possible, the acquisition of a spectrum of the O-H stretching region in an aqueous solution in a birefringent host will not enable determination of its salinity. Indeed, comparison of such a randomly derived spectrum to spectra of standard solutions will result in erroneous salinity values.

8. CONCLUSIONS

The present study reveals basic fundamental knowledge of phase equilibria in salt-water system. Phase equilibria in synthetic fluid inclusions in quartz have been studied by using pure water, binary salt-H_2O ($NaCl$-H_2O, $CaCl_2$-H_2O, $MgCl_2$-H_2O, $FeCl_2$-H_2O, $FeCl_3$-H_2O, $LiCl$-H_2O, $ZnCl_2$-H_2O) and ternary salt-H_2O ($NaCl$-$CaCl_2$-H_2O, $NaCl$-$MgCl_2$-H_2O, $CaCl_2$-$MgCl_2$-H_2O) inclusions. The nucleation of ice and salthydrates at low temperatures is characteristic for inclusions containing dissolved chlorides in an aqueous solution. Investigations of synthetic fluid inclusions allow the observation of low temperature phase equilibria of known salt-H_2O systems. This study reveals, that the phase relationships observed in fluid inclusions differ from expected theoretical behaviour. Initial freezing of the fluid occurs in general well below the theoretic temperatures. Instead of solidification, a supercooled aqueous solution is occasionally metastable present down to -190 °C. Nucleation occurs typically delayed or is even completely inhibited. Due to metastability, expected phase equilibria are rarely observed. Fluid inclusions may behave highly unpredictably at low temperatures, due to the regular formation of metastable phase assemblages. Consequently, eutectic temperatures of fluid mixtures cannot always be obtained by microthermometric investigations.

This study reveals, that optical investigations are not efficient enough to understand the complexity of phase equilibria at low temperatures. Raman spectroscopy offers the only possibility to identify phases and phase assemblages in fluid inclusions during microthermometrical experiments. The stretching region of water (between 2900 to 3900 cm^{-1}) is the most informative region to identify the phases occurring, i.e. liquid, ice and salt hydrates. Salt hydrates can be distinguished by Raman spectroscopical means due to the occurrence of characteristic vibrational modes in the range between 3000 and 3800 cm^{-1} (stretching region of water) at -190 °C. The present study presents Raman spectra of ice and salt hydrates including $NaCl^{\cdot}2H_2O$ (hydrohalite), $CaCl_2{}^{\cdot}6H_2O$ (antarcticite), α-$CaCl_2{}^{\cdot}4H_2O$, γ-$CaCl_2{}^{\cdot}4H_2O$; $CaCl_2{}^{\cdot}2H_2O$ (sinjarite), $MgCl_2{}^{\cdot}12H_2O$, and $FeCl_2{}^{\cdot}6H_2O$, which nucleated during freezing experiments in the synthesised inclusions. In addition, two spectra of hydrates are gained which could not be identified yet, i.e. most probably $MgCl_2$-hydrate and $LiCl$-hydrate phases. The spectra are generally taken at -190 °C, where the most spectroscopic information can be gained. Those spectra can be used for the identification of salt hydrates, which may occur during cooling of natural inclusions. In addition, phase transitions, e.g. first and final melting, can only be fully understood by Raman spectral identification of the phase. Because eutectic points remain hidden due to metastability, the type of dissolved salt in water can only be identified by analyses of salt hydrate spectra in frozen inclusion. Final melting generally occurred in stable phase assemblages, and the temperatures can be used to calculate salinity if the melting phase can be identified.

A first application for identifying the salt composition natural inclusions by using Raman spectroscopy is shown by the analysis of natural fluid inclusions from dolomites collected from the Valdeteja and Barcaliente in the Cantabrian mountains (NW Spain). Complex Raman spectra of salt hydrates are obtained in those inclusions at low temperatures. Ice, hydrohalite and antarcticite could be clearly identified. Nevertheless, a variety of peaks occur, which could not be allocated to specific salt hydrates. This illustrates that reference data (Raman spectra) are still missing to interpret the phase assemblages and thereby the salt components of natural fluid inclusions.

A new method for the estimation of the salinity of inclusions, by analysing Raman spectra in the stretching region of water at room temperature is introduced in the present study. The Raman spectrum of the solutions (H_2O-NaCl mixtures) can be analysed by deconvolution into three Gaussian-Lorentzian contributions. Pure H_2O has peak positions at 3223 cm^{-1} (*Peak1*), 3433 cm^{-1} (*Peak2*), and 3617 cm^{-1} (*Peak3*). The presence of salt in the aqueous solutions has significant influence on the morphology of the spectra. The (shifted) position of the first peak (*Peak1*) can be used to determine the salinity of the aqueous solution by comparing it with reference spectra taken on standard solutions. In addition, the morphology of the Raman spectrum of an aqueous solution is influenced by the optical properties of the host crystal, by the orientation of the quartz-fluid interface, and by the depth of the inclusion within the sample. These effects are directly related to the polarisation of the laser light. The maximum variation in *Peak1* values for NaCl-bearing aqueous solutions that is defined by all polarisation effects is about 33 cm^{-1}. Due to birefringence, the estimated *Peak1* values of pure H_2O fluid inclusions in quartz can vary between significantly. Polarisation caused by reflection, which depends on the orientation of the quartz-fluid interface, results in a variation of about 14 cm^{-1} relative wavenumbers. Horizontal interfaces reveal a larger polarisation effect than steeper interfaces, independent of the relative orientation of the optical indicatrix of the host mineral. The individual effects of birefringence, interface orientation, and depth of the inclusion below the mineral surface have been evaluated with simulated fluid inclusions, i.e. by drilling a small hole in quartz and covering it with a doubly polished quartz plate of selected thickness and crystallographic orientation. The variation in *Peak1* due to birefringence is smaller for quartz plates cut perpendicular to the *c*-axis than for quartz plates cut parallel to the *c*-axis. The effect of birefringence is reduced with increasing depth.

For natural inclusions, the morphology of the Raman spectra of aqueous solutions is simultaneously modified by all of these effects. The possibility to orientate the optical axis of the quartz crystal parallel to the plane of polarisation of the laser beam results in spectra of aqueous inclusions that have almost the same morphology as spectra of reference solutions of the same composition. Raman equipment that does not offer this possibility can be used to analyse the salinity of aqueous solutions by acquiring multiple spectra throughout at least 90° rotation of the sample and determining the lowest peak position of the deconvolved Gaussian-Lorentzian contributions (*Peak1*).

9. REFERENCES

Ananthaswamy A., Atkinson G. (1982) Thermodynamics of concentrated electrolyte mixtures. I. Activity coefficients in aqueous $NaCl-CaCl_2$ at 25 °C. J. Solution Chem.11, 509-527.

Anderson A. J., Mayanovic R. A., Bajt, S. (1995) Determination of the local structure and speciation of zinc in individual hypersaline fluid inclusions by micro-XAFS. The Can. Mineral. 33, 499-508.

Bakker R. J. (2003) FLUIDS 1: Computer programs for analysis of fluid inclusion data and for modelling bulk fluid properties. Chem. Geol. 194. 3-23.

Bakker R. J. (2004) Raman spectra of fluid and crystal mixtures in the system H_2O, H_2O-NaCl and $H_2O-MgCl_2$ at low temperatures: applications to fluid inclusion research. Can. Mineral. 42, 1283-1314.

Bakker R. J., Baumgartner M., Coquinot Y. (2007) Experimental Raman spectra of salt hydrates in fluid inclusions. ECROFI XIX, Bern, Switzerland, 178.

Baldassaro P. M. (1998) Low temperature phase relations in the system H2O-NaCl- $FeCl_2$. Master Thesis, Virginia Polytechnic Institute and University, Blacksburg, Virginia.

Banks D. A., Yardley B. W. D. (1992) Crush-leach analysis of fluid inclusions in small natural and synthetic samples. Geochim. Cosmochim. Acta. 56, 245-248

Baumgartner M., Bakker R.J., (2008): Raman spectroscopy of pure H_2O and NaCl-H_2O containing synthetic fluid inclusions in quartz – a study of polarization effects. Miner. Petrol. 95, 1-15.

Bodnar R. J. (1993) Revised equation and table for determining the freezing point depression of H_2O-NaCl solutions. Geochim. Cosmochim. Acta 57, 683-684.

Bodnar R. J. (1994) Synthetic fluid inclusions: XII. The system H_2O-NaCl. Experimental determination of the halite liquidus and isochors for a 40 wt% NaCl solution. Geochim. Cosmochim. Acta 58, 1053-1063.

Bodnar R. J., Burnham C. W., Sterner S. M. (1985) Synthetic fluid inclusions in natural quartz. III. Determination of phase equilibrium properties in the system H_2O-NaCl to 1000 °C and 1500 bars. Geochim. Cosmochim. Acta 49, 1861-1873.

Bodnar R. J., Sterner S. M. (1987) Synthetic fluid inclusions. In: G.C. Ulmer, H.L. Barnes (Eds.) Hydrothermal Experimental Techniques. John Wiley & sons. New York. 423-457.

Bodnar R. J., Vityk M. O. (1994) Interpretation of microthermometric data for H_2O-NaCl fluid inclusions. In: de Vivo B., Frezzotti M. L. (Eds.) Fluid inclusions in minerals: Methods and applications. Short Course IMA, 117-130.

Borisenko A. S. (1977) Study of the salt composition of solutions of gas-liquid inclusions in minerals by the cryometric method. Geol. Geofiz. 18/8, 16-27.

Burke E. A. J. (2001) Raman microspectrometry of fluid inclusions. Lithos 55, 139-158.

Burke E. A. J., Lustenhouwer W. J. (1987) The application of a mulitchannel Laser Raman microporbe (MICRODIL-28®) to the analysis of fluid inclusions. Chem. Geol. 61, 11-17.

Carey D. M., Korenowski G. M. (1998) Measurement of the Raman spectrum of liquid water. J. Chem. Phys. 108. Number 7. 2669-2675.

Cathelineau M., Marignac C., Boiron M. C., Gianelli G., Puxeddu M. (1994) Evidence for Li-rich brines and early magmatic-rock interaction in the Larderello geothermal system. Geochim. Cosmochim. Acta 58, 1083-1099.

Chumavskii N. A., Rodnikova M. N., Sirotkin D. A. (2001) Cationic effect in aqueous solutions of 1:1 electrolytes by Raman spectral data. J.Mol. Liq. 91. 81-90.

Colmenero J. R., Fernández L. P., Moreno C., Bahamonde J. R., Barba P., Heredia N., Gonzáles F. (2002): Carboniferous. In: Gibson W. and Moreno M. T. (Eds). The Geology of Spain. Geological Society, London. 93-116.

Crawford M. L. (1981) Phase equilibria in aqueous fluid inclusions. In: Hollister L.S., Crawford M.L. (Eds.), Short course in fluid inclusions. Applications to Petrology. Mineralogical Association of Canada 6, 75-100.

Davis D. W., Lowenstein T. K., Spencer R. J. (1990) Melting behaviour of fluid inclusions in laboratory-grown halite crystals in the systems NaCl-H_2O, NaCl-KCl-H_2O, NaCl-$MgCl_2$-H_2O, and NaCl-$CaCl_2$-H_2O. Geochim. Cosmochim. Acta 54, 591-601.

Derome, D., Cathelineau M., Fabre C., Boiron M. C., Banks, D., Lhomme T., Cuney M. (2007) Paleo-fluid composition determined from individual fluid inclusions by Raman and LIBS: Application to mid-proterozoic evaporitic Na-Ca brines (Alligator Rivers Uranium Field, northern territories, Australia). Chem. Geol. 237, 240-254.

Diamond L. (2003) Systematics of H_2O inclusions. In: Samson I., Anderson A., Marshall D. (Eds.). Fluid inclusions. Analysis and Interpreation. Short Course 32. Mineralogical Association of Canada. 55-79.

Dubessy J., Audeoud D., Wilkins R., Kosztolanyi C. (1982) The use of the Raman microprobe MOLE in the determination of the electrolytes dissolved In the aqueous phase of fluid inclusions. Chem. Geol. 37. 137-150.

Dubessy J., Boiron, M. C., Moissette A., Monnin C., Sretenskaya N. (1992) Determinations of water, hydrates and pH in fluid inclusions by micro-Raman spectroscopy. Eur. J. Mineral. 4. 885-894.

Dubessy J., Guillaume D., Buschaert S., Fabre C, Pironon J. (2000) Production of synthetic fluid inclusions in the H_2O-CH_4-NaCl system using laser-ablation in fluorite and quartz. Eur. J. Mineral. 12, 1083-1091.

Dubessy J., Lhomme T., Boiron M. C., Rull F. (2002) Determination of chlorinity in aqueous fluids using Raman spectroscopy of the strecthing band of water at room temperature: Application to fluid inclusions. Appl. Spectrosc. 56. 99-106.

Dubois M., Marignac C. (1997) The H_2O-NaCl-$MgCl_2$ ternary phase diagram with special application to fluid inclusion studies. Econ. Geol. 92, 114-119.

Fortes A. (2004) Computational and experimental studies of solids in the ammonia – water system. Ph.D. Thesis, University College London, United Kingdom.

Franks F. (1973) Water, a Comprehensive Treatise. 1. The Physics and Physical Chemistry of Water. 2. Water in Crystalline Hydrates; Aqueous Solutions of Simple Noneletrolytes. Plenum Press. New York, N.Y.

Furić K., Ciglenečki B., Ćosović B. (2000) Raman spectroscopic study of sodium chloride water solutions. J. Mol. Struct. 550-551. 255-234.

García-Alcalde J. L. (1979) North Gondwanan Emsian events. Episodes 20(4). 241-246.

García-Alcalde J. L., Carls P., Pardo Alonso M. V., Sanz López J., Soto F., Truyols-Massoni M., Valenzulea-Ríos J. I. (2002) Devonian. In: Gibson W. and Moreno M. T. (Eds). The Geology of Spain. Geological Society, London. 67-91.

Gasparrini M. (2003) Large-scale hydrothermal dolomitisation in the southwestern Cantabrian Zone (NW Spain): causes and controls of the process and origin of the dolomitising fluids. Doctoral thesis. Ruprecht-Karls-Universität. Heidelberg.

Gasparrini M, Bakker R. J, Bechstädt T. (2006) Characterization of dolomitizing fluids in the Carboniferous of the Cantabrian zone (NW Spain): A fluid inclusion study with cryo-Raman spectroscopy. J Sed Res 76:1304-1322

Gibbson, W. & Moreno, M.T. (Eds) (2002): The Geology of Spain. Geological Society, London.

Gopalakrishnan S., Jungwirth P., Tobias D. J., Allen H. (2005) Air-liquid interfaces of aqueous solutions containing Ammonium and Sulfate: Spectroscopic and molecular dynamics studies. J. Phys.l Chem. B. 109. 8861-8872.

Grimmer J. O. W. (2002) Fluidassoziierte Brekzien als Monitor dolomitisierender und dedolomitisierender Lösungströme in der Kantabrischen Zone (Nordspanien). Doktorarbeit. Ruprecht-Karls-Universität. Heidelberg

Hack A. C., Mavrogenes J. A. (2006) A cold-sealing design for synthesis of fluid inclusions and other hydrothermal experiments in a piston-cylinder apparatus. Am. Mineral. 91, 203-210.

Haynes F. (1985) Determination of fluid inclusion composition by sequential freezing. Econ. Geol. 80, 1436-1439.

Julivert, M. (1971): Décollment tectonics in the Variscan Cordillera of the northwest Spain. American Journal of Sciences, 270, 1-29

Keppler H., Audétat A. (2005) Fluid mineral interaction at high pressure. In: Miletich R. (Eds.) Mineral behaviour at extreme conditions. EMU Notes in Mineralogy 7, 225-251.

Kerrick D. M. (1987) Cold-seal systems. In: Ulmer G. C., Barnes H.L. (Eds.) Hydrothermal Experimental Techniques. John Wiley & sons. New York. 295-319.

Kirgincev, A N., Trusnikova L. N., Lavrent`eva V. G., Rastvorimost neorganiceskich vescest v vode, Spravocnik, Lenningrad Chimija (1972).

Knight C. L., Bodnar R. J. (1989) Synthetic fluid inclusions: IX. Critical PVTX properties of $NaCl-H_2O$ solutions. Geochim. Cosmochim. Acta 53, 3-8.

Kodĕra P., Lexa, J., Rankin, A. H., Fallick, A. E. (2004) Fluid evolution in a subvolcanic Granodiorite pluton related to Fe and Pb-Zn Mineralization, Banská Stiavnica Ore District, Slovakia. Econ. Geol. 99, 1745-1770.

Kodĕra P., Lexa, J., Rankin, A. H., Fallick, A. E. (2005) Epithermal gold veins in a caldera setting: Banská Hodrusa, Slovakia. Miner. Deposita 39, 921-943.

Kodĕra P., Murphy P. J., Rankin A. H. (2003) Retrograde mineral reactions in saline fluid inclusions: The transformation ferropyrosmalite ↔ clinopyroxene. Am. Mineral. 88, 151-158.

Kodĕra P., Radvanec M. (2002) Comparative mineralogical and fluid inclusion study of the Hnús`a-Mútnik talc-magnesite and Miková-Jedl`ovec magnesite deposit (Western Carpathians, Slovakia). Boletim Paranaese de Geociências 50, 131-150.

Kwak T. A. P., Hing Tan T. (1981) The importance of $CaCl_2$ in fluid composition trend – evidence from the King Island (Dolphin) skarn deposit. Econ. Geol. 76, 955-960.

Laemmlein G. (1929) Sekundäre Flüssigkeitseinschlüsse in Mineralien. Z. Kristallogr. 71, 237-256.

Li R., Jiang Z., Chen F., Yang H., Guan Y. (2004) Hydrogen bonded structure of water and aqueous solutions of sodium halides: a Raman spectroscopic study. J. Mol. Struct. 707. 83-88.

Linke W. F. (1958) Solubilities: Inorganic and metal-organic compounds. Volume I, American Chemical Society, Washington.

Linke W. F. (1965) Solubilities: Inorganic and metal-organic compounds. Volume II, American Chemical Society, Washington.

Linke W. F., Seidell A. (1965) Solubilities: Inorganic and metal-organic compounds. Volume II, American Chemical Society, Washington.

Mapa Geologico de España (1998) La Pola de Gordón. Instituto Tecnológico GeoMinero de España. 103. 13-7

Mapa Geologico de España (1997) Riaño. Instituto Tecnológico GeoMinero de España. 105. 15-7

Meisingset K. K., Grønvold F. (1986) Thermodynamic properties and pahse transitions of salt hydrates between 270 and 400 K. J. Chem. Thermodynamics 18, 159-173.

Mernagh T. P., Wilde A. R. (1989) The use of the Raman microprobe for the determination of salinity in fluid inclusions. Geochim. Cosmochim. Acta 53. 765-771.

Ming Chou I., Blank J. G., Goncharov A. F., Mao H., Hemley R. J. (1998) In situ observations of a High-Pressure Phase of H_2O Ice. Science 281, 809-812.

Molnár F., Watkinson D. H., Everest J. O. (1999) Fluid-inclusion characteristics of hydrothermal Cu-Ni-PGE veins in granitic and metavolcanic rocks an the contact of the Little Stobie deposit, Sudburry, Canada. Chem. Geol. 154, 279-301.

Naden J. (1996) CalcicBrine: A Microsoft Excel 5.0 Add-in for calculating salinities from microthermometric data in the system NaCl-$CaCl_2$-H_2O. PACROFI VI, Madison, USA, 97-98.

Nasdala L., Smith D. C., Kaindl R., Ziemann M. A. (2004) Raman spectroscopy: Analytical perspectives in mineralogical research. In: Beran A., Libowitzky E. (Eds.) Spectroscopic metods in mineralogy. EMU Notes in Mineralogy 6, 281-343.

Ni P., Ding J., Rao B. (2006) In situ cryogenic Raman spectroscopic studies on the synthetic fluid inclusions in the systems H_2O and NaCl-H_2O. Chin. Science Bulletin 51, 1108-114.

Oakes C. S., Bodnar R. J., Simonson J. M. (1990) The system NaCl-$CaCl_2$-H_2O: I. The ice liquidus at 1 atm pressure. Geochim. Cosmochim. Acta 54, 603-610.

Pasteris J. D., Wopenka B., Seitz J. C. (1988) Practical aspects of quantitative laser Raman microprobe spectroscopy for the study of fluid inclusions. Geochim. Cosmochim. Acta 52, 979-988.

Pátek J., Klomfar J. (2006) Solid-liquid phase equilibrium in the systems of LiBr-H_2O and LiCl-H_2O. Fluid Phase Equilib. 250. 138-149.

PeakFit^{Tm} 4.11 for Windows$^{®}$ User`s manual (2002) SYSTAT software Inc. 1/4-1/9

Pironon J. (1990) Synthesis of hydrocarbon fluid inclusions at low temperature. Am. Mineral. 75, 226-229.

Potter II R. W., Clynne M. A., Brown D. L. (1978) Freezing point depression of aqueous sodium chloride solutions. Econ. Geol. 73, 284-285.

Prutton C. F., Tower O. F. (1932) The system calcium chloride-magnesium chloride-water at 0, -15, and -30°. J. Amer. Chem. Soc. 54, 3040-3047.

Radvanec M., Koděra P., Prochaska W. (2004) Mg Replacement at the Gemerská Poloma talc-magnesite deposit, Western Carpathians, Slovakia. Acta Petrologica Sinica 20, 773-790.

Radvanec M., Koděra P., Prochaska W. (2004) Mineralogy, fluid inclusion and C, O, Sr isotope study of the Kosice-Medvedia magnesite deposit, Western Carpathians, Slovakia. Acta Petrologica Sinica 20, 856-876.

Rankin A. H., Ramsey M. H., Coles B., Van Langevelde F., Thomas C. R. (1992) The composition of hypersaline, iron-rich granitic fluids based on laser-ICP and Synchotron-XRF microprobe analysis of individual fluid inclusions in topaz, Mole granite, eastern Australia. Geochim. Cosmochim. Acta 56, 67-79.

Roedder E. (1984) Fluid Inclusions. Rev. Mineral. 12.

Rull F. (2002) Structural investigation of water and aqueous solutions by Raman spectroscopy. Pure Appl. Chem.. 74, No.10. 1859-1870.

Rull F., de Saja, J. A. (1986) Effect of electrolyte concentration on the Raman spectra of water in aqueous solutions. J. Raman Spectrosc. 17. 167-172.

Samson, I.M., Walker, R.T., 2000. Cryogenic Raman spectroscopic studies in the system NaCl-$CaCl_2$-H_2O and implications for low-temperature phase behaviour in aqueous fluid inclusions. Can. Mineral. 38, 35-43.

Schiffries C. M. (1990) Liquid-absent aqueous fluid inclusions and phase equilibria in the system $CaCl_2$-NaCl-H_2O. Geochim. Cosmochim. Acta 54, 611-619.

Schmidt Mumm A., Wolfgramm M. (2002) Diagenesis and fluid mobilisation during the evolution of the North German Basin – evidence from fluid inclusions in sulphur isotope analysis. Mar. Pet. Geol. 19, 229-246.

Shelton K. L., Orville P. M. (1980) Formation of synthetic fluid inclusions in natural quartz. Am. Mineral. 65, 1233-1236.

Shepherd T. J., Rankin A. H., Alderton D. H. M. (1985) A practical guide to fluid inclusion studies.

Sorby H. C. (1857) On the microscopical structure of crystals, indicating the origin of minerals and rocks. Quarterly J. Geol. Soc. 14. 453-500.

Spencer R. J., Lowenstein T. (1992) Phase equilibria in the system $MgCl_2$-H_2O. PACROFI IV, 138-141.

Spencer R. J., Møller N., Weare J. H. (1990) The prediction of mineral solubilities in natural water: A chemical equilibrium model for the Na-K-Ca-Mg-Cl-SO_4-H_2O system at temperatures below 25 °C. Geochim. Cosmochim. Acta 54, 575-590.

Sterner S. M., Hall D. L., Bodnar R. J. (1988) Synthetic fluid inclusions. V. Solubility relations in the system NaCl-KCl-H_2O under vapor-saturated conditions. Geochim. Cosmochim. Acta 52, 989-1005.

Teinturier S., Pironon J. (2003) Synthetic fluid inclusions as recorders of microfracture healing and overgrowth formation. Am. Mineral. 88, 1204-1208.

Tipler P.A. (1991) Physics for scientists and engineers. Third edition. Worth Publisher Inc. New York, 1047-1048

Truyols J., Arbizu M. A., García Alcalde J. L., García López S., Méndez Bedia I. Soto F., Truyols Massoni M. (1990) Cantabrian and Palentian Zones. Stratigraphy: Asturian-Leonese Domain (Cantabrian Zone). In: Dallmexer R. D. and Martínez García E. (Eds.) Pre-Mesozoic Geology of Iberia. Springer Verlag, Berlin. 10-19.

Turrell G., Corset J. (1996) Raman microscopy, Developments and applications. Academ. Press. Harcourt Press & Company, London. pp. 463

Ulmer G. C., Barnes H. L. (1987) Hydrothermal experimental techniques. John Wiley & sons. New York

Vanko D. A., Bodnar R. J., Sterner M. (1988) Synthetic fluid inclusions: VIII. Vapor-saturated halite solubility in part of the system NaCl-CaCl2-H2O, with application to fluid inclusions from oceanic hydrothermal systems. Geochim. Cosmochim. Acta 52, 2451-2456.

Vanko D. A., Griffith J. D., Erickson C. L. (1992) Calcium-rich brines and other hydrothermal fluids In fluid inclusions from plutonic rocks, Oceanographer Transform, Mid-Atlantic Ridge. Geochim. Cosmochim. Acta 56, 35-47.

Walrafen G. E. (1962) Raman spectral studies of the effects of electrolytes on water. J. Chem. Phys. 36. 1035-1042.

Williams-Jones A. E., Samson I. M. (1990) Theoretical estimation of halite solubility in the system NaCl-$CaCl_2$-H_2O: Applications to fluid inclusions. Can. Mineral. 28, 299-304.

Wopenka B., Pasteris J. D., Freeman J. J. (1990) Analysis of individual fluid inclusions by Fourier transform infrared and Raman microspectroscopy. Geochim. Cosmochim. Acta 54, 519-533.

Yamaguchi T., Hayashi S, Ohtaki H. (1989) X-ray Diffraction and Raman studies of Zinc(II) chloride hydrate melts, $ZnCl_2$.RH_2O (R= 1.8, 2.5, 3.0, 4.0, and 6.2). J. Phys. Chem. 93, 2620-2625.

Yanatieva C. K. (1946) Polythermal solubilites. Zh. Prikl. Khim.19, 709-722 (in Russian; translated by Berthold R. and Wolfgramm M.).

Yardley B. W. D., Graham J. T. (2002) The origins of salinity in metamorphic fluids. Geofluids 2, 249-256.

Zeng D., Xu W., Voigt W., Yin X. (2008) Thermodynamic study of the system (LiCl + CaCl2 + H2O). J. Chem. Thermodynamics, *article in press.*

Zeng D., Zhou H., Voigt, W. (2007) Thermodynamic consistency of solubility and vapor pressure of a binary saturated salt + water system. II. $CaCl_2$ + H_2O. Fluid Phase Equilib. 253, 1-11.

Zhang Y. G., Frantz J. D. (1987) Determination of the homogenization temperatures and densities of supercritical fluids in the system NaCl-kCl.Cacl2-H2O using synthetic fluid inclusions. Chem. Geol. 64. 335-350.

Zwart E. W. (1995) Fluid inclusions in carbonate rocks and calcite cements. Ph.D. Thesis, Vrije University Amsterdam, Netherlands.

Zwart E.W., Touret L.R. (1994) Melting behaviour and composition of aqueous fluid inclusions in fluorite and calcite: Applications within the system H_2O-$CaCl_2$-NaCl. E. J. Mineral. 6, 773-786.

10. APPENDIX

Table A-1. Properties of deconvolved peaks of ice Raman spectra (experiment 027) at various temperatures using the program PeakFit v. 4.11 (© SYSTAT Software Inc. 2002). a_o is peak intensity, $a3_1$ is peak position , a_2 is half width at full maximum, and φ the fraction of the Gaussian component.

Temperature	Δν	a_0	a_1	a_2	φ
-50 °C	$\Delta\nu_1^{ice}$	2854 (±240)	3076 (±7)	169 (±8)	1.00 (±0.16)
	$\Delta\nu_2^{ice}$	6206 (±598)	3127 (±2)	66 (±2)	0.59 (±0.10)
	$\Delta\nu_3^{ice}$	1142 (±1016)	3175 (±3)	53 (±22)	1.00 (±1.1)
	$\Delta\nu_4^{ice}$	3445 (±854)	3233 (±13)	101 (±23)	1.00 (±0.84)
	$\Delta\nu_5^{ice}$	2901 (±861)	3331 (±13)	119 (±42)	1.00 (±0.72)
	$\Delta\nu_6^{ice}$	2668 (±864)	3417 (±11)	167 (±15)	0.00 (±0.03)
-60 °C	$\Delta\nu_1^{ice}$	3805 (±250)	3089 (±7)	183 (±7)	1.00 (±0.10)
	$\Delta\nu_2^{ice}$	6827 (±432)	3124 (±)	60 (±2)	0.72 (±0.09)
	$\Delta\nu_3^{ice}$	1379 (±518)	3173 (±1)	50 (±11)	1.00 (±0.79)
	$\Delta\nu_4^{ice}$	3609 (±659)	3234 (±7)	96 (±15)	0.97 (±0.60)
	$\Delta\nu_5^{ice}$	3482 (±547)	3331 (±9)	121 (±24)	1.00 (±0.48)
	$\Delta\nu_6^{ice}$	2787 (±574)	3421 (±6)	159 (±8)	0.00 (±0.03)
-70 °C	$\Delta\nu_1^{ice}$	2831 (±621)	3050 (±12)	137 (±11)	1.00 (±0.43)
	$\Delta\nu_2^{ice}$	5688 (±1099)	3117 (±0)	52 (±4)	0.51 (±0.13)
	$\Delta\nu_3^{ice}$	5507 (±973)	3143 (±11)	180 (±18)	1.00 (±0.78)
	$\Delta\nu_4^{ice}$	3325 (±1110)	3235 (±4)	79 (±12)	0.89 (±0.27)
	$\Delta\nu_5^{ice}$	4067 (±330)	3323 (±5)	133 (±16)	1.00 (±0.49)
	$\Delta\nu_6^{ice}$	2751 (±446)	3421 (±5)	151 (±5)	0.03 (±0.04)
-80 °C	$\Delta\nu_1^{ice}$	2373 (±431)	3039 (±14)	127 (±13)	1.00 (±0.40)
	$\Delta\nu_2^{ice}$	6832 (±985)	3115 (±0)	52 (±3)	0.41 (±0.11)
	$\Delta\nu_3^{ice}$	5112 (±990)	3140 (±11)	114 (±16)	1.00 (±0.54)
	$\Delta\nu_4^{ice}$	3408 (±1177)	3234 (±2)	80 (±15)	0.58 (±0.31)
	$\Delta\nu_5^{ice}$	3737 (±386)	3322 (±7)	127 (±18)	1.00 (±0.45)
	$\Delta\nu_6^{ice}$	2873 (±421)	3416 (±4)	152 (±6)	0.00 (±0.03)
-90 °C	$\Delta\nu_1^{ice}$	1945 (±367)	3018 (±6)	109 (±5)	0.72 (±0.22)
	$\Delta\nu_2^{ice}$	8632 (±903)	3113 (±0)	49 (±3)	0.36 (±0.11)
	$\Delta\nu_3^{ice}$	5862 (±762)	3131 (±6)	130 (±16)	1.00 (±0.25)
	$\Delta\nu_4^{ice}$	3292 (±954)	3233 (±1)	74 (±11)	0.58 (±0.28)
	$\Delta\nu_5^{ice}$	4360 (±259)	3321 (±4)	134 (±13)	1.00 (±036)
	$\Delta\nu_6^{ice}$	2868 (±369)	3419 (±3)	145 (±4)	0.00 (±0.04)
-100 °C	$\Delta\nu_1^{ice}$	1862 (±345)	3018 (±8)	102 (±7)	1.00 (±0.30)
	$\Delta\nu_2^{ice}$	10524 (±881)	3110 (±0)	48 (±2)	0.33 (±0.09)
	$\Delta\nu_3^{ice}$	5535 (±779)	3130 (±7)	129 (16)	1.00 (±0.22)
	$\Delta\nu_4^{ice}$	3665 (±1064)	3231 (±1)	72 (±13)	0.36 (±0.30)
	$\Delta\nu_5^{ice}$	4178 (±358)	3318 (±5)	127 (±15)	1.00 (±0.36)
	$\Delta\nu_6^{ice}$	3154 (±399)	3413 (±3)	148 (±5)	0.00 (±0.03)
-110 °C	$\Delta\nu_1^{ice}$	1844 (±251)	3012 (±4)	93 (±4)	0.80 (±0.22)
	$\Delta\nu_2^{ice}$	11076 (±711)	3108 (±0)	44 (±2)	0.35 (±0.08)
	$\Delta\nu_3^{ice}$	6326 (±622)	3122 (±3)	121 (±10)	1.00 (±0.20)
	$\Delta\nu_4^{ice}$	3964 (±716)	3227 (±1)	70 (±8)	0.50 (±0.24)
	$\Delta\nu_5^{ice}$	4597 (±257)	3318 (±3)	136 (±13)	1.00 (±0.33)
	$\Delta\nu_6^{ice}$	2897 (±384)	3418 (±3)	138 (±4)	0.00 (±0.04)
-120 °C	$\Delta\nu_1^{ice}$	1598 (±180)	3009 (±3)	85 (±4)	1.00 (±0.23)
	$\Delta\nu_2^{ice}$	12535 (±557)	3106 (±0)	42 (±1)	0.29 (±0.06)
	$\Delta\nu_3^{ice}$	5785 (±501)	3120 (±3)	119 (±9)	1.00 (±0.17)
	$\Delta\nu_4^{ice}$	4285 (±709)	3226 (±1)	70 (±8)	0.31 (±0.22)
	$\Delta\nu_5^{ice}$	4371 (±290)	3318 (±3)	132 (±13)	1.00 (±0.29)
	$\Delta\nu_6^{ice}$	2863 (±343)	3415 (±2)	135 (±4)	0.00 (±0.04)
-130 °C	$\Delta\nu_1^{ice}$	1459 (±154)	3005 (±2)	77 (±3)	1.00 (±0.24)
	$\Delta\nu_2^{ice}$	16164 (±526)	3103 (±0)	42 (±1)	0.22 (±0.04)
	$\Delta\nu_3^{ice}$	5418 (±447)	3120 (±4)	126 (±9)	1.00 (±0.15)
	$\Delta\nu_4^{ice}$	4580 (±659)	3224 (±0)	65 (±6)	0.26 (±0.19)
	$\Delta\nu_5^{ice}$	4727 (±259)	3315 (±3)	131 (±11)	1.00 (±0.27)
	$\Delta\nu_6^{ice}$	3136 (±331)	3413 (±2)	133 (±3)	0.00 (±0.04)

Table A-1. Continued

Temperature	$\Delta\nu$	a_0	a_1	a_2	φ
-140 °C	$\Delta\nu_1^{ice}$	1368 (±170)	3002 (±2)	68 (±4)	1.00 (±0.35)
	$\Delta\nu_2^{ice}$	19791 (±589)	3100 (±0)	39 (±1)	1.18 (±0.04)
	$\Delta\nu_3^{ice}$	5341 (±489)	3118 (±4)	127 (±10)	1.00 (±0.18)
	$\Delta\nu_4^{ice}$	5020 (±799)	3222 (±0)	62 (±7)	0.23 (±0.21)
	$\Delta\nu_5^{ice}$	5156 (±309)	3315 (±3)	134 (±13)	1.00 (±0.30)
	$\Delta\nu_6^{ice}$	3178 (±415)	3415 (±2)	125 (±3)	0.00 (±0.05)
-150 °C	$\Delta\nu_1^{ice}$	1237 (±136)	3003 (±2)	65 (±3)	1.00 (±0.30)
	$\Delta\nu_2^{ice}$	21523 (±479)	3098 (±0)	38 (±1)	0.14 (±0.03)
	$\Delta\nu_3^{ice}$	4353 (±393)	3118 (±6)	120 (±11)	1.00 (±0.21)
	$\Delta\nu_4^{ice}$	5332 (±866)	3221 (±0)	63 (±9)	0.08 (±0.21)
	$\Delta\nu_5^{ice}$	4493 (±412)	3313 (±3)	124 (±14)	1.00 (±0.34)
	$\Delta\nu_6^{ice}$	35559 (±403)	3408 (±3)	136 (±3)	0.00 (±0.03)
-160 °C	$\Delta\nu_1^{ice}$	1083 (±119)	3003 (±2)	61 (±3)	1.00 (±0.35)
	$\Delta\nu_2^{ice}$	23657 (±394)	3097 (±0)	36 (±0)	0.11 (±0.03)
	$\Delta\nu_3^{ice}$	3669 (±329)	3121 (±7)	121 (±11)	1.00 (±0.24)
	$\Delta\nu_4^{ice}$	5495 (±802)	3220 (±0)	59 (±8)	0.00 (±0.19)
	$\Delta\nu_5^{ice}$	4439 (±378)	3312 (±3)	122 (±13)	1.00 (±0.34)
	$\Delta\nu_6^{ice}$	3348 (±367)	3407 (±3)	135 (±3)	0.00 (±0.03)
-170 °C	$\Delta\nu_1^{ice}$	949 (±102)	3000 (±1)	52 (±3)	1.00 (±0.45)
	$\Delta\nu_2^{ice}$	27532 (±366)	3094 (±0)	33 (±0)	0.13 (0.02)
	$\Delta\nu_3^{ice}$	4043 (±235)	3117 (±5)	116 (±8)	1.00 (±0.20)
	$\Delta\nu_4^{ice}$	5986 (±712)	3217 (±0)	57 (±6)	0.04 (±0.16)
	$\Delta\nu_5^{ice}$	4812 (±339)	3312 (±2)	126 (±13)	1.00 (±0.32)
	$\Delta\nu_6^{ice}$	3305 (±395)	3409 (±3)	128 (±3)	0.00 (±0.04)
-180 °C	$\Delta\nu_1^{ice}$	733 (±86)	3002 (±1)	52 (±3)	1.00 (±0.59)
	$\Delta\nu_2^{ice}$	30097 (±316)	3092 (±0)	31 (±0)	0.06 (±0.02)
	$\Delta\nu_3^{ice}$	3076 (±183)	3126 (±6)	113 (±6)	1.00 (±0.27)
	$\Delta\nu_4^{ice}$	5961 (±564)	3216 (±0)	51 (±4)	0.00 (±0.12)
	$\Delta\nu_5^{ice}$	4740 (±267)	3312 (±2)	127 (±11)	1.00 (±0.30)
	$\Delta\nu_6^{ice}$	3110 (±360)	3410 (±2)	122 (±2)	0.00 (±0.04)
-190 °C	$\Delta\nu_1^{ice}$	579 (±97)	3000 (±2)	47 (±4)	1.00 (±0.92)
	$\Delta\nu_2^{ice}$	32894 (±320)	3090 (±0)	30 (±0)	0.08 (±0.02)
	$\Delta\nu_3^{ice}$	3082 (±172)	3125 (±6)	111 (±6)	1.00 (±0.31)
	$\Delta\nu_4^{ice}$	6034 (±583)	3215 (±0)	49 (±4)	0.00 (±0.13)
	$\Delta\nu_5^{ice}$	4698 (±303)	3310 (±2)	126 (±13)	1.00 (±0.38)
	$\Delta\nu_6^{ice}$	3194 (±433)	3408 (±3)	123 (±3)	0.00 (±0.05)

Table A-2. Properties of deconvolved peaks of hydrohalite/ice Raman spectra (experiment 027) at various temperatures using the program PeakFit v. 4.11 (© SYSTAT Software Inc. 2002). a_o is peak intensity, $a3_1$ is peak position , a_2 is half width at full maximum, and φ the fraction of the Gaussian component.

Temperature / °C	$\Delta\nu$	a_0	a_1	a_2	φ
-40	$\Delta\nu_2^{ice}$	1209 (±47)	3128 (±2)	111 (±4)	0.00 (±0.04)
	$\Delta\nu_4^{ice}$	476 (±57)	3236 (±2)	82 (±10)	1.00 (±1.17)
	$\Delta\nu_1^{HH}$	432 (±57)	3296 (±1)	16 (±3)	0.00 (±0.42)
	$\Delta\nu_2^{HH}$	712 (±54)	3316 (±0)	12 (±1)	0.36 (±0.34)
	$\Delta\nu_3^{HH}$	7216 (±1628)	3406 (±0)	18 (±1)	0.09 (±0.07)
	$\Delta\nu_4^{HH}$	14709 (±1000)	3420 (±0)	15 (±2)	0.00 (±0.30)
	$\Delta\nu_5^{HH}$	7347 (±1157)	3429 (±2)	27 (±1)	0.00 (±0.05)
	$\Delta\nu^{bg}$	1586 (±61)	3441 (±3)	248 (±3)	1.00 (±0.05)
	$\Delta\nu_6^{HH}$	3802 (±34)	3542 (±0)	14 (±0)	0.11 (±0.03)
-60	$\Delta\nu_2^{ice}$	1342 (±34)	3122 (±1)	102 (±3)	0.00 (±0.03)
	$\Delta\nu_4^{ice}$	562 (±39)	3235 (±1)	81 (±6)	1.00 (±0.80)
	$\Delta\nu_1^{HH}$	534 (±51)	3296 (±1)	17 (±2)	0.00 (±0.32)
	$\Delta\nu_2^{HH}$	910 (±51)	3317 (±0)	11 (±1)	0.00 (±0.17)
	$\Delta\nu_3^{HH}$	8854 (±719)	3405 (±0)	16 (±1)	0.10 (±0.02)
	$\Delta\nu_4^{HH}$	20994 (±725)	3420 (±0)	14 (±1)	0.00 (±0.11)
	$\Delta\nu_5^{HH}$	7821 (±868)	3432 (±0)	22 (±0)	0.00 (±0.03)
	$\Delta\nu^{bg}$	1667 (±32)	3448 (±2)	243 (±3)	1.00 (±0.04)
	$\Delta\nu_6^{HH}$	5335 (±34)	3541 (±80)	12 (±0)	0.15 (±0.02)
-80	$\Delta\nu_2^{ice}$	1527 (±37)	3117 (±1)	85 (±3)	0.00 (±0.03)
	$\Delta\nu_4^{ice}$	608 (±38)	3231 (±1)	86 (±5)	1.00 (±0.74)
	$\Delta\nu_1^{HH}$	576 (±48)	3296 (±0)	15 (±2)	0.00 (±0.29)
	$\Delta\nu_2^{HH}$	976 (±48)	3317 (±0)	11 (±1=	0.00 (±0.16)
	$\Delta\nu_3^{HH}$	9362 (±235)	3405 (±0)	14 (±0)	0.13 (±0.02)
	$\Delta\nu_4^{HH}$	24480 (±272)	3420 (±0)	12 (±0)	0.00 (±0.04)
	$\Delta\nu_5^{HH}$	8778 (±347)	3432 (±0)	19 (±0)	0.00 (±0.02)
	$\Delta\nu^{bg}$	1633 (±25)	3467 (±3)	247 (±3)	1.00 (0.04)
	$\Delta\nu_6^{HH}$	5630 (±37)	3540 (±0)	11 (±0)	1.00 (±0.04)
-100	$\Delta\nu_2^{ice}$	2166 (±33)	3112 (±0)	76 (±2)	0.00 (±0.03)
	$\Delta\nu_4^{ice}$	712 (±38)	3230 (±1)	86 (±4)	1.00 (±0.60)
	$\Delta\nu_1^{HH}$	609 (±50)	3297 (±0)	14 (±2)	0.00 (±0.29)
	$\Delta\nu_2^{HH}$	1088 (±52)	3318 (±0)	11 (±1)	0.00 (±0.16)
	$\Delta\nu_3^{HH}$	13340 (±89)	3404 (±0)	12 (±0)	0.14 (±0.01)
	$\Delta\nu_4^{HH}$	31226 (±129)	3420 (±0)	10 (±0)	0.14 (±0.02)
	$\Delta\nu_5^{HH}$	9824 (±139)	3432 (±0)	16 (±0)	0.00 (±0.02)
	$\Delta\nu^{bg}$	1646 (±23)	3438 (±2)	255 (±3)	1.00 (±0.05)
	$\Delta\nu_6^{HH}$	6837 (±44)	3538 (±0)	9 (±0)	0.24 (±0.02)
-120	$\Delta\nu_2^{ice}$	1823 (±49)	3106 (±0)	57 (±2)	0.00 (±0.05)
	$\Delta\nu_4^{ice}$	682 (±33)	3229 (±1)	107 (±9)	0.00 (±0.24)
	$\Delta\nu_1^{HH}$	581 (±45)	3298 (±0)	12 (±2)	0.00 (±0.28)
	$\Delta\nu_2^{HH}$	1062 (±49)	3319 (±0)	10 (±1)	0.00 (±0.16)
	$\Delta\nu_3^{HH}$	13286 (±55)	3404 (±0)	10 (±0)	0.12 (±0.01)
	$\Delta\nu_4^{HH}$	36013 (±80)	3419 (±0)	9 (±0)	0.10 (±0.01)
	$\Delta\nu_5^{HH}$	11281 (±74)	3432 (±0)	13 (±0)	0.00 (±0.01)
	$\Delta\nu^{bg}$	1289 (±28)	3455 (±3)	236 (±4)	1.00 (±0.06)
	$\Delta\nu_6^{HH}$	8026 (±46)	3538 (±0)	8 (±0)	0.21 (±0.02)
-140	$\Delta\nu_2^{ice}$	2052 (±29)	3102 (±0)	49 (±1)	0.00 (±0.04)
	$\Delta\nu_4^{ice}$	759 (±41)	3220 (±2)	74 (±5)	0.00 (±0.17)
	$\Delta\nu_1^{HH}$	660 (±78)	3305 (±2)	65 (±6)	0.58 (±0.58)
	$\Delta\nu_2^{HH}$	844 (±69)	3320 (±0)	7 (±1)	0.43 (±0.40)
	$\Delta\nu_3^{HH}$	16450 (±60)	3403 (±0)	8 (±0)	0.09 (±0.01)
	$\Delta\nu_4^{HH}$	43415 (±67)	3419 (±0)	7 (±0)	0.12 (±0.01)
	$\Delta\nu_5^{HH}$	12801 (±56)	3432 (±0)	11 (±0)	0.00 (±0.01)
	$\Delta\nu^{bg}$	1181 (±28)	3464 (±5)	222 (±7)	1.00 (±0.06)
	$\Delta\nu_6^{HH}$	9093 (±48)	3536 (±0)	8 (±0)	0.36 (±0.02)

Table A-2. Continued

Temperature / °C	$\Delta\nu$	a_0	a_1	a_2	φ
-160	$\Delta\nu_2^{ice}$	2249 (±35)	3097 (±0)	41 (±1)	0.00 (±0.05)
	$\Delta\nu_4^{ice}$	730 (±39)	3220 (±2)	72 (±6)	0.00 (±0.19)
	$\Delta\nu_1^{HH}$	623 (±76)	3306 (±2)	61 (±5)	0.99 (±0.90)
	$\Delta\nu_2^{HH}$	878 (±84)	3320 (±0)	6 (±1)	0.62 (±0.55)
	$\Delta\nu_3^{HH}$	17853 (±74)	3403 (±0)	7 (±0)	0.08 (±0.02)
	$\Delta\nu_4^{HH}$	50985 (±80)	3419 (±0)	6 (±0)	0.14 (±0.01)
	$\Delta\nu_5^{HH}$	16200 (±67)	3432 (±0)	10 (±0)	0.00 (±0.01)
	$\Delta\nu^{bg}$	1035 (±24)	3469 (±5)	220 (±8)	1.00 (±0.09)
	$\Delta\nu_6^{HH}$	10684 (±62)	3537 (±0)	7 (±0)	0.34 (±0.02)
-180	$\Delta\nu_2^{ice}$	3194 (±33)	3093 (±0)	35 (±1)	0.00 (±0.03)
	$\Delta\nu_4^{ice}$	903 (±81)	3216 (±1)	71 (±4)	0.00 (±0.13)
	$\Delta\nu_1^{HH}$	640 (±81)	3306 (±2)	66 (±5)	1.00 (±0.84)
	$\Delta\nu_2^{HH}$	809 (±75)	3321 (±0)	6 (±1)	0.38 (±0.44)
	$\Delta\nu_3^{HH}$	20758 (±71)	3403 (±0)	6 (±0)	0.15 (±0.01)
	$\Delta\nu_4^{HH}$	54875 (±72)	3419 (±0)	6 (±0)	0.17 (±0.01)
	$\Delta\nu_5^{HH}$	15681 (±62)	3434 (±0)	8 (±0)	0.00 (±0.01)
	$\Delta\nu^{bg}$	916 (±27)	3460 (±6)	231 (±9)	1.00 (±0.09)
	$\Delta\nu_6^{HH}$	11247 (±57)	3534 (±0)	7 (±0)	0.44 (±0.02)
-190	$\Delta\nu_2^{ice}$	3527 (±33)	3092 (±0)	32 (±1)	0.00 (±0.03)
	$\Delta\nu_4^{ice}$	811 (±43)	3214 (±1)	62 (±5)	0.00 (±0.14)
	$\Delta\nu_1^{HH}$	697 (±81)	3304 (±2)	61 (±7)	0.00 (±0.35)
	$\Delta\nu_2^{HH}$	914 (±97)	3321 (±0)	6 (±1)	0.00 (±0.33)
	$\Delta\nu_3^{HH}$	21439 (±73)	3402 (±0)	6 (±0)	0.14 (±0.01)
	$\Delta\nu_4^{HH}$	59611 (±77)	3419 (±0)	5 (±0)	0.19 (±0.01)
	$\Delta\nu_5^{HH}$	17027 (±67)	3433 (±0)	8 (±0)	0.00 (±0.01)
	$\Delta\nu^{bg}$	780 (±28)	3462 (±8)	233 (±12)	1.00 (±0.11)
	$\Delta\nu_6^{HH}$	10564 (±63)	3534 (±0)	6 (±0)	0.40 (±0.03)

Table A-3. Properties of deconvolved peaks of antarcticite Raman spectra (experiment 021) at various temperatures using the program PeakFit v. 4.11 (© SYSTAT Software Inc. 2002). a_o is peak intensity, $a3_1$ is peak position , a_2 is half width at full maximum, and φ the fraction of the Gaussian component.

Temperature / °C	Δν	a_0	a_1	a_2	φ
-60	$\Delta\nu_1^{ant}$	1181 (±32)	3238 (±0)	21 (±1)	0.00 (±0.09)
	$\Delta\nu_2^{ant}$	3105 (±268)	3388 (±0)	30 (±1)	1.00 (±0.33)
	$\Delta\nu^{bg}$	2639 (±150)	3399 (±2)	278 (±2)	1.00 (±0.05)
	$\Delta\nu_3^{ant}$	4196 (±194)	3407 (±0)	12 (±0)	1.00 (±0.22)
	$\Delta\nu_4^{ant}$	23761 (±244)	3428 (±0)	20 (±0)	0.00 (±0.02)
	$\Delta\nu_5^{ant}$	7273 (±356)	3435 (±1)	92 (±1)	1.00 (±0.15)
-80	$\Delta\nu_1^{ant}$	1224 (±40)	3241 (±0)	14 (±1)	0.16 (±0.13)
	$\Delta\nu_2^{ant}$	6058 (±410)	3289 (±0)	27 (±1)	1.00 (±0.15)
	$\Delta\nu^{bg}$	7975 (±484)	3407 (±0)	13 (±0)	1.00 (±0.18)
	$\Delta\nu_3^{ant}$	2207 (±269)	3420 (±2)	242 (4)	1.00 (±0.10)
	$\Delta\nu_4^{ant}$	36220 (±727)	3428 (±0)	17 (±0)	0.00 (±0.02)
	$\Delta\nu_5^{ant}$	5372 (±259)	3446 (±4)	76 (±4)	1.00 (0.29)
-80	$\Delta\nu_1^{ant}$	1224 (±40)	3241 (±0)	14 (±1)	0.16 (±0.13)
	$\Delta\nu_2^{ant}$	6058 (±410)	3289 (±0)	27 (±1)	1.00 (±0.15)
	$\Delta\nu^{bg}$	7975 (±484)	3407 (±0)	13 (±0)	1.00 (±0.18)
	$\Delta\nu_3^{ant}$	2207 (±269)	3420 (±2)	242 (4)	1.00 (±0.10)
	$\Delta\nu_4^{ant}$	36220 (±727)	3428 (±0)	17 (±0)	0.00 (±0.02)
	$\Delta\nu_5^{ant}$	5372 (±259)	3446 (±4)	76 (±4)	1.00 (0.29)
-100	$\Delta\nu_1^{ant}$	1482 (±55)	3240 (±0)	13 (±1)	0.33 (±0.16)
	$\Delta\nu_2^{ant}$	8265 (±220)	3389 (±0)	26 (±0)	1.00 (±0.08)
	$\Delta\nu^{bg}$	13635 (±370)	3407 (±0)	13 (±0)	1.00 (±0.10)
	$\Delta\nu_3^{ant}$	2138 (±224)	3417 (±3)	249 (±5)	1.00 (±0.10)
	$\Delta\nu_4^{ant}$	45904 (±654)	3428 (±0)	14 (±0)	0.02 (±0.02)
	$\Delta\nu_5^{ant}$	5341 (±163)	3450 (±3)	72 (±3)	0.99 (±0.28)
-120	$\Delta\nu_1^{ant}$	1868 (±85)	3241 (±0)	13 (±1)	0.53 (±0.24)
	$\Delta\nu_2^{ant}$	9334 (±219)	3389 (±0)	27 (±1)	1.00 (±0.10)
	$\Delta\nu^{bg}$	21121 (±337)	3407 (±0)	13 (±0)	1.00 (±0.08)
	$\Delta\nu_3^{ant}$	1853 (±186)	3410 (±4)	262 (±7)	1.00 (±0.10)
	$\Delta\nu_4^{ant}$	52333 (±573)	3428 (±0)	12 (±0)	0.06 (±0.02)
	$\Delta\nu_5^{ant}$	5289 (±177)	3453 (±3)	71 (±3)	0.71 (±0.22)
-140	$\Delta\nu_1^{ant}$	1584 (±99)	3241 (±0)	12 (±1)	0.58 (±0.33)
	$\Delta\nu_2^{ant}$	8279 (±174)	3389 (±0)	25 (±1)	1.00 (±0.11)
	$\Delta\nu^{bg}$	19969 (±268)	3407 (±0)	13 (±0)	1.00 (±0.08)
	$\Delta\nu_3^{ant}$	1306 (±159)	3412 (±5)	270 (±12)	1.00 (±0.13)
	$\Delta\nu_4^{ant}$	51963 (±411)	3429 (±0)	11 (±0)	0.08 (±0.02)
	$\Delta\nu_5^{ant}$	4203 (±157)	3455 (±2)	68 (±3)	0.66 (±0.23)
-160	$\Delta\nu_1^{ant}$	1264 (±96)	3241 (±0)	12 (±1)	0.32 (±0.32)
	$\Delta\nu_2^{ant}$	6866 (±135)	3387 (±0)	22 (±0)	1.00 ((±0.13)
	$\Delta\nu^{bg}$	17417 (±177)	3407 (±0)	13 (±0)	1.00 (±0.08)
	$\Delta\nu_3^{ant}$	983 (±164)	3426 (±5)	259 (±16)	1.00 (±0.18)
	$\Delta\nu_4^{ant}$	46693 (±308)	3430 (±0)	9 (±0)	0.09 (±0.02)
	$\Delta\nu_5^{ant}$	2924 (±162)	3457 (±2)	62 (±3)	1.00 (±0.39)
-180	$\Delta\nu_1^{ant}$	1394 (±112)	3241 (±0)	11 (±1)	0.32 (±0.34)
	$\Delta\nu_2^{ant}$	9931 (±144)	3387 ± (0)	20 (±0)	1.00 (±0.10)
	$\Delta\nu^{bg}$	24478 (±191)	3407 (±0)	12 (±0)	1.00 (±0.06)
	$\Delta\nu_3^{ant}$	1013 (±200)	3427 (±6)	247 (±18)	1.00 (±0.20)
	$\Delta\nu_4^{ant}$	57524 (±317)	3431 (±0)	8 (±0)	0.08 (0.02)
	$\Delta\nu_5^{ant}$	3457 (±199)	3456 (±2)	60 (±3)	0.75 (±0.32)
-190	$\Delta\nu_1^{ant}$	1315 (±203)	3241 (±1)	11 (±2)	0..33 (±0.65)
	$\Delta\nu_2^{ant}$	7815 (±276)	3386 (±0)	21 (±1)	1.00 (±0.23)
	$\Delta\nu^{bg}$	18876 (±297)	3407 (±0)	13 (0)	1.00 (±0.15)
	$\Delta\nu_3^{ant}$	1020 (±292)	3429 (±8)	251 (±31)	1.00 (±0.32)
	$\Delta\nu_4^{ant}$	58874 (±397)	3430 (±0)	8 (±0)	0.05 (±0.02)
	$\Delta\nu_5^{ant}$	2444 (±312)	3461 (±2)	55 (±5)	1.00 (±0.77)

Table A-4. Properties of deconvolved peaks of a α-tetrahydrate Raman spectrum (experiment 021) at -190 °C, using the program PeakFit v. 4.11 (© SYSTAT Software Inc. 2002). a_o is peak intensity, $a3_1$ is peak position , a_2 is half width at full maximum, and φ the fraction of the Gaussian component.

$\Delta\nu$	a_0	a_1	a_2	φ
$\Delta\nu_1^{\alpha}$	3088 (±861)	3189 (±3)	37 (±3)	0.63 (±0.37)
$\Delta\nu_2^{\alpha}$	3416 (±401)	3220 (±6)	52 (±7)	1.00 (±0.91)
$\Delta\nu^{bg}$	3920 (±3739	3299 (±26)	195 (±22)	1.00 (±0.11)
$\Delta\nu_3^{\alpha}$	18308 (±1054)	3364 (±0)	53 (±2)	0.45 (±0.08)
$\Delta\nu_4^{\alpha}$	17941 (±920)	3422 (±)	25 (±1)	0.19 (±0.06)
$\Delta\nu_5^{\alpha}$	25025 (±6209)	2446 (±0)	18 (±3)	0.13 (±0.23)
$\Delta\nu_6^{\alpha}$	10260 (±5936)	3470 (±4)	46 (±27)	1.00 (±0.43)
$\Delta\nu_7^{\alpha}$	3653 (±3643)	3511 (±38)	53 (±30)	1.00 (±2.02)
$\Delta\nu^{bg}$	2185 (±946)	3543 (±22)	126 (±22)	1.00 (±0.48)

Table A-5. Properties of deconvolved peaks of a γ-tetrahydrate Raman spectrum (experiment 021) at -190 °C, using the program PeakFit v. 4.11 (© SYSTAT Software Inc. 2002). a_o is peak intensity, $a3_1$ is peak position , a_2 is half width at full maximum, and φ the fraction of the Gaussian component.

$\Delta\nu$	a_0	a_1	a_2	φ
$\Delta\nu_1^{\gamma}$	9613 (±297)	3339 (±3)	253 (±3)	1.00 (±0.03)
$\Delta\nu_2^{\gamma}$	6518 (±555)	3403 (±5)	106 (±5)	1.00 (±0.33)
$\Delta\nu_3^{\gamma}$	1161 (±197)	3432 (±0)	19 (±2)	1.00 (±0.72)
$\Delta\nu_4^{\gamma}$	9169 (±760)	3459 (±1)	76 (±3)	0.54 (±0.14)
$\Delta\nu_5^{\gamma}$	3426 (±340)	3533 (±4)	111 (±5)	1.00 (±0.09)

Table A-6. Properties of deconvolved peaks of a sinjarite Raman spectrum (experiment 021) at -190 °C, using the program PeakFit v. 4.11 (© SYSTAT Software Inc. 2002). a_o is peak intensity, $a3_1$ is peak position , a_2 is half width at full maximum, and φ the fraction of the Gaussian component.

$\Delta\nu$	a_0	a_1	a_2	φ
$\Delta\nu_1^{si}$	2481 (±212)	3188 (±1)	45 (±2)	0.34 (±0.14)
$\Delta\nu_2^{si}$	2551 (±770)	3239 (±1)	33 (±3)	1.00 (±0.42)
$\Delta\nu_3^{si}$	2397 (±467)	3278 (±3)	51 (±17)	1.00 (±1.26)
$\Delta\nu_4^{si}$	1358 (±676)	3318 (±1)	21 (±5)	1.00 (±1.19)
$\Delta\nu_5^{si}$	2629 (±624)	3350 (±0)	17 (±2)	1.00 (±0.64)
$\Delta\nu_6^{si}$	10934 (±1739)	3377 (±0)	23 (±2)	0.14 (±0.20)
$\Delta\nu_7^{si}$	8493 (±598)	3393 (±5)	244 (±3)	1.00 (±0.04)
$\Delta\nu_8^{si}$	13668 (±1907)	3403 (±0)	31 (±5)	0.00 (±0.37)
$\Delta\nu_9^{si}$	15397 (±1818)	3426 (±0)	21 (±2)	0.00 (±0.10)
$\Delta\nu_{10}^{si}$	10870 (±253)	3467 (±0)	35 (±1)	0.00 (±0.03)
$\Delta\nu_{11}^{si}$	1874 (±64)	3562 (±0)	23 (±1)	0.90 (±0.24)

Table A-7. Properties of deconvolved peaks of a $MgCl_2{\cdot}12H_2O$ Raman spectrum (experiment 025) at -190 °C, using the program PeakFit v. 4.11 (© SYSTAT Software Inc. 2002). a_o is peak intensity, $a3_1$ is peak position , a_2 is half width at full maximum, and φ the fraction of the Gaussian component.

$\Delta\nu$	a_0	a_1	a_2	φ
$\Delta\nu_2^{ice}$	7280 (±62)	3087 (±0)	35 (±1)	0.12 (±0.03)
$\Delta\nu_1^{Mg12}$	15396 (±828)	3188 (±1)	48 (±1)	0.00 (±0.03)
$\Delta\nu_4^{ice}$	2279 (±803)	3220 (±2)	32 (±14)	1.00 (±2.20)
$\Delta\nu_2^{Mg12}$	1635 (±640)	3249 (±2)	22 (±4)	1.00 (±1.11)
$\Delta\nu_3^{Mg12}$	5586 (±844)	3325 (±0)	38 (±5)	0.05 (±0.24)
$\Delta\nu^{bg}$	8504 (±987)	3378 (±5)	230 (±4)	1.00 (±0.04)
$\Delta\nu_4^{Mg12}$	23694 (±629)	3402 (±0)	30 (±1)	0.00 (±0.04)
$\Delta\nu_5^{Mg12}$	2271 (±152)	3430 (±0)	17 (±1)	1.00 (±0.63)
$\Delta\nu_6^{Mg12}$	884 (±251)	3458 (±0)	8 (±1)	1.00 (±1.98)
$\Delta\nu_7^{Mg12}$	2055 (±174)	3484 (±0)	16 (±1)	1.00 (±0.68)
$\Delta\nu_8^{Mg12}$	16263 (±144)	3511 (±0)	17 (±0)	0.10 (±0.03)

Table A-8. Properties of deconvolved peaks of a $FeCl_2{\cdot}6H_2O$ Raman spectrum (experiment RJB 007) at -190 °C, using the program PeakFit v. 4.11 (© SYSTAT Software Inc. 2002). a_o is peak intensity, $a3_1$ is peak position , a_2 is half width at full maximum, and φ the fraction of the Gaussian component.

$\Delta\nu$	a_0	a_1	a_2	φ
$\Delta\nu_2^{ice}$	10121 (±42)	3086 (±0)	29 (±0)	0.04 (±0.01)
$\Delta\nu_4^{ice}$	1302 (±53)	3210 (±0)	31 (±1)	0.63 (±0.24)
$\Delta\nu_1^{bg}$	2209 (±180)	3312 (±6)	336 (±4)	1.00 (±0.08)
$\Delta\nu_1^{Fe6}$	3849 (±176)	3370 (±0)	17 (±1)	0.80 (±0.22)
$\Delta\nu_2^{Fe6}$	6899 (±239)	3389 (±0)	12 (±0)	0.00 (±0.10)
$\Delta\nu_2^{bg}$	1592 (±473)	3390 (±2)	114 (±6)	1.00 (±0.87)
$\Delta\nu_3^{Fe6}$	10625 (±164)	3411 (±0)	10 (±0)	0.00 (±0.06)
$\Delta\nu_4^{Fe6}$	5602 (±139)	3427 (±0)	13 (±0)	0.00 (±0.05)

Table A-9. Properties of deconvolved peaks of a $LiCl_2{\cdot}nH_2O$ Raman spectrum (experiment 056) at -190 °C, using the program PeakFit v. 4.11 (© SYSTAT Software Inc. 2002). a_o is peak intensity, $a3_1$ is peak position , a_2 is half width at full maximum, and φ the fraction of the Gaussian component.

$\Delta\nu$	a_0	a_1	a_2	φ
$\Delta\nu_1^{Li}$	11879 (±204)	3358 (±0)	22 (±1)	0.00 (±0.05)
$\Delta\nu_2^{Li}$	10129 (±217)	3377 (±0)	19 (±1)	0.00 (±0.06)
$\Delta\nu^{bg}$	2593 (±107)	3389 (±2)	204 (±5)	1.00 (±0.10)

Table A-10. Properties of deconvolved peaks of pure water Raman spectra (experiment 027) at various temperatures using the program PeakFit v. 4.11 (© SYSTAT Software Inc. 2002). a_o is peak intensity, $a3_1$ is peak position , a_2 is half width at full maximum, and φ the fraction of the Gaussian component.

Temperature / °C	Peak	a_0	a_1	a_2	φ
0 °C	1	3545 (±66)	3208 (±1)	216 (±2)	0.62 (±0.02)
	2	4579 (±30)	3420 (±1)	259 (±4)	1.00 (±0.04)
	3	624 (±55)	3619 (1)	108 (±4)	1.00 (±0.30)
20 °C	1	3748 (±70)	3218 (±1)	220 (±2)	0.61 (±0.02)
	2	5333 (±33)	3433 (±1)	257 (±4)	1.00 (±0.03)
	3	789 (±64)	3619 (±1)	108 (±4)	1.00 (±0.26)
40 °C	1	4152 (±83)	3226 (±2)	221 (±2)	0.54 (±0.02)
	2	6510 (±42)	3441 (±1)	256 (±4)	1.00 (±0.03)
	3	1044 (±88)	3618 (±1)	109 (±4)	1.00 (±024)
60 °C	1	3641 (±85)	3231 (±2)	219 (±2)	0.53 (±0.02)
	2	6613 (±46)	3446 (±1)	256 (±5)	1.00 (±0.03)
	3	1098 (±105)	3615 (±1)	116 (±5)	1.00 (±0.24)
80 °C	1	3356 (±110)	3240 (±3)	222 (±3)	0.61 (±0.03)
	2	6736 (±70)	3454 (±1)	248 (±6)	1.00 (±0.04)
	3	1201 (±157)	3612 (±1)	121 (±6)	1.00 (±0.27)
100 °C	1	2748 (±93)	3242 (±3)	215 (±2)	0.51 (±0.02)
	2	6328 (±67)	3456 (1±)	247 (±6)	1.00 (±0.04)
	3	1261 (±177)	3606 (±2)	133 (±6)	1.00 (±0.21)
120 °C	1	2372 (±84)	3246 (±3)	208 (±2)	0.50 (±0.03)
	2	5949 (±86)	3457 (±2)	237 (±8)	1.00 (±0.04)
	3	1556 (±233)	3598 (±2)	149 (±6)	1.00 (±0.13)
140 °C	1	2179 (±92)	3248 (±3)	202 (±3)	0.57 (±0.04)
	2	6111 (±170)	3456 (±5)	230 (±10)	1.00 (±0.05)
	3	2088 (±437)	3589 (±5)	162 (±6)	1.00 (±0.09)
160 °C	1	1852 (±96)	3252 (±4)	194 (±4)	0.56 (±0.06)
	2	4496 (±514)	3435 (±12)	200 (±14)	1.00 (±0.14)
	3	3675 (±684)	3563 (±12)	184 (±7)	1.00 (±0.09)

Table A-11. Properties of the deconvolved peaks obtained from the reference salt solutions using the program PeakFit v. 4.11 (© SYSTAT Software Inc. 2002). a_o is peak intensity, a_1 is peak position , a_2 is half width at full maximum, and φ the fraction of the Gaussian component.

	Peak	a_0	a_1	a_2	φ
H_2O	1	12936 (±90)	3222 (±1)	228 (±1)	0.52 (±0.01)
	2	13741 (±58)	3433 (±0)	230 (±2)	1.00 (0.02)
	3	2310 (±87)	3617 (±1)	106 (±2)	1.00 (0.13)
2 mass% NaCl	1	12608 (±91)	3227 (±1)	230 (±1)	0.53 (±0.01)
	2	14381 (±62)	3437 (±0)	227 (±2)	1.00 (±0.02)
	3	2307 (±91)	3617 (±1)	105 (±2)	1.00 (±0.13)
4 mass% NaCl	1	12518 (±92)	3230 (±1)	230 (±1)	0.53 (±0.01)
	2	15121 (±65)	3440 (±0)	224 (±2)	1.00 (±0.02)
	3	2312 (±95)	3617 (±1)	104 (±2)	1.00 (±0.14
6 mass% NaCl	1	12117 (±88)	3234 (±1)	231 (±1)	0.52 (±0.01)
	2	15491 (±64)	3443 (±0)	222 (±2)	1.00 (±0.02)
	3	2251 (±92)	3617 (±1)	103 (±2)	1.00 (±0.14)
8 mass% NaCl	1	12070 (±91)	3236 (±1)	232 (±1)	0.52 (±0.01)
	2	16349 (±67)	3445 (±0)	220 (±2)	1.00 (±0.02)
	3	2238 (±96)	3617 (±1)	102 (±2)	1.00 (±0.14)
10 mass% NaCl	1	11647 (±89)	3240 (±1)	232 (±1)	0.54 (±0.01)
	2	16640 (±69)	3447 (±0)	217 (±2)	1.00 (±0.02)
	3	2175 (±96)	3616 (±1)	100 (±2)	1.00 (±0.15)
12 mass% NaCl	1	11295 (±87)	3243 (±1)	230 (±1)	0.51 (±0.01)
	2	17223 (±66)	3448 (±0)	215 (2)	1.00 (±0.02)
	3	2149 (±93)	3617 (±1)	99 (±2)	1.00 (±0.15)
14 mass% NaCl	1	11390 (±92)	3246 (±1)	231 (±1)	0.52 (±0.01)
	2	18374 (±72)	3450 (±0)	213 (±2)	1.00 (±0.02)
	3	2185 (±99)	3616 (±1)	99 (±2)	1.00 (±0.15)
16 mass% NaCl	1	11402 (±95)	3250 (±1)	231 (±1)	0.50 (±0.01)
	2	19498 (±76)	3451 (±0)	210 (±1)	1.00 (±0.02)
	3	2239 (±102)	3616 (±1)	98 (±2)	1.00 (±0.15)
18 mass% NaCl	1	10687 (±90)	3253 (±1)	229 (±1)	0.48 (±0.01)
	2	19269 (±73)	3452 (±0)	207 (±1)	1.00 (±0.02)
	3	2139 (±98)	3616 (±1)	96 (2)	1.00 (0.15)
20 mass% NaCl	1	10664 (±93)	3256 (±1)	228 (±1)	0.49 (±0.01)
	2	20400 (±76)	3453 (±0)	204 (±1)	1.00 (±0.02)
	3	2215 (±100)	3616 (±1)	97 (±2)	1.00 (±0.15)
22 mass % NaCl	1	10605 (±104)	3260 (±1)	228 (±1)	0.42 (±0.01)
	2	20558 (±87)	3453 (±0)	200 (±1)	1.00 (±0.02)
	3	2184 (±111)	3617 (±1)	102 (±2)	1.00 (±0.16
24 mass% NaCl	1	10210 (±106)	3264 (±1)	227 (±1)	0.42 (±0.01)
	2	20915 (±90)	3455 (±0)	197 (±1)	1.00 (±0.02)
	3	2196 (±110)	3617 (±1)	102 (±2)	1.00 (±0.15)

Table A-12. Deconvolved values of *Peak1* of the natural negative-crystal-shaped fluid inclusion during the rotation of the sample up to 180°. Measurements were made at six different locations (*m*, *s*, r_1, r_2, r_3, r_4), as shown in Figure 4.5.

Rotation (°)	*m* (cm^{-1})	*s* (cm^{-1})	r_1 (cm^{-1})	r_2 (cm^{-1})	r_3 (cm^{-1})	r_4 (cm^{-1})
0	3234 (±2)	3236 (±2)	3236 (±2)	3232 (±2)	3235 (±2)	3234 (±2)
15	3234 (±2)	3232 (±2)	3236 (±2)	2340 (±3)	3236 (±2)	3234 (±2)
30	3241 (±2)	3240 (±2)	3241 (±2)	3246 (±3)	3242 (±3)	3235 (±2)
45	3244 (±2)	3239 (±2)	3243 (±2)	3254 (±4)	3246 (±3)	3237 (±2)
60	3237 (±2)	3236 (±2)	3239 (±2)	3238 (±3)	3240 (±3)	3234 (±2)
75	3232 (±2)	3233 (±2)	3234 (±2)	3233 (±2)	3233 (±3)	3231 (±2)
90	3233 (±2)	3230 (±2)	3231 (±2)	3233 (±2)	3238 (±3)	3234 (±2)
120	3242 (±2)	3235 (±2)	3239 (±2)	3244 (±3)	3233 (±3)	3236 (±2)
150	3234 (±2)	3236 (±2)	3237 (±2)	3240 (±3)	3235 (±3)	3235 (±2)
180	3231 (±2)	3231 (±2)	3233 (±2)	3234 (±2)	3237 (±3)	3232 (±2)

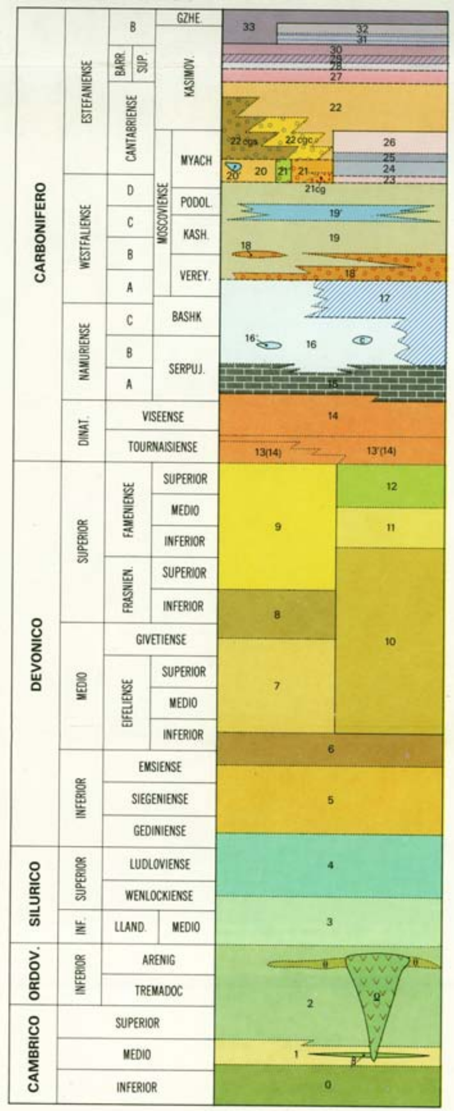

Fig A-1. Legend „Unidades Esla-Valsurvio y Pisuerga Carrion“. Mapa geologico de españa. Sheet: Riano 15-7 (105).

33 Conglomerados, areniscas, lutitas y capas de carbón
32 Areniscas, lutitas y capas de carbón (Fm. Herrera)
31 Areniscas y lutitas (Fm. Quemados)
30 Lutitias, areniscas y capas de carbón (Fm. Sucesiva)
29 Lutitas (Fm. Gonzalo)
28 Lutitas, arensicas y colglomerados (Fw. Raposa)
27 Conglomerados y areniscas (Fm. Alejico)
26 Areniscas, lutitas y capas de carbón (Fm. Prado)
Areniscas y lutitas margosas (Fm. Otero)
Lutitas, arensicas, conglomerados calcáreos y capas de carbón (Fm. Villamonte)
25 Lutitas (Fm. Morgovejo)
24 Areniscas, lutitas, conglomerados calcáreod y capas de carbón (Fm. La Espina)
Areniscas y lutitas (Fm. Los Coralles)
Areniscas, lutitas y capas de carbón (Fm. Viallanueva-Choriza-Acebal)
23 Lutitas, lutitas margosas, areniscas y capas de carbón (Las Heras)
Lutitas, areniscas y capas de carbón (Fm. Tarillonte-Santibañez)
Lutitas y capas de carbón (Fm. Tomasones-Cantoral-Requejeda)
22 Conglomerados, areniscas, lutitas y capas de carbón (Grupo Cea)
cgs-conglomerados silíceos. cgc-conglomerados polimiciticos
cgc-conglomerados sin especificiar
21 Conglomerados silíceos y mixtos
21 Conglomerados (cg) areniscas y lutitas (Gr. Conjas)
20´ Olistolitos calcáreos
20 Lutitas, brechas clacáreas y conglomerados
19´ Calizas (Calizas del Pando)
19 Areniscas, lutitasy (cg) conglomerados (Fm. Lechada)
18 Conglomerados (Fm. Curavacs)
17 Conglomerados calcáareos (Fm. Triollo)
16´ Olistolitos y brechas calcáreas (Fm. Prioro-Perapertú)
16 Lutitas, arensicas, conglomerados
15 Calizas negras
14 Calizas rojas y radiolaritas (Fm. Alba)
13` Lutitas y lutitas negras con nodulos de fosfao (Fm- Vegamian)
13 Calizas (Fm. Bleas)
12 Calizas nodulosas (Fm- Vidrieros)
11 Cuarcitas (Fm. Murcia)
10 Lutitas y calizas nodulosas (Fm. Cardaño-Gustalapierda)
9 Areniscas (Fm- Ermita)
Lutitas (Fm. Fueyo)
Arensicas y calizas (Fm. Nocedo)
8 Calizas y niveles lutiticos (Fm. Portilla)
7 Areniscas y lutitas (Fm. Huergas)
6 Calizas (Fm. Santa Lucía)
5 Dolomías, calizas y lutitas (Grupo La Vid)
4 Arensicas rojas y lutitas (Fm. San Pedro)
3 Lutitas y arensicas (Fm. Formigosa)
2 Cuarcitas (Fm. Barrios)
1 Areniscas y lutitas (Fm. Oville)
0 Dolomías, calizas y calizas rojas (Fm. Lancara)

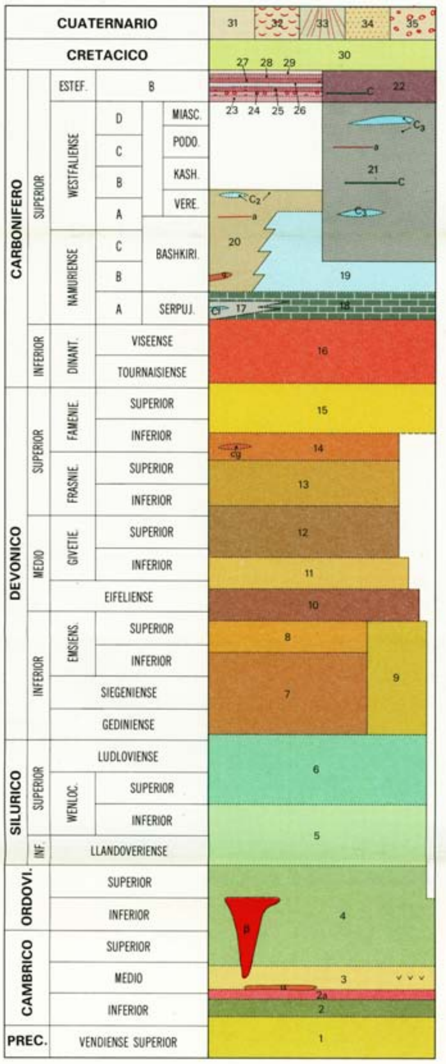

Fig A-2. Legend „La pola de Gordón“. Mapa geologico de españa. Sheet: La Pola de gordón 13-7 (103)

35 Avalanchas de rocas
34 Depósitos glaciares, llanuras y depósitos proglaciares
33 Coluviones, cnachales y abanicos torrenciales
32 Flujos y movimientos en masa
31 Laanura aluvial
30 Arenas y arcillas (Utrillas)
29 Alternancia de areniscas, pizarras y capas de carbón (Fm- Matallana)
28 Areniscas, conglomerados fluviales, lutitas y capas de carbón (Fm. Bienvenidas)
27 Lutitas con carboneros y capas de carbón (Fm. San Jose)
26 Lutitas, areniscas, carboneros y suelos de vegetación (Fm. Roguera)
25 Lutitas arenosas, arensicas y carbones (Fm. Cascajo)
24 Lutitas, arensicas, capas de carbón y colglomerados fluviales (Fm. Pastora)
23 Conglomerados calcáreos y dos capas de carbón (Fm. San Francisco)
22 Conglomerado cuarcíticos, arensicas, lutitas y carbón
21 Alternancia de pizarras y arenisca, limolitas, calizas y algunos carboneros o capas de carbón
20 Calizas grises bioclásticas y/ó bioconstruidas, margas, lutitas, arensicas, brechas clacáreas, conglomerados y capas de carbón (Fm. San Emiliano)
19 Calizas grises claras masivas, bioclástica y bioconstruidas (Fm. Valdeteja)
18 Calizas micríticas negras, fétidas y tableadas, localmente deslizadas (Fm. Barcaliente)
17 Alternancia de lutitas y areniscas en secuendcias turbiditicas con lentejones Cl-Niveles (Fm. Olleros)
16 Calizas encriníticas rosadas y blanquecinas. Lutitas negras, niveles de liditas y nódulos fosfáticos. Calizas rojas nodulosas y algunos niveles de lutitas intercaladas. Intercalación de radiolaritas (Fm. Baleas y/ó Fm. Vegamian y Fm. Genicera-Alba)
15 Areniscas, cuarcitas, areniscas ferruginosas, microconglomerados con intercalaciones de limolitas, lutitas y biocalcernitas en lentejones (Fm. Ermita)
14 Lutitas con nódulos, areniscas en banco finos y conglomerados polimícticos (Fm. Fueyo)
13 Areniscas, arensicas ferruginosas, lutitas y uno o varios tramos de calizas bioclásticas (Fm. Nocedo)
12 Calizas grises bioclásticas y bioconstruídas con niveles intermedios de pizzaras, margas y arensicas (Fm. Portilla)
11 Pizzaras oscuras con algunos niveles de arensicas ferruginosas y niveles con nodulos (Fm. Huergas)
10 Calizas grises bioclásticas con intercalaciones margosas, calizas rojizas bioclásticas y margas rojizas y verdosas (Fm. Santa Lucía)
9 Pizzaras, calizas y dolomías
8 Pizzaras con intercalaciones calcáreas, margas y calizas encriníticas (Fms. Pizzaras de Valporquero y Calizas de Coladilla)
7 Dolomías y calizas bioclásticas (Fmx. Dolomias de Felmín y Calizas de la Pedrosa)
6 Arensicas ferruginosas caon intercalaciones de areniscas blancas y lutitas. Areniscas tobaceas con niveles de tobas vitroaeosas. Niveles con concetnracíon de Lapilli (Fm. San Pedro)
5 Pizzaras negras y marrones con intercalaciones de areniscas ahacia techo (Fm. Formigoso)
4 Areniscas cuarcíticas y arensicas blancas, alternancia de lutitas a arenicas, tonstein de caolinita (Fms. Barrios, Luarca, Gettino y Viodod)
3 Pizzaras verdes, lutitas grises y arensicas. Localmente con perticipación volcánica (Fm. Oville)
2 Calizas y dolomías. Calizas rojas nodulosas a techo (Fm. Láncara)
1 Areniscas, Cuarzoarebitas, lututas, limonitas, calizas y conglomerados (Fm. Herrería)